THE UNIVERSITY
of EDINBURGH

INVESTIGATING THE ROLE OF CHEMICAL AND GEOCHEMICAL TRACERS FOR CO_2 TRANSPORT AND STORAGE

Rachel Kilgallon

Thesis submitted for the degree of Doctor of Philosophy

School of GeoSciences

The University of Edinburgh

2016

Author's declaration

I declare that this thesis has been composed solely by myself and that it has not been submitted, either in whole or in part, in any previous application for a degree. Except where otherwise acknowledged, the work is entirely my own.

Rachel Kilgallon

2016

Abstract

Changes in the atmospheric concentration of greenhouse gases and aerosols alter the energy balance of the climate system. CO_2 is the most significant anthropogenic greenhouse gas. The primary source of the increased atmospheric concentration of CO_2 since the preindustrial period is from fossil fuel exploitation. As the global need for energy is currently met by combustion of fossil fuels it is imperative that a method of reducing the levels of CO_2 being emitted is used.

Carbon capture and storage (CCS) is the combination of CO_2 capture from large point sources, with the transport of CO_2 to a suitable geological storage site where it can safely be contained. Geological CCS technology has the potential to a make a significant contribution to a low carbon technology future. As with any technology, it is imperative to identify techniques that could be used to form part of the monitoring programme. In this thesis, the role of chemical and geochemical tracers are investigated during the transport and storage of CO_2.

For the first part of this research, a review of the natural gas and CO_2 pipeline network in North America and United Kingdom has been compiled from published literature and historical experience. Using this information, research was carried out to determine why odourising has been suggested for CO_2 pipeline transport and what benefit it would add. Based on experience from natural gas, it is concluded that high pressure pipelines of CO_2 through sparsely populated areas could have odourant added, but will gain little safety benefit. However, adding odourant to CO_2 gas phase pipes could aid detection of leaks as well improve public assurance and should be considered in more detail.

For the second part of this research, a specially constructed flow cell was designed and built to investigate how noble gases could be used as effective early warning tracers for CO_2 migration in storage sites. From this equipment, experimental breakthrough curves for noble gases and SF_6 travelling through a sample of Fell sandstone in relation to CO_2 over a pressure gradient range of 10,000 – 50,000 Pa were generated. Although noble gases are described as conservative tracers, comparing the breakthrough curves over a range of pressure gradients show that they do not behave as simply as previously assumed. These results were then modelled using a one dimensional advective dispersion transport equation to fit curves to the experimental outputs using two different modelling approaches. A statistical approach can derive the input parameters for an analytical approach, which is needed to understand the dispersivity behaviour of the tracers. A set of values for the dispersivity of noble gases, SF_6

and CO_2 through porous media is presented in this research. Using a baseline value approach, initial arrival times for krypton and xenon from this research suggest that they could be used as a means of detecting CO_2 migration. While helium, neon and argon appear to be unsuitable as early warning tracers for initial detection of CO_2, this suggests that they can be used as part of mixture to fingerprint individual CO_2 storage sites that may be in close proximity to one another.

Results from the experimental and modelling analysis, identify a system where preferential paths exist depending on the change in pressure gradient. The different transport channels progress from a Darcy linear flow regime to a non-linear laminar flow. These results propose an explanation for the patterns observed from tracers in large-scale reservoirs but the output values obtained are limited by scale-dependence and would not be suitable for direct upscaling.

Lay summary

Gases such as carbon dioxide (CO_2) and methane trap heat in the atmosphere and are known as greenhouse gases. Without these gases, the Earth's surface would be a lot colder than it is today. Anthropogenic (produced by human activity) CO_2 emissions enter the atmosphere through burning fossil fuels, the burning of trees and wood products and the manufacture of certain products such as concrete. CO_2 is naturally removed from the atmosphere by plants (as part of photosynthesis), however, there is more CO_2 being released into the atmosphere faster than plants can remove it. Carbon capture and storage (CCS) is a technology that involves the capture of CO_2 from large sources, such as a power station, transporting it and injecting it into a storage site. CCS can prevent the further release of CO_2 into the atmosphere and limit the effects of changes to the climate. With any technology, it is important that clear monitoring strategies be in place. My thesis investigates ways of monitoring CO_2 while being transported and then stored.

The first part of my thesis investigates the history of transporting CO_2 via pipelines. For many years, CO_2 has been transported globally by pipeline, lorry and ship for commercial reasons. CO_2 for CCS will most likely be transported using pipelines due to the larger distances between CO_2 sources and storage sites. This is very similar to the natural gas transport network. Pure natural gas is odourless, the addition of a smell (called a mercaptan), is to help the public identify any leaks; the same suggestion has been made for CO_2. My research investigates this idea, using the existing experience with natural gas pipelines. My research showed that only very low pressure natural gas pipelines, that enter homes, contain the added smell. The high pressure pipelines that are underground and do not reach populated areas, contain no smell. In addition, there are very few occasions where these pipelines have leaked. Other monitoring methods are regularly used to ensure pipelines are safe. Therefore, it may not be entirely necessary to add odour to CO_2 pipelines; however, it might be worthwhile if it reassures the public.

The second part of my thesis involves tracing CO_2 beneath the surface once it is has been stored. CO_2 will be stored for a long period (>10,000 years). A suitable CO_2 storage site must consist of a reservoir (a rock with many pores/spaces), which the CO_2 fills; it should have a way to trap CO_2 and prevent it from moving to unwanted areas. My research looks at tracers for monitoring the CO_2, by seeing if it has moved. Noble gases are very suitable tracers, as they do not interact with anything and are naturally occurring. My research involved building equipment that represents a CO_2 reservoir, using a 1 m length of rock (sandstone). Pulses of

CO_2, noble gases and sulfur hexafluoride (SF_6) (another popular tracer) were passed through the rock and detected using a specialised piece of equipment called a mass spectrometer. These experiments were completed over a range of low pressures. The timing of each of the tracers provides information about the reservoir as well as how the gases travel between the spaces. Results from this research show that all the tracers take different times to travel through the same length of rock. It also shows that as the pressure increases, the gases will travel through different spaces within the rock. These results show that all the noble gases and SF_6 could be used as early warning signs of CO_2 movement. This research recommends the use of noble gases instead of SF_6 as tracers for CO_2 as SF_6 is also a greenhouse gas that can trap heat in the atmosphere.

Acknowledgments

'Somewhere out there in the vast nothingness of space...

Somewhere far away in space and time…

Staring upwards at the gleaming stars in the obsidian sky…

We're marooned on a small island,

In an endless sea,

Confined to a tiny spit of sand,

Unable to escape

But tonight, on this small planet

On Earth, we're going to rock civilisation.'

PENDULUM

I would never have completed this thesis without the help of so many people. I hope that I remember to mention everyone that has been part of this journey, but those that I have missed is purely down to exhaustion rather than lack of appreciation.

Firstly, much love to all who have shared Room 401 since I arrived. A room of laughter, tears, music (only quality pop tunes of course), golf and support. Thanks to Jen, Niklas, Rudra, Grant, Jamie, Claire, Sophie, Yutong and Nick. Special thanks to Nick and his patience during the final hurdles.

Secondly, gentle squeezes to the lovely people of Melville Terrace, after four years and multiple squatters, I think most of the department has spent a night there. No funny business! Occupants included, but were not limited to, Lukey, Robyn, Amber, Lizzie, Matty, Andrew, Johannes, Matteo, Tom, Jakob, Robyn, Amelia, Nick and Amelia.

There are some super amazing people based in the GeoSciences department. I feel at some point, each one of them has assisted me academically and personally. However, some of them have had to put up me more frequently and deserve special thanks. These people have more patience than I ever could muster - Nicki, Helena, Alan, Jimmy, Alex, everyone in Finance but particularly Denise, Ian, Colin, John, Bob, Richard, Stephanie, Mark N., everyone in Room 400 actually and the folk in IT.

To my friends that I have pestered, snapped at, drank with and ‘occasionally’ spoke with about PhD woes. You have kept me sane during a process that tested me every day. I love you all. Amber, Andrew, Breandán, Cees, Gillian, Gus, Jamie, Jen, Johannes, John, Kit, Lauren, Lizzie, Luke, Maddie, Maddy, Matt, Matteo, Matty, Mike, Neil, Nick, Niklas, Robyn, Romesh, Rory, Sophie and my choir. Definitely missed some people…oh and wine. Thanks wine.

My lovely Ireland pals, thank you for your patience and making time for me when I am home. I miss you every day. Special love to Aisling, Anna, Aoife, Clare, Conor, Foxy, Graham, Peadar, Shana and Viv.

The guidance given by my supervisory team has led me along the winding PhD pathway. Thank you for seeing me the entire way through. Stuart, Chris, Stuart H., Katriona and Mark. Such patience.

My beautiful and loving family. The amount of support you have given me has been incredible. Despite not always understanding what I do, you listened and cared. I hope I have always been a person you could be proud of. D-Bird, G-Dog, Sarah, Cengiz, Mark and my style icon May. Thank you. Special love to Leo and Kaya. I will make you both geologists one day. To my daft brother Peter, you guided me as far as the first day of my life at Edinburgh. You made the journey with me, hugged me when I cried, helped me settle and gave me advice that I have tried to live by. And then you were gone. You have left me more heart broken than I ever thought imaginable but with a strength, I did not know I had.

‘It's just nice to meet another human that shares my affinity for elf culture.’

BUDDY

Table of contents

List of figures

List of tables

Chapter 1 - Introduction and thesis outline

1.1 Introduction

Changes in the atmospheric concentration of greenhouse gases and aerosols alter the energy balance of the climate system (IPCC, 2007). CO_2 is the most significant anthropogenic greenhouse gas. Global atmospheric conditions for the concentrations of CO_2, methane and nitrous oxide have increased markedly since 1750. The global atmospheric concentration of CO_2 has increased from a preindustrial value of 280 ppm to 391 ppm in 2011 (Myhre *et al.*, 2013). It has since surpassed the 400 ppm mark (Figure 1) (NOAA, 2015). The primary source of the increased atmospheric concentration of CO_2 since the preindustrial period is from fossil fuel exploitation. The global need for energy is currently met by combustion of fossil fuels; emissions from fossil fuel combustion from countries in the Organisation for Economic Co-operation and Development (OECD) equated to 12 Gt CO_2 in 2013. Over 84% of the energy consumption for the United Kingdom came from fossil fuels in 2010-2014 (OECD/IEA, 2015). Fossil fuels are likely to remain one of the primary sources of energy for decades to come (Haszeldine, 2009). As such, it is imperative to find a method of reducing the levels of CO_2 emitted from fossil fuel combustion.

Carbon capture and storage (CCS) is the combination of CO_2 capture from large point sources, with the transport of the CO_2 to a suitable geological storage location where it can safely be contained. This technology was first conceived in the 1970's but it is only in the last 10 years that small-scale pilot projects have been established (Markusson *et al.*, 2012). As with any technology, it is imperative to identify techniques that could be used to form part of the monitoring programme. A monitoring programme detects any unplanned deviations to a system and can be an active or passive approach, depending on the timeframes and methods involved. One of the risks associated with CCS involves the unplanned release and leakage of CO_2 during transport, injection and storage. This research investigates the role of chemical and geochemical tracers as a means of monitoring CO_2 transport and storage. My PhD research aims to tackle these concerns by approaching two distinct areas of research; the first part of the research explores the necessity of odourising CO_2 pipelines. This is a social history review and investigates the importance of public perception of CO_2 transport and wider acceptance of CCS technology. The objective of this research is to explore why odourising has been suggested for CO_2 pipeline transport and whether it would be worthwhile. The second part of

the research investigates how noble gases may be used as effective early warning tracers of CO_2 migration in engineered storage sites. The objective of this work is to compare transport models to experimental breakthrough curves for noble gases travelling through porous media in relation to CO_2.

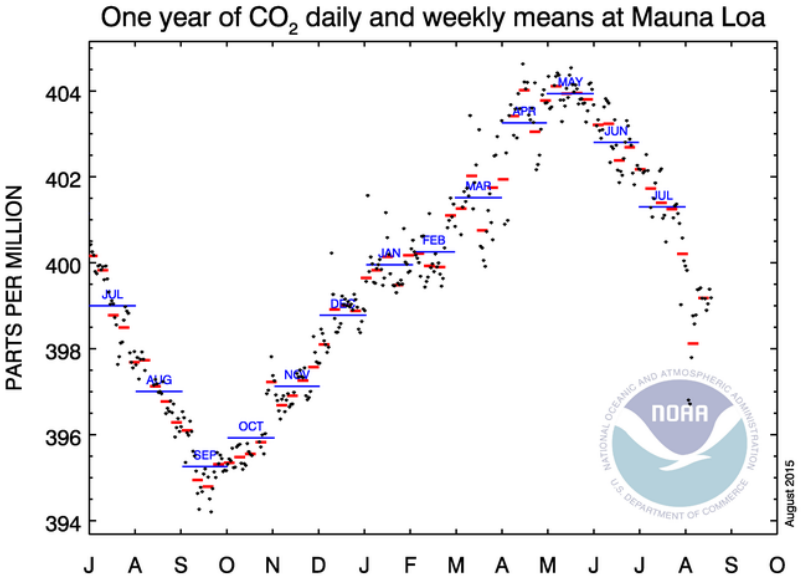

Figure 1: One year of CO_2 daily and weekly means (ppm) at Mauna Loa. Preliminary weekly (red line), monthly (blue line) and daily (black points) averages for the past year (NOAA, 2015).

This chapter is an introduction to CCS that describes the key processes involved with a particular emphasis on current experience of monitoring and the importance of public perception.

1.2 Background and literature review

1.2.1 What is carbon capture and storage?

The capture and long-term storage of CO_2 in the subsurface is one of the most significant methods of mitigating the current level of CO_2 being released from large power and industrial point sources (Edenhofer *et al.*, 2014, Haszeldine, 2009). Carbon capture and storage (CCS) is a technology that involves the separation of CO_2 from large point sources, such as power stations; once it is separated the CO_2 is transported and stored under secure conditions (Figure 2). The result is that the CO_2 is removed from the atmosphere and stored safely and indefinitely to mitigate any climatic impact. The CCS process can be divided into three distinct steps before the CO_2 can be considered safely stored – capture, transport and injection/storage.

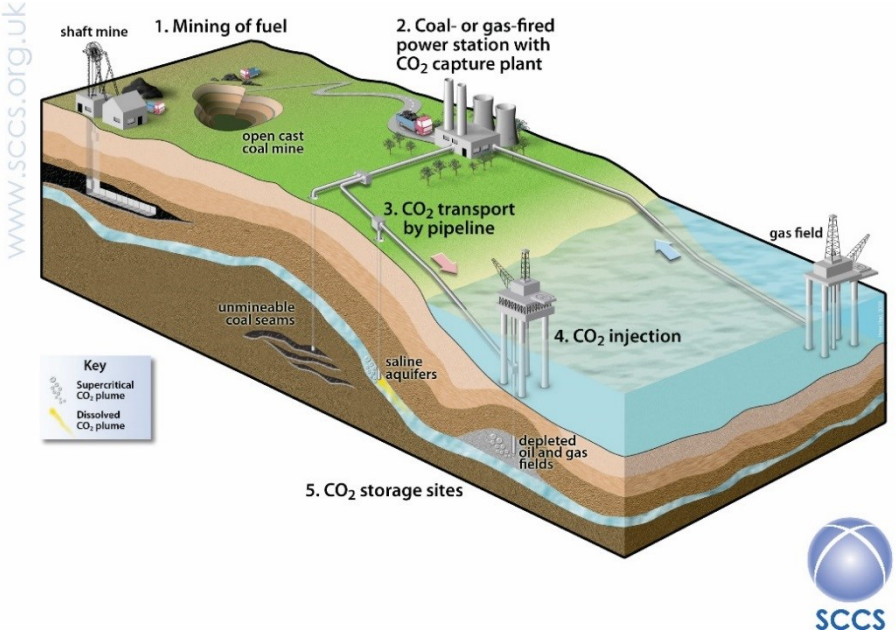

Figure 2: Illustration showing the life cycle chain of fossil fuel use when integrated with CCS. CO_2 is captured from a point source and transported to a suitable storage site. Figure credit to SCCS, www.sccs.org.uk.

1.2.1.1 Capturing CO_2

Before CO_2 from an anthropogenic source can be transported and stored, it must first be captured. Initial strategies for CO_2 capture would be for large point sources, such as a power plant; but there have been suggestions for smaller capture units. In 2013, power generation was the largest emitting sector for CO_2 (Figure 3). There are currently three main types of

capture being investigated: pre-combustion, post-combustion and oxy-fuel (Figure 4). These methods involve further sub-divisions of the materials involved in capturing CO_2 (National Energy Technology Laboratory, 2013).

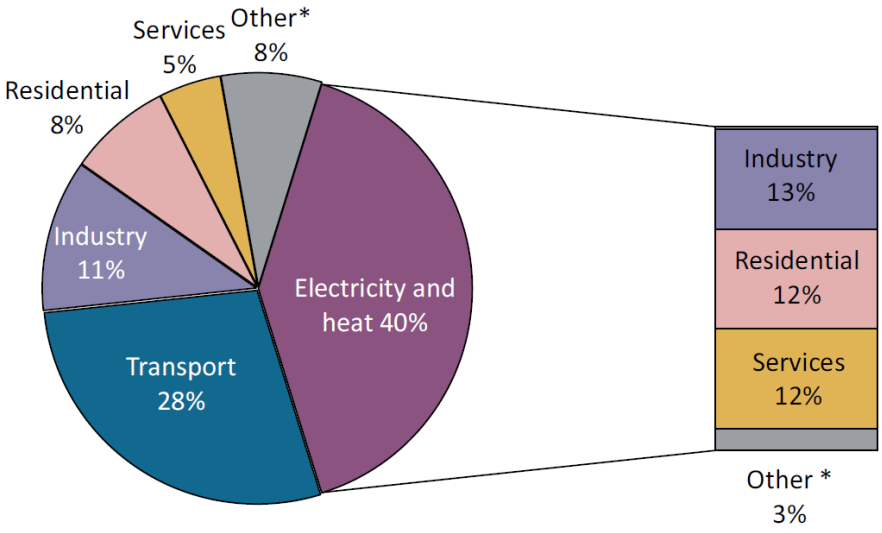

Figure 3: OCED CO_2 emissions by sector for 2013. Other includes agriculture/forestry, fishing and other emissions not specified elsewhere (OECD/IEA, 2015).*

- Pre-combustion

Pre-combustion involves managing the primary fuel into a gaseous mixture of hydrogen and CO_2. Pre-combustion involves an air separation unit, which produces a stream of nearly pure oxygen with nitrogen as a by-product (Yang *et al.*, 2008). This oxygen passes into a gasifier where it reacts with the fuel to produce a syngas (a mixture of hydrogen, CO, water and CO_2) (Yang *et al.*, 2008). Steam is added to the gas in a shift reactor converting the CO into CO_2 and hydrogen. The hydrogen can then be separated and burnt to make electricity. The CO_2 is captured, compressed and dehydrated for transport. The excess heat is recovered and used for steam turbines. The fuel conversion steps for pre-combustion are more complex than that of post-combustion and hence is more suited for installation at new-build power plants.

- Post-combustion

Post-combustion involves capturing CO_2 from the exhaust of a combustion process using a liquid solvent or other separation methods. Fuel is injected into a boiler and combusted in air. This produces steam to power turbines and a flue gas of CO_2, nitrogen and water. This flue gas passes through a chemical wash that separates the CO_2. Once the CO_2 is absorbed by the solvent, the CO_2 is released by heating to form a high purity CO_2 stream. The CO_2 is captured, compressed and dehydrated for transport. Other methods for separating CO_2 include high-pressure membrane filtration, adsorption/desorption process and cryogenic separation (Yang *et al.*, 2008, National Energy Technology Laboratory, 2013). This form of capture can be useful for retrofitting existing power plants and extending the life of the system.

- Oxy-fuel combustion

Oxy-fuel combustion involves the uses of oxygen rather than air for the combustion of the fuel. An air separation unit removes nitrogen from the air producing oxygen that is injected with the fuel into a boiler where combustion takes place (Olajire, 2010). This produces steam and is used to power turbines and make electricity. The flue gas is made up of CO_2 and water vapour. This flue gas is recirculated to control boiler temperature and cooled (Olajire, 2010). The captured CO_2 is compressed and dehydrated for transport.

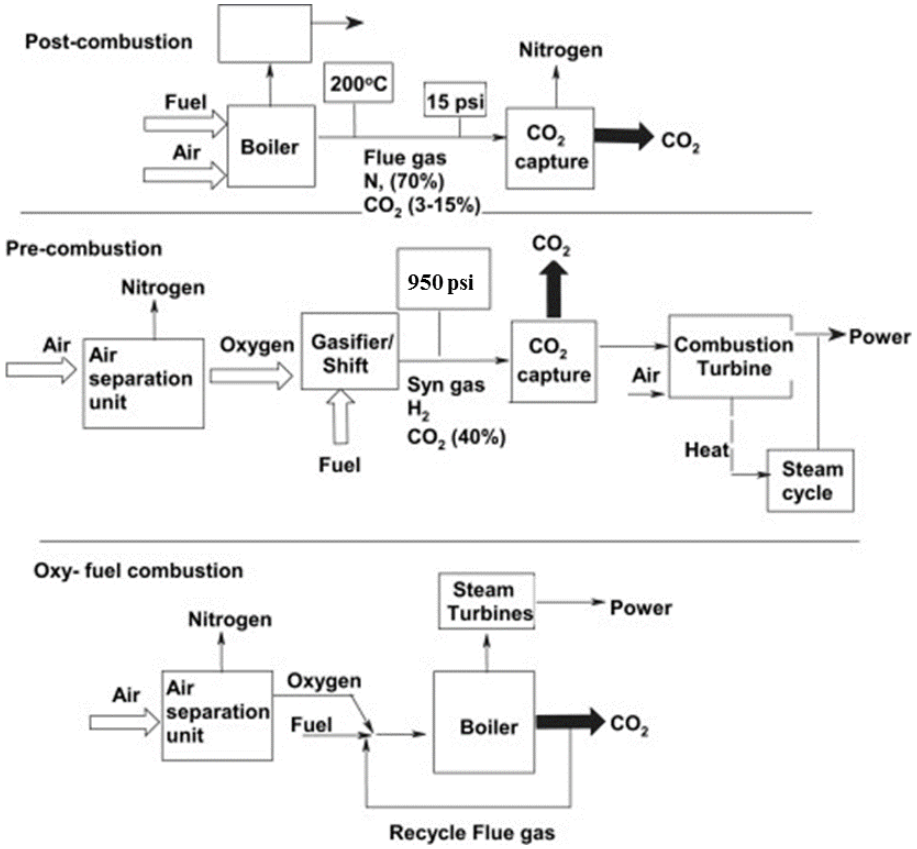

Figure 4: Block diagrams illustrating pre-combustion, pre-combustion and oxy-fuel combustion techniques. Diagram from Olajire (2010).

1.2.1.2 Transporting CO_2

Capturing of CO_2 will initially be carried out at sources, such as power stations, close to a storage site as the process is evaluated. With an increase in scale, it is likely that the sources of CO_2 will not be close to suitable storage sites. This means that the CO_2 will require transportation to these storage sites. Transport refers to the movement of the CO_2 after the capture process until it is safely stored in a suitable location. This can also mean intermediate storage locations. CO_2 for CCS can be transported as a solid, liquid or gas, and is carried out principally by ship or by pipeline (Figure 5). Although other methods can be used, such as rail, these will not be described here, as only ships, pipelines or a combination of these have been proven economically feasible (Svensson *et al.*, 2004). Figure 6 summarises the distance travelled versus the costs involved for both shipping and pipelines.

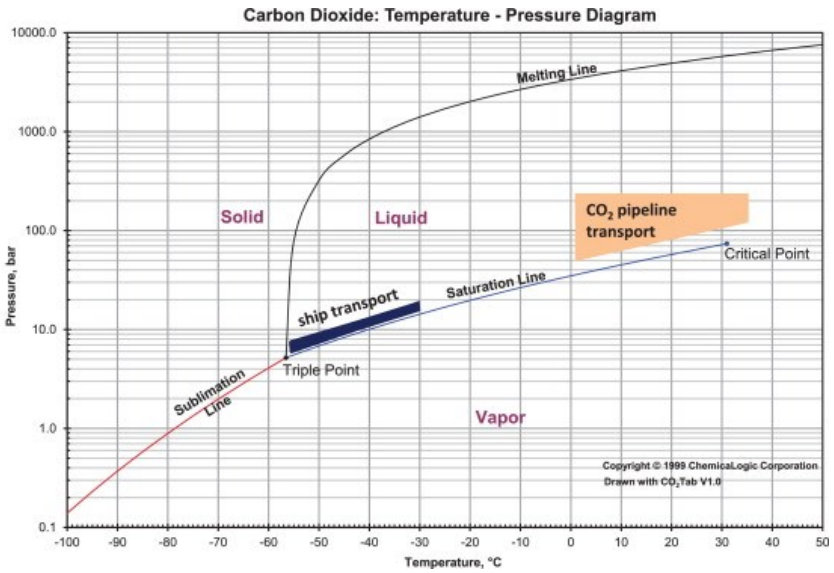

Figure 5: Phase diagram for pure CO_2 with typical operation envelopes for CO_2 ship and pipeline transport (Knoope et al., 2015, Det Norske Veritas, 2010b, ZEP, 2010).

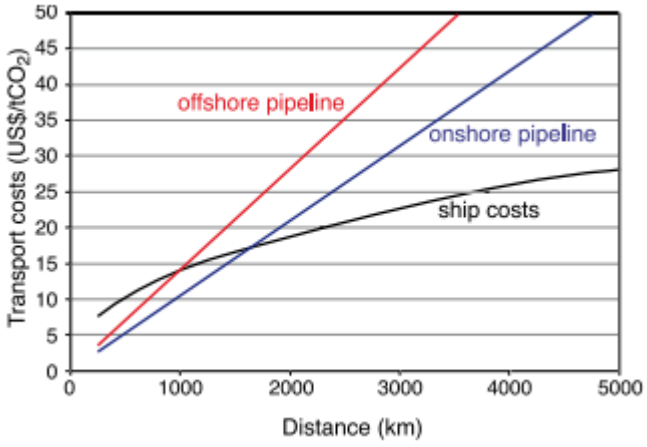

Figure 6: Cost comparison of ship and pipeline transport of CO_2 (Doctor et al., 2005).

- Shipping

Shipment of CO_2 already takes place on a small scale in Europe as part of the food industry (to help increase shelf life of products). These are in the range of 10^8 kg of CO_2 annually (Svensson *et al.*, 2004). Larger scale shipment of CO_2 would be needed for a CCS project and would be similar to the shipment of liquefied petroleum gas (LPG). The concept of using shipping would remove the issue of a single source to sink link in particular for countries where there are no suitable onshore storage locations. Much work has been done to date

investigating the role of shipping for CO_2 transport in terms of costs, efficiency and additional CO_2 emissions. A recent study led by Knoope *et al.* (2015), evaluated the role of ships for CCS. They concluded that ships are preferable for small volumes over large distances (Figure 7).

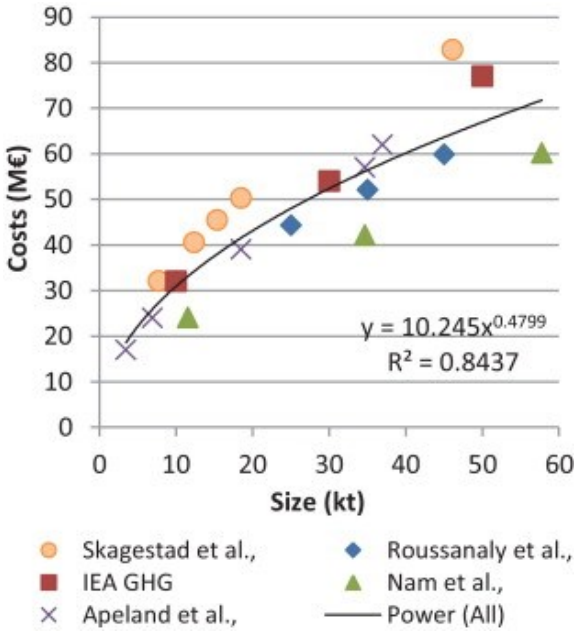

Figure 7: Capital expenditures for CO_2 ships as summarised by Knoope et al. (2015) and references therein.

- Pipelines

Pipelines are and will be the most common method of transporting large quantities of CO_2 for CCS. Approximately 6,000 km of CO_2 pipelines are in operation onshore in North America (Amann, 2010). These have been used for enhanced oil recovery (EOR) since the 1970's with a very low incident rate. For offshore pipelines, the incidence of failure in service is again low (Doctor *et al.*, 2005). Most failures from pipelines are the result of human error.

The scale of pipeline infrastructure needed to support long-term CO_2 transport is considerable. CO_2 in pipelines can be transported in its gas phase or its dense phase although ideally it would be the latter form (as shown in Figure 5). The term dense phase is a collective term for CO_2 when it is either in the supercritical or liquid states. Ideally, CO_2 should be transported in its dense phase, as a smaller pipeline would be needed to provide the same mass flow rate. Issues may arise with two-phase flow where the pressure cannot be maintained, or if there are

impurities within the captured stream. In the existing scenarios for CCS, a CO_2 transport network would evolve from individual pipes to more complex networks where additional sources of CO_2 are progressively fed-in to increase the throughput in a shared 'common-carrier' trunk pipeline (Stewart *et al.*, 2014). In some cases, it may be possible to reuse existing disused pipelines depending on the proposed storage location. This kind of network approach would considerably reduce the costs involved in CCS with proper consideration prior to construction and development. Figure 8 summarises the possible lengths, overall capital cost estimates and capital cost per tonne of CO_2 transported for the different pipeline networks generated for the low, mid and high CCS deployment scenarios in 2030 and 2050 for the European CO_2 transport network.

All Storage Available

Scenario	Total Length (km)	Total Cost (€m)	Cost per Tonne CO2 transported (€)
2030 Low	6879	2074	1.45
2030 Medium	9719	4011	1.16
2030 High	12384	7592	0.78
2050 Low	11775	6785	0.89
2050 Medium	14334	10901	0.65
2050 High	15013	12667	0.58

Offshore Storage Only

Scenario	Total Length (km)	Total Cost (€m)	Cost per Tonne CO2 transported (€)
2030 Low	8971	3434	2.40
2030 Medium	10829	5747	1.66
2030 High	14908	11206	1.15
2050 Low	13746	9560	1.25
2050 Medium	18635	16439	0.98
2050 High	20041	19781	0.90

Offshore Storage Only- No Baltic

Scenario	Total Length (km)	Total Cost (€m)
2050 High	20189	21824

Figure 8: Summary image from Stewart et al. (2014) of CO_2 pipeline network length, and capital costs for 2030 and 2050 deployment scenarios as outlined in the EU Commission Energy Roadmap (European Commission (EC), 2011).

Pipelines have shown to be the most important part of a CCS network to the public (Wallquist *et al.*, 2012). Public attitudes may be influenced not only by any risks or by impact associated with the pipeline itself but by a host of other factors such as a lack of familiarity with the

technology, local, contextual and institutional factors (Gough *et al.*, 2014). Development of pipeline systems can be hindered in certain areas if there is no clear incentive between the benefits gained and how safe pipelines are perceived to be (Wallquist *et al.*, 2012). Odourising CO_2 during pipeline transport as a method of monitoring has been suggested in relation to CCS (Barrie *et al.*, 2004, Gale and Davison, 2004); to date only limited research has been undertaken into how effective or necessary it will be. Existing monitoring strategies in place for CO_2 pipelines will be presented in Chapter 2 and in Table 5.

1.2.1.3 Storage of CO_2

The purpose of the storage site is to trap and keep the CO_2 in place and removed from the atmosphere. Where the CO_2 is stored requires certain characteristics to ensure it is a suitable trap for the CO_2. An effective CO_2 storage site should have a cap rock/seal at the top of the formation to contain the CO_2. It should have a suitable level of porosity and permeability to allow the CO_2 to disperse from the injection site. Typical storage sites include unmineable coal seams, saline formations, and depleted oil and gas reservoirs (or CO_2-EOR) (Figure 9).

- Unmineable coal seams

CO_2 could potentially be stored in seams where it is not financially viable to mine the coal, e.g. where the seam lies too deep. The CO_2 would be held in coal fractures, which create some permeability in the seams. In addition to this, the solid sections of coal have a high number of large micropores that the CO_2 molecules could sorb to. This process could also be of benefit for the fuel industry by forcing out otherwise trapped methane from the coal beds – this is known as enhanced coal bed methane (Holland and Gilfillan, 2013).

- Deep saline formations

Deep rock formations saturated with formation waters or highly concentrated brines are referred to as saline aquifers. These are potentially the largest storage site for CO_2, as they exist worldwide. Prior to CCS research, these had poor commercial use and as a result very little was known about the geology and storage capacity of the aquifers. In the last decade, extensive research has been undertaken to review the theoretical and effective storage efficiency in these deep saline aquifers for CO_2 (Bachu, 2015).

- Depleted oil and gas reservoirs

For several reasons depleted oil and gas reservoirs are viewed as the prime candidates for CO_2 storage. The most apparent reason is the proven ability to trap substances. These reservoirs have retained oil and gas for millions of years. Time, money and research have gone into understanding and quantifying these reservoir sites. The geological structure as well as the physical properties of these fields have been greatly researched. With wells and equipment already in place, these sites have the potential to be converted into CO_2 storage sites with some alteration to the existing infrastructure. CO_2 is currently used in several oil and gas fields for improving the amount of product recovered (offshore at Lula, Brazil and onshore at Weyburn, Canada) (Riding and Rochelle, 2005, Eiken *et al.*, 2011). In these cases, the CO_2 tends to also be recovered and reused. However, a small percentage of the CO_2 is also being simultaneously trapped within the reservoir and the surrounding rock. The use of existing reservoirs also comes with added risks, which can cause changes in initial structure and fluid chemistry due to depressurisation from extraction of oil/gas. Multiple boreholes could become unplanned migration pathways for stored CO_2 to escape leading to potential for changes in CO_2 phases with depth and pressure.

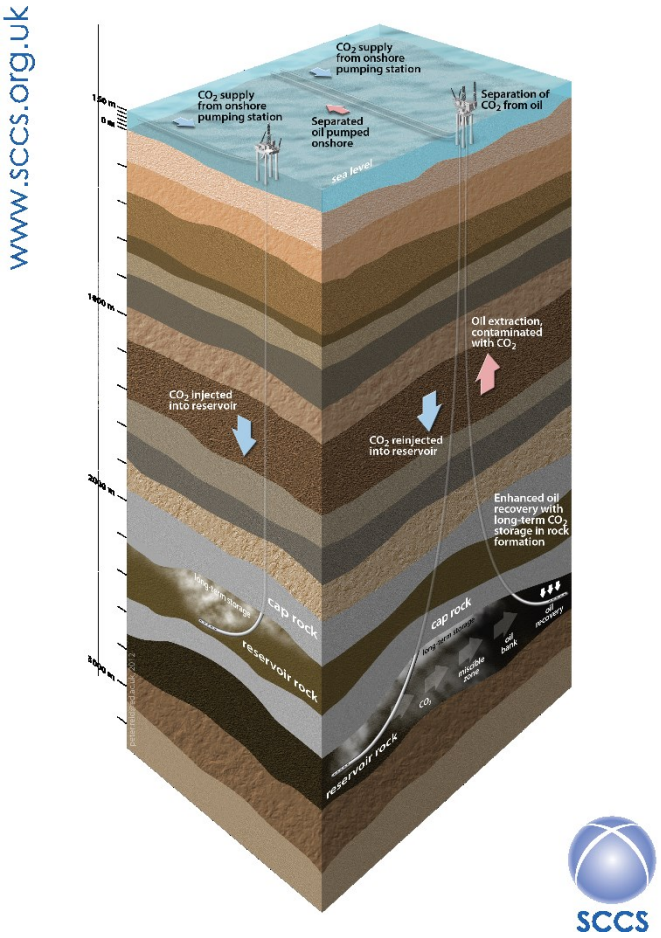

Figure 9: Diagram illustrating offshore storage of CO_2. Figure credit to SCCS (www.sccs.org.uk).

1.2.2 Trapping and transport mechanisms for CO_2 in storage sites

The effectiveness of geological storage relies on how the CO_2 is trapped within the site. There are four ways in which CO_2 can be trapped (Figure 10). Each site is unique, so the proportion of trapped CO_2 in individual sites will vary between locations. The initial trapping method would be structural. As CO_2 is more buoyant than water, it will generally pass upward through the pore spaces until it reaches an impermeable boundary. In terms of underground storage, this normally implies a caprock such as a shale or mudstone. A smaller percentage of CO_2 can be trapped within dead end pore spaces by displacing formation water of the rock as it migrates. This is known as residual trapping. CO_2 will also become trapped by dissolution, whereby the CO_2 dissolves within the formation water. This mechanism will eliminate the buoyant force of the CO_2 and, over time, this denser water will no longer exist as a separate phase. The final type of storage is by mineral trapping. CO_2 dissolved in water forms a weak carbonic acid, which has the potential to react with minerals in the reservoir rock. If the

conditions are suitable, new minerals can form, trapping small amounts of CO_2 within them (Heinemann *et al.*, 2013). This process can be extremely slow and depends on the storage rock composition (presence of carbonate or silicate minerals).

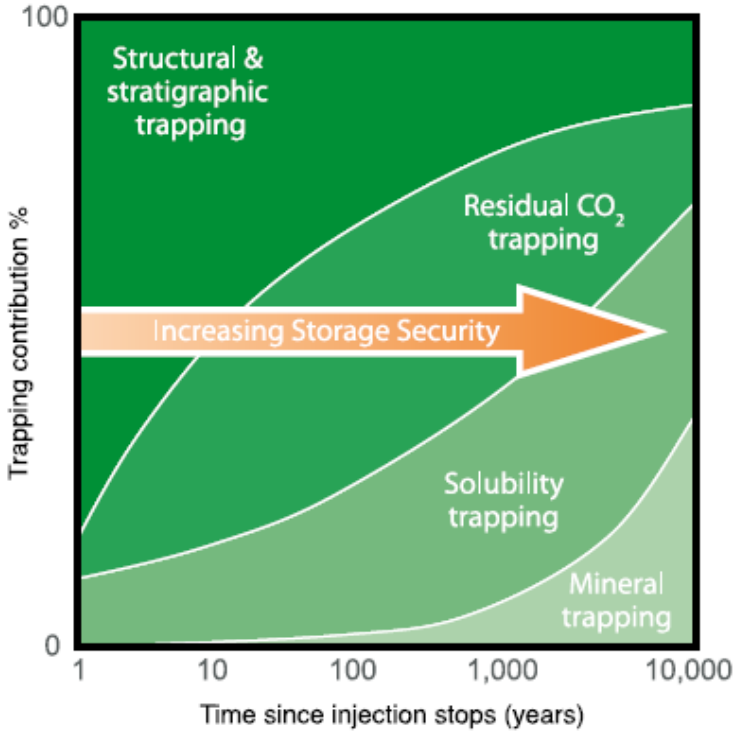

Figure 10: Possible physical and geochemical processes contributing to the trapping of CO_2 in a storage site over time (Benson et al., 2005).

Unplanned migration of CO_2 can be the result of a number of mechanisms that may be the result of human interference to the subsurface during the injection or natural geochemical and geomechanical characteristics of the injection site. After the CO_2 has been injected, it is possible that migration of CO_2 will occur via poorly cemented injection wells. CO_2 injection can lead to an increase in reservoir pressure, which may induce hydraulic fracturing of the structural trap or reactivation of naturally existing faults. The activation of such faults may act as a migration route for CO_2. Similarly, the addition of CO_2 to a formation can increase the pressure of the fluids within the pores of a reservoir and the initial reservoir pressure can change. This shift can exceed the capillary entry pressure of the structural seal and allow CO_2 to migrate through the caprock. When trapping mechanisms fail, lateral migration of CO_2 may also take place. CO_2 can continue to flow as it is dissolved in formation water during solubility

trapping; similarly, a structural trap as such as fault, may fail to prevent boundary crossing. The depth of a CO_2 injection site can determine the phase in which CO_2 would be stored, due to the phase transition of CO_2 with an increase in temperature and pressure gradients (Figure 5). Supercritical CO_2 storage sites would be based in reservoirs with a depth greater than 1 km. Gaseous CO_2 reservoirs may be more likely to leak due to the buoyant nature of gaseous CO_2 compared to supercritical CO_2 where preferential flow paths are available (Edlmann *et al.*, 2013).

1.2.3 Monitoring a CO_2 storage site

The unplanned migration of CO_2 does not necessarily imply that the storage site has failed, thus there is a difference between migration and leakage. Leakage implies that during migration, the CO_2 enters environmentally sensitive regions (e.g. groundwater aquifers, or escaping to the surface) where it may result in damage to the environment, human health or release back into the atmosphere. Monitoring a CO_2 storage site before, during and after injection is vital and a crucial part of the regulatory framework for CCS. Continuous monitoring of a site and the surrounding environment minimises the potential risk of leakage of CO_2, as well improving the opportunity to mitigate any changes that may occur over time (Haszeldine, 2009).

A number of factors should be taken into account when planning a monitoring strategy to be used for a CO_2 storage site. The implementation of baseline measurements prior to injection is crucial; establishing the background measurements for comparison as a project progresses allows a project to identify any unplanned outcomes. Depending on the time scale associated with a CO_2 injection project, it is important that short term and long term monitoring strategies be in place. A monitoring strategy for a storage site should ensure wide spatial coverage with sensitive detection thresholds. Cost should be taken into account when organising the types of monitoring involved, especially for long-term assessment of a storage site. Some methods of monitoring may offer wide spread coverage but low resolution, while others may provide higher accuracy but prove to be significantly more expensive. A range of monitoring techniques are available for CO_2 storage sites that can be applied to deep and shallow focused observations. The type of monitoring chosen will also depend on whether the CO_2 injection site is onshore or offshore. All storage sites will follow different monitoring regimes depending on the injection site location. As a standard, all sites should carry out operational

monitoring; recording any changes identified in temperature gauges, downhole pressures, casing and wellhead integrity as well as fluid sampling (for pH, geochemical and microbial monitoring). The following section will introduce some examples of the additional monitoring approaches used for detecting migration of CO_2, classified under the headings of physical or chemical monitoring approaches.

1.2.3.1 Physical monitoring approaches

Seismic surveys carried out over the lifetime of a storage site can be compared to previous records to determine any changes in the reservoir once the CO_2 has been injected. When acquiring 3D seismic through time, it can be referred to as 4D or time-lapse surveys. These surveys are taken at set time intervals and can be very sensitive to the presence of low levels of CO_2. Seismic surveys have been very successful at tracking CO_2 plume development as part of deep-focussed monitoring. This process has been undertaken at several locations, such as Weyburn Field and Aquistore in Saskatchewan (onshore) and offshore for Sleipner, North Sea, Norway (offshore) (White *et al.*, 2015, Zhu *et al., 2015,* Davis *et al.*, 2003). Shallow seismic techniques and acoustic detection systems have proven to be useful as part of a monitoring regime at the QICS controlled release experiment at Ardmucknish Bay, Scotland (Blackford *et al.*, 2015).

Differential satellite interferometry (DInSAR) uses multiple synthetic aperture radar images gathered from satellites to monitor for millimetre-scale ground displacements (Onuma and Ohkawa, 2009). Remote sensing was used as part of the extensive monitoring strategy (along with 3D seismic surveys) at In Salah, Algeria. The processed, interpreted satellite interferometry data from the In Salah site shows surface displacement (up to 7 mm per year) relating to subsurface pressure increase due to CO_2 injection although no leakage of CO_2 was reported during the lifetime of the project (Onuma and Ohkawa, 2009, Zhang *et al.*, 2015). Injection has since ceased (2011) due to issues with seal integrity because of fault reactivation, identified from analysis of reservoir, seismic and geomechanical data (Stork *et al.*, 2015).

Electrical resistivity tomography (ERT) has been used for monitoring at Ketzin, Germany at the test facility (Schmidt-Hattenberger *et al.*, 2013) as part of its ongoing monitoring strategy. The ERT measurements at Ketzin were taken using electrodes that are permanently installed

behind the casing of the observation wells (Martens *et al.*, 2014). The resistivity of the formation between the electrodes is measured allowing the CO_2 plume to be tracked since it is more resistive than the saline formation fluids. Inversion modelling is then used create a 3D image of sub-surface resistivity and hence how the CO_2 is distributed. Modelling of the reservoirs can also help predict the pathway of the CO_2 over time as well as interactions with the brine. The monitoring at Ketzin pilot site has given no indication of CO_2 leakage.

1.2.3.2 Chemical monitoring approaches

The term 'chemical monitoring' in application to CO_2 injection refers specifically to a substance (solid, liquid or gas) that can be measured to characterise it before, during and after the monitoring process. A chemical tracer can be any substance used to understand the physical movements of fluid through a system. It has been shown that chemical tracers can be complementary to physical monitoring methods (Myers *et al.*, 2013). The majority of tracer applications within CCS are related to either understanding the subsurface, quantifying the trapping capacity or determining containment and leakage rates for monitoring (Myers *et al.*, 2012). The main advantages of chemical tracers are that they can be used to make measurements that are difficult to access physically and can cover large scales. Monitoring injected CO_2 can be challenging, as it is a reactive compound, highly soluble and subject to multiple phases depending on pressure and temperature changes. Thus, the use of chemical tracers that have limited interactions with the injection fluids and surrounding reservoir are the dominant choice; they track fluid pathways of migration by moving at the same rate. These non-reactive types of tracers are described as conservative. Common tracers for CO_2 injection monitoring include synthetic chemicals such as SF_6 and perfluorocarbon tracers (PFTs), isotopic labelled gases and noble gases.

PFTs are a group of synthetic tracers that have been used for atmospheric and subsurface monitoring applications; only a small amount is required to use them as a tracer. There are many different PFTs available to use. Although they are identified as a successful conservative tracer to co-inject with CO_2 to identify breakthrough plumes on short-term scales (McCallum *et al.*, 2005), they are also shown to have longer retention times than expected under certain conditions (Maxfield *et al.*, 2005). SF_6 is another synthetic tracer that has proven to be a successful tracer in monitoring projects such as in groundwater, nuclear testing as well as for CCS sites (Carrigan *et al.*, 1996, Lu *et al.*, 2012, Stalker *et al., 2015*). The Frio brine aquifer

in Texas was part of pilot study based on two small volume CO_2 injections in 2004 and 2006. During the Frio Brine Pilot Test, PFTs and SF_6 (along with noble gases) were used to establish the flow paths and thereby understand the preferential flow for assessing the storage efficiency of geologic CO_2 sequestration The problem of using these synthetic gases is that they are fluorinated. In general, fluorinated gases are the most potent and longest lasting type of greenhouse gas emitted by human activities. SF_6 is 23,900 times more potent that CO_2 when compared over a 100 year period. Although the amount of SF_6 released is low compared to CO_2, it still has a very high global warming potential and a long atmospheric lifetime. There are strict laws in place for the licence to procure this gas in the UK (and EU) (Department for Environment Food and Rural Affairs and Environemnt Agency, 2014). This will limit the access to using it as well as increasing the costs involved.

Isotopic signatures can be naturally present with a system or artificially controlled during injection. At CO_2 sites, carbon isotope compositions can be measured in CO_2 and CH_4 gas samples, as well as oxygen and hydrogen isotopes in brine and groundwater samples (Gilfillan *et al.*, 2009), hydrogen isotopes can also be measured in CH_4 (Stalker *et al.*, 2015). However, complexities arise with this technique when the isotopic signature ranges overlap with different natural sources (Figure 11). Such is the case with natural CO_2 concentration fields as this will overlap with the range for magmatic degassing as well as carbonate breakdown. Thus, different signatures cannot be readily distinguished and may prove to be unsuitable to use as the sole method of monitoring (Holland and Gilfillan, 2013).

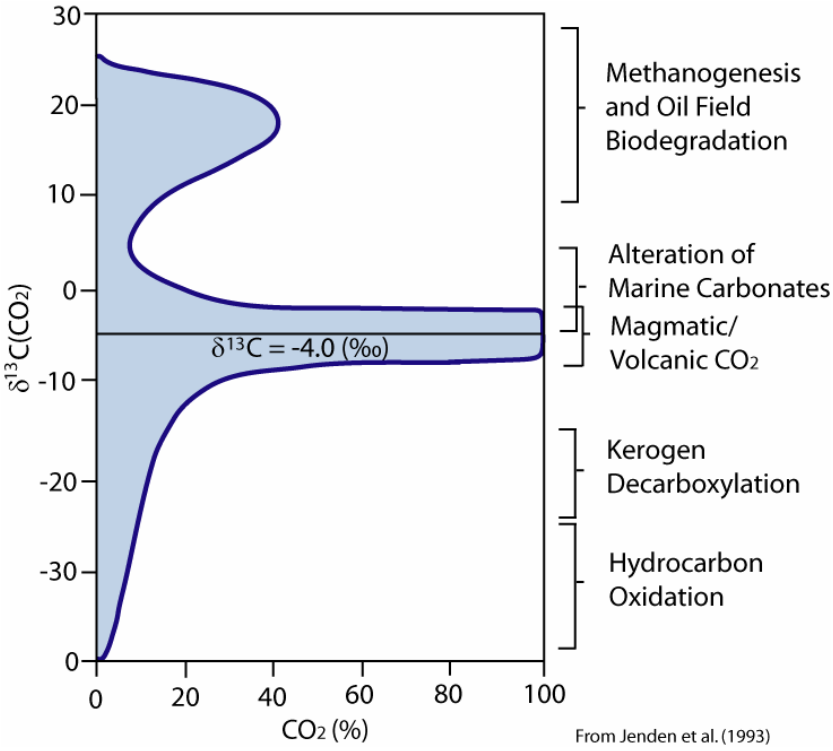

Figure 11:Plot of CO_2 concentration against $\delta^{13}C$ signatures for multiple origins of natural subsurface CO_2 (Jenden et al., 1993).

1.2.3.3 Noble gases as tracers

Noble gases are typically highly unreactive except when under particular extreme conditions. The 'inertness' of noble gases makes them very suitable for applications where observations are required rather that do not involve chemical reactions. Their distribution within an injected site is a result of physical interaction between the matrix and different fluid phases (Warr *et al.*, 2015). As noble gases possess different physical properties due to their atomic mass, induced polarisation and sizes, they each possess a unique response to a dynamic system. Noble gases exist in trace amounts in natural systems. The noble gases and their isotopes are able to provide unique constraints on certain geological processes owing to their inert behaviour, such as the duration of geologic events (Burnard *et al.*, 2013).

The noble gases make up a group of six elements (helium, neon, argon, krypton, xenon and radon), which occupy the last column of the periodic table. Each has stable isotopes associated with them, with exception of radon. Radon is radioactive resulting from the indirect decay of uranium or thorium; its most stable isotope is ^{222}Rn, which has a half-life of 3.8 days. Radon

is best suited for short-term system analysis, such as estimating submarine groundwater discharge (Burnett *et al.*, 2008). As no stable isotopes of radon exist and given their short half-lives, their usefulness as geological tracers in the context of CCS is restricted. Radon will not be discussed further in terms of noble gas use for CCS. Table 1 summarises some of the properties associated with noble gases. For comparative purposes SF_6, a popular tracer for CO_2 monitoring, has been included Table 2.

*Table 1: A selection of the properties of noble gases (NIST, 2002). *Bulk cost personal quote from BOC, 2014.*

	He	Ne	Ar	Kr	Xe
Atomic Number (Z)	2	10	18	36	54
Relative Atomic Mass (A)	4.003	20.180	39.948	83.798	131.293
Natural Stable Isotopes	2	3	3	6	9
Density (273.15 K, 0.1MPa) (g L^{-1})	0.18	0.90	1.78	3.75	5.89
Critical Pressure (MPa)	0.227	2.769	4.898	5.525	5.841
Critical Temperature (K)	5.19	44.50	150.87	209.41	289.77
Triple Point (MPa)	0.0051	0.0432	0.0690	0.0732	0.0816
Triple Point (K)	2.19	24.57	83.81	115.78	161.41
Atomic Radius (pm)	31	38	71	88	108
Van der Waals radius (pm)	140	154	188	202	216
Covalent radius (pm)	28	58	106	116	140
Average Valence Electron Energy (Allen)	4.16	4.79	3.24	2.97	2.58
Bulk Cost*	£44.00	£37	£64	£211	£800
Cylinder Size: 2 L H_2O	250 L	50 L	300 L	50 L	50 L
Cost per L	£0.18	£0.74	£0.21	£4.22	£16.00

Table 2: A selection of the properties of SF_6 and CO_2 (NIST, 2002).

	SF_6	CO_2
Molar Mass ($g\ mol^{-1}$)	146.06	44.01
Density (273.15 K, 0.1MPa) ($g\ L^{-1}$)	6.17	1.98
Critical Pressure (MPa)	3.76	7.38
Critical Temperature (K)	318.65	304.25
Triple Point (MPa)	0.231	0.518
Triple Point (K)	223.55	216.55
Bonds	Single Covalent	Double Covalent
Molecular Shape	Octahedral	Linear
Maximum Atom Distance (pm)	220	235

- Natural production sources of noble gases

Production of noble gases comes from two primary sources – those produced via the cosmic formation of atoms (nucleosynthesis) and isotopes that have been formed by nuclear decay (Holland and Gilfillan, 2013). The noble gases that are "trapped" within the Earth can be classified under three distinct reservoirs – the atmosphere, the crust and the mantle. Figure 12 summarises the different isotopic signatures that can be associated with crustal fluids.

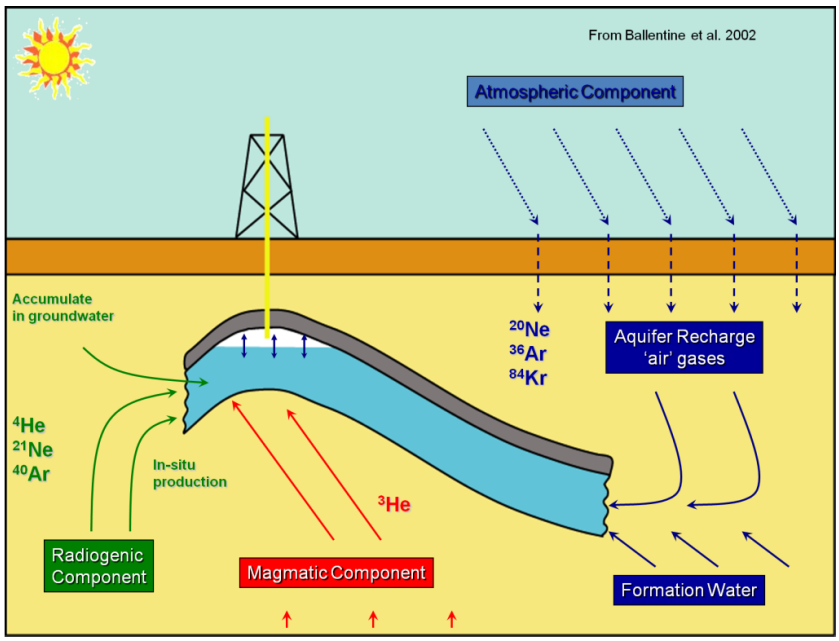

Figure 12: Schematic diagram depicting the different noble gas isotopes which can be found in the three distinct components within the Earth (Ballentine et al., 2002).

- The atmosphere

Due to their volatile nature, much of the noble gases formed in the Earth have been lost into the atmosphere. With the exception of helium, the atmosphere is the primary reservoir of the noble gases (Burnard *et al.*, 2013). The noble gas composition of the atmosphere is well-constrained (Porcelli *et al.*, 2002); as a result, it is commonly used as the standard for comparative data. The atmospheric reservoir was initially formed during early mantle degassing and mirrors the volatile composition during the Earth's accretionary period (Ballentine and Holland, 2008). Helium is supplied to the atmosphere through volcanic activity, fault movements, erosion and groundwater circulation (Sano *et al.*, 2013). Due to its low mass, helium is not retained by the Earth's atmosphere and escapes into space. Therefore, the helium composition of the atmosphere is controlled by rates of outgassing from the mantle/ crust and loss to space. The residence time of helium in the atmosphere is 10^6 years (Sano *et al.*, 2013, Torgersen, 1989), as this is significantly longer than the mixing time of ^{3}He/^{4}He, atmospheric helium can be used as a natural isotope standard. Argon is compositionally the dominant noble gas in the atmosphere (Sano *et al.*, 2013). Argon is the third most common gas in the Earth's atmosphere at 0.93%. It is more than 500 times more dominant than the next noble gas, neon. Argon composition in the atmosphere is dominated by radiogenic ^{40}Ar but it

contains almost the entire inventory of ^{36}Ar (Porcelli *et al.*, 2002). Other key isotopes present in the atmosphere are ^{20}Ne, ^{22}Ne, ^{38}Ar, ^{84}Kr, ^{129}Xe and ^{132}Xe (Porcelli *et al.*, 2002).

- The mantle

Xenon isotopes are of particular interest in the mantle; the presence of excess ^{129}Xe is only produced by the decay of the extinct ^{129}I isotope; and the presence of excess ^{129}Xe in the atmosphere demonstrates that it was partly formed during early in Earth history by massive degassing of the mantle, in the first ~10^8 years (Boulos and Manuel, 1971). Degassing of the mantle continues today measured by the ^{3}He flux. Present day mantle contains both primordial (^{3}He, ^{20}Ne, ^{36}Ar, ^{130}Xe) and radiogenic (^{4}He, ^{40}Ar, ^{129}Xe, ^{136}Xe) isotopes; these vary in different proportions depending on the geological environment (Moreira and Kurz, 2013). Mid Oceanic Ridge Basalts (MORB) and Oceanic Island Basalts (OIB), display these different isotopic ratios of the noble gases. OIBs are thought to originate from mantle plumes; this implies that these are a sample of lower mantle uncontaminated by other noble gas sources. This is in contrast to the relatively homogenous data exhibited by MORB that samples from the upper portion of the convective mantle.

- The crust

The crust behaves both as a source and a reservoir for noble gas isotopes (Figure 12). The noble gas inventory of the crust is extremely variable as it is dependent on several factors including its geological history and composition. The crustal region possesses significant amount of the Earth's radioactive material (Kendrick and Burnard, 2013). The most notable radiogenic isotopes produced in this reservoir are ^{4}He, ^{21}Ne and ^{40}Ar which are produced both directly and indirectly by the decay of ^{235}U, ^{238}U, ^{232}Th and ^{40}K (Ozima and Podosek, 2002). Although ^{3}He is also produced because of this decay, the ^{4}He production rate is much higher (Ozima and Podosek, 2002).

- Noble gases as tracers in CO_2 reservoirs
    - Noble gases as natural environmental tracers

Tracers that track fluid pathways of migration by moving at the same rate are known as conservative tracers. Noble gases exist in trace amounts in natural systems, they can be considered as conservative tracers within natural CO_2 reservoirs. The formation of a natural CO_2 field and its evolution involves the interaction of at least two chemically distinct phases. There can be single events such as the injection of magmatic derived CO_2 into the reservoir or continuous events such as subsurface groundwater migration; it can also be a combination of the two. Natural CO_2 reservoirs are widespread and the released CO_2 can originate from a number of sources (Figure 11) (Gilfillan *et al.*, 2008).

The isotopic and abundance measurements of the noble gases present can be used to constrain CO_2 origins and how it has interacted with the groundwater systems (Holland and Gilfillan, 2013). Early work describes the use of primordial noble gas isotopes (Ballentine *et al.*, 2005) with more recent work assessing the full noble gas data set (Jeandel *et al.*, 2010, Lafortune *et al.*, 2009, Wilkinson *et al.*, 2010, Gilfillan *et al.*, 2008). Noble gas analysis carried out by Gilfillan *et al.* (2008) of samples of CO_2, primarily from the natural CO_2 reservoirs of the Colorado Plateau determined a primarily magmatic origin for the CO_2. The oldest magmatic activity in the region ranged from 42 to 70 Ma and was close to the McElmo Dome reservoir. This implied that the CO_2 in that reservoir had been stored for at least 40 Ma. Natural subsurface CO_2 accumulations can be used as key analogues for how the engineered sites will behave and whether they have the ability to store CO_2 over geological timescales (Wilkinson *et al.*, 2010).

    - Noble gases as artificial environmental tracers

Noble gases become distinctive tracers when non-natural isotopic compositions are used (Nimz and Hudson, 2005). Small amounts of noble gas blends can be intentionally added to the CO_2 being injected for storage and used as tracers to monitor CO_2 movement. This distinct mixture of noble gas isotopic compositions can be identified during monitoring as being associated with injected CO_2.

Noble gas solubility in waters and brines in the crust, and their temperature dependence, are well known (Ballentine *et al.*, 2002, Ballentine and Burnard, 2002, Myers *et al.*, 2012). In reality, there will be partitioning of the noble gases between the CO_2 and other phases present such as water. It is important to quantify the distribution of noble gases between these phases in order to use it effectively as a tracer. Few studies examine how they will behave within two-phase systems (CO_2-water). Recent experimental work carried out by Warr *et al.* (2015) presented data that defines noble gas partitioning in CO_2-water systems. This work identified that at low-pressure conditions, there was no difference between measured noble gas partitioning and what has been presented for noble gas solubility in waters and brines; when the density of the CO_2 increases because of pressure the partition coefficients deviate significantly from a pure noble gas-water system. Thus, noble gas utility is linked to a strong understanding of their physical chemistry within a specific geological system (Warr *et al.*, 2015).

Research undertaken with xenon (Nimz and Hudson, 2005) at the Mabee Enhanced Oil Recovery field in West Texas indicates that unique noble gas isotopic compositions within a CO_2 injection stream can be detected and readily identified in outlying wells. The use of xenon in particular is of interest due to its high number of isotopes. In contrast, earlier research at nuclear testing sites, shows that it would be incorrect to assume that the lighter noble gases will travel the fastest through fractures (Carrigan *et al.*, 1996), the lighter noble gases (such as helium) may be susceptible to diversions that a CO_2 molecule would perhaps be too large to pass through. It does suggest that a xenon tracer could migrate faster than leaking CO_2 and act as an early-warning system (Nimz and Hudson, 2005). Other research has injected krypton (along with SF_6) at Cranfield, Mississippi (Lu *et al.*, 2012) and at the CO2CRC Otway Project, Victoria (Boreham *et al.*, 2011, Stalker *et al.*). The overall trends from these studies will be compared in detail to this research's experimental results, as part of the discussion in Chapter 7.

1.2.4 Public perception and CCS

The management of a robust monitoring strategy is important for the success of a project; it ensures that any safety specifications are adhered to. However, a monitoring programme is also needed to gather the support of the public. Public acceptance of any new technology is crucial to ensure its success. CCS technology is no exception to this. Without the support of

the public, any project can be substantially hindered or even cancelled. There is an ongoing body of social research available that has highlighted the importance of public acceptance. Within these reports, there are reoccurring themes because of the responses made by the public. These key themes have been highlighted by the summary report prepared on behalf of the Global CCS Institute (2013). The themes are interconnected when implementing CCS (Figure 13). Perceptions matter for decision-making (Markusson *et al.*, 2012); by ensuring that all these themes are considered when developing a CCS project, the opportunity for public acceptance is greatly improved. The following section summarises these main headings as presented in Ashworth *et al.* (2013).

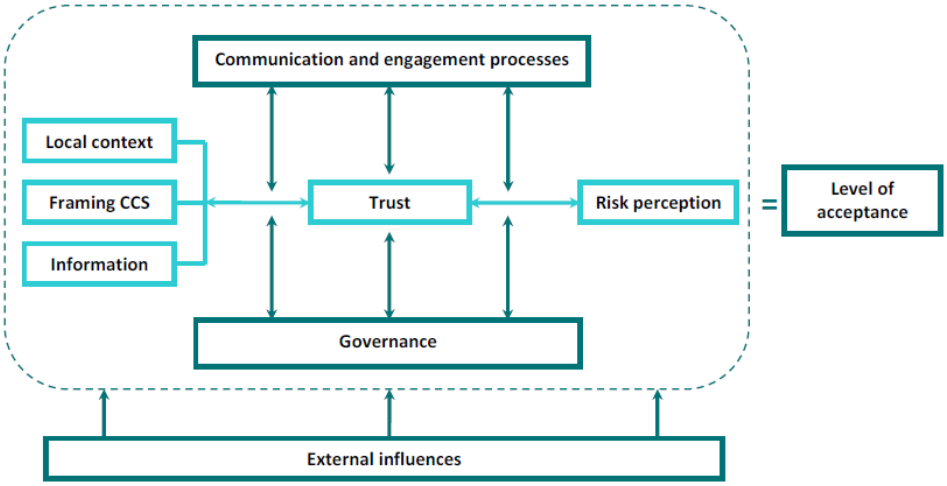

Figure 13: Illustration of the framework of interactions for CCS projects showing how their interactions could assist the success of CCS projects (Ashworth et al., 2013).

a) Framing CCS

There is some difficulty in how to present CCS. Depending on the target audience, the purpose of it being undertaken and their interest in CCS can change. The reasons that an invested stakeholder may want CCS to happen could be very different to that of the local community. From a geoscientist perspective, CCS technology has been viewed as a CO_2 mitigation method; this view comes from an acceptance of climate change. However, perceptions of climate change can range from acceptance to denial. Even those that are well aware of the implications of climate change may not accept the role that CCS has in this. It could be

worthwhile to acknowledge that CCS is one of many low carbon energy alternatives (Ashworth *et al.*, 2013).

b) Local context

The communities in close proximity to CCS projects require attention and support during the planning and developing process (Ashworth *et al.*, 2010). Timing is important and it is crucial to engage early on in a project. Developing this understanding of local communities is crucial to ensuring the smooth deployment of CCS. Available information on the social, political, economic, cultural and ethical landscape of the community needs to be deliberated (Wade and Greenberg, 2011). Communities with existing infrastructure, current employment or historical relationships with related technology might have a positive response to CCS (Reiner and Nuttall, 2011), particularly near existing point sources and storage sites.

c) Trust

Developing and maintaining a high level of trust when developing a CCS project is incredibly important. Development of trust is dependent on a variety of levels, from who delivers the information and how it is shared to develop relationships through open and candid engagement among those involved with the project. Again, timing is important when trying to grow such a relationship by allowing a sufficient amount of time to allow the processing of information (Ashworth *et al.*, 2012). Trust in national non-governmental organisations (NGOs), local NGOs, friends, and the internet, as opposed to public sector organisations, local government, national newspapers, and scientists, was negatively correlated with correct understanding of CCS (Itaoka *et al.*, 2012).

d) Communication and engagement

This theme is closely connected to trust and information. There is much deliberation as to the best way to develop opportunities for engaging stakeholders and the public. The use of best practice approaches and engagement resources for communication can be crucial in the early development of relationships in CCS projects. The establishment of a baseline understanding with the local community is a frequently reoccurring topic – to understand how a CCS project may fit; as well identifying the needs and expectations of the key stakeholders (Ashworth *et al.*, 2012).

e) Information

This theme deals with the availability of information dealing with CCS. It is important that clear, accurate information is available in multiple forums (formal and informal) and with different degrees of complexity (technical and simple) (Ashworth *et al.*, 2013). In conjunction with this, it should be relatable to where CCS fits in the energy network and climate change context. Indeed, exploring the public's knowledge of CO_2, CCS and climate change is important. How the public have developed their initial opinions and where that information came from is important. Additional information provided in interviews, focus groups and surveys were found to promote a better understanding of the topic but ultimately will not change the perceptions on CCS (Itaoka *et al.*, 2012).

f) Risk perception

With any introduction to a new technology, the issue of risk is raised. Depending on the interested party, the risk may be financial, the safety of the public or damage to the environment. The level of risk perception by individuals can be varied; the extent of which is linked to sociological or ideological concerns influenced by factors such as friends, family, fellow workers and public officials (Slovic, 1987). The technologies involved with implementing CCS are complex and difficult to a layperson. Without an understanding how the public think about the risk associated with CCS, policies may be ineffective (Slovic, 1987). Development of sections of the CCS chain, such as pipeline systems, can be hindered in certain areas if there is no clear incentive between the benefits gained and how safe it is perceived to be (Wallquist *et al.*, 2012). In some scenarios, the implementation of certain policies may be the result of demand rather than necessity.

g) Governance

Governance is a term used when decisions are made beyond a 'typical government'; it includes industry, non-government organisations, professional bodies and the wider lay public (Markusson *et al.*, 2012). CCS projects are unusual for determining the 'when and how' degree of governance and responsibility required; the period of a project ranges from initial launching of the CCS chain, to storage on a 'geological' timescale. The restrictions and legal responsibilities should be rationally assigned. Projects require clearly defined processes for

communities and other key stakeholders to provide input into project decisions (Ashworth *et al.*, 2013).

1.2.5 Current status of CCS

CCS is a constantly changing technology. The wide range of projects that are currently in planning, operational or completed, reflects this. Unfortunately, as part of this process, many projects do not make it past the proposition phase. In 2014, 13 schemes were in operation with nine in construction; another 32 projects were in various stages of planning. Partnerships such as SCCS and organisations like Global CCS Institute have catalogued and continuously monitor worldwide CCS progress (Scottish Carbon Capture & Storage, 2015, Global CCS Institute, 2015).

In October 2014, the Boundary Dam, Saskatchewan project became the first post-combustion coal fired CCS project. The project retrofitted a coal fired generation unit so that the CO_2 could be transported by pipeline for CO_2-EOR. Excess CO_2 not required for EOR is accepted for the Aquistore project. Aquistore is an independent research and monitoring project that injects CO_2 into a saline saturated system, which began injecting in April 2015.

In the United Kingdom, there were two CCS demonstration projects applying for the Government's CCS Commercialism Competition funding – Peterhead CCS Project, Aberdeenshire and White Rose CCS Project, North Yorkshire. Both projects are currently completing the Front-End Engineering Design (FEED) phase. Following the 2015 Spending Review and Autumn Statement, this funding is no longer available and the fate of these two projects are currently uncertain.

1.3 Outline of thesis

A major issue regarding acceptance of both CO_2 transport networks and subsurface sites for CCS is the risk of failure of CO_2 containment and the subsequent environmental impact. The primary aim of this study is to investigate the role of chemical and geochemical tracers during the transport and storage of CO_2. To challenge this aim, the body of the thesis has been sub-divided into two distinct areas of research.

a) Odourisation of CO_2 pipelines in the UK: Historical and current impacts of smell during gas transport

The first part of the research is literature based, and in this portion explores the necessity of odourising CO_2 pipelines. This is a social history review and investigates the importance of public perception of CO_2 transport and wider acceptance of CCS technology. The objective of this portion of the research is to explore why odourising has been suggested for CO_2 pipeline transport and whether it would be worthwhile. The International Journal of Greenhouse Gas Control has published this body of work. An extended version of this paper is presented as Chapter 2.

Published as: KILGALLON, R., GILFILLAN, S. M. V., HASZELDINE, R. S. & MCDERMOTT, C. I. 2015. Odourisation of CO_2 pipelines in the UK: Historical and current impacts of smell during gas transport. *International Journal of Greenhouse Gas Control,* 37**,** 504-512.

b) Investigating the role of noble gases as a tracer for CO_2 storage

The second part of the research is primarily laboratory based. It involves the design, construction and implementation of experiments, which investigate the fundamental transport mechanisms for tracers in porous media. The aim of this work is to investigate how noble gases could be used as effective early warning tracers of CO_2 migration in engineered storage sites. The objective of this work is to generate experimental breakthrough curves for noble gases travelling through porous media in relation to CO_2 over a pressure gradient range of 10,000 – 50,000 Pa (0.1 – 0.5 bar). This in turn will assess the physical interaction of noble gases and CO_2 with solids, and investigate the fundamental mechanisms that drive transport in porous media. For comparative purposes SF_6, a popular tracer for CO_2 monitoring, has been

included under the same experimental conditions. This research covers the remainder of the thesis with a chapter division as follows:

Chapter 3: Development of experimental design and method

Prior to the commencement of research, there was no existing layout that could sufficiently provide real-time analysis of gas transport in porous media. For this reason, purpose-built equipment was designed and constructed. This system allowed for the determination of breakthrough curves of tracers in gaseous phase. This chapter provides a detailed overview of the designed equipment and techniques used for analysis. For reference, a brief overview of the principles of mass spectrometry is also provided.

Chapter 4: Sample description and preparation

A suitable sample that represented a porous media was needed for the flow experiments. This chapter presents the procedures involved in the acquisition, preparation and analysis of the Fell sandstone sample selected for the flow cell experiments. Results obtained from XRD analysis, SEM images and pore network identification are presented.

Chapter 5: Experimental results and analysis of breakthrough curves for tracer transport in homogenous porous media

This chapter presents the results from tracer experiments using the methodology outlined in Chapter 3. Experiments were performed using the specially designed flow cell outlined with the sample sandstone core described in Chapter 4. Tracer release experiments were carried out using noble gases (excluding radon) and SF_6 using CO_2 as a carrier gas. For comparative purposes, experiments were also carried out under the same conditions for CO_2 using N_2 as a carrier gas.

Chapter 6: Analysis of experimental flow results using a one dimensional advection dispersion model

The aim of this chapter is to provide analytically modelled data, which can be compared to tracer results from the core flow experiments already described and presented in Chapter 5. Models describing the transport of a tracer in homogeneous porous media can be formulated using a one dimensional advection dispersion transport equation with distance or time dependent transport coefficients. This chapter will use the one dimensional advective dispersion transport equation to fit curves to the experimental outputs by approaching the solution via statistical and analytical methods. The first part of this chapter will describe the processes involved and the necessary equations used to calculate the transport behaviour of the different tracers. Subsequently, the resulting modelled data and experimental breakthrough curves will be compared in order to understand the mechanisms involved in transporting CO_2 and noble gases. Based on the modelling curves fitted to the experimental breakthrough data, this information is used to discuss the flow mechanisms involved in the sandstone cell.

Chapter 7: Discussion and synthesis of work

This chapter provides a discussion of the presented research and its main findings. This chapter refers to and discusses existing examples where artificially introduced noble gases and SF_6 are used as tracers for transport monitoring and how they relate to the experimental results from this research. Recommendations will be presented for the role of noble gases as early warning tracers for CO_2 migration. In addition, this chapter discusses the difficulty of upscaling the experimental results and modelling outputs.

Chapter 8: Future work and conclusion

Concluding remarks and concepts for further work are presented in this chapter.

Chapter 2 - Odourisation of CO_2 pipelines in the UK: historical and current impacts of smell during gas transport

R. Kilgallon[a,*], S.M.V. Gilfillan[a], R.S. Haszeldine[a] and C.I. McDermott[a]

[a]*School of GeoSciences, James Hutton Road, University of Edinburgh, EH9 3FE, Scotland, UK*

Submitted to International Journal of Greenhouse Gas Control September 2014

Accepted with corrections April 2015

Published June 2015

Associative Authors:

S.M.V. Gilfillan made comments and contributions

R.S. Haszeldine made comments and contributions

C.I. McDermott provided constructive feedback

Abstract

Commercial scale Carbon Capture and Storage (CCS) will require CO_2 to be transported from industrial point sources to storage sites, potentially over distances of hundreds of kilometres. One of the most efficient means of transporting fluids over large distances is via pipeline. Pipeline leaks can be problematic, especially when transporting colourless and odourless gases such as natural gas and CO_2. One of the current methods of risk mitigation for natural gas transport is odourisation. The aim of this study is to determine why odourising has been suggested for CO_2 pipeline transport and what benefit it would add. This article reviews the history of gas odourisation during pipeline transportation. It also discusses the existing practices with respect to odourant use for CO_2 and natural gas transport in pipelines. Based on experience from natural gas, it is concluded that high pressure pipelines of CO_2 through sparsely populated areas could have odourant added, but will gain little safety benefit. However, adding odourant to CO_2 gas phase pipes could aid detection of leaks as well improve public assurance and should be considered in more detail.

Keywords: carbon dioxide; leakage; natural gas; odour; pipeline; transport

2.1 Introduction

The capture and long term storage of CO_2 in the subsurface is one of the most favourable ways of mitigating the current level of CO_2 being released from large power and industrial point sources (Edenhofer *et al.*, 2014, Haszeldine, 2009). The proven ability to transport CO_2 safely is an important requirement for the success of Carbon Capture and Storage (CCS) technology. Public acceptance of any new technology is crucial to ensure its success. CCS technology is no exception to this. Without the support of the public, any project can be substantially hindered or even cancelled. Pipelines have shown to be the most important part of a CCS network to the public (Wallquist *et al.*, 2012). Public attitudes may be influenced not only by any risks or impact associated with the pipeline itself but by a host of other factors such as a lack of familiarity with the technology, local, contextual and institutional factors (Gough *et al.*, 2014). Development of pipeline systems can be hindered in certain areas if there is no clear incentive between the benefits gained and how safe pipelines are perceived to be (Wallquist *et al.*, 2012). There is existing literature for assessing individual and societal risk associated with natural gas and CO_2 pipelines (Cleaver and Hopkins, 2012, Knoope *et al.*, 2014, Koers *et al.*, 2010). With work focusing on existing approaches used for natural gas systems (Cleaver and Hopkins, 2012), it is clear that when different phases of CO_2 are involved the risk levels change (Knoope *et al.*, 2014). Ensuring the low individual risks of 10^{-6}, (the likelihood per annum that a person at a fixed location is fatally injured) is more complicated for CO_2 transport than for natural gas, since CO_2 can be transported in a gaseous or dense phase. However, public perception is very important when addressing risk issues for pipelines (Jo and Crowl, 2008).

Pure CO_2 is colourless and virtually odourless. The artificial addition of impurities that enable olfactory detection ('odourising') could provide an additional attribute of safety in the event of unplanned CO_2 leakage, reducing the level of risk involved. Odourising CO_2 during pipeline transport has been suggested in relation to CCS (Barrie *et al.*, 2004, Gale and Davison, 2004); to date only limited research has been undertaken into how effective or necessary it will be. The aim of this paper is to explore why odourising has been suggested for CO_2 pipeline transport and whether it would be worthwhile.

Here we investigate the implications of odourising CO_2 in pipelines for CCS and CO_2 Enhanced Oil Recovery (CO_2-EOR). We first review the social history of gas pipelines, in particular how odourising agents in gas have influenced public perception of natural gas

transport. Then, we discuss the existing practices of natural gas transport and CO_2 in pipelines, with particular emphasis on the United Kingdom and North America. Finally, we consider the implications of odourant for transport of CO_2 in the United Kingdom.

2.2 Odourising natural gas

An odour is the property of a substance that gives it a characteristic scent or smell. The choice of odourant relies on the physical and chemical properties of the mixture. A suitable odourant for detection purposes should be able to permeate through soil but not through intact pipeline material. The odourant also needs to be nontoxic at the levels detectable by humans but strong enough for a sensible recognition threshold; in short it should have a low threshold (perceived by human sense of smell) and with maximum impact.

2.2.1 History of odourisation

R. Von Quaglio first proposed odourisation of gas in Germany during the 1880's (Amirbekyan, 2013, Tenkrat *et al.*, 2010). Efforts were made to add an odour to blue water gas (an industrial gas developed by Sir William Siemens, similar to town gas, composed almost entirely of carbon monoxide and hydrogen) using nitrobenzene and ethanethiol. By 1918, Germany began small-scale odourisation, with the United States of America doing so shortly after (Amirbekyan, 2013). The rise of automobiles and the onset of the Second World War led to many new chemicals and technologies for odourising being developed (Amirbekyan, 2013).

2.2.2 North America

Odourisation was initially performed on a voluntary basis in North America, with no government regulations to enforce it. In some areas of the continent, where 'gasoline' or butane was refined, untreated residue gases were gathered and returned to the lines either to be used as a boiler fuel or flared off. While it was not overtly approved, many public facilities in these particular areas obtained their gas directly from these low pressure residue lines, with no odourisation.

2.2.2.1 New London School gas explosion

On 18th March 1937, a natural gas explosion at the New London School in Texas killed 298 people (May Jr, 2010); this would become a significant event to introduce mandatory odourising of gas. Earlier that year, the school board cancelled their natural gas contract and had plumbers install a tap into Parade Gasoline Company's residue gas line. The odourless gas had been leaking from the residue line tap, and built up inside an enclosed crawlspace that ran

the entire length of the building. Shortly after 3.00pm, the instructor for manual training turned on an electric sander in a room with a mixture of air and non-odourised gas. The electric switch ignited the gas in the room and caused an explosion, which led to the destruction of the entire building.

An investigation by the United States Bureau of Mines following the disaster discovered the faulty connection to the gas line. On 28th May 1937, the State Board of Registration for Professional Engineers was created by the 45th Texas Legislature (Texas State Library and Archives Commission, 2006). Within weeks of this incident, the Texas Legislature mandated the addition of thiols (commonly referred to as mercaptans) to natural gas. This procedure then became worldwide; a major turning point for natural gas transportation procedures.

2.2.3 The United Kingdom

2.2.3.1 Coal gas

Coal gas (historically referred to as town gas) was first used in a practical application in 1792 (Gledhill, 2008) to heat the personal home of William Murdoch in Redruth, Cornwall. The first process used to form coal gas was destructive distillation: the liberation of gas by decomposing coal using high temperatures. Depending on the source of coal used and the level of refinement, the final product contains a variety of gases, primarily hydrogen (~49%), methane, CO_2 and carbon monoxide, as well as volatile hydrocarbons. Coal gas was dominantly used until the 1960's, when other forms of natural gas replaced it. Coal gas has a naturally distinctive smell associated with it, the result of an organic sulfur compound known as thiophene (a heterocyclic compound, C_4H_4S). This distinct sweet smell acted as an automatic safety device during the 1800's in the United Kingdom, which was important as some town gas (such as at the Poole Plant, Dorset) could have up to 15% carbon monoxide in it. Carbon monoxide is an extremely poisonous gas with a 0.0025% threshold, which can prove fatal above concentrations of 0.08% (EPA, 2013, Sonley, 2012).

2.2.3.2 Reformed gas

Technical advances improved the efficiency of gas manufacture. From the late 1950's, various high temperature reforming processes were utilised to make gas from petroleum products such as naphtha or propane; this reformed gas (gas produced from oil) had no discernible odour associated with it (Sonley, 2012). In keeping with the regulations as outlined by the Gas Acts

during that time, a method of detection was necessary. At the time, operations were controlled by twelve area Gas Boards, which were governed by the Gas Council. Discussions took place to add a smell, which would be suitable and meet the Gas Acts requirements. Based on the odourants used in America, thiolane (THT, $(CH_2)_4S$) a saturated analogue of thiophene was selected (Sonley, 2012). Additionally, many of the coal gas pipes were reused which retained the distinct coal gas odour. This meant the reformed gas also retained the familiar warning smell the public were accustomed to for a limited amount of time.

2.2.3.3 Natural gas

Reformed gas was the dominant gas source for less than a decade. By 1959, the first liquefied natural gas was imported into Britain from the Gulf of Mexico. By 1965, natural gas was discovered in the West Sole field in the North Sea (Bamberg, 2000). In 1967, the natural gas conversion process commenced in Britain, which took up to ten years to complete (Arapostathis, 2011). As part of the conversion to North Sea natural gas, many of the original cast iron gas pipes installed in towns and cities for town gas were replaced with plastic pipes. It was also necessary to adapt or replace gas appliances around the United Kingdom, as the chemical makeup of the natural gas produced from the North Sea was overwhelmingly methane, different from the manufactured gas (Arapostathis, 2011). Natural gas from the North Sea is mostly odour free, although gas from some fields contains sulfur compounds giving the gas a 'rotten egg' odour. Initially THT was used in pipelines just as it had been for reformed gas (Sonley, 2012). Odourisation plants injected natural gas dosed up with 5 ppm THT in newly replaced high pressure transmission pipes, which transported gas at 6 MPa (Sonley, 2012). However, it was observed that samples of gas further down the line had lost the THT odour and in other cases, the gas had retained only some of the chemical components and developed a different smell. For example, in the Poole area during this period, the Customer Service Department for the local gasworks responded to a call where a woman had a strong smell of beetroot in her house. Upon investigation, the smell was due to a significant gas leak adjacent to her home (Sonley, 2012). Thus, the odourisation system had 'worked' in the local distribution network, but was imperfectly understood.

2.2.4 Current natural gas pipelines

Natural gas pipeline systems are complex and their development has been influenced by other uncertainties – particularly those associated with political, regulatory and economic regimes

(Arapostathis, 2011). The natural gas network is made up of a variety of pipelines, which have different conditions and purposes. A transmission line refers to a pipeline that transports gas from a gathering line (connection from a storage facility to a distribution centre, another storage facility, or large volume customer such as a power plant). It is normally maintained at high pressure. A transmission pipeline may carry gas at 11 $m.s^{-1}$ across long distances and geographical boundaries (CEPA, 2015). A distribution pipeline refers to a lower pressure system, which delivers gas to end consumers via local service pipelines, and to appliances. Figure 14 shows a summary of the history of gas from North America and the United Kingdom.

2.2.4.1 North America

Today in the United States of America, the odourisation of transported gas is regulated under Federal legislation (US Government, 2012)**.** All combustible gases transported in distribution lines are required to contain a natural or added odour that is readily detectible by a person with a 'normal' sense of smell. North American regulations require that natural gas distributed to end consumers must be detected at $1/5^{th}$ of its lower explosive limit; this equates to 5% natural gas in air (US Government, 2012). Therefore, a fit individual with a normal sense of smell must be able to detect odourised natural gas at a concentration of 1% in air (Ivanov *et al.*, 2009); the same requirement applies to the United Kingdom. Odourising of natural gas within transmission pipelines is not normally required unless they are in close proximity to households (US Government, 2012). Records show 2,059 accidents causing 106 fatalities and 382 injuries related to natural gas (and hazardous gas) pipelines occurred from 2002 to 2008 in the United States of America (Parfomak and Folger, 2007). Odourisation of low pressure pipes has been part of a great safety improvement in natural gas transport since 1937.

2.2.4.2 The United Kingdom

Over time and with research, alternative odour mixtures have been developed. Modern day natural gas in the United Kingdom is odourised in only the lower pressure distribution pipelines using an odour blend referred to as NB (New Blend). NB is a mixture of 80% 2-Methylpropane-2-thiol (TBM, $(CH_3)_3CSH$) with 20% methylthiomethane (DMS, $(CH_3)_2S$) (National Grid, 2006). The mixture of the two compounds performs well for detection of natural gas leaks (a mixture of rotten eggs with a cabbage-like smell). This type of mixture can have an odour threshold (lowest concentration detectable by sense of smell) as low as 0.1

ppb (Tenkrat *et al.*, 2010). Today the National Transmission System (NTS) is a large network of gas pipelines (over 7,600 km) which operates in the United Kingdom; it is owned and maintained by National Grid plc. These high pressure pipelines are not odourised and as gas leaves this transmission network, it is odourised for natural gas supplies that flow through local distribution systems at 6 mg sm^{-3} (Marcogaz, 2006, Marcogaz, 2012, National Grid, 2014). The eight lower pressure distribution networks for domestic use are maintained for end consumers by local gas transporters and third party independent systems. Deaths from gas pipelines have continued to fall because of progressive replacement of iron mains pipes; in 1990-2012, there were 1.4 fatalities per year, since 2002, just 0.4 per year (Health and Safety Executive, 2012/13).

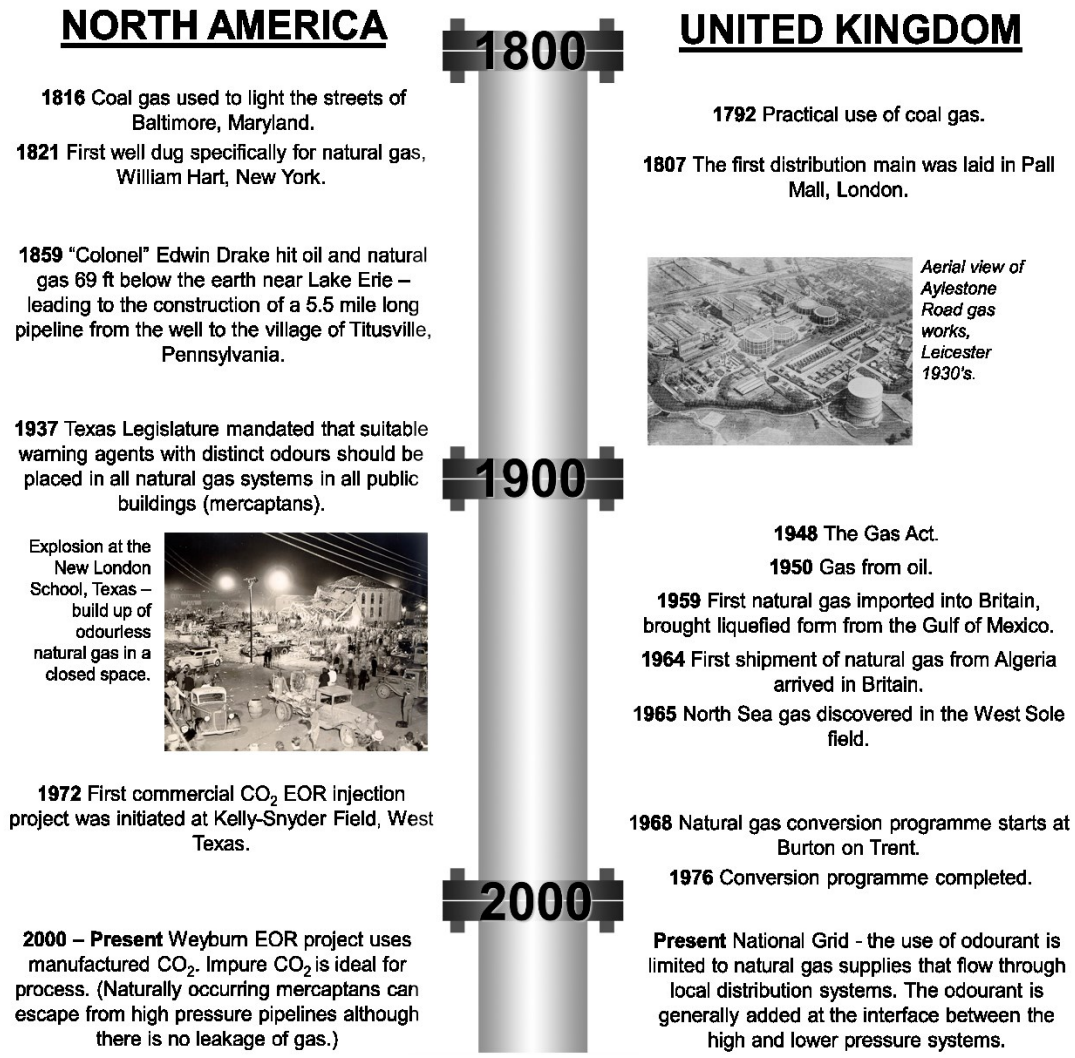

Figure 14: Timeline of gas history in the United Kingdom and North America. Images: (Gamble, 1974, Texas State Library and Archives Commission, 2011).

2.3 Odour fade in pipelines

Here we define odour fade as the gradual reduction of a distinctive smell. The reduction in the performance of an odourant in transported gas is not a new problem (Usher, 1999). The causes of odour fade may be the result of odour fatigue; however, in some cases it can be the result of olfactory adaptation by people. For the purpose of this paper, odour fade refers to reduction in the efficiency of an odourant gas itself. This is an operational issue, as opposed to olfactory adaption whereby an individual loses the ability to distinguish a particular odour after prolonged exposure to it. In most cases, this is a temporary loss of ability, but can prove to be a degenerative issue too (Stevens *et al.*, 1987). Odour fade can be a major issue, if odourisation is the primary means of detection. This section of the paper will focus on the reduction of efficiency in transmitting smell due to odour fade.

2.3.1 Causes of odour fade

Odour fade occurs when the odourant added to gas within the pipe are reduced because of physical and chemical processes (Usher, 1999). These are important processes to consider when identifying potential issues. The processes involved are:

2.3.1.1 Adsorption

Odourant molecules adhere to the interior of the steel pipe. During adsorption, the odourant creates a film on the surface of the pipe. Adsorption is a consequence of surface complexation reactions, surface bonding and electrostatic interactions at the surface. The pipe surface is not wholly surrounded by other atoms and as a result can attract adsorbates i.e. the odourant. During adsorption, the nature of the bonding depends on the involved species. Adsorption can be divided into *physisorption*, which is governed by weak van der Waals forces; and *chemisorption*, which usually involves covalent bonding. The level of odourant lost to adsorption is calibrated by isotherms (a curve giving the functional relationship between adsorbate and adsorbent in a constant-temperature adsorption process). The amount of odourant lost on the surface of a pipe is a function of its pressure (for a gas) or concentration (for a liquid) at constant temperature.

2.3.1.2 Absorption

Odourant molecules dissolve into, or combine with, the pipeline material. Absorption involves the whole volume of the bulk material. Until sorption equilibrium is reached, the odour concentration will continue to reduce. Absorption is a combined physical and chemical process. Physical absorption occurs between a gas mixture and liquid solvent. Chemical absorption is a reactive process. The nature of absorption of an odourant is dependent on the stoichiometry of the system as well as the odourant concentration.

It is important to note that as well as sorption processes, desorption may also occur. This is exemplified by the intentional odourisation of reformed gas in the United Kingdom during the 1950's, in pipelines which previously transported naturally odourised town gas.

2.3.1.3 Oxidation

This occurs when iron oxide or other compounds react with the odourant to change its chemical composition. Oxidation is the loss of electrons; although it may also be an increase in oxidation state (the actual transfer of electrons may never occur). Oxidation of thiols to disulfides may be represented by the following equation (such a reaction is faster if supplied with iron oxides):

$$2R - SH + {}^{1}/_{2}\, O_2 \rightarrow R - SS - R + H_2O \qquad (1)$$

Oxidation is more common in new steel pipes than plastic or old steel pipes. When a new natural gas steel pipe is installed, the inner walls are porous, contain metal oxides such as rust, and mill scale (flaky surface of hot rolled steel, iron oxides consisting of Fe (II) and Fe (III) oxides, hematite and magnetite). Metals oxides are very reactive with odourants and can produce disulfides, which are less odourous than the original mix (e.g. TBM).

2.3.1.4 Remediation of odour fade

To overcome the issue of the odour fade in gas pipelines, it is necessary to perform a process known as 'pickling' to a pipeline. Every pickling regime is different depending on the length and diameter of the pipe, the material involved and the type of gas to be transported. However, there are three basic methods that can be used to for pickling and gas pipeline pre-odourisation. These are:

1) The injection of highly odourised gas (40 ppm).

2) Slugging: this involves the injection of a bulk amount of odourant into a defined and isolated length of pipe.

3) Continuous injection of a controlled volume of liquid odourant into the gas stream flowing through the pipe (Ivanov *et al.*, 2009).

Even after over-odourising the gas pipeline through the pickling process, odour fade can start again after a few months and the process may need to be repeated. In addition to any odour interaction with pipeline materials, any released odourant in a gas leak will be affected by contact with soils. Soils with high clay content tend to remove and retain odour more effectively than sandy soil. Soils with high iron or metal content will react with the odourant to reduce its olfactory strength.

2.4 Odourising CO_2

The quantity of odourant required for odourising a CO_2 pipeline will depend on a number of factors. Currently the common amount of odourant added to a low pressure natural gas pipeline ranges from 2-4 ppmV (by volume, by gas) (Max Machinery Inc., 2015). This amount is well above the minimum detection threshold of most commonly used odourants. In the event of a breach, it must account for many possibilities, including but not limited to clear recognition, odour fade, soil penetration and dispersion rate from the pipe.

There are no existing recommendations for odourising CO_2 pipelines. If odourants are to be used to assist monitoring leakage of CO_2 then it could be apt to follow the procedures initially and recommendations used when transporting natural gas in pipelines. However, the addition of odorant should be based on the toxicity of CO_2 rather than lower explosive limit (as CO_2 is not flammable). The actual volume of odourants added depends on the potency of the mixture chosen, the flow rates/velocity of the fluid, baseload capacity of the capture station, the phase of the fluid and the purity/quality of the fluid being transported. Difficulty may also arise where two-phase flow may occur along the pipeline system.

2.4.1 Impurities in CO_2

CO_2 transport is complicated by the presence of impurities within the transported CO_2. How much of each impurity is present depends on the source reservoir geochemistry or the type of capture technology if it is from an anthropogenic process (Allis *et al.*, 2001, IEAGHG, 2011). Common contaminants can be nitrogen, oxygen, argon and moisture (IEAGHG, 2004). None of the CO_2 capture methods (pre-combustion, post-combustion, oxyfuel) seem to produce any thiols during the process (IEAGHG, 2011). However, there can be traces of hydrogen sulfide and other sulfur compounds that could lead to an unintentional odourising effect.

These impurities may require treatment prior to transportation. Impurities influence the hydraulic parameters such as the pressure and temperature conditions, but also the density and viscosity of the fluid, depending on what impurities are present. For example, the presence of hydrogen or nitrogen can produce larger pressures and temperature drops in transported CO_2 (Health and Safety Laboratory, 2009). Excessive water content in CO_2 can cause formation of highly corrosive carbonic acid, which can corrode and alter the integrity of the pipelines (Heggum *et al.*, 2005, Li *et al.*, 2011). While the solubility of water in pure CO_2 is well known as a function of pressure and temperature, few data are available for the effect of trace chemicals on solubility. Use of carbon steel pipelines for CO_2 transport will require that the

CO_2 be dried to eliminate any free water. Moisture in the gas should be removed prior to transportation or inhibitors should be used to reduce corrosion caused by the free water. Carbonic acid can lead to corrosion rates of up to 1-2mm within two weeks on standard carbon steel pipelines (Seiersten, 2001). A drop in pressure would result in two-phase flow leading to some gaseous phase being formed; compressor stations between fixed distances would reduce this. The distance between the stations would depend on many variables of the system including initial temperature and pressure, the conditions of travel and the chemical composition of the fluid (IEAGHG, 2004).

2.4.2 CO_2 pipeline experience in North America

Approximately 6,000 km of CO_2 pipelines are in operation in North America (Amann, 2010) and these have experienced few serious accidents. Thirty-one leaks from CO_2 pipelines were reported from 2002 through 2008, none resulting in personal injuries (Parfomak and Folger, 2007). It is difficult to directly compare natural gas and CO_2 incidents, as the CO_2 pipeline network is only ~1% of the size of the natural gas network i.e. about the length of the United Kingdom gas pipe network. In addition to this, the CO_2 pipelines primarily run through remote areas and are normally transporting CO_2 as a dense phase.

The oldest long distance CO_2 pipeline in the United States of America is the Canyon Reef Carriers Pipeline in Texas; it is 225 km in length and has been in use since the early 1970's (Table 3). Many other pipelines have been constructed since then and opened up the network for CO_2-EOR (Amann, 2010). The properties of CO_2 make it an especially effective solvent for EOR. The CO_2 transported in these pipelines are derived from a variety of sources: naturally occurring underground reservoirs, natural gas processing facilities, ammonia manufacturing plants, as well as coal gasification plants producing synfuel. Currently, most of the CO_2 for EOR is sourced from natural CO_2 reservoirs and synfuel. However, as CCS gradually develops, the use of anthropogenic sources for EOR would provide a demand for CO_2 and require additional transport infrastructure to make it feasible. In the United States of America, CO_2 pipelines are subject to diverse local, state and federal regulatory oversight (Serpa *et al.*, 2011). Currently, there is no evidence that CO_2 pipelines in North America are being intentionally odourised during CO_2 transport; nor are they legally obliged to do so.

Table 3: Existing long distance CO_2 pipelines within North America (Gale and Davison, 2004).

Pipeline	Location	Origin of CO_2	Capacity ($Mt\ CO_2\ yr^{-1}$)	Length (km)
Cortez	USA	McElmo Dome	19.3	808
Sheep Mountain	USA	Sheep Mountain	9.5	660
Bravo	USA	Bravo Dome	7.2	350
Canyon Reef Carriers	USA	Gasification Plants	5.2	225
Val Verde	USA	Val Vede Gas Plants	2.5	130
Weyburn	USA and Canada	Gasification Plant	5.0	330

2.4.2.1 North America - high pressure pipeline transport to onshore storage site

The Great Plains Synfuels Plant, Beulah, North Dakota, United States of America (owned by Dakota Gasification Company) provides anthropogenic CO_2 to the Weyburn oilfield for EOR. The Great Plains Synfuels Plant receives crushed lignite from the nearby Freedom Mine (The North American Coal Corporation, 2006). The lignite contains 37% water, has an ash content of 7.5% and a sulfur content of 0.8% (Riding and Rochelle, 2005). The normal feedstock for the gasification plant is lignite but the Dakota Gasification company also occasionally use waste, biomass and car tyres. This could lead to a variation in the composition of the synthetic fuels and products produced. The resulting CO_2 contains several different kinds of thiols as well as H_2S (Table 4). Dakota Gasification Company does not add any additional odourant. The mined lignite does not appear to have any properties that make it unique compared to other lignite feedstock. Thiols can account for a percentage of the natural sulfur content in lignite (Elsevier and IEA Coal Research, 2013). The gasification process used to produce the CO_2 (Perry and Eliason, 2004) also has the ability to contribute to the level of thiols found in the CO_2 formed.

Table 4: CO_2 gas composition from Dakota Gasification Company (updated 2008, average of >300 samples) (Dakota Gasification Company, 2008).

Parameter	Units	Typical Result
CO_2	Mole %	96
C2+ and Hydrocarbons	Mole %	2
Hydrogen Sulfide	Mole %	1
Nitrogen	Mole %	0.4
Methane	Mole %	0.9
Oxygen / Argon	Mole %	<0.01
Thiols and other Sulfides	Mole %	0.03
Moisture	ppmV	<20

The captured CO_2 is transported via a 330 km long, carbon steel pipe (Riding and Rochelle, 2005). Three compressors are used to increase the pressure of the CO_2 to a very high pressure of about 15.2 MPa to maintain the transport as a dense fluid through the pipeline. The pipeline is 14 inch (355 mm) diameter from the Dakota Gasification Company Plant to the Tioga junction in North Dakota and is 12 inch (305 mm) the rest of the way to Weyburn. Early in the EOR operations, the removal of the thiols was investigated to reduce the odours from operational CO_2 release in the area of the injection wellheads, but ultimately it was decided that it would have been too expensive for the benefit gained (Riding and Rochelle, 2005). Instead, all CO_2 injection wells are enclosed within housing facilities to reduce the emission of thiols to the public in the area of the EOR field (Perry and Eliason, 2004).

The Great Plains Synfuels Plant currently has pipeline capacity designed for transporting around 6,500,000 $sm^3.d^{-1}$ of CO_2. The CO_2 that they currently transport has a mole percentage of 0.03 of thiols (and other sulfides); this is 300 ppmV (~1000 $mg.sm^{-3}$) and is substantially greater than the recommended 6 $mg.sm^{-3}$ amount currently added to United Kingdom natural gas pipelines. It is possible to consider this high pressure CO_2 pipeline as an example of a 'transmission pipeline' in the same manner as natural gas networks. This suggests that coal

gasification plants may produce thiols in the CO_2 and clearly shows that existing CO_2 high pressure pipeline infrastructure has the ability to transport large amount of thiols without any major detriment to the system (Miller and Pouliot, 2008). In addition to this, it suggests that any existing sulfur content in the CO_2 streams may produce enough smell without additional thiols added (this would be dependent on the capture method as well as the source of the CO_2). However, extensive technologies are already in place for monitoring along the pipeline. Dakota Gasification Company carries out a series of scheduled jobs that consist of preventive maintenance and patrols (Table 5). Since pipeline maintenance is already well established for the high pressure pipeline, added odourant might not be considered as necessary. In North America, few of the CO_2 transported in other existing pipelines from natural reservoirs contain detectable levels of sulfur compounds, with the exception of at McElmo Dome, Colorado and Big Piney, Wyoming (Allis *et al.*, 2001).

Table 5: Pipeline maintenance carried out on high pressure CO_2 pipeline (Dakota Gasification Company, 2008).

Scheduled Jobs	Annual Frequency
Aerial patrols	26 times a year
Population density survey	once every two years
Right of way inspection	26 times a year
Valve maintenance and inspection	twice a year
Emergency systems check	once per year
Rectifier maintenance	six times a year
Cathodic protection survey (for external corrosion)	once per year
Internal inspection of pipeline (electronic tool)	every five years
Overpressure safety devices	once per year
Public awareness and damage prevention programme	once per year

2.4.3 United Kingdom – low pressure pipeline transport to offshore storage site

There are no clear specifications for the composition of CO_2 transported within Europe, other than that the level of impurities present should not adversely affect the integrity of the storage site, transport system or be a risk to the surrounding environment/human health (EU Directive, 2009). The following information is based on the environmental statement which investigated the retrofitting of CCS technology to the Longannet Power Station, released by the Scottish Power Consortium (despite detailed investigations this demonstration failed to receive sufficient funding to go ahead) (ScottishPower CCS Consortium, 2011a). Research undertaken for the test pipelines provided potential design specifications for CO_2 transported from Longannet Power Station (Table 6); it also recommended that only minimal quantities (ppb) of carbon monoxide, hydrogen sulfide, methane or hydrocarbons should be permitted in a CO_2 pipeline.

Table 6: Provisional CO_2 design specification for transfer from onshore to offshore pipeline via compressor outlined by Scottish Power Consortium (ScottishPower CCS Consortium, 2011a).

Component	Units	Minimum	Maximum
CO_2	Mole Fraction	0.9940	1.0000
N_2	Mole Fraction	0	0.006
H_2	Mole Fraction	0	0.003
Ar	Mole Fraction	0	0.006
O_2	ppmV	0	1
H_2O	ppmW	0	50
Hg	ppb	0	<1
Particulates	microns	0	<7

The construction of an additional portion of pipeline (approximately 1.35 km) would be needed to connect the captured CO_2 from the Longannet Power Station (Fife, Scotland), to the existing 250 km reused natural gas pipeline to transport it to the St. Fergus Gas terminal

(Peterhead, Aberdeenshire). Once at Peterhead, there is c. 100 km of offshore pipeline to reach the Goldeneye Platform. The odourisation of the transported CO_2 would only be required from the capture site to the terminal at Peterhead (once offshore the CO_2 would be pressurised and away from the general population). The CO_2 in the onshore portion of the pipeline would be transported as gas phase, well below the maximum operating pressure of the system; for this reason it is possible to consider this CO_2 pipeline as a 'distribution pipeline' in the same manner as natural gas systems. The addition of odourant in this case would be potentially valuable in public detection of minor leaks by smell.

2.5 Pipeline leaks

Different countries legislate for pipeline integrity monitoring in different ways (Stafford and Williams, 1996). Pipelines are subject to preventive maintenance as well as monitoring by a variety of methods (Dakota Gasification Company, 2008, Stafford and Williams, 1996). If sufficient damage is inflicted to a pipeline, the system will fail and loss of containment can incur. The cause of failure can be a number of individual factors or a combination such as natural events, human factors, material defects and corrosion, and transport variables.

2.5.1 Health effects of natural gas and CO_2 leaks

Natural gas and CO_2 have very different chemical and physical properties. How they may affect the health of the public during exposure is determined by these properties. Natural gas has a very low density and is mainly composed of methane. In terms of public safety, this means that natural gas is an extremely flammable gas that can spread over long distances. CO_2 is denser than air but non-flammable, meaning it can 'pond' in sheltered locations at hazardous concentrations, and displace the normal oxygen concentration in the air. CO_2 is a poison which can cause hypercapnia (the incomplete exchange of gas in the lungs leading to increased concentration of CO_2 in the blood) (Roberts *et al.*, 2011), and as a result unplanned release of CO_2 can lead to the poisoning and injury or death of animals or humans in that area, at concentrations above 5-10%. For CO_2 to reduce the oxygen concentration down to a level that is immediately dangerous to life, the CO_2 concentration would need to as high as 50% (Harper *et al.*, 2011). Much work has been done to advise the amount and level of exposure of CO_2 to humans (Health and Safety Executive, 2011, Knoope *et al.*, 2014). Table 7 summarises the main possible side effects of being exposed to both.

Table 7: Effects of natural gas and different phases of CO_2.

Material	Description
Natural Gas	Extremely flammable gas that will ignite – burns/death.
(methane + others)	Headaches, breathlessness from low level exposure.
	Flu-like symptoms from high level exposure.
	Prolonged exposure leads to loss of consciousness (/death).
CO_2 (gas)	Adverse effects on the respiratory, cardiovascular and central nervous system due to increased acidity from low level exposure - hypercapnia symptoms (>3%).
	Increased respiration, confusion, unconsciousness, coma/death (>15%).
	High levels (>50%) immediately dangerous to life - but unclear whether death due to toxicological effects of CO_2 or due to oxygen depletion.
CO_2 (dense phase)	Rapid depressurising leads to poisoning from vapours emitted.
	Contact with skin causing cold burns.
CO_2 (solid)	Sublimation to a vapour leads to poisoning.
	Loss of containment leading to the emission of high velocity solid particles.

2.5.2 Natural gas leaks

With a natural gas pipeline leak, depending on the pressure, there will be an immediate and rapid depressurisation within the pipeline, followed by a relatively stable release of gas if pumping through the pipeline continues. Leak detection is heavily dependent on the leak size; safety monitoring sensors should activate in response to the pressure decrease and flow will be stopped once the necessary valves have been shut down (Stafford and Williams, 1996). Issues with a leakage from a high pressure natural gas pipeline include the explosive projection of pipeline material, a high level of noise as the gas is released and the possibility of ignition

of the initial gas in the form of a flare. If a release of gas does not ignite immediately, it will form a buoyant cloud less dense that air, which will disperse over large distances. If a cloud of gas ignites (once it has reached its lower explosive limit), it may burn back as a flash fire to the point of origin. The hazard range for a pipeline release depends on the type of release as well the prevailing weather at the time of release.

2.5.3 CO_2 pipeline leaks

When the structural integrity of a pipeline is compromised, there is a chance of a failure. A pipeline failure is defined as an uncontrolled release of CO_2 and commonly known as a blowout. During a blowout, if supercritical CO_2 is being transported it will convert from the supercritical state to vapour phase as it expands. When the CO_2 is rapidly released, it will make a loud 'hissing' noise as the CO_2 cools and expands. This is known as the Joule-Thomson effect (Det Norske Veritas, 2010a). This vapour is not flammable, but is denser than air, so can concentrate locally in hollows or low points of buildings, potentially leading to CO_2 poisoning. Once the CO_2 stream falls beneath the triple point temperature and pressure (216.55 K and 0.517 MPa) (Det Norske Veritas, 2010), solid dry ice particles can form. This cold CO_2 condenses water in the atmosphere, resulting in a white vapour cloud. It should be noted that there is some difficulty in modelling and therefore predicting the behaviour of CO_2 once it transitions from its dense phase to a gas phase upon depressurisation.

The solvent properties of pure supercritical CO_2 on its own can damage some elastomers commonly used in valves, gaskets, coatings and O-rings used for sealing purposes in pipelines (Mohitpour *et al.*, 2008). Elastomers can be permeable to CO_2 and may allow the CO_2 to diffuse into the body of the material. Care must be taken when choosing a suitable material and re-using existing natural gas pipelines. This increases the susceptibility of a pressure release, which may cause explosive decompression and blistering. Some synthetic lubricants can harden in the presence of CO_2. However, experience from pipelines transporting CO_2 under constant pressurised conditions show no detrimental effects (Mohitpour *et al.*, 2008). Problems arise when there is rapid decompression within a CO_2 pipeline. As the pressure outside the elastomer falls below that of the CO_2 contained in the elastomer, the CO_2 begins to expand and move towards the surface, which can lead to fractures or ruptures (Mohitpour *et al.*, 2008).

Research has suggested that escaping gaseous CO_2 has a larger 10^{-6} location risk distance than dense phase CO_2 (Knoope *et al.*, 2014). This is due to the dense phase being rapidly released as the CO_2 cools and expands to form a smaller but higher jet that has a higher mixing rate with the air than the gaseous CO_2 blanket (Knoope *et al.*, 2014).

2.6 Discussion - Odourisation for CO_2 pipelines

Discussion of historical evolution

This paper has described the past and current experiences with odourisation of natural gas and CO_2 transport networks. Engineering experience started with transport of coal town gas; initially these pipelines contained odour as part of the gas manufacture, and this proved to be a useful aid to detection of leaks from local, low pressure, pipeline networks. Compulsory odourisation was introduced into pipelines as an additional inherent safety measure of detection of an invisible, odourless, potentially hazardous gas that may have been unintentionally released. However, odourisation does require additional design and maintenance – the odourants need to be carefully chosen, injected and maintained. Odourants can fade, by sorption processes in pipes, especially with iron, steel, or rust; this may require regular interruption to normal services to impregnate pipes with odourant and minimise the fade of smell. Subsequently, the natural gas network in both the United Kingdom and North America has developed into a highly integrated system of transmission and distribution lines established to accommodate the demand for energy. In the United Kingdom and North America all distribution and service natural gas pipelines operate at a low pressure range and contain odourants for identifying an unintentional release. These lines enter populated areas, and the lowest pressures transmit odourised gas into domestic houses. In such cases, the addition of smell adds an important additional safety aspect, and smell detection by the public is clearly implicated in avoidance of many accidents. Consequently, there is a well-established and positive public perception of gas odour as a safety measure. Gas in high pressure, long distance, transmission pipelines is transported at a much higher pressure; these pipes run beyond heavily populated areas. Any gas leaks can be readily and rapidly detected by pressure drops, and so the gas is not routinely odourised.

Different purposes of natural gas and CO_2 pipelines

It is important to realise that the developmental reasons behind an odourised natural gas and CO_2 network are very different (Arapostathis, 2011). These differing origins, purposes and geographic extent of the pipe network, are expected to influence how society interacts with the operation of pipelines. Natural gas is an energy source, introduced pervasively throughout urban areas to replace the less efficient and less sustainable town gases. It is also buoyant and does not poison humans because it is dispersed rapidly – the main risk is explosive combustion. CCS is a technology designed for mitigating the current level of CO_2 being released from large

industrial point sources. The intention is to gather CO_2 from industrial sites and aggregate this to shared-access regional transmission pipelines, which are intended to operate with dense phase CO_2 at high pressures (greater than 70 MPa). CO_2 is an odourless gas and can lead to poisoning if released and ponded, or to asphyxiation in high concentration. CCS, and its pipes, does not have a direct relationship with the population. CO_2 is not consumed in the same way as natural gas, and provides no direct benefits for individual households. There is no need for physical transport of CO_2 from or to individual households. Nevertheless, as with the natural gas network, it would become more complex and closer to more densely populated regions as it developed. There is existing experience since 1972 in operating CO_2 pipelines in the United States of America and Canada. These are effectively single pipes, at high pressure, which flow under controlled conditions to feed CO_2 into CO_2-Enhanced Oil Recovery projects. These are currently not required to be odourised but do predominately pass through sparsely populated regions.

Development of a CCS network for the United Kingdom

In the existing scenarios for CCS, a CO_2 transport network would evolve from individual pipes, to more complex networks where additional sources of CO_2 are progressively tied-in to increase the throughput in a shared 'common-carrier' trunk pipeline (Stewart *et al.*, 2014). These could be viewed as analogous to the local distribution and the long distance transmission pipes for natural gas. This evolution, and clustered gathering, is important because it could produce different approaches through time and space in monitoring and odourising of CO_2. For example, the published design for post-combustion CCS on the Longannet power plant in Scotland (ScottishPower CCS Consortium, 2011b), planned to re-use an existing natural gas transmission pipeline capable of operating at high pressure. It would be necessary to build a specific new link from the power plant, to link in to the transmission line. Even though route choice was careful, this was planned to be in a congested area (ScottishPower CCS Consortium, 2011b). Therefore, in that sense, this project is a vision of second or third generation of power plant, linking in to an established transmission system. To obtain easier Health and Safety Executive clearance, and avoid public dissent, the link pipe was planned to be operated as a pressured CO_2 gas, analogous to local distribution in natural gas. A surprising feature of the design was the quantity of CO_2 was small, at 2.5 $Mt.yr^{-1}$, which was much smaller than the >10 $MtCO_2.yr^{-1}$ capacity of the high pressure pipe. This was likely due to design pressures along the system to avoid two phase flow (IEAGHG, 2013); the decision was taken to run the long distance transmission pipe at low pressure of 2.8 – 3.4 MPa (ScottishPower

CCS Consortium, 2011b). Therefore, in this project, both pipeline types were to be run at low pressure and, even with a scaled up project, the local distribution pipe would transport the CO_2 as a gas at 3 MPa. Consequently, some of the arguments for enabling detection of small leaks by smell, which favoured adding odourant to low pressure natural gas pipelines, could apply. The mass of CO_2 running through a local CO_2 pipe, even at a low pressure, will be very large – at least 1 $MtCO_2.yr^{-1}$. In a long distance pipe, the inherent pressure drop along the route and the variability in operating pressure due to fluctuating CO_2 supply make it difficult to use small losses of pressure as failsafe method for detecting leaks.

There are additional important differences between CO_2 transport and natural gas transport. Captured CO_2 from CCS will have a different chemistry which could contain up to 5% in a variety of impurities depending on the CO_2 source and capture technique used (IEAGHG, 2011; Serpa *et al.*, 2011). A CCS pipeline will not have static flow due to the imbalance of supply from source to storage point. Intermittent transport can trap excess CO_2 with impurities, which can react with the pipeline materials. Existing North American pipelines used to transport CO_2 for EOR generally pass through remote, unpopulated onshore areas. Pipelines for the transport of CO_2 destined for storage would be significantly closer to populated areas in European countries, and in the United Kingdom, some will be offshore (Cosham and Eiber, 2008). This is an important factor to consider when deciding how best to monitor the pipelines for leakage.

Although CO_2 is not currently regulated as a dangerous fluid (Health and Safety Laboratory, 2009), under the Pipeline Safety Regulations 1996, Part II of those regulations defines the legal standards for pipeline design and operation (Parliament of the United Kingdom, 1996); other regulations also already exist to cover the transport of CO_2; the Health and Safety at Work etc. Act 1974 requires employers to manage risks from CO_2 at every stage along the pipeline (Parliament of the United Kingdom, 1974).

2.7 Conclusion

Existing technologies for monitoring are already well established for high pressure natural gas pipelines as well as for CO_2 pipelines without using odourisation as a detection method. However, public perception is very important when addressing risk issues for pipelines. As CO_2 pipeline networks are established into regions which are not familiar with CO_2 transport (i.e. outside of North America), then for public reassurance it may well be beneficial to odourise the gas phase, low pressure, CO_2 pipelines during the first projects developed. To date there are no clear specifications for the composition of CO_2 transported within Europe. In the United States of America, CO_2 pipelines endure diverse local, state and federal regulatory oversight. There are no direct specifications in place for odourisation of CO_2. For management of odourisation of CO_2 pipelines, further investigation is needed into the interaction of specific impurities associated with captured CO_2 on the odourants, the transport of different phases of CO_2 and the result of intermittent operations; the financial costs involved for effective implementation must also considered.

Acknowledgements

Rachel Kilgallon is funded by the Scottish Power Academic Alliance and the Scottish Energy Technology Partnership for this project. Stuart Gilfillan is funded by EPSRC, SCCS, the EU and the Scottish Government and NERC. Christopher McDermott is funded by the EU and SCCS. Stuart Haszeldine is funded by SCCS, EPSRC, NERC, Scottish Power, Scottish Funding Council, and a consortium of power and CO_2 storage companies. The research leading to these results has received funding from the European Community's Seventh Framework Programme FP7/2007-2013 under the grant agreement No. 282900 as part of the PANACEA project. The authors have no shareholdings or other competing interests. The authors wish to extend special thanks to Jennifer Roberts, Matt Gilfillan, Barry Wilkinson and John M. Sonley for their invaluable expertise.

Chapter 3 - Development of experimental design and method

3.1 Introduction

To investigate the potential role of noble gases as tracers for CO_2 storage, an experimental approach was needed in order to assess the physical interactions of noble gases and CO_2 within the porous medium. A common method to observe the behaviour of fluids under laboratory conditions is to carry out one dimensional flow through column experiments; these columns can be built from cores of natural rock or artificially constructed using materials such as packed silica beads (Edlmann *et al.*, 2013, Liu *et al.*, 2014). Flow is considered one dimensional if the transport parameters (such as advective velocity and pressure,) only vary in the direction of flow. One of the main objectives of this research was to generate real-time experimental breakthrough curves for noble gases (as well as SF_6 and CO_2) travelling through porous media. This required design specifications that would allow gases to be immediately available for analytical identification. Upon commencement of the research, no existing equipment was available within the department to sufficiently provide real-time analysis of gas transport in porous media. A significant aspect of this project was the design, purchase and construction of a purpose-built flow cell to fulfil this part of this project. This flow cell system enables the determination of breakthrough curves of tracers in the gaseous phase over a low pressure gradient range of 10,000 - 50,000 Pa (0.1 – 0.5 bar).

This chapter provides a detailed overview of the designed equipment and techniques used for analysis of noble gases, SF_6 and CO_2 through porous media. The flow cell was equipped with a mass spectrometer to measure the breakthrough curves generated. For reference, a brief overview of the principles of mass spectrometry is also provided.

3.2 Principles of mass spectrometry

3.2.1 Theoretical basis of mass spectrometry

Mass spectrometry is an analytical technique for measuring the characteristics of a compound from the molecular or atomic mass of its constituents within a sample. Measuring a compound is possible by comparing the relationship between the mass (m) and charge of each ion (z) within a sample. In mass spectrometry, ions are separated by their mass to charge ratio (m/z) and detected qualitatively and/or quantitatively. A mass spectrometer system is designed to ionise, separate and detect each species ingested. Each part of this procedure is carried out respectively within three distinct regions of the mass spectrometer – the ion source, a mass analyser and a detector. How a mass spectrometer completes these processes at each stage depends on the type of approach used. For this research, a HPR20-QIC quadrupole mass spectrometer (QMS) was used to carry out experimental analysis. An overview of this method of mass spectrometry is discussed in the following section.

3.2.1.1 HPR-20 QIC quadrupole mass spectrometer

For the experimental analysis, a Hiden quadrupole mass spectrometer (QMS) was used. The model is a HPR-20 QIC research grade bench top gas analysis system. This gas analysis system consists of a Hiden HAL 201 RC mass spectrometer with a Faraday/Multiplier detector. The ion source is gold plated to minimise source outgassing, with thoria (ThO_2) coated iridium twin filaments; the standard energy of ionisation is set to 70 eV. It has a mass range of 200 amu with a minimum partial pressure detection of 5×10^{-14} mbar and a maximum operating pressure of 1×10^{-4} mbar. The HAL 201 RC is a residual gas analyser (RGA) designed and configured for ultrahigh vacuum (UHV) applications. A RGA allows the examination of the molecular components present in a system in real time. The QMS consists of an ion source with twin filaments, a quadrupole mass filter and a detector including a Faraday cup and a single channel electron multiplier.

a) Ionisation – Election impact ionisation

In order to render a sample responsive to a magnetic/electrical field it must first be ionised. This operation depends on the conversion of gas molecules into charged particles. Ionisation depends on the nature of the species involved and how readily is can be ionised. Ionisation is achieved by electron impact by a thermionic process from a hot filament. A typical current is

1 x 10^{-4} Amps. The electrons emitted from the filament are then attracted to a positively charged discharge anode creating an electron beam. Neutral particles entering the storage cage pass through and interact with this electron beam. This interaction produces positively charged ions. These ions are then accelerated and extracted into the mass filter. The mass filter only allows ions that travel parallel to the analyser to pass through. This technique leads to a focused ion beam that enters the mass filter.

b) Quadrupole mass filter

A mass filter differentiates between the ions produced and selects the species for detection. The HPR20-QIC is a quadrupole mass spectrometer, meaning it uses a quadrupole mass filter. This filter consists of four metallic rods – two pairs of parallel, equidistant metal rods with opposite potentials. The twin potentials contain fixed direct current (DC) and alternating radio frequency (RF) components. By varying the RF component the resultant field produced by the rods can be varied and thus the electrostatic potential field within the analyser is in permanent flux. This means that the positive ions are repeatedly being repelled and attracted by the electrodes. These ions are then deflected from their original trajectory and the velocity of each ion is continually changing. The extent of deflection of any ion entering the field is dependent of its mass to charge ratio (m/z). At any interval on the RF scan, only one m/z resonates with the field allowing the ion to pass along. This alone will reach the end of the analyser and enter the detector. All other species are deflected and neutralised by impacting on one of the quadrupole rods. By progressively changing the RF voltage, it is possible to isolate and measure the mass of each species. The HPR20-QIC can measure a mass range of 1 – 200 amu.

c) Detector (Faraday cup and secondary electron multiplier)

Once a sample has been ionised and isolated by the system, the species can be detected by allowing the filtered ions to strike a detector, which results in a small current being emitted. There are two main types of detector:

- Faraday cup

The Faraday cup is an earthed passive conducting surface with a suppressor electrode to avoid false measurement. Ions that have made it through the mass filter collide with the surface of the Faraday cup. These fast moving ions striking the cup cause a shower of secondary

electrons. The shape of the detector allows for all the electrons to be collected. Each individual collision neutralises the positive ion with a single electron; the rest of the electrons are emitted and provide amplification. The cup can then be discharged to measure a small current equivalent to the number of impinging ions. This can be used to determine the number of charges being carried by the ions in the system. This method is low cost as the detector is extremely robust and highly accurate. However, the measurement is relatively slow near the detection limit of the QMS (10^{-11} Torr).

- Secondary Electron Multiplier

If measurements are required at detection limits of 10^{-14} – 10^{-13} Torr, the Secondary Electron Multiplier (SEM) provides a higher sensitivity result. The surface is designed to generate secondary electrons. A single ion arriving at the surface generates two or three electrons, which travel to the Faraday cup and allow more collisions with the surface to generate more electrons in a cascade effect until it amplifies the voltage.

3.3 Standardisation of experimental samples using calibration gases

The use of a calibration gas allows the comparison of replicated experiments using the QMS. The HPR-20 QMS comes equipped with the basic MASsoft software package that does not require the input of calibration gases prior to experimental commencement; however, the outputs are given as raw partial pressure values (Torr) where the values are normalised relative to nitrogen. The advanced QGA Professional package can also be acquired. The QGA Professional software requires loaded calibration values to perform and the main output is quantitative data. Data provided by the QGA Professional package is given in raw, calibrated and percentage/ppm values. Ideally, all the experiments would be carried out using calibration gases and the QGA Professional package. Due to budget limitations and order availability of calibration bottles needed for the experiments, three of the seven different tracer experiments were completed using a calibration gas and the QGA Professional software; the three gas mixtures used for calibration were He/CO_2, Ar/CO_2 and CO_2/N_2 (tracer gas/feeder gas). For these three combinations of gases, a 1%, 5%, 10% and 20% tracer gas to remainder feeder gas were certified. These gases were used to check the sensitivity, precision and accuracy of the QMS. The remaining four non-calibrated gas mixtures were measured using the basic MASsoft software; the three gas mixtures used without calibration were Ne/CO_2, Kr/CO_2, Xe/CO_2 and SF_6/CO_2.

3.3.1 Range precision

Prior to commencing experiments, the percentage volume of tracer injected was estimated based on the size of the trace loop, rock type and pressure gradients used in the flow cell; the value estimated was to have a tracer concentration peak percentage of no more than 5%. Due to the experiment objectives, the ratio of tracer to feeder gas was expected to change as the breakthrough curves were recorded. It was therefore necessary to determine the sensitivity of the calibration gas used as the detection ratio changed over sampling time. This value was not expected to peak above 5% contribution to the signal but was likely to fall beneath minimum detection levels as the curve subsided. This test was carried out for helium, argon and CO_2 calibration mixtures. For these three combinations of gases, a 1%, 5%, 10% and 20% tracer gas to remainder feeder gas percentages were tested.

Using the QGA Professional software, the instrument was calibrated for 1% tracer gas to remainder feeder gas. Using this loaded calibration value a series of pulse releases were carried

out using the 1%, 5%, 10% and 20% mixtures of the same tracer (Figure 15 to Figure 17). In these figures, each point represents the average of 10 s sampling of the calibration gas, repeated five times. Error propagation has been carried out for the standard deviation values. The dotted line represents what would be expected for results if they matched the intended values (1:1). The filled line is a best fit to the actual values achieved.

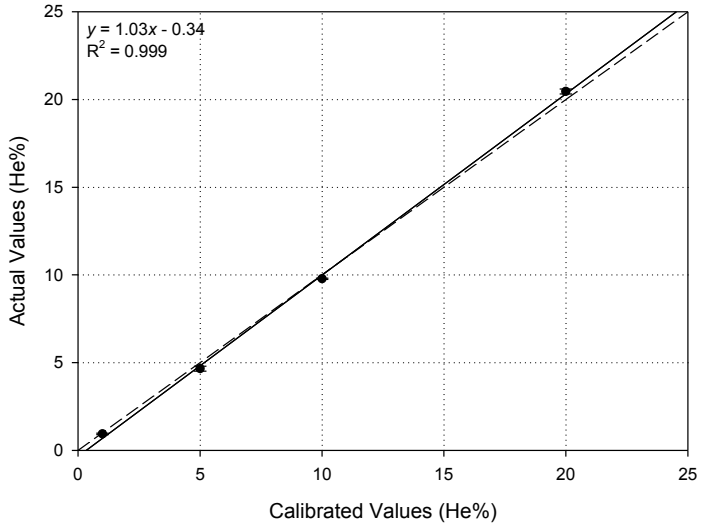

Figure 15: Graph showing the precision and accuracy of the calibration bottles in the QMS. Using QGA software, the instrument was calibrated for 1% helium to remainder CO_2. The dotted line represents what would be expected for results if they matched the intended values (1:1). The filled line is a best fit to the actual values achieved.

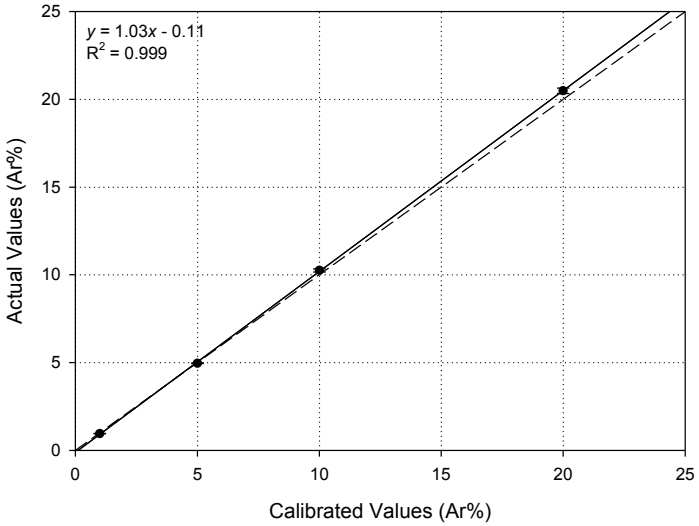

Figure 16: Graph showing the precision and accuracy of the calibration bottles in the QMS. Using QGA software, the instrument was calibrated for 1% argon to remainder CO_2. The dotted line represents what would be expected for results if they matched the intended values (1:1). The filled line is a best fit to the actual values achieved.

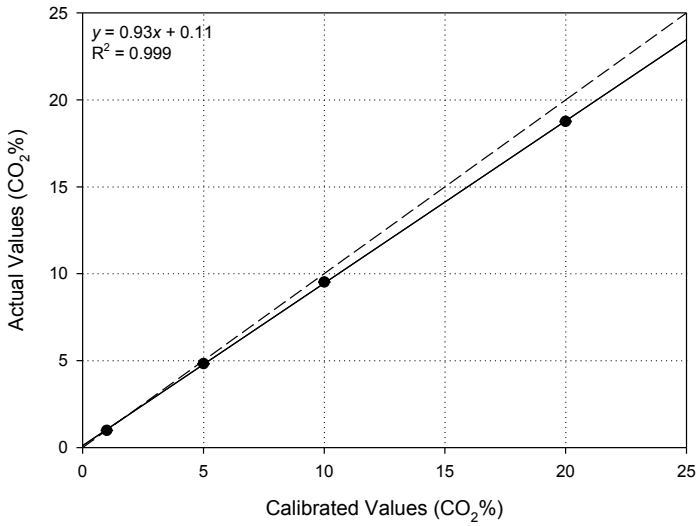

Figure 17: Graph showing the precision and accuracy of the calibration bottles in the QMS. Using QGA software, the instrument was calibrated for 1% CO_2 to remainder nitrogen. The dotted line represents what would be expected for results if they matched the intended values (1:1). The filled line is a best fit to the actual values achieved.

When using a 1% calibration bottle for testing the precision of the QMS, it is apparent that helium deviates from the ideal 1:1 ratio (Figure 15). This may be the result of increased quadrupole transmission at low mass. Repeat experiments with the same calibration ratio underestimate the value, in addition to concentrations below 10%. The ratio is overestimated as the values increase to 20%. Thus, for 1% helium calibration, the QMS shows high levels of precision but varies in accuracy above and below one order of magnitude difference. Results from the 1% argon calibration provide a more reliable output (Figure 16). The 1% and 5% calibration values are accurately detected with a high level of precision. As there is an increase in the ratio change, the 1% calibration settings deviate from the 1:1 ratio and overestimate the amount of argon present in the system. This implies that by using the 1% argon ratio calibration gas the QMS can provide highly precise outputs, but it decreases in accuracy when the order of magnitude increases by one. Results from the 1% calibration using CO_2 as the tracer gas also shows a high level of precision (Figure 17). Unlike the results from argon, it shows deviation from the 1:1 ratio at 5% calibration values; it continues to underestimate the ratio of CO_2 present above one order of magnitude.

Using the observations made here, it was apparent that the QMS could sufficiently detect a change in ratio within one order of magnitude of the calibration gas value. As a similar amount was expected from the tracer pulse, it was decided that the 5% calibration gas would suffice as the baseline value used for all three sets of experiments.

3.3.2 Day variation

In addition to understanding the precision of the QMS with a change in ratio concentration, it is also important to understand analytical variation of values over time and whether the results are repeatable. Due to time constraints, replicate experiments are carried out throughout the day, and thus it is important to understand how much variation occurs on a longer time scale. Over a 10 hour sampling period, the 5% tracer calibration bottles were used to verify the extent of changes in detection (Figure 18 to Figure 20). In these figures, the calibrated percentage output is presented. Each point represents the average of 10 s sampling of the calibration gas. The error bars represent the standard deviation from the readings; the shaded region is calculated using standard deviation from the mean average of all 10 sampling points (represented as a dashed line). Figure 21 shows the same percentage results, but in conjunction with the raw and corrected values obtained.

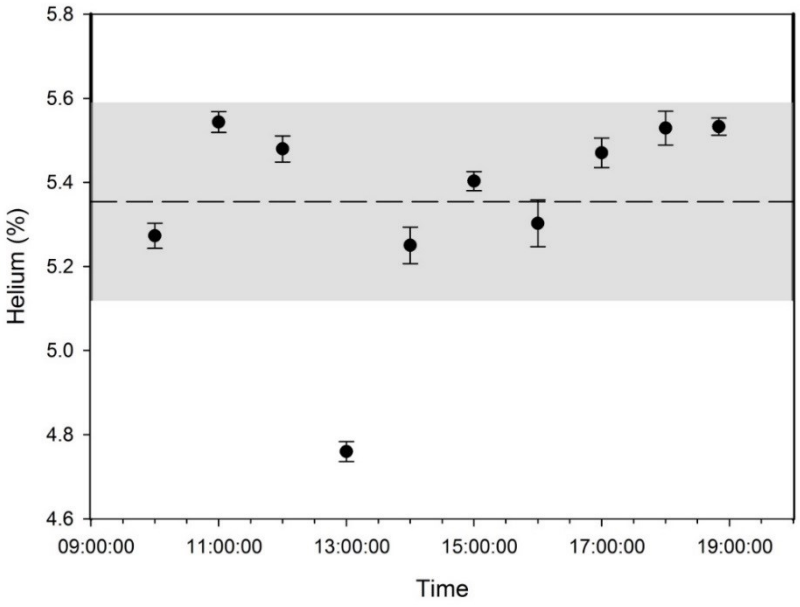

Figure 18: Plot of measured helium abundance against 5% helium calibration, illustrating the signal exhibited by the QMS over a 10 hour period. Shaded area represents mean percentage of 5.35 ± 0.237%.

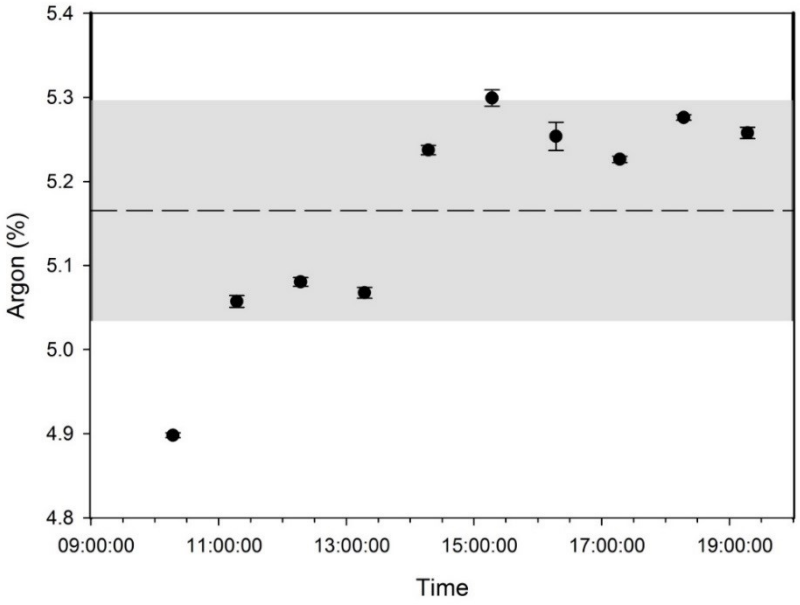

Figure 19: Plot of measured argon abundance against 5% argon calibration, illustrating the signal exhibited by the QMS over a 10 hour period. Shaded area represents mean percentage of 5.17 ± 0.131%.

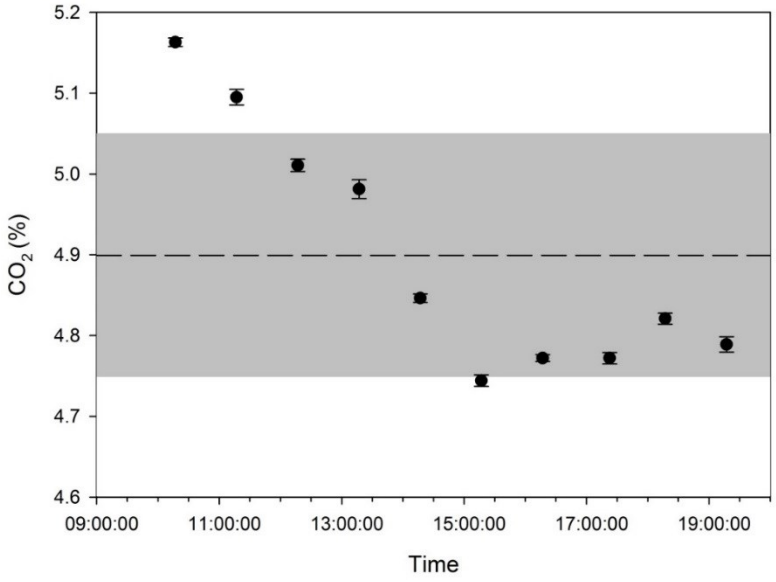

Figure 20: Plot of measured CO_2 abundance against 5% CO_2 calibration, illustrating the signal exhibited by the QMS over a 10 hour period Shaded area represents mean percentage of 4.90 ± 0.151%.

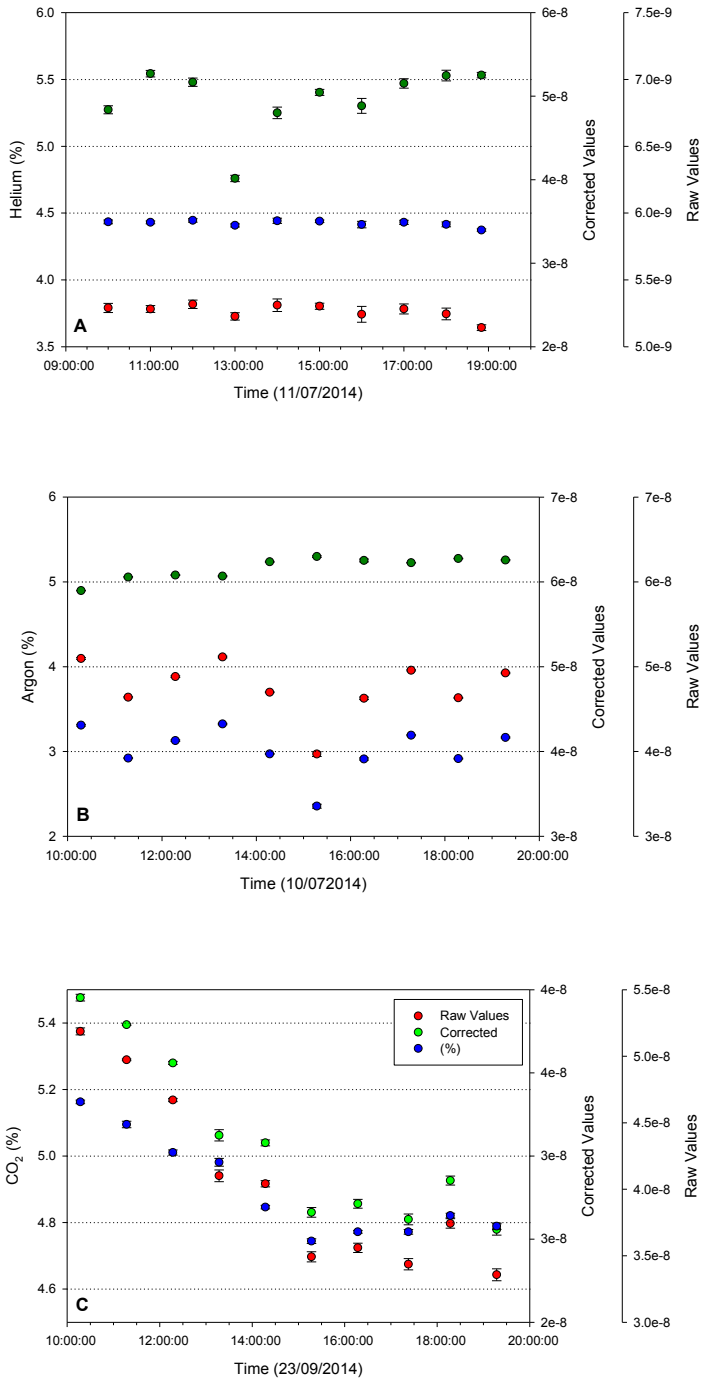

Figure 21: Plots of raw, corrected and percentage values from 5% tracer ratio for (a) helium, (b) argon and (c) CO_2 with variation over a 10 hour period. Corrected and raw values are measured as partial pressures in Torr.

For helium, the raw, calibrated and percentage values do not appear to shift significantly over the course of 10 hours. The relationship between the raw and calibrated values remain constant. With the exception of one anomalous value, the hourly values for helium stay within the mean percentage range. This range for the ratio of helium has a mean percentage of 5.35 ± 0.237%, which suggests the accuracy of the QMS for detecting helium is over estimated throughout the day. This is in contrast to the argon results - with a mean percentage of 5.17 ± 0.131%, which has a closer value to the calibration value of 5%. It is apparent that over the 10 hour period, there is a gradual increase in percentage ratio of the tracer gas. The raw and calibrated values show a constant relationship during the 10 hour sampling period, suggesting there is some minor drift in the QMS throughout the day. In contrast, the CO_2 readings for the 10 hour period decrease throughout the day with a mean percentage of 4.90 ± 0.151%. In addition, the raw and corrected values follow a disconnected path when compared. It is possible that this is not related to drift in the instrument outputs over the 10 hour period; rather it could be the result of the species themselves or perhaps a sampling issue with the calibration bottle.

These results show that although there is some variation throughout the day, the mean values for all the tracer gases do not exceed 7% above or below the supposed calibration amount. Thus, although there is some variation, it is not significant enough to warrant concern.

3.3.3 Long-term variation

As well as testing the variation of the QMS over a 10 hour period, the long term variation was also evaluated. The purpose of this was to test the presence of any drift in the QMS and to determine how often it was necessary to recalibrate the instrument. These experimental observations were carried out over a seven week period (July/August 2014). Using a 10% argon calibration gas, a sample was tested once a week at the same time. A pulse reading was taken for 10 s and the raw, corrected and percentage values are presented in Figure 22. In addition to this, the room temperature was recorded over the same period.

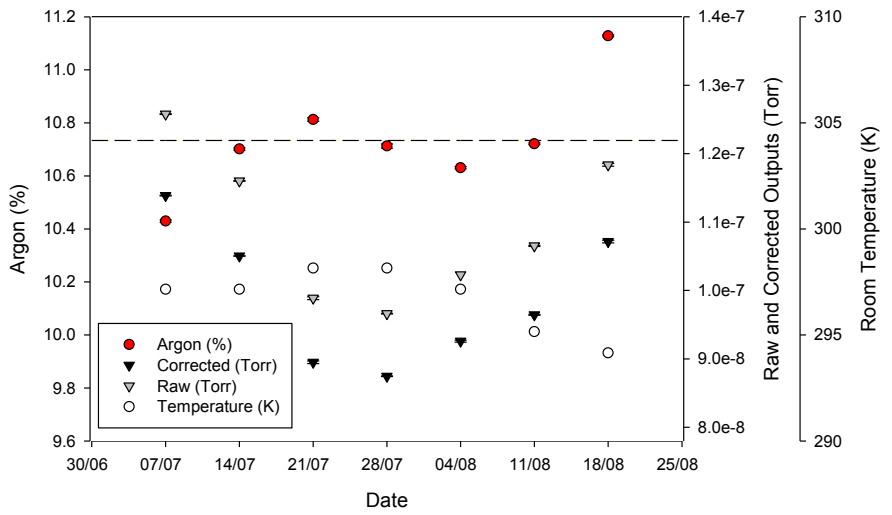

Figure 22: Weekly recorded variation in 10% calibration average of 10 s readings of argon during July/August 2014. Mean percentage of the seven readings is 10.734 ± 0.211% (depicted by grey area with mean value as dashed line). In addition, room temperature was recorded at the time of sampling.

Of the seven samples, the first and last values are the only ones that do not fall within the mean percentage range of 10.734 ± 0.2108%. Ionisation in the QMS is achieved by electron impact by a thermionic process from a hot filament. This should heat up the sample so that the room temperature should not have a significant impact on the species. However, it may be possible that a sufficient increase in temperature may affect the electron ionisation energy. The drop in temperature recorded on the 18/08/14 may have resulted in the increased argon percentage, although there is no direct evidence that this is the case. The overall trend of the output values are above the 10% calibration amount. The final value (18/08/14) is 11% greater than what should be expected (10% calibrated value) and 7% greater than the first recorded value (07/07/14).

The mean percentage for this experimental calibration period was 10.7%; after five weeks, the output values were still beneath this average. It is recommended that the instrument be re-calibrated after a maximum of five weeks for a set of experiments. Alternatively, experiments that need to be compared directly could be completed as one batch.

3.4 The one dimensional flow cell experimental system

3.4.1 Development of the experimental system

One of the main objectives of this research was to generate real-time experimental breakthrough curves for noble gases (as well as SF_6 and CO_2) travelling through porous media. This required design specifications that would allow gases to be immediately available for analytical identification. As no existing equipment was available to sufficiently provide real-time analysis of gas transport in porous media, a purpose-built flow cell was designed, purchased and constructed, including the acquisition of the HPR-20 QMS.

The constructed flow cell was designed to ensure that the initial aim of the research was maintained; this was carried out by an iterative process of design adaptation and testing. The final design in place for the flow cell system allowed for the determination of breakthrough curves of tracers in gaseous phase over a range of low pressure gradients (10,000 – 50,000 Pa) through air-dried porous media. The development process and timeline for the development of the current layout has been summarised in the following time chart (Figure 23).

3.4.2 Current layout of experimental system

The specifically designed equipment for flow experiments is represented in Figure 24 (and Table 8). It consists of a series of pipelines, which allows a pulse of tracer gas to be loaded and released at a determined time through a feeder gas. This gas travels through the core where it is sampled downstream by the QMS. The entire system is subdivided into the tracer loop section, the feeder gas section, the purging section and the flow cell/end plate design that contains the porous media. The different sections of the layout will be explained in detail below.

3.4.2.1 Tracer loop

A 20 cm length of Swagelok 1/8" tube piping (0.307 cm^3) can be filled with the desired tracer gas and sealed off by a pair of plug valves (Figure 25). The gas within this tracer is trapped at a desired pressure using the pressure regulator set by the gas output and recorded by the digital pressure gauges up to 150,000 Pa. While the tracer is stored in the loop, any other gas can still

be transported through the pipeline system unaffected. A third plug valve is in place to force the feeder gas to divert and mix with the tracer using the 0.33 (ID) x 7.62 cm static mixer.

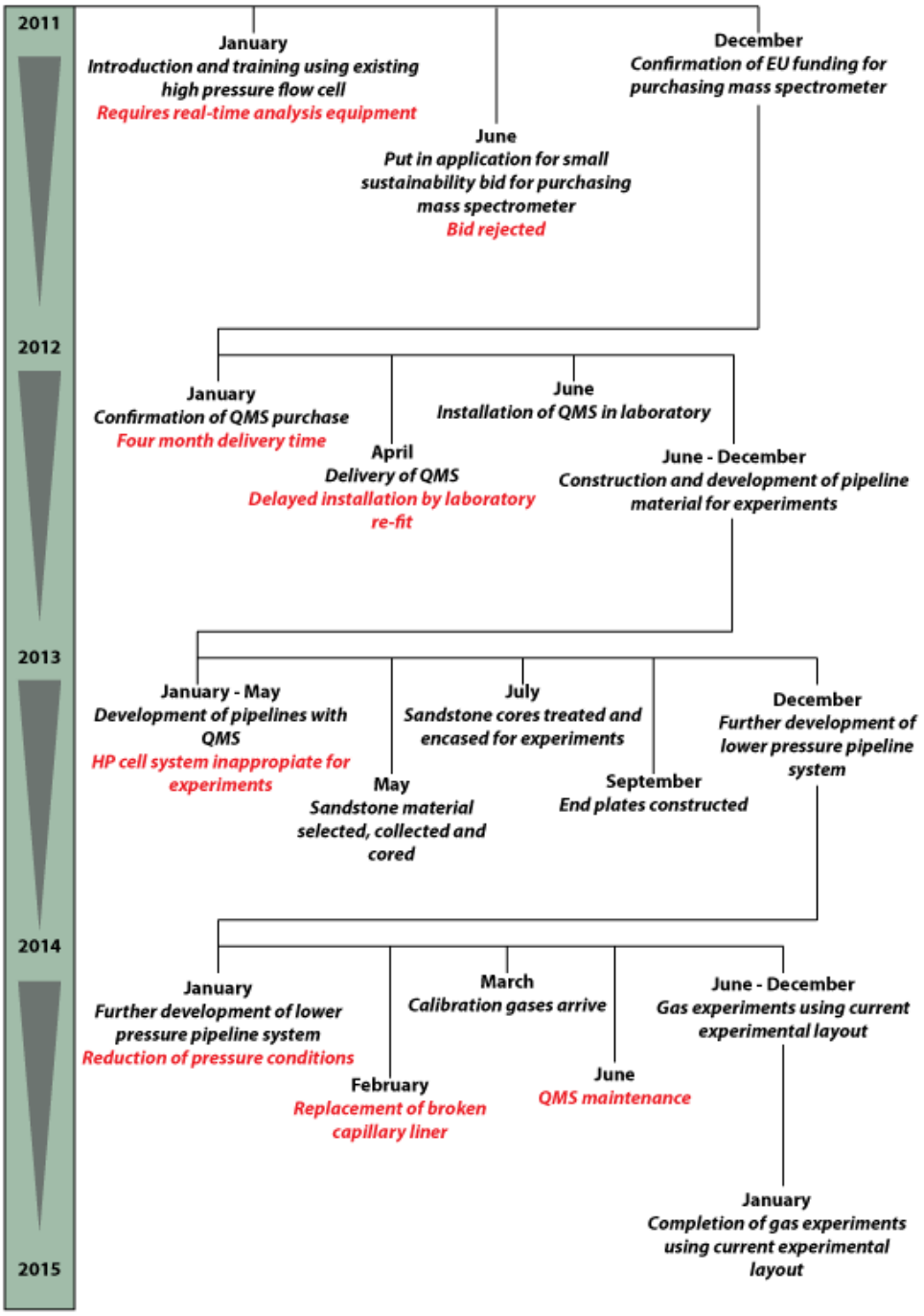

Figure 23: Time flow chart of experimental design and process for the current flow cell layout used in this research project.

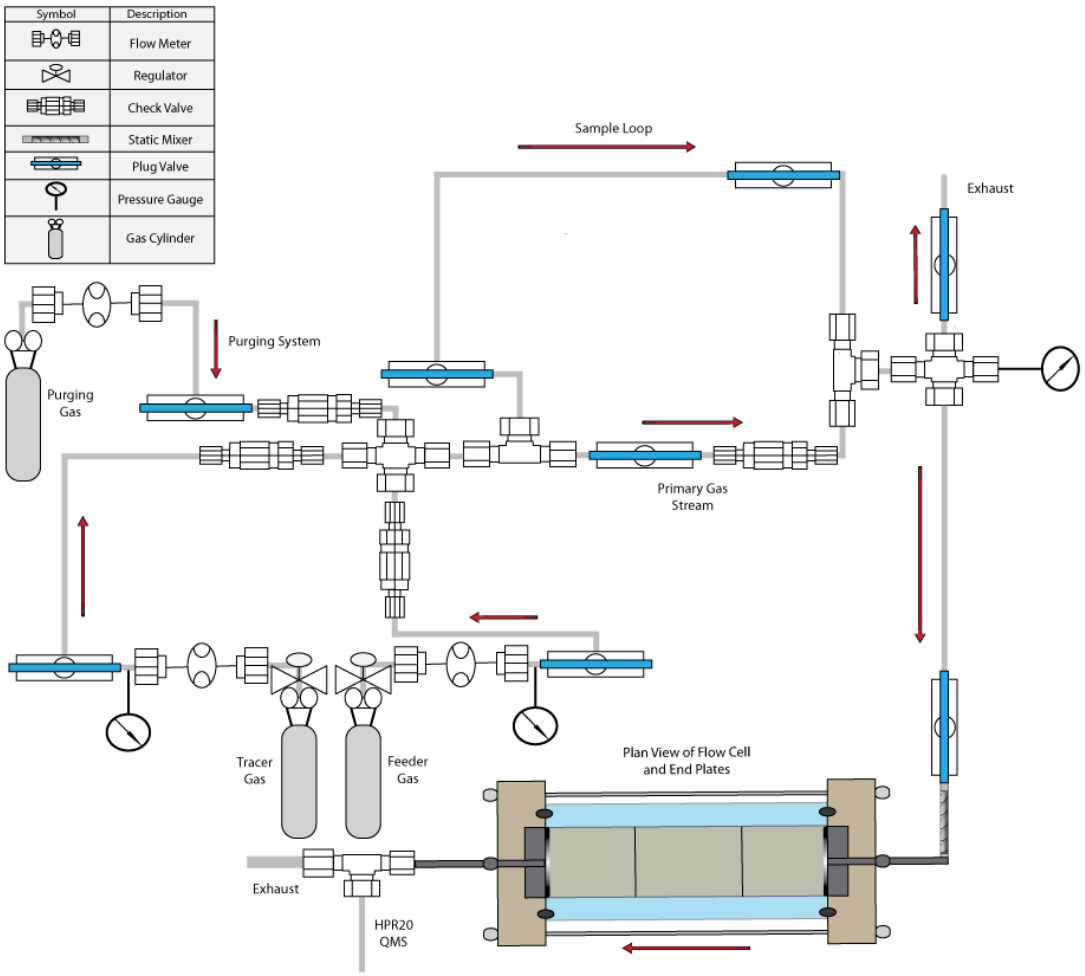

Figure 24: Current layout of experimental equipment used for flow experiments.

Table 8: Additional information on equipment ranges and accuracys.

Equipment	Range	Accuracy
Acrylic flowmeter kit	maximum 1.0 sL min^{-1}	± 5% full scale
Digital pressure gauge	range 0 – 0.207 MPa	± 0.25% full scale
Check valve	minimum 0.003 MPa poppet 41.3 MPa	-
Plug valve	$C_v = 0.10$	-

3.4.2.2 Feeder gas

The system is set up to use CO_2 as the feeder gas during experiments (with the exception of the CO_2/N_2 experiments when N_2 is the feeder gas). The feeder gas will pass either through the pipeline bypassing the tracer loop or through it during the pulse release. The feeder gas pressure is held using the cylinder regulator as well as a step down regulator to ensure the values do not exceed 150,000 Pa. Check valves are in place to ensure that the gas does not return upstream during experiments. Flow meters and pressure gauges are also installed to monitor the gas progress (Figure 25).

3.4.2.3 Purging system

To ensure that the flow cell is void of any residual gas from previous experiments, N_2 has been connected via a union cross. This is used during the purging process for the noble gas and SF_6; it can be vented via an exhaust through the flow cell (Figure 25).

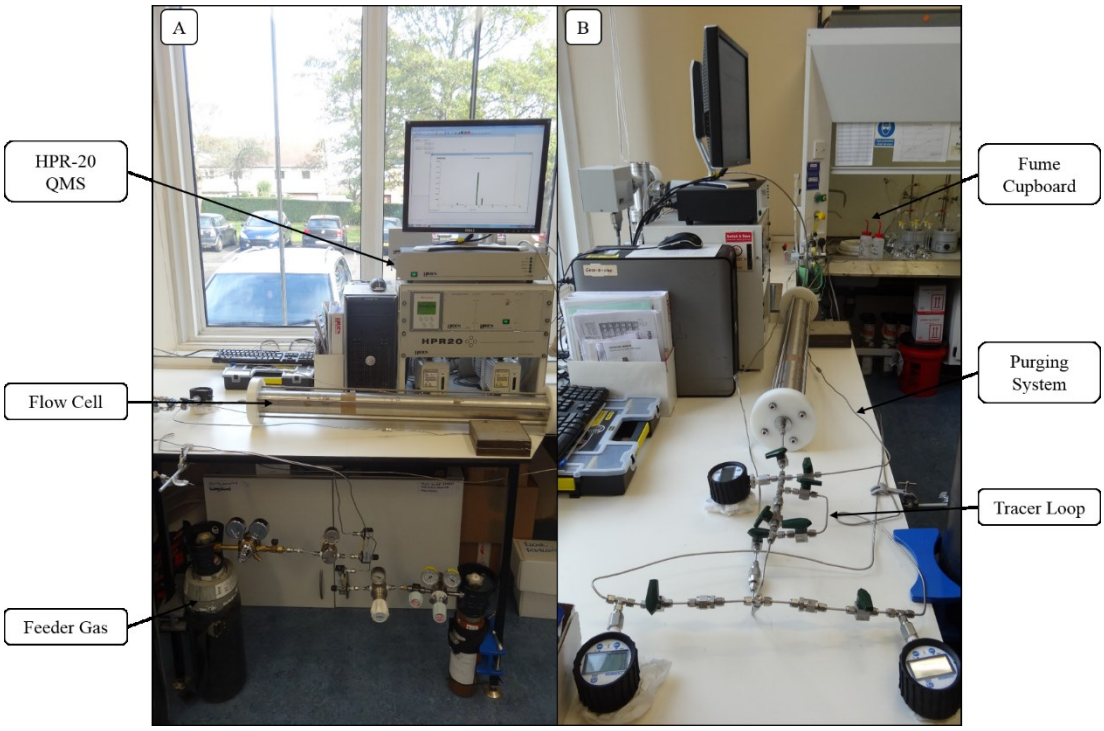

Figure 25: Photographs of the flow cell system from the (A) front and (B) upstream end of flow cell.

In the case of the CO_2/N_2 experiments, it is used as the purging gas as well as the feeder gas for the procedure; in this instance, the change in function of N_2 is noted by reducing from high pressure purging to the lower pressure of the experimental range.

3.4.2.4 Flow cell and plate design

A large intact block of Fell sandstone was selected at the local stone works. Due to the shape and size of the block, a specially purchased drill bit was required. It was not possible to ensure that the sandstone would remain intact if drilled as an intact 3.6 cm x 1m piece. Therefore, it was decided to drill it as three equal length pieces. A diamond core bit was procured for the Hilti mounted system at The University of Edinburgh that allowed the extraction of nine 3.6 cm x 40 cm sandstone cores. The cored samples were trimmed and sanded down to the desired length (~33 cm long); the cores were given a flush finish with a constructed device designed to square the ends of samples (at the University of Edinburgh, designed and built by Dr. Ian Butler and Dr. Stephen Elphick).

Once the samples were cored and squared, they were allowed to air dry. The samples were weighed, measured and logged (Figure 26 and Table 9). These were sent to Core Laboratories, Aberdeen along with aluminium foil (to ensure the core was gas tight) and three 7.62 cm OD x 100 cm long stainless steel tubing. At Core Laboratories, the samples were set end to end, wrapped in aluminium foil and treated within resin to suspend the samples before they were returned (Figure 27). The nine sandstone cores meant that three complete flow cells were available. Out of the three, one was selected as viable for experiments. In this instance, viable means the cores had not shifted during the setting process.

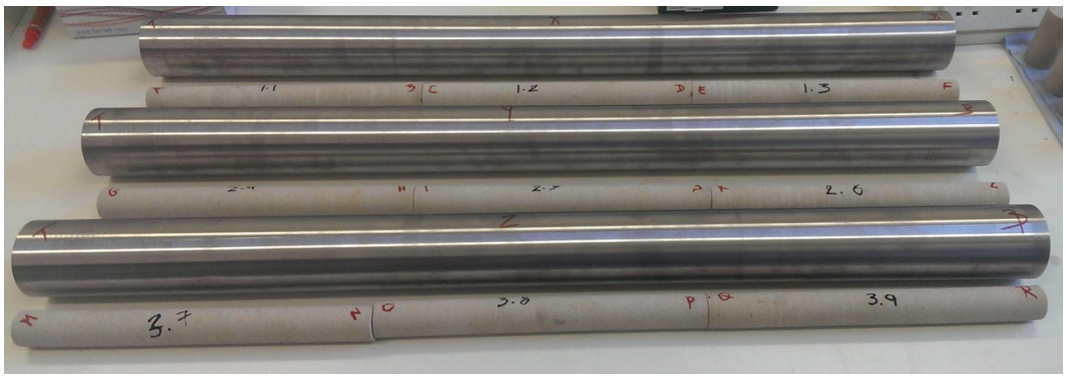

Figure 26: Image of the three sets of core samples and stainless steel tubing that was sent to Core Laboratories. Number on cores can be related to Table 9.

Table 9: Recorded measurements of the core samples sent to Core Laboratories for resin treatment.

Description	Weight (g)	Length (cm)	Diameter (cm)	Volume (cm^3)	Density (kg m^3)
1.1 (AB)	680	32.2	3.6	328	2076
1.2 (CD)	689	33.0	3.6	336	2051
1.3 (EF)	686	32.5	3.6	331	2074
2.4 (GH)	687	32.9	3.6	335	2052
2.5 (IJ)	674	31.2	3.6	327	2064
2.6 (KL)	678	32.2	3.6	328	2069
3.7 (MN)	696	33.1	3.6	337	2064
3.8 (OP)	672	32.2	3.6	328	2050
3.9 (QR)	695	33.0	3.6	336	2068

The original length of the cores were 1 m when combined. The length was reduced during construction of the flow cell to ensure a fresh, flush surface against the end plates. On either end of the core, is a set of purpose designed end plates (Figure 28). These end plates allow any gas stream to interact with the entire end surfaces of the rock core. The downstream end plate connects the flow cell to the QMS for sampling (Figure 29). There is a flush fit between the end plates and the flow so that no gas can leak during the experiments. A description of the rock sample used in this flow cell is described in detail in Chapter 4.

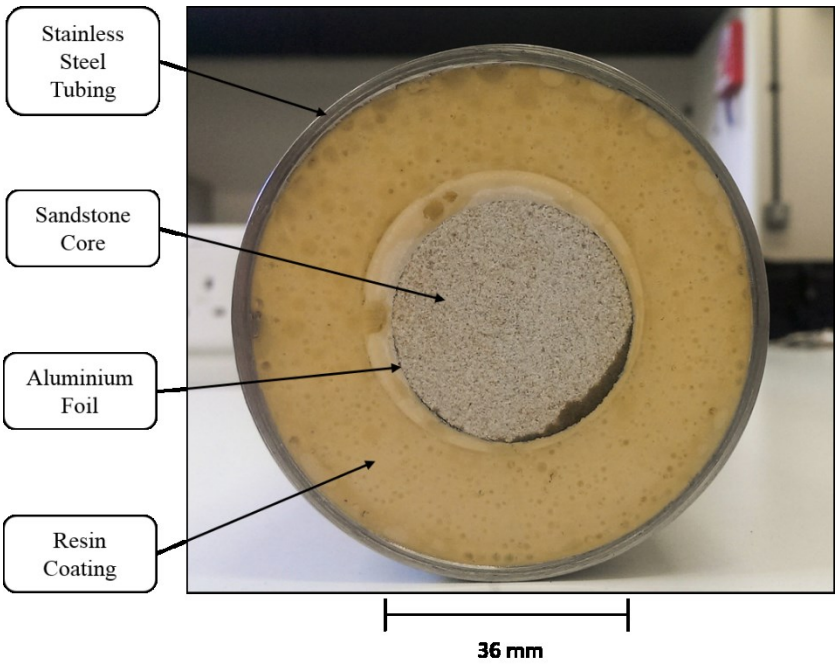

Figure 27: Image of how the core is stored within the flow cell. The sandstone cores are covered in aluminium foil and surrounded in epoxy resin. This is held in place by a 1 m length of stainless steel tubing.

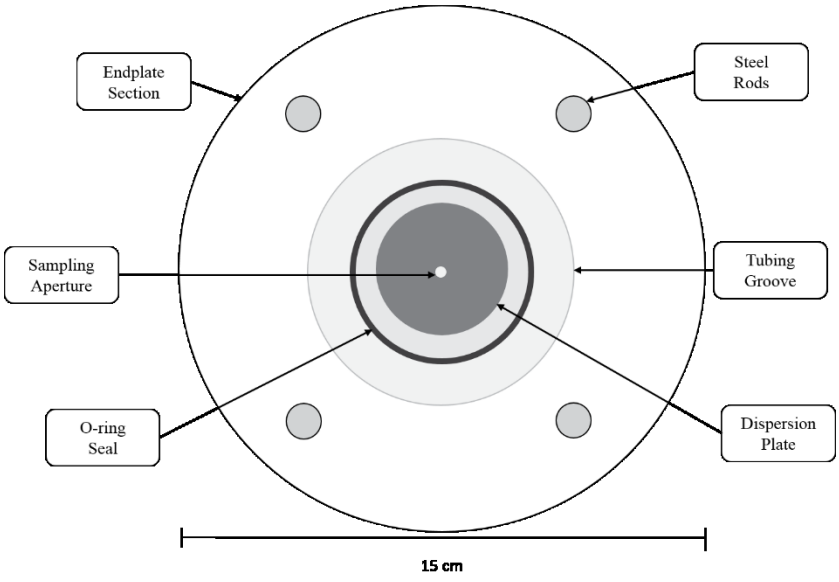

Figure 28: Diagram of end plate design for flow cell. The core shown in Figure 27 is designed to provide a flush fit with the tubing groove.

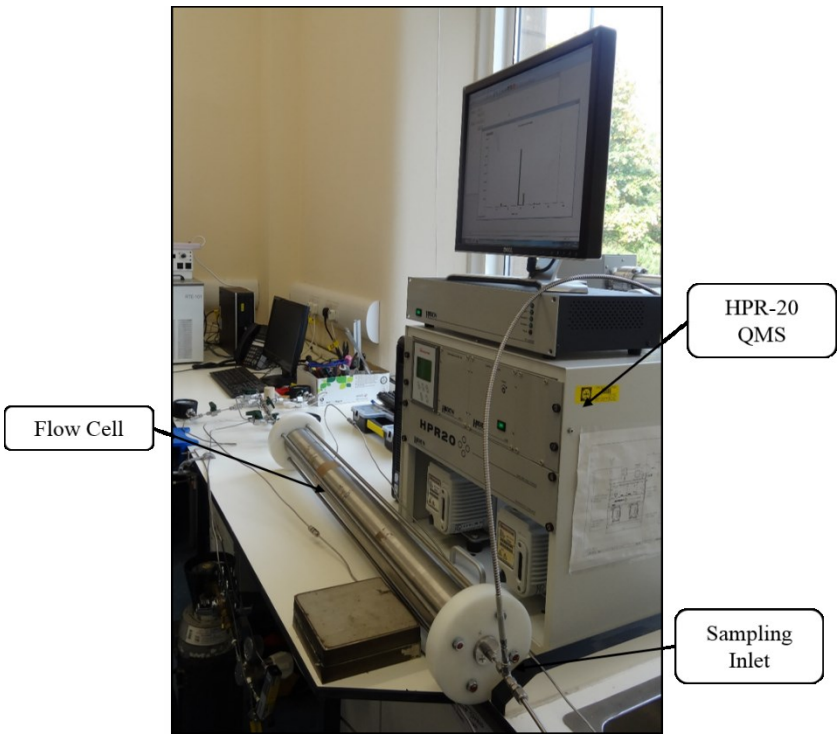

Figure 29: Downstream end of flow cell with sampling inlet for QMS.

3.4.2.5 Contribution of pipeline volume to the experimental layout

The pipeline and fittings used for the equipment were stainless steel 316 Swagelok material. The pipeline was primarily 1/8" in diameter, although there was some variance depending on the section (increasing to 1/4" for purging exhaust, 3/16" static mixer and decreasing to 1/16" for inlets to flow cell). The stainless steel material was not necessary for the low pressure, dry and non-reactive (with the exception of CO_2) system; however, it was preferable to keep the material all the same to remove any possibility of reaction. The fittings work by 'swaging' – the permanent external compression of the outside wall of the tubing. This is ensured by the use of ferrules that conform to the fitting and create a seal when tightened.

It is important to know the total volume of pipeline involved during experiments as it can inadvertently contribute to the sampling results. A method of reducing the contribution of pipeline volume to the flow cell system was to ensure the sample loop was as close as possible to the upstream end of the flow cell. In addition, there were check valves in place to discount portions of the pipeline and the downstream side of the flow cell was connected directly to the QMS sampling capillary inlet.

Fittings such as unions and tee pieces can contribute additional volume to the system – the void volume. The swept volume in fittings refers to the portion of the internal volume that is directly related to the flow of the gas. For experimental work, it is ideal to have this volume as low as possible. This removes the amount of pipeline volume that is unnecessarily contributing to the flow timings of the tracers, which could lead to false delays in the results. Thus, it is important to ensure this swept volume is as long as possible by trying to maintain the same size pipeline with minimal connections once within the contributing section of the flow cell (past the check valves).

A final portion of internal volume that can affect the results of the experiments is dead volume. This refers to the dead end portions of the fittings where the gases may travel to and become trapped, leading to delayed results. By using minimal fittings and ensuring optimal connection by only using a fitting with the original port to which it was fitted, the contribution of dead volume to the system can be significantly reduced.

The maximum volume of pipeline contributing to the experimental results (upstream and downstream of the flow cell) accounts for less than 0.45% of it (pore volume 1.74 $x10^{-4}$ m^3, tubing volume 7.66 x 10^{-7} m^3). This is calculation does not account for the dead volume, but due to the low contribution percentage, it is unlikely that the dead volume of the fittings significantly changed the final breakthrough curve results.

3.5 Experimental procedure

The following section describes the experimental procedure carried out using the flow cell experimental system in conjunction with the HPR-20 QMS. This procedure was documented and repeated for all the noble gases and SF_6 tracer experiments. There are some exceptions in place for CO_2/N_2, as it required the change of CO_2 from a feeder to a tracer gas. Where this is the case, any changes have been outlined.

3.5.1 Sample loading and purging

Prior to experiment commencement using the QMS, the tubing and flow cell system must be sufficiently purged and loaded with the tracer that is being used. To do this, the successive steps and procedures were followed:

- Ensure the plug valves to the purge system, the feeder gas and the flow cell are closed. All other plug valves are opened so that the tracer gas will travel from regulator and out via the exhaust upstream of the flow cell.
- Set the regulator system to the desired pressure conditions. Record the flow rate and pressure at the regulator. Allow the tracer gas to flow for 30 s. Close the exhaust plug valve and permit the pipeline to reach a pressure above the desired levels. Open the exhaust plug valve and allow the pressure to drop. Ensure flow is still occurring. Close the bypass plug valve and allow the tracer gas to flow for 30 s.
- Drop the pressure on the regulator and close the exhaust plug valve. Observe the output of the tracer pressure gauge and the upstream pressure gauge. Close the plug valves associated with the tracer loop when the desired sample pressure has been reached. This step may take several attempts to ensure that the pressure is correct and stable. Record the captured pressure within the tracer loop.
- Shut down tracer cylinder and vent to system exit using exhaust plug valve. Close plug valve to tracer loop and open plug valve to purge gas. Set purge gas to 50,000 Pa and a flow rate 0.2 sL min^{-1}. Allow the purge gas to vent to exhaust for 30 seconds. Open bypass plug valve, close exhaust plug valve and open upstream plug valve to flow cell.
- Purge the entire system for 30 minutes and record upstream pressure gauge every 10 minutes. During this purge, the QMS is connected and using peak mode in MASsoft to identify the complete removal of any other gas except for the purge gas.

The system purge time is based on the estimated pore volume of the core. The entire volume of the core is approximately 998 cm^3. Since the porosity (Section 4.2.2) was initially calculated

as 20.3%, this accounts for 203 cm^3 or 0.203 L of the core volume. The purge flow rate is 0.2 sL min^{-1}; in theory, this means that in one minute the core volume has been roughly replaced with a new volume of purging gas. This is repeated 30 times prior to every experiment to ensure that any gas that may be trapped in pore end spaces is also purged.

- Once the purge process is complete, shut down the purge cylinder and the plug valve. Set the experimental pressure for the feeder gas using the feeder pressure gauge and the upstream pressure gauge; record the flow rate. Ensure that the MASsoft software is running and observe until it is the feeder gas only. The time for this to happen depends on the experimental pressure (10,000 Pa gradient can take several minutes to reach this compared to 50,000 Pa gradient). (In the case of the CO_2/N_2 system experiments, there is no true feeder gas flow time prior to experiment, as the purge gas and feeder gas were both N_2. Instead the pressure is dropped to the experimental pressure after sufficient purging has occurred.)
- The pipeline system is now ready for the experiment to begin using the QMS for detecting pulses of tracer.

3.5.2 Experiment

Once the sample is in the tracer loop and the system is suitably purged, the experiment can begin. The following section describes the procedure followed to ensure the tracer is released correctly.

Using QGA Software for non-calibrated mixtures:

- Ensure, using MASsoft that there is only feeder gas in the system, using peak and MID mode.
- Load the QGA software with calibration file for the chosen gas ratio.
- Record the values given by the digital pressure gauges and flow meter.
- Switch on the QMS filament and start the experiment.
- After two minutes of the software running, release the tracer gas. This is completed by closing the bypass plug valve and opening the two sample loop plug valves. Record the values given by the digital pressure gauges.
- Allow the experiment to run until the breakthrough curve values fall below the background values once more.
- Stop the experiment and save the file.

- Turn off the feeder gas cylinder valve, close the upstream plug valve and open the upstream plug valve, allowing excess gas to vent to the fume cupboard. System is then ready to start purging for the next experiment.

Using MASsoft Software for calibrated mixtures:

- Ensure using MASsoft that there is only feeder gas in the system, using peak and MID mode.
- Keep MASsoft software open.
- Record the values given by the digital pressure gauges and flow meter.
- Switch on the QMS filament and start the experiment in MID mode for detecting tracer and feeder gas.
- After two minutes of the software running, release the tracer gas. This is completed by closing the bypass plug valve and opening the two sample loop plug valves. Record the values given by the digital pressure gauges.
- Allow the experiment to run until the breakthrough curve values fall below the background values once more.
- Stop the experiment and save the file.
- Turn off the feeder gas cylinder valve, close the upstream plug valve and open the upstream plug valve, allowing excess gas to vent to the fume cupboard. System is then ready to start purging for the next experiment.

3.5.3 Data extraction

The type of data output depends on the software that was used during the experiment. The QGA Professional software requires loaded calibration values to perform using template setup routines and features automatic spectral removal algorithms and correction factor determination to output quantitative data. Data provided by the QGA Professional software is given in raw, calibrated and percentage/ppm values. MASsoft 7 professional is supplied with the QMS. It allows for quick and simple control of the QMS; data is provided in raw values. It also has the scope to provide output data in percentage/ppm values but this requires scan templates with calibration data. As already described, the helium, argon and CO_2 experiments were carried out using the QGA Professional software; the neon, krypton, xenon and SF_6 experiments did not have calibration gases and were carried out using the MASsoft 7 professional software.

3.6 Summary

This chapter presented the principles behind the HPR20-QIC quadrupole mass spectrometer (QMS) that was used to carry out experimental analysis. This included the standardisation of the experimental samples using calibration gases to investigate the accuracy and precision of the QMS. A detailed description of the one dimensional flow cell experimental system and the methodology has also been outlined.

Chapter 4 - Sample description and preparation

4.1 Introduction

The flow cell presented in Chapter 3 is designed to hold a ~1 m length of core with a 3.6 cm diameter, which can be used to carry out the fluid flow experiments. To understand the transport mechanisms involved during tracer migration, a suitable sample representing a reservoir sandstone was required. This sandstone would generate experimental breakthrough curves for noble gases travelling through porous media. A sandstone sample from the Fell Formation was selected for the flow experiments to represent a porous medium. This chapter introduces the selection criteria for the Fell sandstone in addition to the acquisition, preparation and analysis of the sandstone sample selected for the flow cell experiments.

4.2 Sample description

4.2.1 Sample selection and overview

A sample with relatively homogeneous mineralogy (primarily siliciclastic), a moderate permeability and with an average porosity (~15 - 25%) was required to represent a porous media. The selected sample needed to be portable but large enough to core samples from, which were used in the bench sized laboratory investigations of tracer transport in sandstones. For logistical reasons an active quarry was chosen as the location from where samples were taken. Samples of the Fell sandstone were sourced from a local stone works (known as Hazeldean sandstone for commercial purposes) (Figure 30). It is quarried at South Charlton, near Alnwick in Northumberland. The Fell sandstone was selected due to its high quartz content (~95%) and low carbonate content (trace amounts) implying there should be minimal mineral alteration and interaction with CO_2 during the flow experiments.

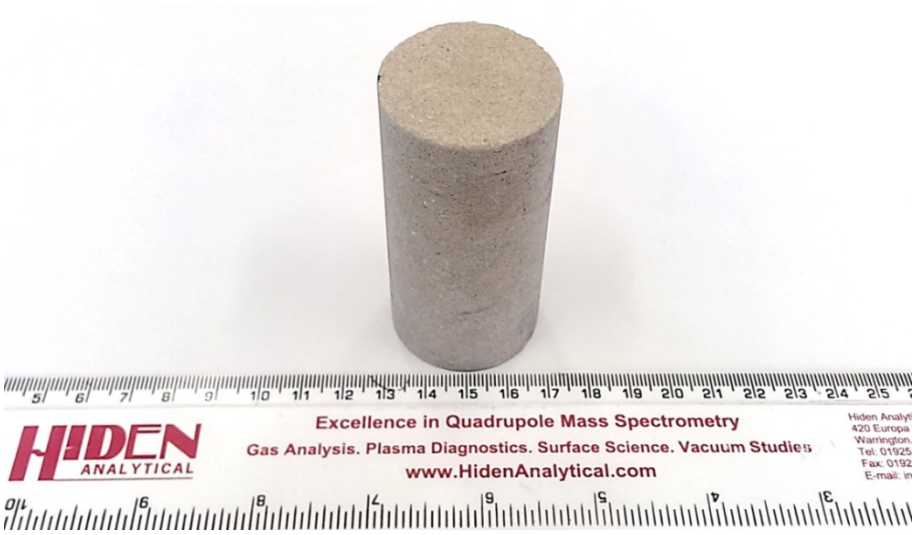

Figure 30: Photograph of a Fell sandstone plug used to test the porosity and permeability of the rock.

The Fell Formation is Chadian to Holkerian (Carboniferous) in age (British Geological Survey). It is a medium to thick bedded, fine to coarse grained cross-bedded sandstone. It is locally conglomeratic, with siltstone, mudstone, seatearth and some thin coals. These rocks were formed from rivers depositing mainly sand and gravel detrital material in channels to form riverbank terrace deposits. The Fell Formation contains floodplain alluvium deposits from fine silt and clay from overbank floods, as well as estuarine and coastal plain deposits.

The physical information for the Fell Formation provided by the local stone works is summarised in Table 10. Table 11 gives a general overview of the Fell sandstone; it is identified it as a semipermeable rock with average porosity The porosity and permeability values presented are experimentally derived from laboratory experiments. This porosity value differs from the average value given by Hutton Stone due to formation heterogeneity.

Table 10 Physical information for the Fell sandstone provided by Hutton Stone Co. Ltd. (2013)

Physical Information	
Bulk density ($Kg.m^{-3}$)	2240
Compressive strength ($N.mm^2$)	84.0
Flexural strength (MPa)	4.1 (wet) – 5.2 (dry)
Porosity (%)	13.1
Absorption (%)	3.7
Saturation co-efficient	0.73
Acid immersion	Passed

Table 11: Summary characterisation of the sandstone sample used in the fluid flow experiments.

Sample Description	
Rock name	Hazeldean Sandstone
Formation name	Fell Sandstone
Age	Lower Carboniferous
Depositional environment	River setting
Rock type	Quartz arenite
Grain shape and sorting	Well sorted, sub-angular to rounded
Tested porosity	20.3%
Tested permeability	221.3 mD

There are some limitations associated with the selection of the Fell sandstone for experiments; it is not a freshly cored sample sourced from point of primary sedimentation. There is evidence of some supergene processes in the rock using SEM images Figure 34, most likely from meteoric water circulation. Additionally, it is not a direct analogue to any current proposed United Kingdom CO_2 reservoirs. However, the Fell sandstone is a relatively homogeneous rock and implies the results produced are reflective of the fundamental transport mechanisms involved. This is of benefit as it improves the understanding of mass transport of tracers in porous media.

4.2.2 Porosity and permeability tests

To obtain an accurate value for the sample obtained for the flow cell, experimental porosity and permeability tests were carried out (by the Institute of Petroleum Engineering at Heriot-Watt University) on a single 3.8 cm x 7 cm cylindrical plug of the sandstone (Figure 30). A single representative sample was chosen due to the apparent homogeneous behaviour of the sandstone. The permeability was determined using a nitrogen gas permeameter. The nitrogen gas flow is controlled in a steady state which allows a flow range of 0 – 2000 $cc.min^{-1}$ and pressures of 0 – 0.7 MPa. This allows control of Darcy flow conditions in the core. A differential pressure transmitter is attached to detect pressure drop across each of the three capillary flow tubes and provide an accurate measurement of gas flow rate. The permeability of the plug is obtained by inputting the recorded values using Darcy's Law. The permeability was determined as 221.33 mD (Figure 31). This is described as a moderate permeability value for a sandstone.

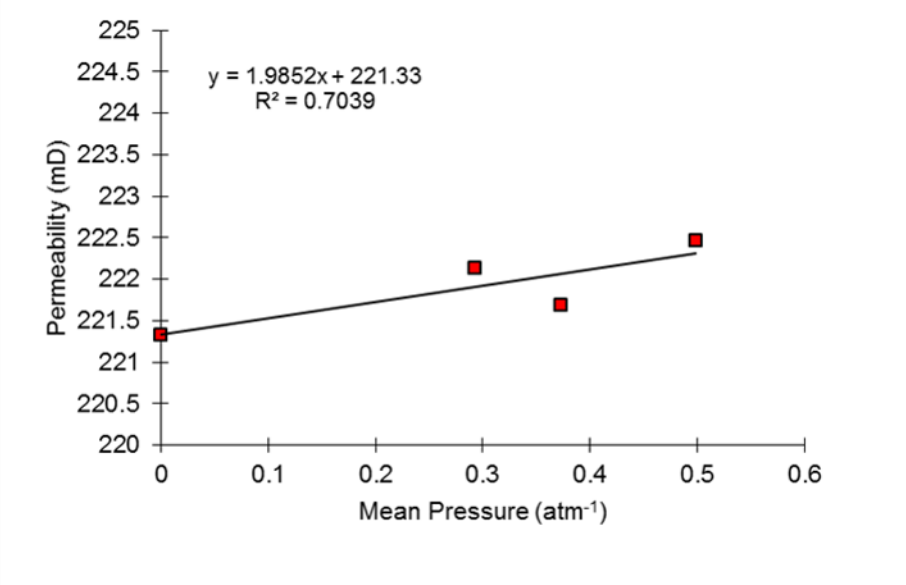

Figure 31: Results from Fell sandstone plug (Heriot-Watt University) with a permeability value of 221.33 mD.

The porosity provided by Hutton Stone was 13.1% and represents the average value for sandstone sourced from the quarry. An experimental porosity for the section of sandstone selected for the experiments was determined using a helium gas expansion porosimeter. Analysis is based on Boyle's Law – that at constant temperature for a fixed mass, the absolute pressure and volume of gas are inversely proportional. Helium gas is allowed into a reference space (a space of known volume) and is fixed at a certain pressure. It is then allowed to expand in a second space, which also has a known volume. The 3.8 cm x 7 cm piece of sandstone was placed in the second space; by measuring the final pressure of the gas in the space, the unknown sandstone volume can be calculated. The calculated porosity for the piece of core was determined as 20.3%. As previously mentioned, the value calculated for the plug differs to the value given by Hutton Stone. The difference is most likely due to variation in the sandstone porosity through the entire formation.

4.2.3 XRD for Fell sandstone

X-ray diffraction (XRD) is an instrumental technique that is used to identify minerals by the arrangement of the atoms in crystals and the distances between crystal faces present in a sample. XRD uses the crystal lattice of minerals in a powdered sample to diffract X-rays. When X-rays are transmitted through a powdered rock sample, the X-rays are diffracted at

internal crystal angles depending on the crystal arrangement. These cause a single spike at specific detector angles. It is important to have a sufficient number of correctly aligned crystals available for detection to ensure an even distribution at all crystal orientations. During a scan, the detector is rotated over a range of angles to ensure all diffracted x-rays from correctly aligned crystals are identified. These series of characteristic peaks can be used to identify the minerals present within the sample.

XRD analysis was carried out on a sample at The University of Edinburgh. A jaw crusher was used to roughly reduce the size of a sample of Fell sandstone. This smaller sample was then placed in a Tema mill to further reduce the particle size. To ensure that the particles sizes were correct for XRD analysis, the powder was further ground by hand using an agate mortar and pestle. The sample was deposited on a flat plate and any excess powder was removed using a glass slide. This prepared sample was loaded up and analysed using copper tubing with a Bruker D8 ADVANCE (by Dr. Nicholas Odling at The University of Edinburgh). This method is considered to be semi-quantitative; the intensity of the diffraction pattern and the estimated peak area of detected mineral is proportional to its concentration. For a semi-quantitative analysis purposes, anything less than 1% was considered a trace amount due to minimum detectability of minerals in the sample. Table 12 shows the data obtained using XRD analysis. Figure 32 shows the produced diffractogram of peaks recorded for the Fell sandstone. When the trace minerals were discounted, the results show that the Fell sandstone is mostly comprised of quartz (95%), with some feldspar and clay minerals present; it can be classified as a quartz arenite, which is complimentary to previous research (Bell, 1978).

Table 12: Semi-quantitative XRD analysis of Fell sandstone. Any minerals detected below 1% were considered as a tracer mineral (TM).

	Formula	Type	Actual (%)	Corrected (%)
Quartz	SiO_2	Silicate mineral	93.5	95
Microcline	$KAlSi_3O_8$	K-rich alkali feldspar	2.21	2
Bytownite (An85)	$(Ca,Na)[Al(Al,Si)Si_2O_8]$	Ca+ member of plagioclase	1.6	2
Kaolinite	$Al_2Si_2O_5(OH)_4$	Clay mineral	1.05	1
Chlorite	$(Mg,Fe)_3(Si,Al)_4O_{10}$	Phyllosilicate mineral	0.6	TM
Illite	$(K,H_3O)(Al,Mg,Fe)_2(Si,Al)_4O_{10}[(OH)_2,(H_2O)]$	Mica - Phyllosilicate	0.31	TM
Muscovite	$KAl_2(AlSi_3O_{10})(F,OH)_2$ or $(KF)_2(Al_2O_3)_3(SiO_2)_6(H_2O)$	Mica - Phyllosilicate	0.18	TM
Gypsum	$CaSO_4 \cdot 2H_2O$	Sulfate mineral	0.124	TM
Calcite	$CaCO_3$	Carbonate mineral	0.091	TM
Pyrite	FeS_2	Sulfide mineral	0.083	TM
Ankerite	$Ca(Fe,Mg,Mn)(CO_3)_2$	Carbonate mineral	0.08	TM
Oligoclase (An16)	$(Ca,Na)(Al,Si)_4O_8$	Member of plagioclase	0.05	TM
Dolomite	$(CaMg)(CO_3)_2$	Carbonate mineral	0.04	TM

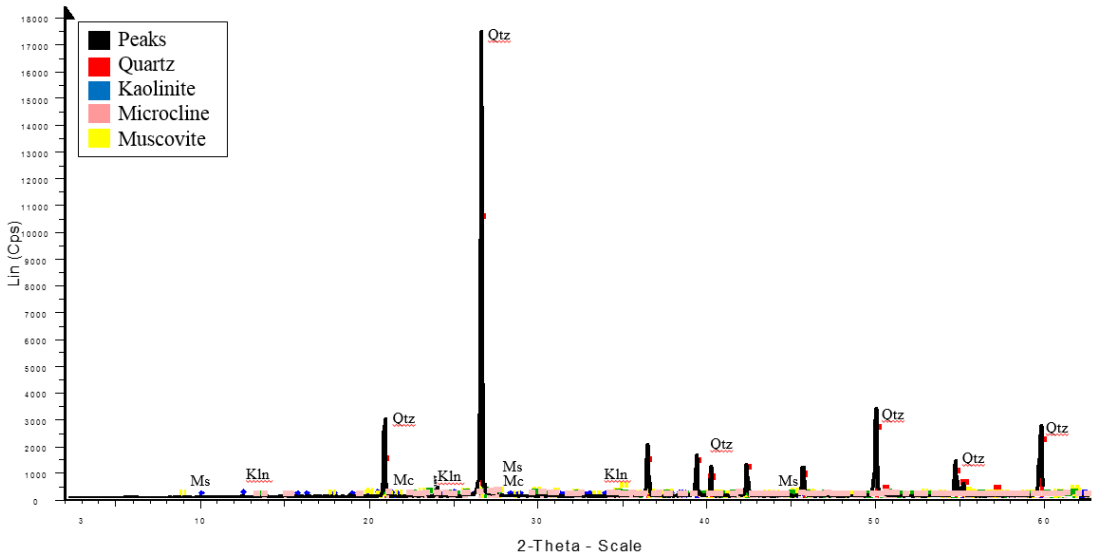

Figure 32: Example of diffractogram for peaks obtained using XRD analysis for Fell sandstone.

4.2.4 Scanning electron microscope

A scanning electron microscope (SEM) is a type of electron microscope that uses a focused beam of electron to produce an image. Qualitative analysis of the prepared samples was carried out using the Philips XL 30 CP SEM at the School of GeoSciences; a computer controlled SEM with automated specimen stage. Images were collected using detection of a secondary electrons and backscatter electrons. The PGT Spirit X-Ray analysis system provided qualitative mineral identification.

4.2.4.1 Thin section preparation for backscatter images

A polished section was cut, ground, polished and ultrasonically cleaned for a flat unscratched surface for SEM analysis by Mike Hall at The University of Edinburgh. Once the polished section was prepared, it was cleaned ultrasonically with deionised water; it was wiped with petroleum ether and dried using compressed air. Handling of the sample from this point was carried out whilst wearing gloves and with minimum contact to the surface. The sample was then carbon coated using a Denton Vacuum BTT-IV (carbon evaporation). After coating, the section was treated with silver paint to form a conductive bridge from the top surface of the sample to the sample holder. Images of the Fell sandstone sample were taken using backscatter electrons (Figure 33). Images show that the sandstone predominately consists of quartz grains. Microcline feldspar is the second most abundant mineral identified, with some alteration to

kaolinite being present. In addition, mica in the form of muscovite and lithic fragments were also observed. This corresponds with the XRD results in Table 12. The backscatter images taken were used for pore size and distribution analysis using ImageJ, which is described below.

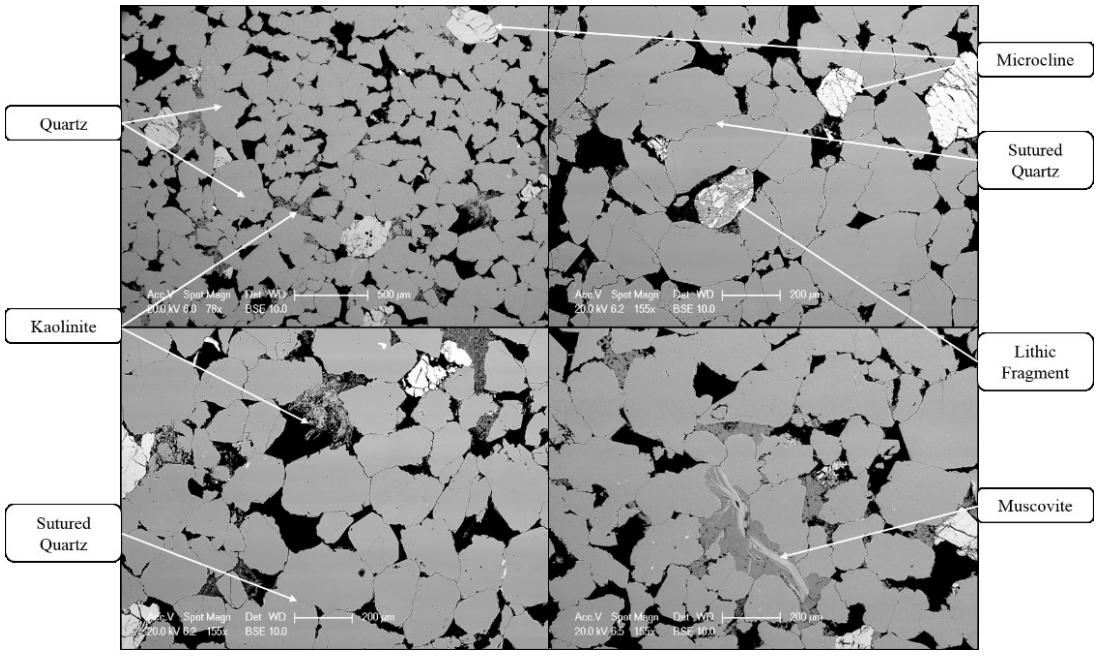

Figure 33: Backscatter images taken of Fell Sandstone. Results show a predominantly quartz-rich sandstone with some alteration of microcline to kaolinite. The individual quartz grains are closely packed and with some interlocking (suture) textures observed.

4.2.4.2 Sample mount for secondary electron images

Small chips (~1cm) of the Fell sandstone that showed good unaffected surfaces were chosen for mounting. Handling of the sample from this point was done wearing gloves and with minimum contact to the surface. These were mounted onto a stub using epoxy. The sample was then treated with gold for its high secondary electron yield using a BAL-TEC SCD 050 (sputter coater). After coating, the sample was treated with silver paint to form a conductive bridge from the top surface of the sample to the sample holder. Images of the mounted samples were obtained using SEM analysis. A selection of the images obtained are shown in Figure 34. Although the sample primarily consists of quartz grains, there is evidence of feldspars that have been altered by dissolution processes. Pitting within the feldspar and overgrowths of kaolinite as a secondary mineral suggest that supergene processes may have taken place. Kaolinite is a product of the chemical weathering of aluminium silicate minerals such as

feldspar. These processes should not affect the overall aim of the research. However, if the sample was intended to be analogous to an offshore reservoir, then these processes may be important.

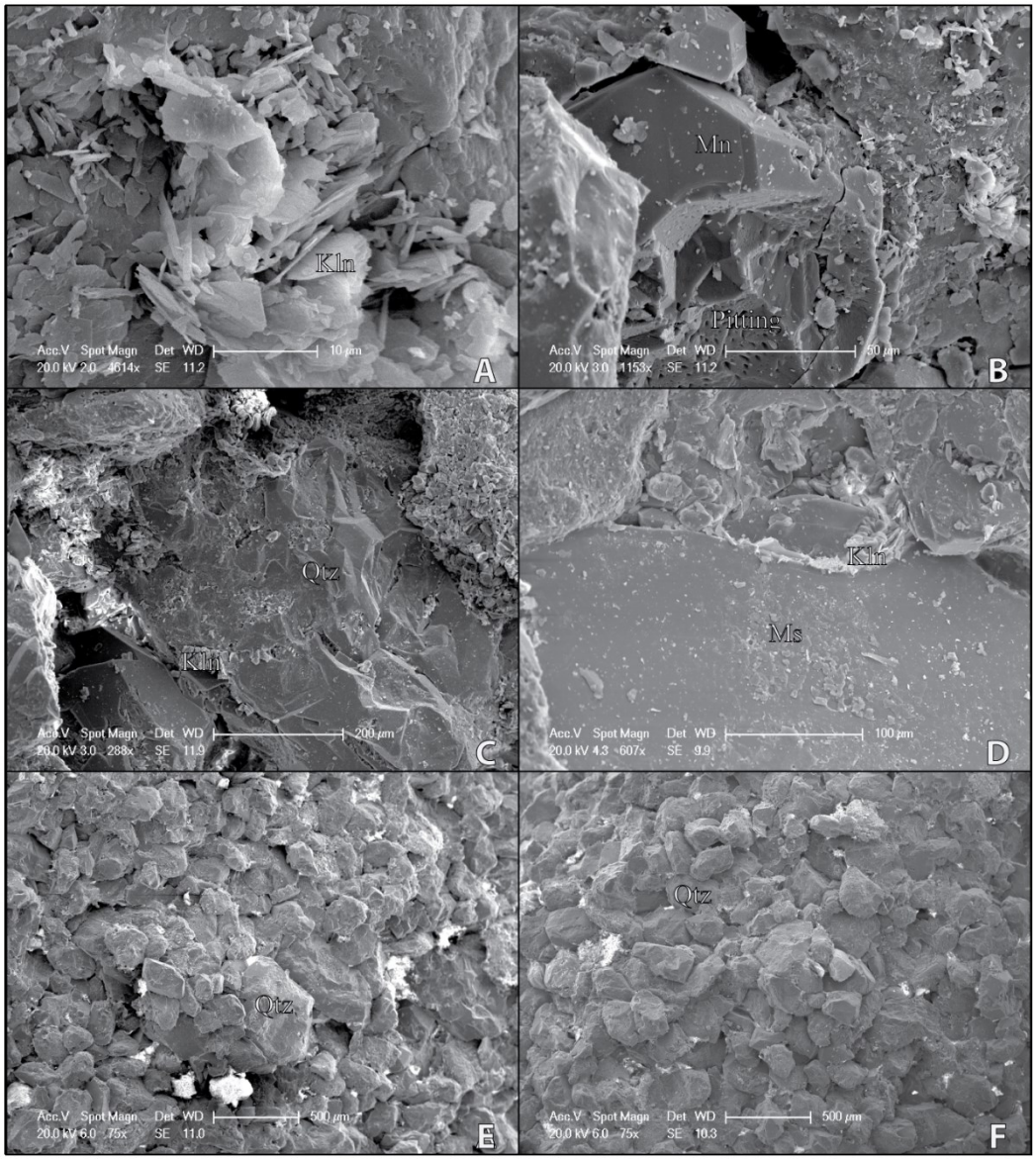

Figure 34: Rough surface SEM images of Fell sandstone. Image A: Kaolinite secondary overgrowths. Image B: Pitting in a microcline crystal. Supergene changes - weak dissolution of feldspar. Image C: Quartz with secondary kaolinite. Image D: Muscovite with intergranular kaolinite. Image E & F: Grain boundary interactions between predominately quartz crystals.

4.2.4.3 Pore network identification

In addition to sections cut and polished for SEM analysis, thin sections were prepared for light microscopic identification (by Mike Hall, the University of Edinburgh). ImageJ is a public domain image-processing programme. Using ImageJ it was possible to use these images to learn more about the pore network, distribution and interactions within the rock. Understanding the network of the Fell sandstone will be advantageous when evaluating the mechanism involved in the transport of the noble gases, SF_6 and CO_2 tracers. Four thin sections are presented using this analysis method; two optical microscope (OM) sections and two backscatter sections (BS) were used for the analysis. The two OM sections were scaled at 1000 µm; the BS images used were 500 µm and 200 µm. The different image sources were chosen to identify any changes in pore network with scale.

For this research the relation between pore length and pore area is simplified by defining the pore length as the square root of the pore area. Consequently, the pore area value measured by the image analysis program easily can be converted to a pore length value. The threshold pore area, at which we define the cut-off for separating the macropores and micropores in the database is based on the classification of pore spaces in Table 13.

Table 13: Classification of pore spaces in rocks (Fischer and Gaupp, 2004).

	Pore Diameter	Petrographical Pore Space Classification	Colloid Chemistry Pore Space Classification
	>10 µm	Macro pores	-
<10 µm	>50 nm	Micro pores	Macro pores
	2-50 nm		Meso pores
	0.02 – 2 nm		Micro pores

Point counting of a thin section can be slow and time consuming; ImageJ can provide a more accurate result in a short timescale (Grove and Jerram, 2011). The following methodology was used to determine the overall porosity of the sample within thin section:

- Open thin section image in ImageJ.
- Select Analyse>Set Measurements; ensure that area fraction and limit to threshold have been selected.

- Select the straight tool on the tool bar. Drag this across a known scale bar for the image. Analyze>Set Scale and choose the length and the units. Selecting 'Global', will ensure all other images will be set to the same scale.
- Select Image>Type>8-bit.
- Select Image>Adjust>Threshold and control the sliders until the pore spaces are red. This is subject to bias; it may be useful to keep the original image nearby to determine if the best layout has been selected.
- Analyze>Measure will give a text window with the results, which will show what the porosity for the sample is, based on the threshold that was selected. This value can then be compared to the bulk sample porosity experimental derived by the Institute of Petroleum Engineering at Heriot-Watt University.

In addition to determining the overall porosity of a sample, it is important to understand the complex pore structures in place. The following methodology was used to determine the void distribution and characterisation within the thin section:

- Using the same image that has been binarised, the distribution of pore space within the image can be analysed.
- Analyze>Analyze Particles command counts and measures objects in binary or thresholded images.

Due to the size distribution of the grains, it was found that setting the macropore values to be greater than 10 μm in diameter, meant that much of the data were bulked into that category. Thus, while still using the values from Table 13, the macro pore selected was further broken down into that shown in Table 14

The binarised images from the OM provide macroporosity information (Figure 35 and Figure 36); in comparison to the BS images that show greater detail of the microporosity (Figure 37 and Figure 38). The results from Figure 35 and Figure 36 with the same magnification show a similar porosity range (16.51% and 18.03%). Porosity values using the high magnification gave results of 14.65% for the 500 μm and 19.78% for 200 μm. These values are lower than that obtained experimentally from a sandstone plug (Section 4.2.2). The higher value from the sandstone plug is most likely due to the bulk composition and does not detect small variations in the porosity.

Table 14: Summary of values used to determine pore areas based on classification of pore spaces in rocks. Four thin sections are presented here; two optical microscope (OM) sections and two backscatter sections (BS) were used for the analysis. The two OM sections were scaled at 1000 µm; the BS images used were 500 µm and 200 µm.

Diameter Range (µm)	**Area Range (μm^2)**	**Figure 35 (1000 µm)**	**Figure 36 (1000 µm)**	**Figure 37 (500 µm)**	**Figure 38 (200 µm)**
Macro pores					
≥500 - Infinity	≥$2.50x10^5$ - Infinity	No particles detected	Image H	No particles detected	No particles detected
≥400 - <500	≥$1.60x10^5$ - <$2.50x10^5$	Image H	No particles detected	No particles detected	No particles detected
≥300 - <400	≥$9.00x10^4$ - <$1.60x10^5$	Image G	Image G	No particles detected	No particles detected
≥200 - <300	≥$4.00x10^4$ - <$9.00x10^4$	Image F	Image F	Image F	Image F
≥100 - <200	≥$1.00x10^4$ - <$4.00x10^4$	Image E	Image E	Image E	Image E
≥10 - <100	≥$1.00x10^2$ - <$1.00x10^4$	Image D	Image D	Image D	Image D
≥10 - Infinity	***≥$1.00x10^2$ - Infinity***	-	-	-	-
Micro pores					
≥0.05 – <10	***≥$2.50x10^{-3}$ - <$1.00x10^2$***	Image C	Image C	Image C	Image C
≥0.002 – <0.05	***≥$4.00x10^{-6}$ - <$2.50x10^{-3}$***	No particles detected	No particles detected	No particles detected	No particles detected
0.00002 – <0.002	***≥$4.00x10^{-10}$ - <$4.00x10^{-6}$***	No particles detected	No particles detected	No particles detected	No particles detected

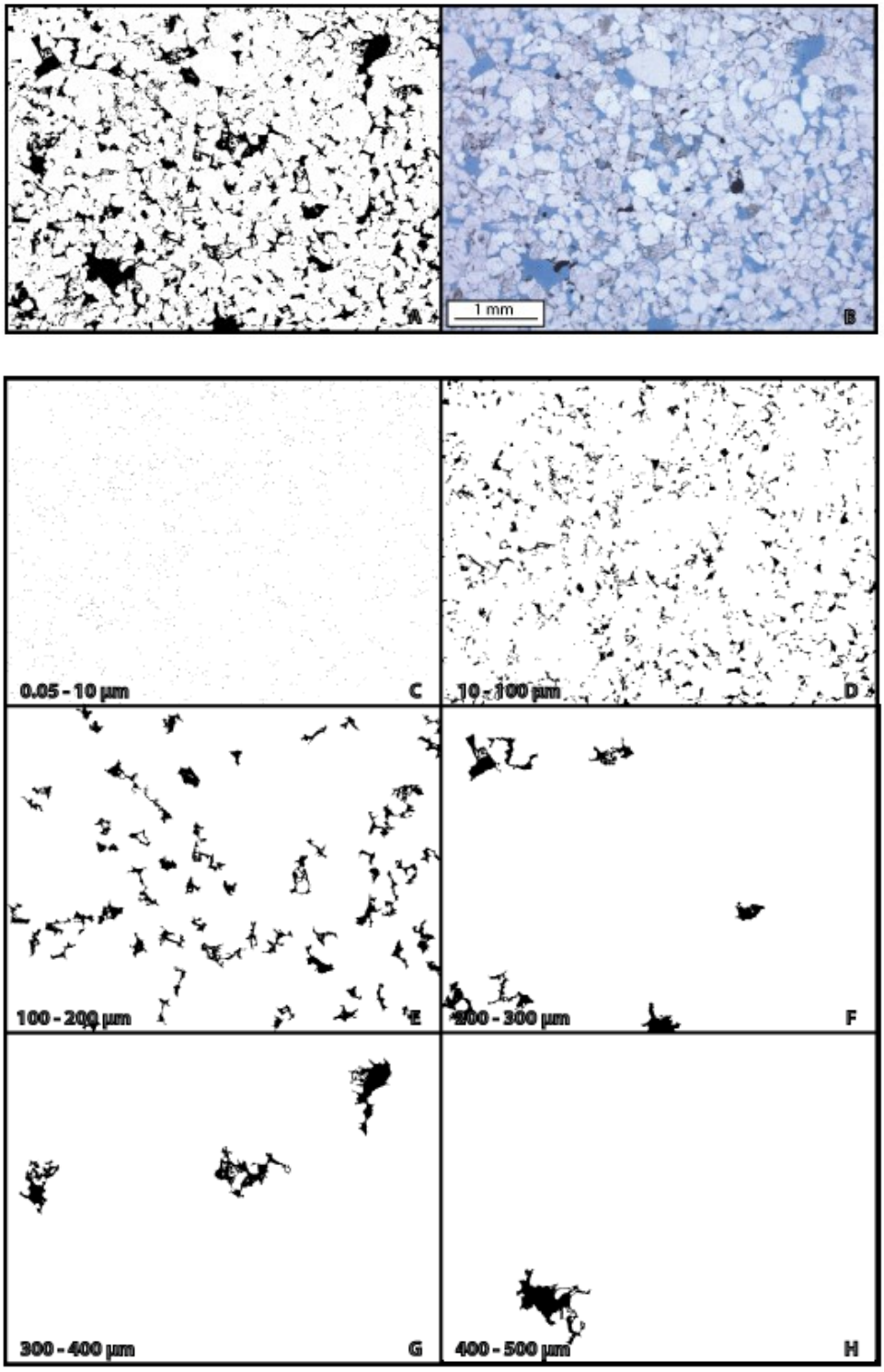

Figure 35: Image (A) shows the threshold results of pores spaces of Image (B). Threshold values used were 71 – 165. Porosity was recorded as 16.51%. Images (C-H) show the area distribution for different pore space sizes.

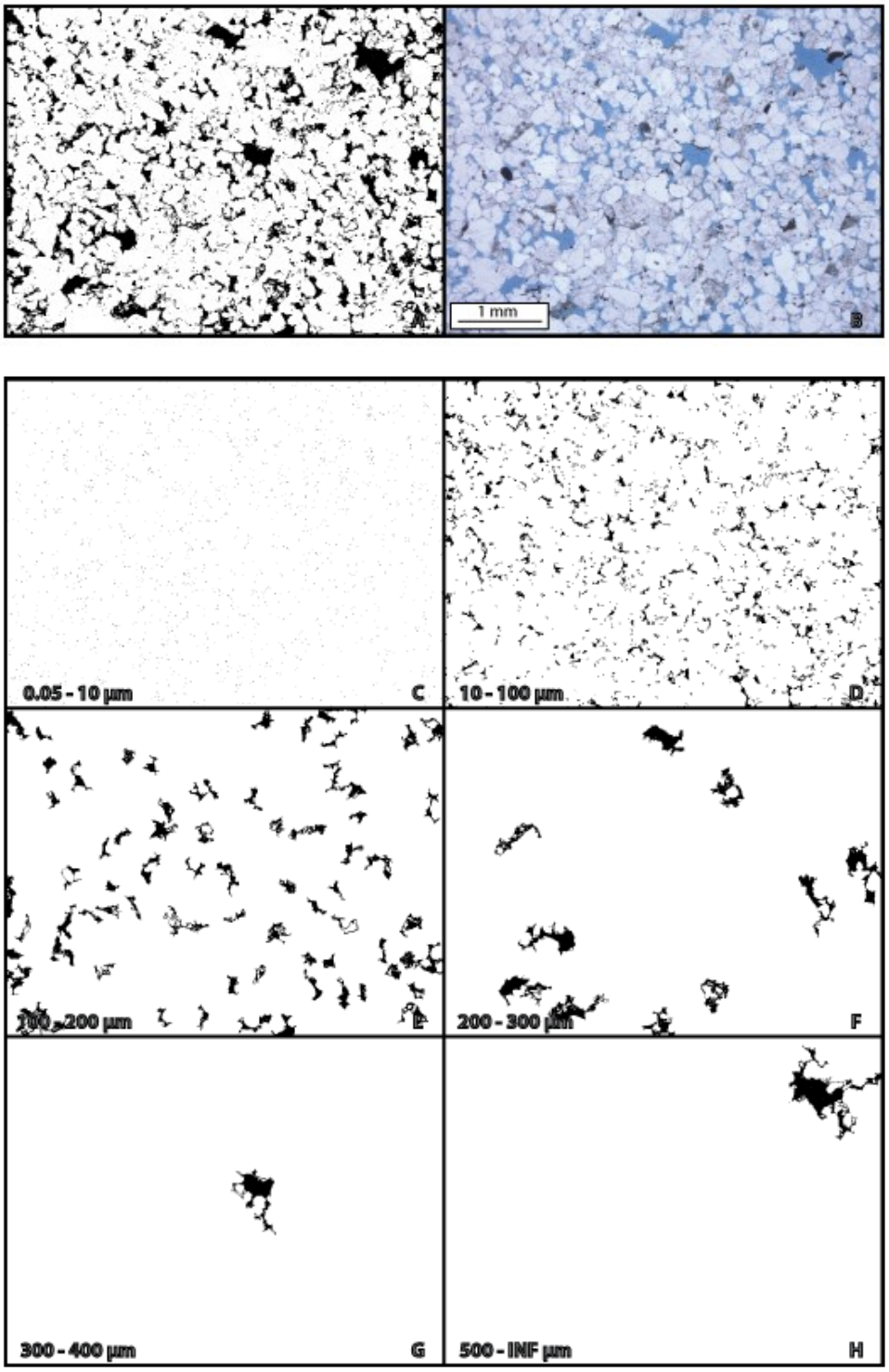

Figure 36: Image (A) shows the threshold results of pores spaces of Image (B). Threshold values used were 103 – 169. Porosity was recorded as 18.03%. Images (C-H) show the area distribution for different pore space sizes.

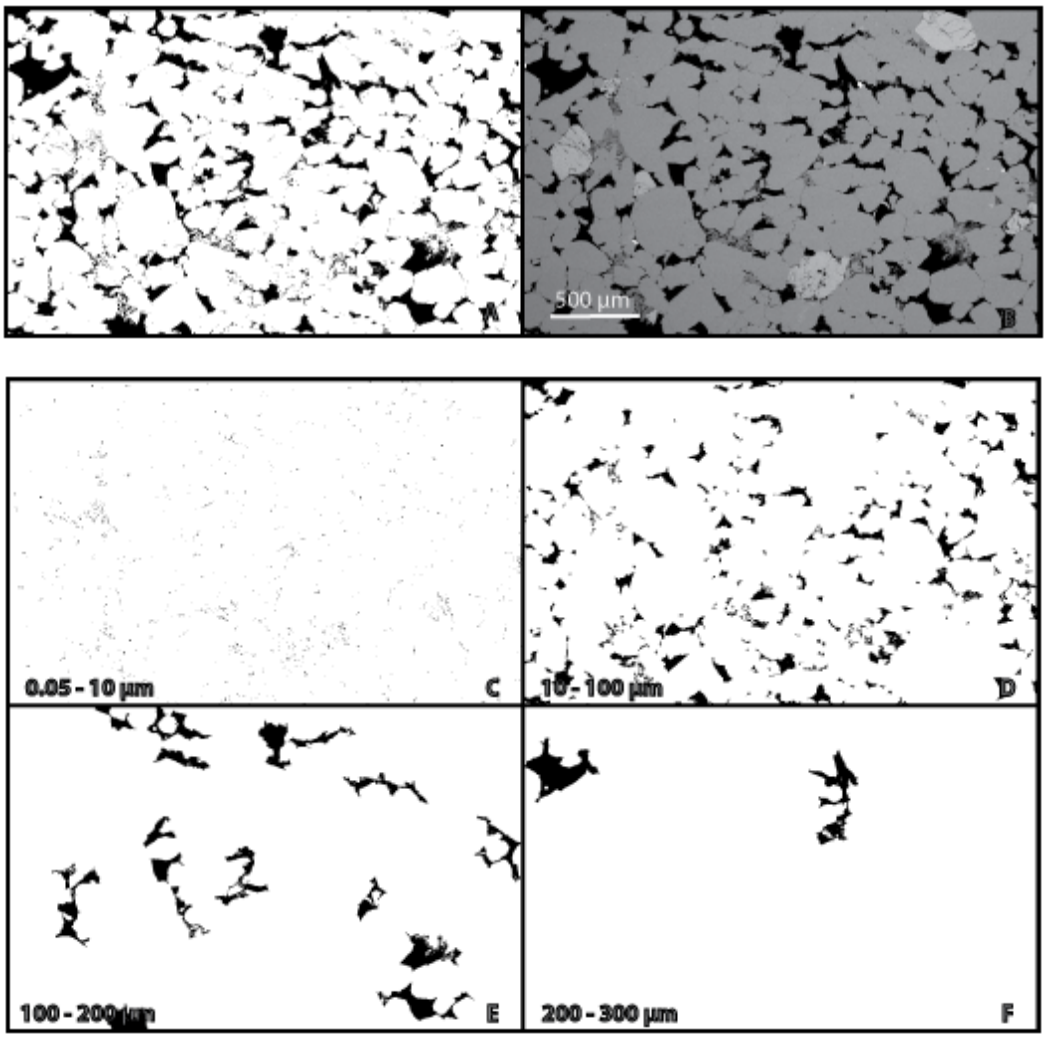

Figure 37: Image (A) shows the threshold results of pores spaces of Image (B). Threshold values used were 0 - 59. Porosity was recorded as 14.65%. Images (C-F) show the area distribution for different pore space sizes.

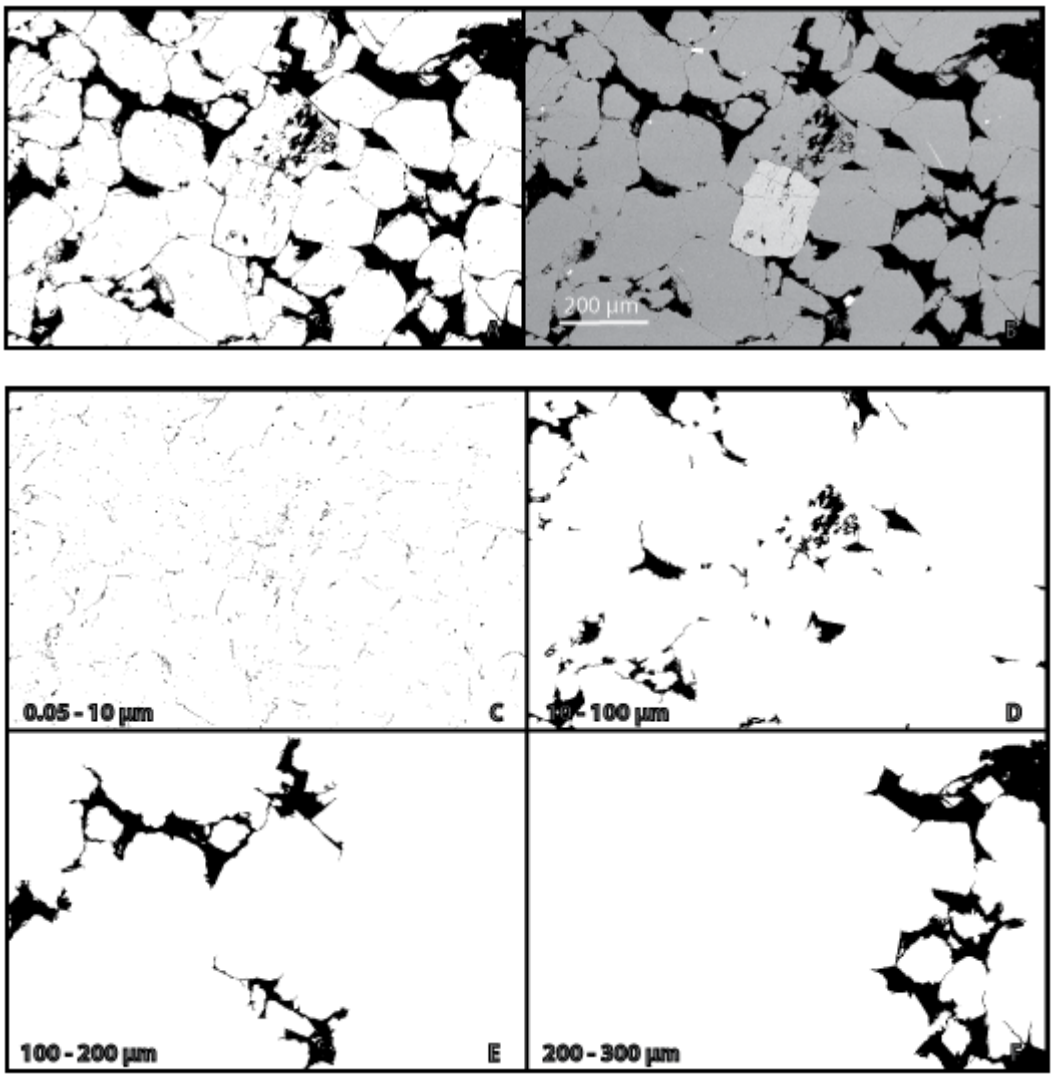

Figure 38: Image (A) shows the threshold results of pores spaces of Image (B). Threshold values used were 0 - 46. Porosity was recorded as 19.78%. Images (C-F) show the area distribution for different pore space sizes.

The pore size distributions for all four sections were plotted as barplots using the eight values of the pore sizes in Table 14. These are shown in Figure 39 to Figure 42. The term 'pore size' in these figures refers to the minimum pore diameter needed to classify the pore space with that size category. This is plotted as the contribution of any pore sizes within that classification to the total porosity calculated for the field of view. Results suggest that most of the pore spaces in the Fell sandstone samples are within the 100 – 200 µm range, within the macropore range. Unsurprisingly, the lower magnification settings identify the larger pore spaces as it covers a wider field of view.

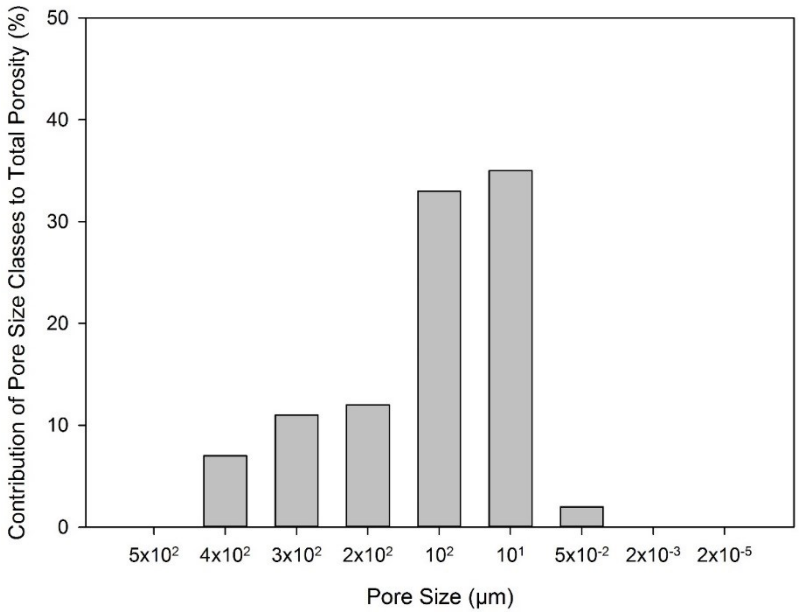

Figure 39: Boxplot of pore size distribution of Fell sandstone optical microscope sample using data from Figure 35. Each pore size class is labelled as the minimum value needed to class the pore space. Porosity was recorded as 16.51%.

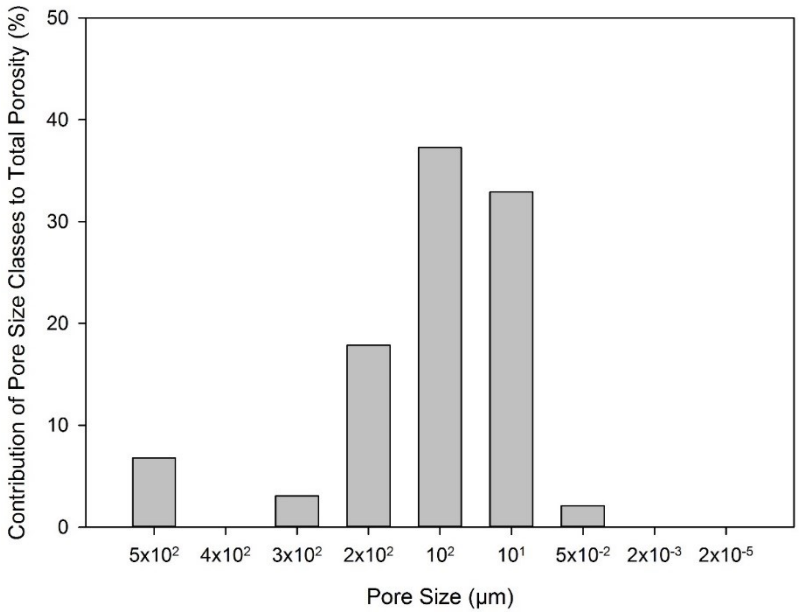

Figure 40: Boxplot of pore size distribution of Fell sandstone optical microscope sample using data from Figure 36. Each pore size class is labelled as the minimum value needed to class the pore space. Porosity was recorded as 18.03%.

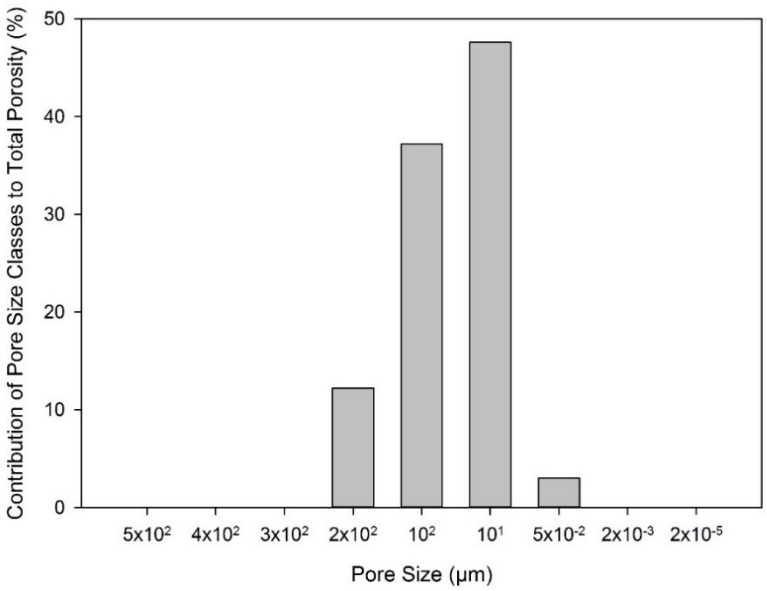

Figure 41: Boxplot of pore size distribution of Fell sandstone backscatter sample images using data from Figure 37. Each pore size class is labelled as the minimum value needed to class the pore space. Porosity was recorded as 14.65%.

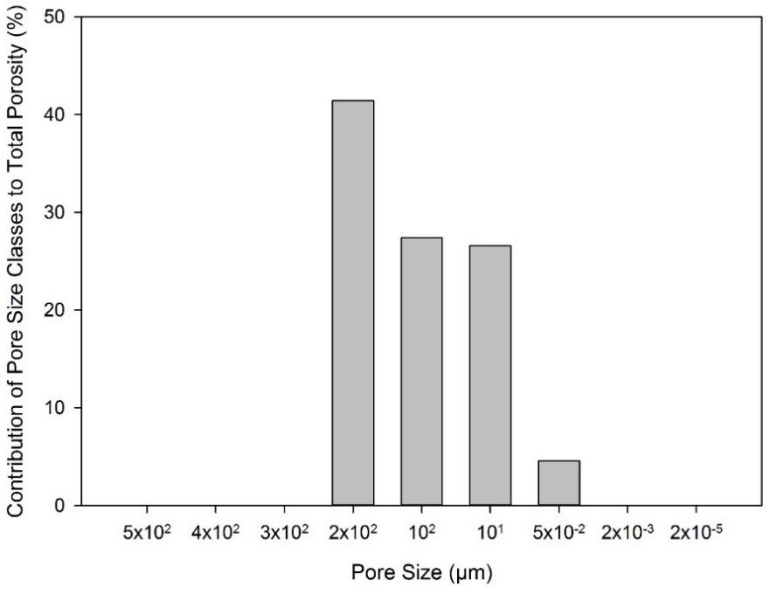

Figure 42: Boxplot of pore size distribution of Fell sandstone backscatter sample image using data from Figure 38. Each pore size class is labelled as the minimum value needed to class the pore space. Porosity was recorded as 19.78%.

Thresholding is a very effective method of measuring the pore spaces within a sample. However, if a stray pixel falls within the chosen threshold range it will be included and could lead to misleading results. As such, caution is needed to ensure the most suitable threshold value range has been selected for the region of interest. Using the 200 μm backscatter image, a sensitivity analysis was carried out to highlight the effect of changing the threshold values on the pore size distribution and porosity. Figure 43 shows two examples of segmentation with threshold values either side of the range used in the pore network analysis. It is evident from the results that if the incorrect values are chosen, the grain boundaries are incorrectly identified. Since the threshold values are selected manually, it is important that understand that a certain amount of user-bias will occur during segmentation.

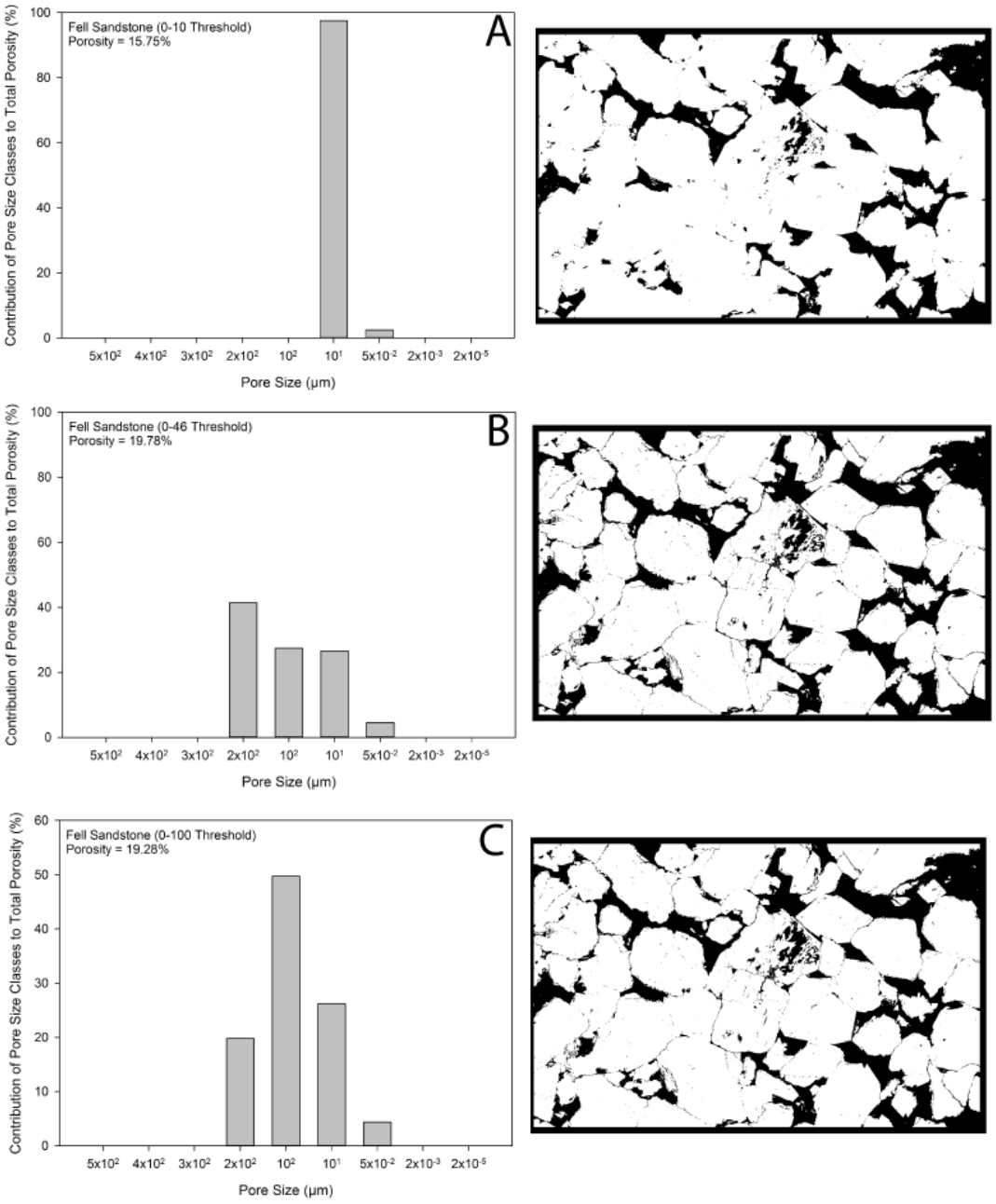

Figure 43: ImageJ results from sensitivity analysis using the 200 µm backscatter image as an example. Image (A) shows the pore size contribution at threshold values set at 0-10, which results in an estimated porosity of 15.75%. Image (B) shows the pore size contribution at threshold values set at 0-46, which are the selected values for the original analysis. Image (C) shows the pore size contribution at threshold values set at 0-100, which results in an estimated porosity of 19.28%.

In addition to calculating the distribution of pore space, pore shape analysis was completed on the images obtained from the OM and BS images. As previously mentioned the shape of the pores and how they connect is an important aspect of understanding the permeability of the system and how it may affect flow transport. Based on existing literature, the following formula was used (Anselmetti *et al.*, 1998):

$$\gamma = \frac{P}{2\sqrt{\pi A}} \quad (2)$$

P = pore perimeter (μm)

A = pore area (μm^2)

γ is a dimensional value that represents the pore geometry; with the formula, no values should be negative. A spherical pore is seen as a circle in a 2D image and would have a γ value equal to one. Pore spaces will become more complex and diverging as the γ value increases. The input P is part of the results produced during the particle analysis of the images.

For this analysis, four images were used over three magnifications (as used in Figure 35 - Figure 38); the twenty pores with the largest areas from each of the images were measured. Figure 44 shows the calculated pore size diameter measured against γ. The values were limited to twenty as it provided an unbiased depiction of the trends without too much background noise. Although values smaller than one are not possible, they may occur due to the way that ImageJ analyses particles. The dotted line represents the median value taken for each pore space range and shows that the smaller pores have lower γ values. These median values suggest that the smaller pores are simple and well rounded but become more complex with an increase in size (Anselmetti *et al.*, 1998). These results suggest there are some simple pores present as well as some highly branching pathways. These results form part of the understanding of mass transport within the Fell sandstone and will be considered when proposing a model to describe the experimental breakthrough curves produced by the different tracers.

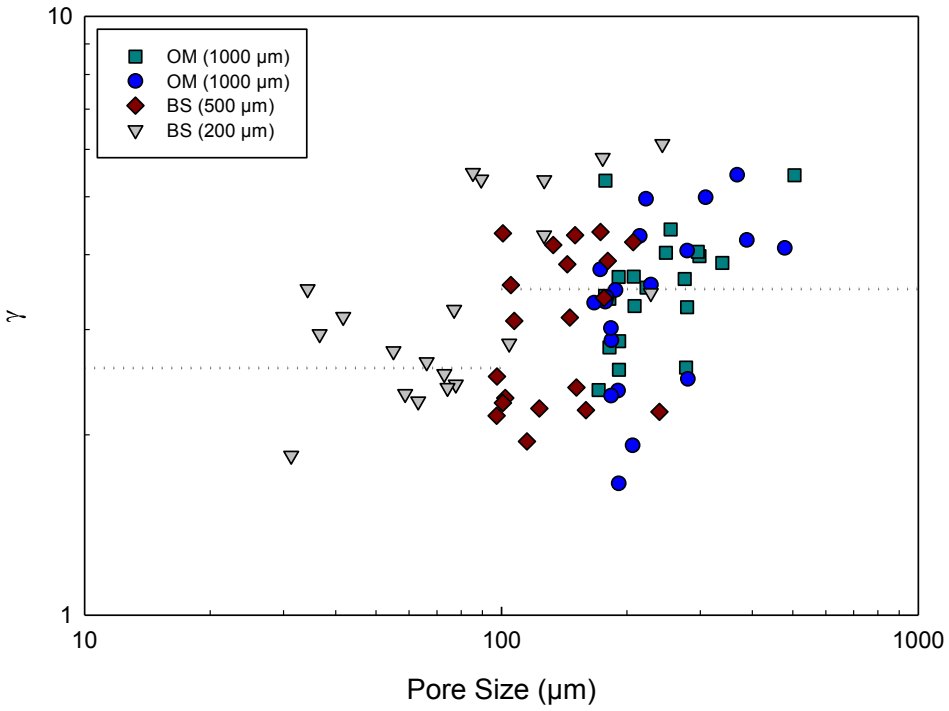

Figure 44: Plot of pore shape parameter (γ) with the macro pore space (>10 µm) for individual pores of the Fell sandstone. The plot presents the image analysis of four images taken at three magnifications (1,000, 500 and 200 µm). The 20 largest area pores spaces were chosen from each of the four images. The dotted line represents the median value taken for each pore space range (2.59 for 10 – 100 µm and 3.51 for 100 – 1,000 µm). The median values suggest that the smaller pores are simple and well rounded; but become more complex and branched with an increase in size (Anselmetti et al., 1998).

4.2.4.4 Pore architecture models

Images taken from SEM analysis were used in a digital rock reconstruction methodology to generate a 3D model of the rock and infer the pore space. The method used was pore architecture modelling (PAM) as developed by Wu *et al.* (2006). The resulting 3D models (referred to as a PAM) can be used in a multiphase flow simulator to determine the multiphase flow dynamics as well as understand the geometry and topological properties of the pore system. For this research, a PAM can be used to understand the variations fluid pathways occurring with a change in image/model scale. Higher resolution models should capture the finer detail of the pore systems, which may be important for pore connectivity. As such, a higher resolution model should reproduce the pore scale features and fluid properties more

accurately. Dr. Zeyun Jiang, at the Institute of Petroleum Engineering at Heriot-Watt University, generated the PAMs presented in this section.

A 3D PAM can be generated using 2D images from either thin sections or backscatter SEM images (Wu *et al.*, 2006). The initial 2D image is binarised into a black and white image where the pore spaces are represented as black voxels and the matrix is represented as white voxels. This binarised image acts as a statistical template for generating a 3D model. Ideally, three orthogonal images would be used to preserve any anisotropic matrix and as such, flow properties of the system (van der Land *et al.*, 2013). However, it is also acceptable to use one image and triplicate it into the three orthogonal directions assuming the rock is homogeneous in nature. In the reconstruction, a third order Markov-Chain/Monte Carlo approach generates a 3D model based on a multiple voxel interaction scheme to predict global features and construct a 3D model that is statistically similar to the original 2D input images (Wu *et al.*, 2004). Subsequent to PAM generation, the pore network can be extracted by systematically eroding the 3D pore model. The network is simplified into a series of nodes and bonds; straight tubular throats (bonds) represent the connected pores and where they intersect are pore bodies (nodes) (Jiang *et al.,* 2007, Kallel *et al.*, 2015).

The Fell sandstone sample used in this study was sourced from a quarry meaning that the way up direction is unknown. As such, directional images were not generated here. The sample was considered as relatively uniform, so a single image could be used to generate a PAM. Two BS images at different magnifications of 200 μm and 500 μm (with resolutions of 1.005 μm/pixel and 2.05 μm/pixel, Figure 45A) were selected and used to generate two individual 3D PAMs (Figure 45B). A pore network was extracted from each model before flow simulation was performed. Primary drainage is the injection of oil into an initially water-saturated medium and Figure 45C shows the extracted pore network from each model after undergoing primary drainage. Here, the blue nodes and bonds are water saturated and the red nodes and bonds are oil saturated. From the visualisation of these flow simulations, difference in the pore network and fluid flow properties can be observed. In the lower resolution model (2.05 μm/pixel), it is apparent that the injected oil does not equally invade all the pore spaces, suggesting that there may be preferential pathways. These preferential pathways appear to have some tortuous behaviour associated with them. With an increase in resolution (1.005 μm/pixel), it is apparent that the oil injection can become impeded and trapped between grains.

A potential reason for this is the oil is unable to overcome the capillary threshold pressure. In order to exhaust additional pore spaces during fluid transport, it could require an increase in pressure.

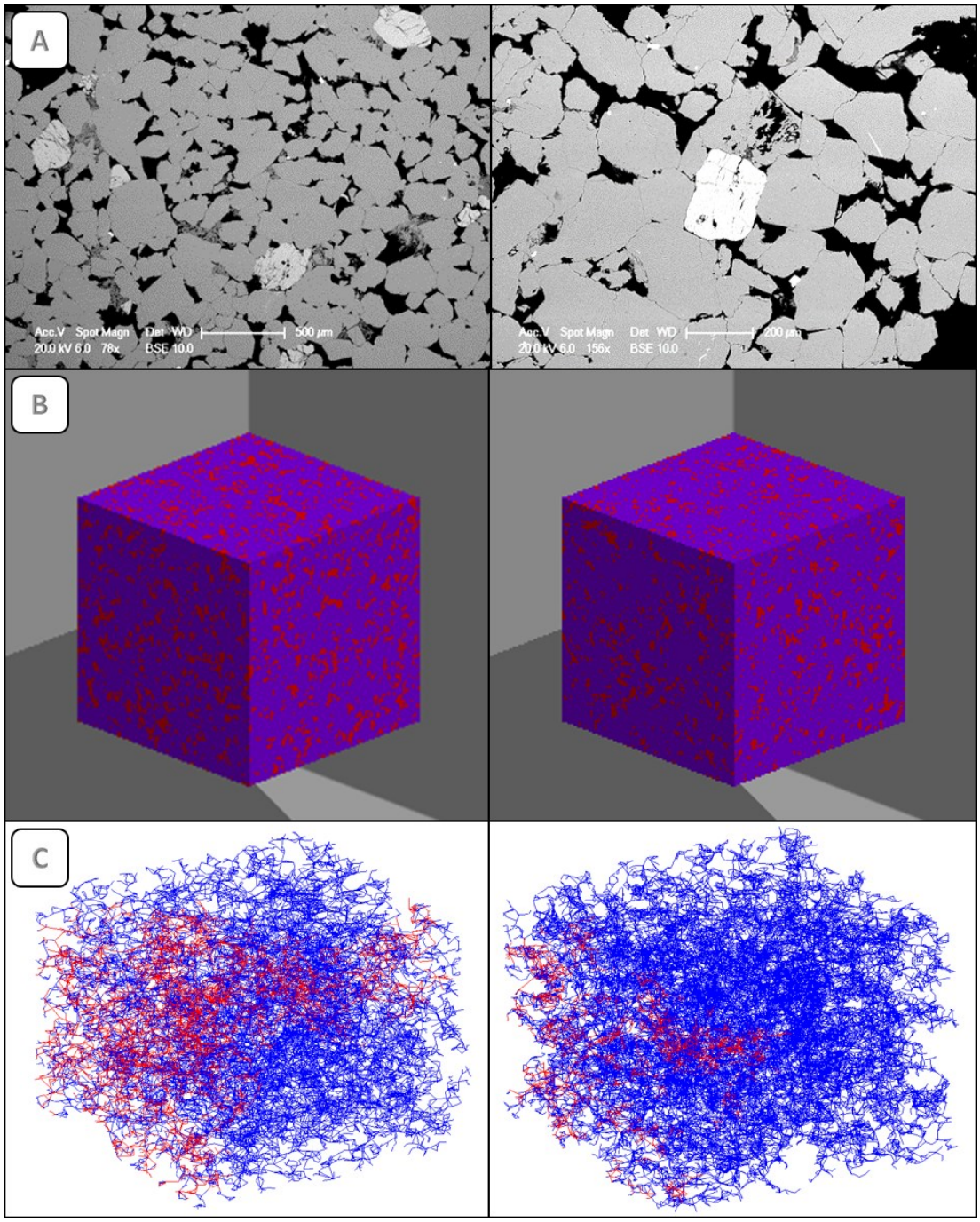

Figure 45: Results from pore architecture modelling using two BS images to generate digital reconstructions. Each column represents a separate original image and final model. (A) Original BS images used togenerate the PAMs. (B) 3D model generated using the BS images. (C) Drainage simulation within the pore network extracted from each PAM.

4.2.4.5 Permeability and porosity variations

Permeability values were measured for the flow cell sample using experimental outputs. Permeability was calculated using incompressible flow from Carman (1956):

$$k = \frac{Q}{A}\mu_a\left(\frac{x}{P_1 - P_2}\right) \quad (3)$$

k = intrinsic permeability (m^2)

Q = volumetric flow rate ($m^3\ s^{-1}$)

A = cross sectional area (m^2)

μ_a = dynamic viscosity of the gas (Pa s^{-1})

P_1 = pressure input (Pa)

P_2 = pressure output (Pa)

x = length of the flow path (m)

Flow rates were measured using a Cole-Parmer acrylic flowmeter kit. For argon, the flow rate maximum was 1.0 sL min^{-1} in 0.1 increments. The accuracy of this flowmeter was ± 5% full scale (± 0.05 sL min^{-1}). Table 15 shows the permeability range calculated from the pressure end-members during the experiments. The intrinsic permeability calculations will not be the same with a drop in flow rate due to a decrease in accuracy. The values presented in Table 15 are most likely the representative permeability as they were calculated accounting for the flow rate and the core itself. However, with the low level of accuracy using the flowmeter, these permeability calculations require further investigation and will be compared to modelling outputs in Section 6.3.3.2.

Table 15: Calculated permeability values for the Fell sandstone 0.96 m length core under experimental conditions using Equation (3).

Pressure	Permeability (k)		Flow Rate (Q)	Error
(Pa)	(m^2)	(mD)	($m^3\ s^{-1}$)	($m^3\ s^{-1}$)
50,000	9.31×10^{-13}	943.71	3.33×10^{-6}	$\pm 8.33 \times 10^{-7}$
10,000	1.16×10^{-12}	1,179.63	8.33×10^{-7}	

Additional permeability and porosity values were estimated using the BS images and the generated 3D pore network image and are compared to the ImageJ analysis in Table 16. The PAM results provided much lower permeability values than the plug and experimentally derived values. The major differences found in the permeability values are most likely the result of scale and relative sample sizes. The PAM images were produced using BS images and compared to the scale of the experiments (~1 m length), would miss the larger pores that may conduct the biggest proportion of flow. It is possible that the permeability values are lower due to the use of a single binaries image to construct the PAM. Ideally, three orthogonal images would preserve the directionality of the model (van der Land *et al.*, 2013) and this could have affected the permeability results. Additionally, the binarisation of the BS images can be a source of error as highlighted with the ImageJ analysis, which may reduce the connectivity of pores (Figure 43).

The porosity estimations obtained from the images using ImageJ are a close comparison to those estimated by Dr. Zeyun Jiang, at the Institute of Petroleum Engineering; the slight differences may be due to the different techniques that set the detection thresholds. As previously mentioned the value from the sandstone plug is most likely due to the bulk composition and does not detect small variations in the porosity that the thin sections would highlight. The selection process for the representative porosity value used for the flow cell will be discussed in Section 6.3.4.

Table 16: Results of permeability and porosity values generated from PAM analysis (by Dr. Zeyun Jiang, at the Institute of Petroleum Engineering). For comparison, the ImageJ values for the same field of view and the plug results (HW) have been included.

Sample (μm)	Permeability (k) (mD)		Porosity (n_e) (%)			
	PAM	HW	PAM	Image	HW	ImageJ
500	34.61	221.33	14.49	16.34	20.3	14.65
200	4.43	221.33	15.28	15.28	20.3	19.78

4.3 Summary

This chapter presented the sample used as part of the one dimensional flow cell experimental system. The Fell sandstone will represent porous media in the experiments. The Fell sandstone is mostly comprised of quartz (95%), with some feldspar and clay minerals present and can be classified as quartz arenite. Data from ImageJ and PAM analysis suggest there are some simple pore spaces present as well as some highly branching pathways. Overall, the Fell sandstone is sample with relatively homogeneous mineralogy (primarily siliciclastic), an average porosity and a moderate permeability range.

Chapter 5 - Experimental results and analysis of breakthrough curves for tracer transport in homogenous porous media

5.1 Introduction

It is important to monitor a storage site for unplanned migration of CO_2. The use of tracers have proven to be a successful method of monitoring the subsurface. Understanding processes that affect the transport of gas through porous media is necessary to interpret the behaviour of tracers during CO_2 storage. The establishment of an experimental methodology that monitors gas phases during leakage would be beneficial. This chapter presents the results from experimental breakthrough curves for gas tracers through a sandstone sample. Experiments were performed using the specially designed flow cell outlined in Chapter 3 using the Fell sandstone core described in Chapter 4. The Fell sandstone is a relatively homogeneous rock selected for understanding mass transport of tracers in porous media.

Pulse release experiments were carried out using noble gases (excluding radon) and SF_6 tracers using CO_2 as a carrier gas over a range of pressures (10,000 – 50,000 Pa). For comparative purposes, experiments were also carried out under the same conditions for CO_2 using N_2 as a carrier gas. A discussion is formulated to analyse the results of the breakthrough curves of the different tracers and how these relate to the transport mechanism involved. These experimental results are compared to analytically modelled data in Chapter 6. A further discussion of the combined results will provide an understanding of the controlling mechanisms involved in tracer transport.

5.2 Data presentation from experimental results

Due to budget limitations and availability of calibration bottles needed for the experiments, three of the seven different tracer experiments were completed using a calibration gas. The experiments carried out under calibrated conditions were helium and argon to remainder CO_2 (He/CO_2 and Ar/CO_2), and CO_2 to remainder N_2 (CO_2/N_2). The use of a calibration gas allows the comparison of replicated experiments using the QGA Professional software. The remainder experiments of neon, krypton, xenon and SF_6 to remainder CO_2 (Ne/CO_2, Kr/CO_2, SF_6/CO_2 and Xe/CO_2) were carried out using the basic MASsoft software package. Output from these experiments were limited to raw values. Further information about the calibration process can be found in Chapter 3 (Section 3.3).

To compare the results across the experiments, it was necessary to normalise all the values. To do this, baseline values were deducted from the output values; baseline values were obtained from background readings in the experiment prior to pulse release. The corrected curves were plotted using C/C_{max}. C/C_{max} is defined as the current value (or concentration) of the gas at a given time over the peak value obtained during the experiment. As shown in Figure 46 and Figure 47 for a sample argon experiment, the agreement between the curves are apparent and thus comparable. Data are taken from a sample experiment sampling argon at 10,000 Pa through CO_2 feeder gas. By plotting all results as $C/C_{max,}$ it allows for comparison of calibrated results with those of the breakthrough curves where calibration gases could not be procured.

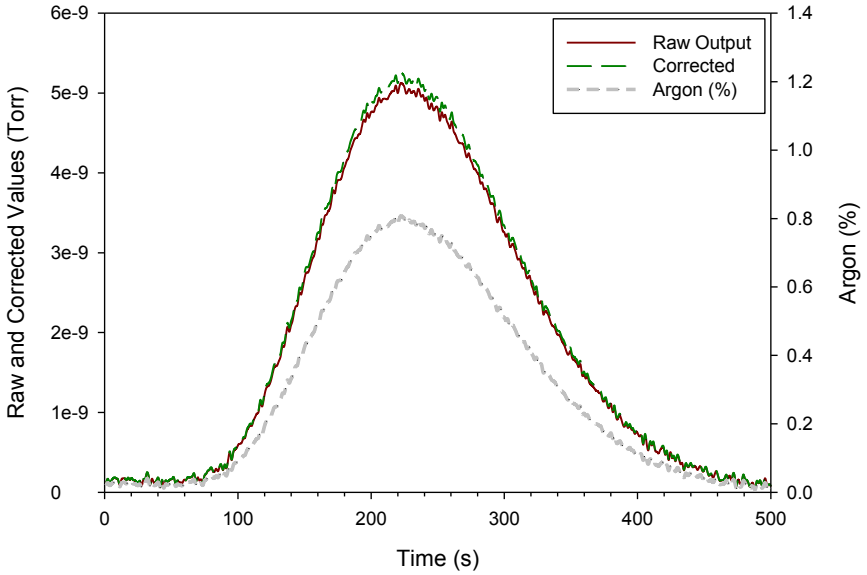

Figure 46: Comparison of the calibrated breakthrough curves for the same experiments using the output data from QMS. Baseline values have been deducted from the data.

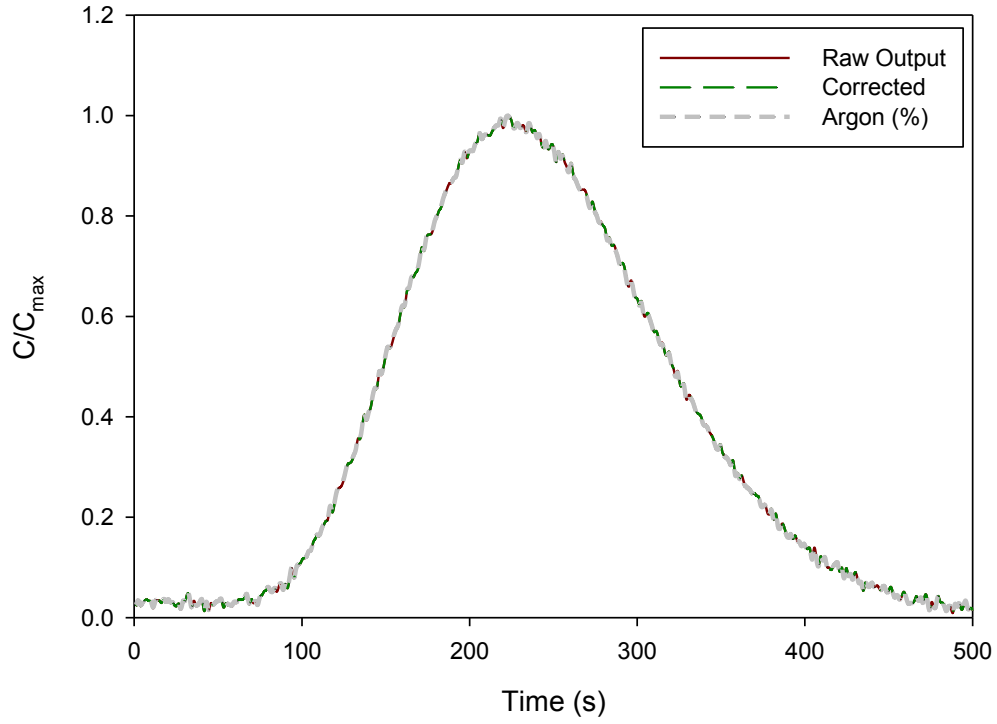

Figure 47: Comparison of the breakthrough curves from the same experiment using the output data from QMS when changed to C/C_{max} from Figure 46. Data has been normalised using the individual experimental peak concentration value.

Table 17, Figure 48 and Figure 49 show an example of calibrated results from five repeated experiments for argon at 50,000 Pa. Results from the argon experiments using the QGA Professional software provided a ratio/percentage between the tracer and the carrier gas. It is apparent that the estimated mass of tracer released with each experiment differs by less than 2% from the average. The ratio results are determined by the pressure difference during the experiment. Experiment Argon R1 shows a higher argon percentage result despite the close mass values. This is likely due to the greater pressure difference of the carrier gas for this experiment (Table 17). When the samples are normalised to C/C_{max} (Figure 49), the results show the same breakthrough curve pattern. This highlights the importance of repeating the experiments to identify the characteristic behaviour of the tracer. In addition, monitoring the conditions of the system eliminates the suggestion that variations in the peak is due to retention of the sample.

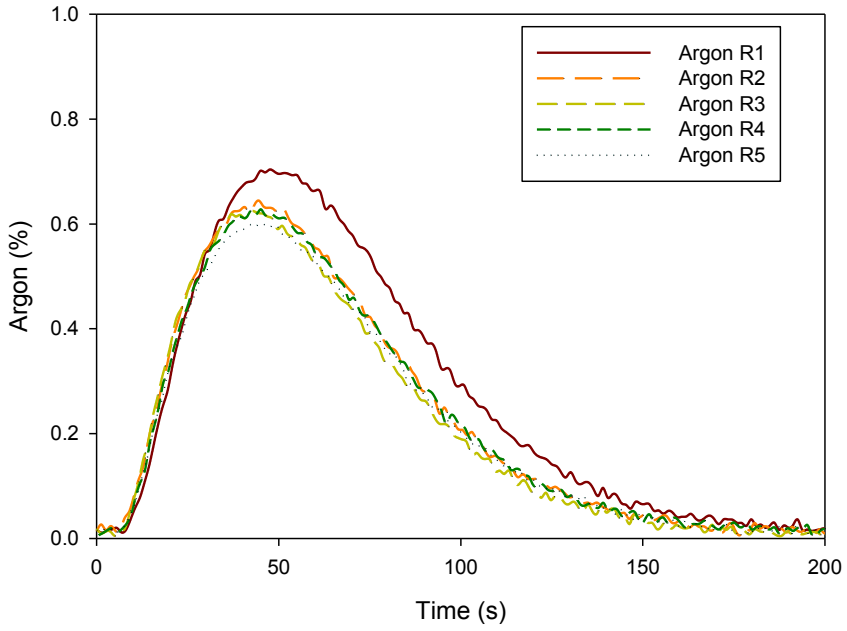

Figure 48: Results for the five repeat experiments for argon at 50,000 Pa. The results are the breakthrough curves over time against percentage. All the curves have been plotted with the baseline value removed.

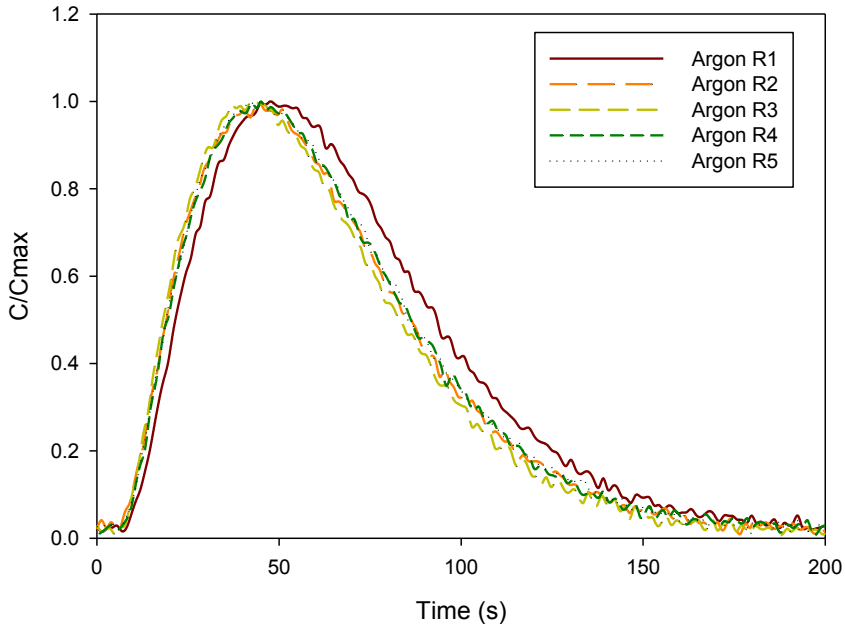

Figure 49: Normalised results from the five repeat experiments for argon at 50,000 Pa. The results are the breakthrough curves over time against C/C_{max}. All the curves have been plotted with the baseline value removed.

Table 17: Data extracted for the five repeat experiments for argon at 50,000 Pa. Table shows the mass of tracer captured in the 20 cm length of pipe using the ideal gas law PV=nRT. Differences in pressure of the captured pulse are compared to the pressure of the carrier gas at time of release.

Experiment Reference	Mass of Tracer (mg)	Tracer (Pa)	Carrier Gas (Pa)	Difference (Pa)
Argon R1	0.2426	48,770	43,410	5360
Argon R2	0.2401	48,270	48,050	220
Argon R3	0.2455	49,350	49,850	-500
Argon R4	0.2488	50,010	47,730	2280
Argon R5	0.2406	48,370	47,690	680

5.3 Results of breakthrough curves produced from tracer experiments

5.3.1 Overview of experimental inputs and results

Each of the specific tracer gas experiments were repeated five times. This replication was to ensure that the variability associated with the transport of the tracer could be estimated. Table 18 identifies the capture pressure of each of the tracer experiments. All the breakthrough curve plots commence at 0 s, which represents the moment at which the tracer pulse was released. The timing of the tracer pulse is recorded during the experiment and correspond with the timing of the QMS. A smoothed line was derived for each of the pressures as a result of these five replications. Smoothed lines were derived from the smooth.spline() function in RStudio. This provided smooth curves that fitted the data using a cubic spline function. Table 19 shows the peak breakthrough value of the smoothed line for each of the tracer pressures. Table 20 shows the mean (including standard deviation) of the five experiments run at each pressure for each tracer mixture. These values are also represented in Figure 50 for all the experiments.

Table 18: Sampling pressure (Pa) of captured tracer for each of the replicate experiments carried out.

	He	**Ne**	**Ar**	**Kr**	**Xe**	**SF_6**	**CO_2**
				50,000 Pa			
	50,930	49,970	48,770	49,680	49,500	49,430	49,230
	51,860	49,850	48,270	49,950	49,570	49,950	50,450
	49,140	50,190	49,350	49,860	49,450	50,380	50,760
	50,040	50,000	50,010	50,360	50,000	49,980	49,010
	50,010	50,110	48,370	50,070	49,570	49,600	51,250
Average	*50,400*	*50,020*	*48,950*	*49,980*	*49,620*	*49,870*	*50,140*
SD ±	*1,040*	*130*	*730*	*250*	*220*	*370*	*980*
				40,000 Pa			
	40,080	39,990	38,710	39,830	39,450	39,850	40,910
	40,000	39,870	39,390	40,010	39,520	39,950	40,830
	40,020	39,550	39,990	39,560	39,520	39,990	40,150
	40,480	39,730	39,380	39,950	39,830	40,550	41,880
	40,160	39,710	40,440	39,960	40,160	39,920	39,140
Average	*40,150*	*39,770*	*39,580*	*39,860*	*39,700*	*40,050*	*40,580*
SD ±	*200*	*170*	*660*	*180*	*300*	*280*	*1,020*

				30,000 Pa			
	31,710	30,030	29,600	30,180	29,900	30,990	30,370
	30,020	29,810	29,330	30,130	29,920	29,890	29,030
	29,700	29,940	28,980	30,000	29,680	29,870	29,800
	30,100	30,090	29,670	29,960	29,660	30,000	31,260
	30,090	30,120	28,450	29,930	22,980	29,930	30,490
Average	*30,320*	*30,000*	*29,210*	*30,040*	*28,430*	*30,140*	*30,190*
SD ±	*790*	*130*	*500*	*110*	*3,050*	*480*	*830*
				20,000 Pa			
	20,890	20,090	18,990	19,550	19,680	20,020	19,840
	21,590	19,800	23,340	20,000	19,650	20,020	20,380
	20,070	19,790	19,460	20,080	19,680	20,050	19,880
	20,010	19,750	19,250	19,550	19,850	19,800	20,900
	20,470	19,890	20,120	20,530	19,930	20,200	21,630
Average	*20,610*	*19,860*	*20,230*	*19,940*	*19,760*	*20,020*	*20,530*
SD ±	*650*	*140*	*1,790*	*410*	*120*	*140*	*750*
				10,000 Pa			
	10,720	10,930	12,020	10,730	9,790	9,880	10,310
	10,130	9,910	11,100	9,920	9,510	10,160	10,400
	10,940	9,820	9,610	9,970	9,580	10,520	10,860
	10,000	10,050	9,550	9,950	10,530	11,100	10,000
	10,990	9,540	10,200	10,300	9,700	10,140	10,770
Average	*10,560*	*10,050*	*10,500*	*10,170*	*9,820*	*10,360*	*10,470*
SD ±	*460*	*530*	*1,060*	*350*	*410*	*470*	*350*

Table 19: Time (s) of peak breakthrough value using C/C_{max} for all gases. This value was obtained from the smoothed line fitting to a scatter plot of the five replications of each experiment.

	He	**Ne**	**Ar**	**Kr**	**Xe**	**CO_2**	**SF_6**
Pressure				*Peak Arrival Time*			
(Pa)				*(s)*			
50,000	53	40	45	40	40	79	38
40,000	65	55	55	51	53	112	49
30,000	88	70	75	73	75	150	69
20,000	126	120	113	113	113	237	108
10,000	247	234	226	230	243	483	237

Table 20: Time (s) of peak breakthrough value using C/C_{max} for all gases. This value was obtained from the average of the five replications of each experiment.

	He	**Ne**	**Ar**	**Kr**	**Xe**	**CO_2**	**SF_6**
Pressure				Peak Arrival Time			
(Pa)				(s)			
50,000	54 ± 3	42 ± 2	45 ± 1	40 ± 1	40 ± 2	82 ± 4	38 ± 2
40,000	63 ± 4	54 ± 5	55 ± 2	52 ± 2	53 ± 1	110 ± 6	49 ± 2
30,000	87 ± 7	67 ± 6	76 ± 3	73 ± 1	75 ± 3	150 ± 9	69 ± 2
20,000	129 ± 5	109 ± 1	112 ± 7	113 ± 4	115 ± 2	239 ± 20	109 ± 3
10,000	242 ± 13	234 ± 8	225 ± 3	233 ± 9	240 ± 15	485 ± 32	236 ± 16

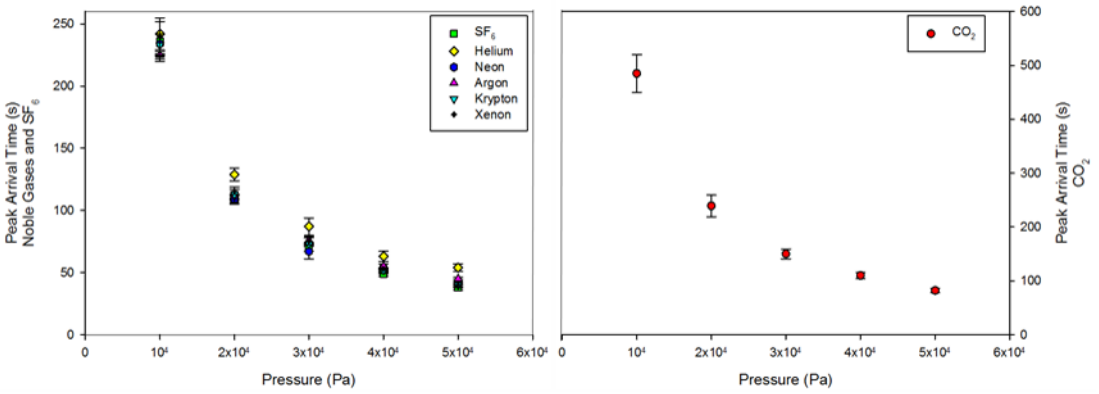

Figure 50: Time (s) of peak breakthrough value using C/Cmax for all gases. Standard deviation was obtained from five replications of each experiment shown in Table 20.

The following sections show the results from experiments. The raw output for all the experiments are available in an electronic format (Appendix V). The resulting breakthrough curves have been plotted to show the arrival times of the individual seven tracer experiments over the sampling pressure range (10,000 – 50,000 Pa). The tracer values are additionally displayed according to the five sampling pressures for analysis using fixed concentration intervals. By doing so, it highlights the complexity and individuality of the curves produced. Overall trends of the gases over the range of pressures are then compared using colour contour data.

5.3.2 Arrival times of tracer gases at different pressures

Figure 51 to Figure 57 shows the noble gases (helium, neon, argon, krypton and xenon), SF_6 and comparative CO_2 experiments for sandstone flow cell as outlined in Chapter 3 and 4. Each experiment was repeated five times for each of the sampling pressures ranging from 10,000 – 50,000 Pa. These experiments are then normalised using C/C_{max}. The five repeated experiments for each pressure are represented as scatter plots. A smoothed line has been attached as a means of highlighting any trends from the results.

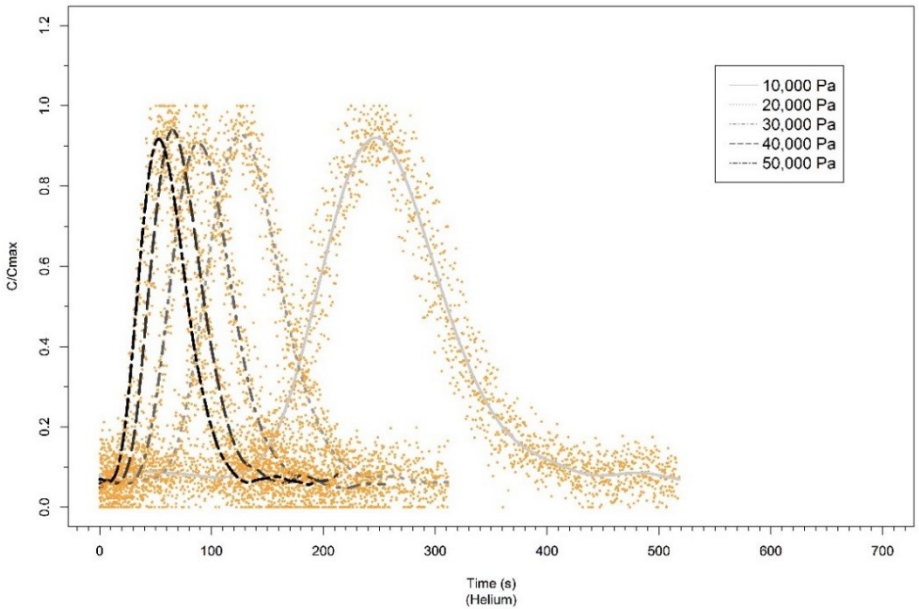

Figure 51: Scatterplots of flow experiments of helium through the flow cell. Smoothed lines have been plotted for the gas concentrations (C/C_{max}) over time (s) as an average of the five experiments.

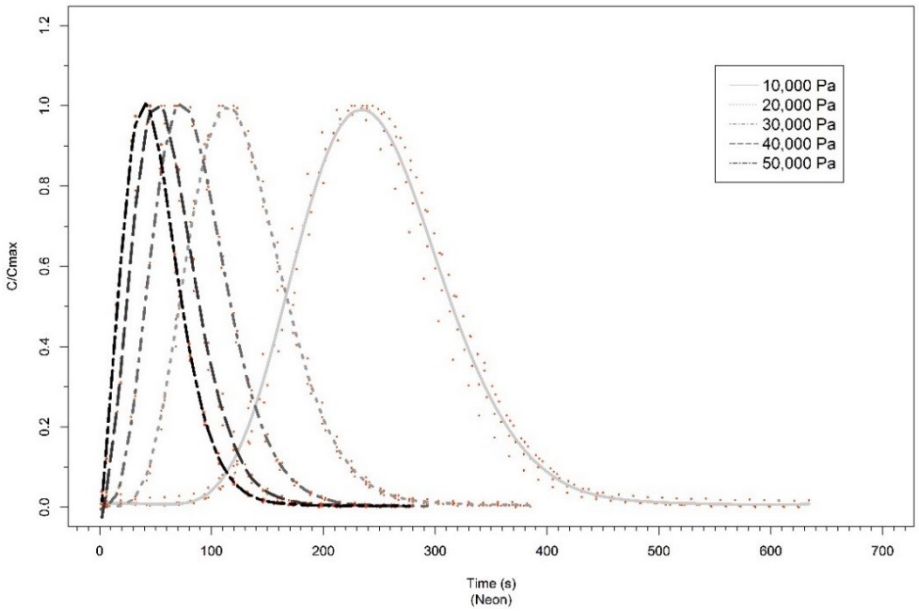

Figure 52: Scatterplots of flow experiments of neon through the flow cell. Smoothed lines have been plotted for the gas concentrations (C/C_{max}) over time (s) as an average of the five experiments.

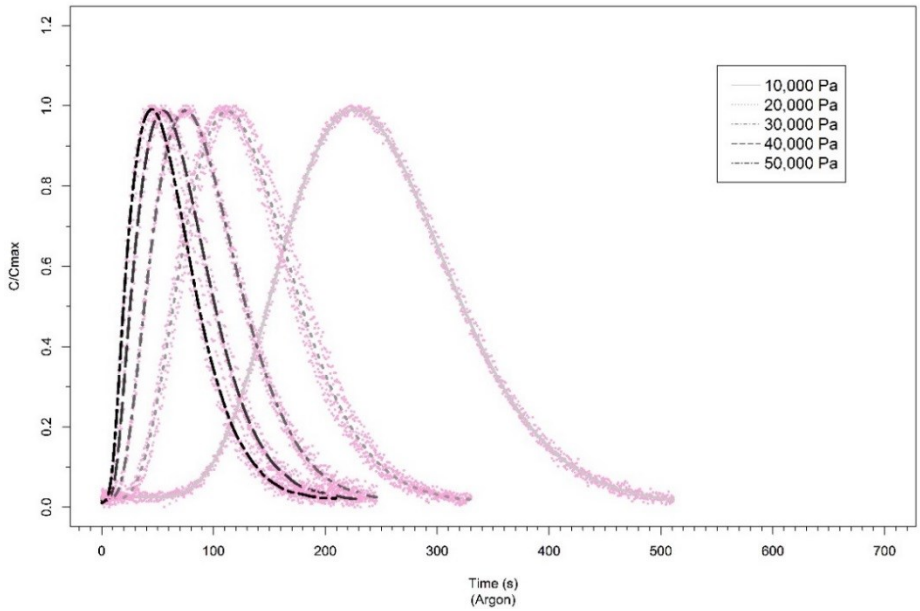

Figure 53: Scatterplots of flow experiments of argon through the flow cell. Smoothed lines have been plotted for the gas concentrations (C/C_{max}) over time (s) as an average of the five experiments (only four were deemed suitable at 10,000 Pa).

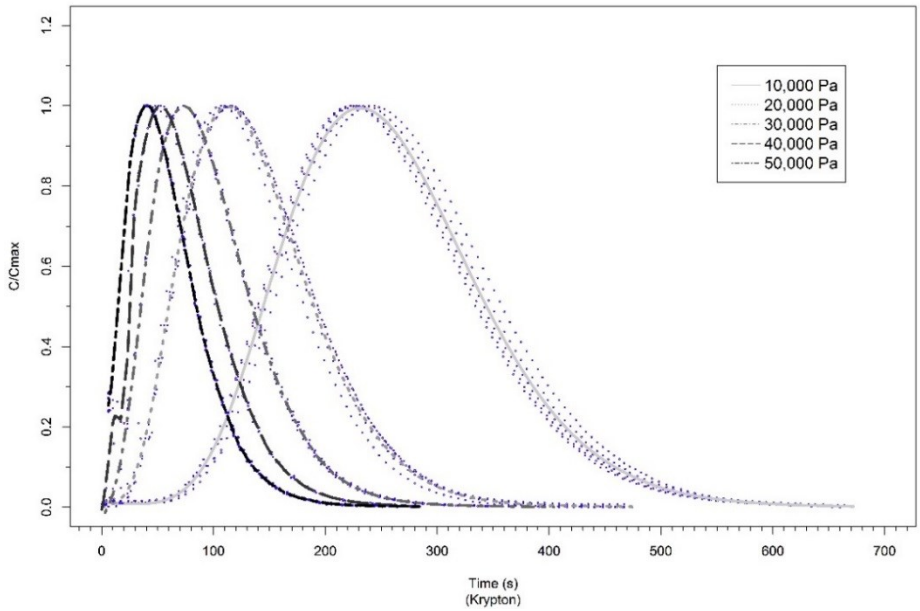

Figure 54: Scatterplots of flow experiments of krypton through the flow cell. Smoothed lines have been plotted for the gas concentrations (C/C_{max}) over time (s) as an average of the five experiments.

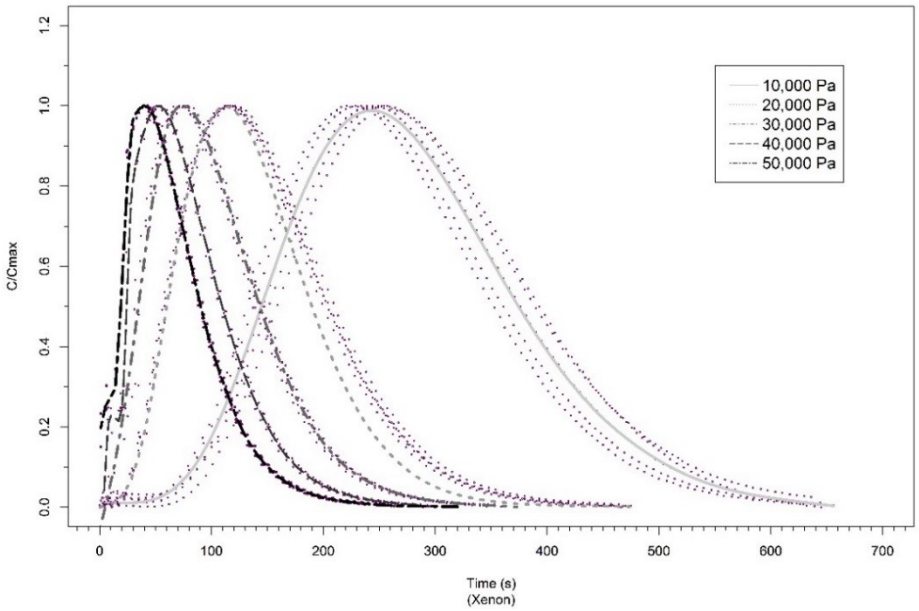

Figure 55: Scatterplots of flow experiments of xenon through the flow cell. Smoothed lines have been plotted for the gas concentrations (C/C_{max}) over time (s) as an average of the five experiments.

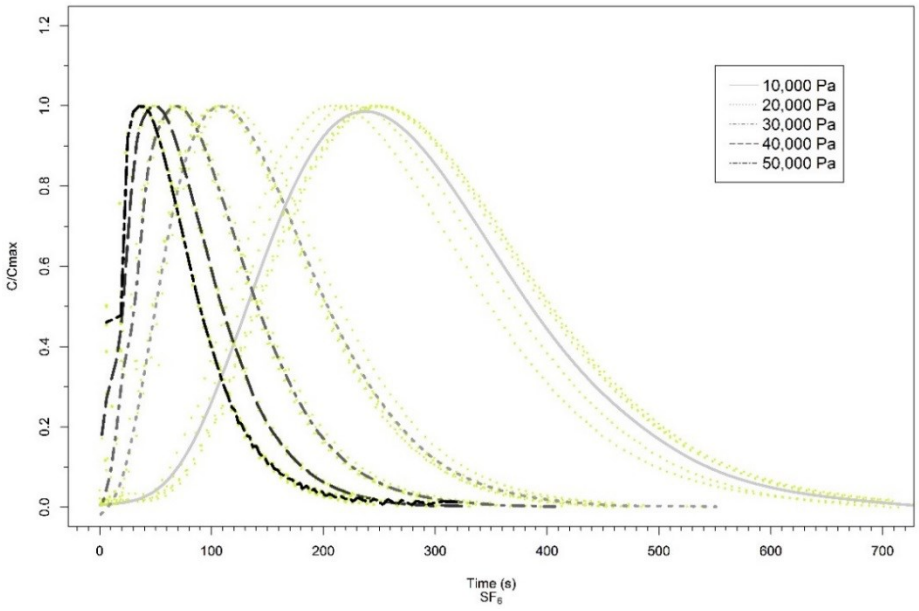

Figure 56: Results of flow experiments of SF_6 through the flow cell. Results are plotted as scatter plots. Smoothed lines have been plotted for the gas concentrations (C/C_{max}) over time (s) as an average of the five experiments.

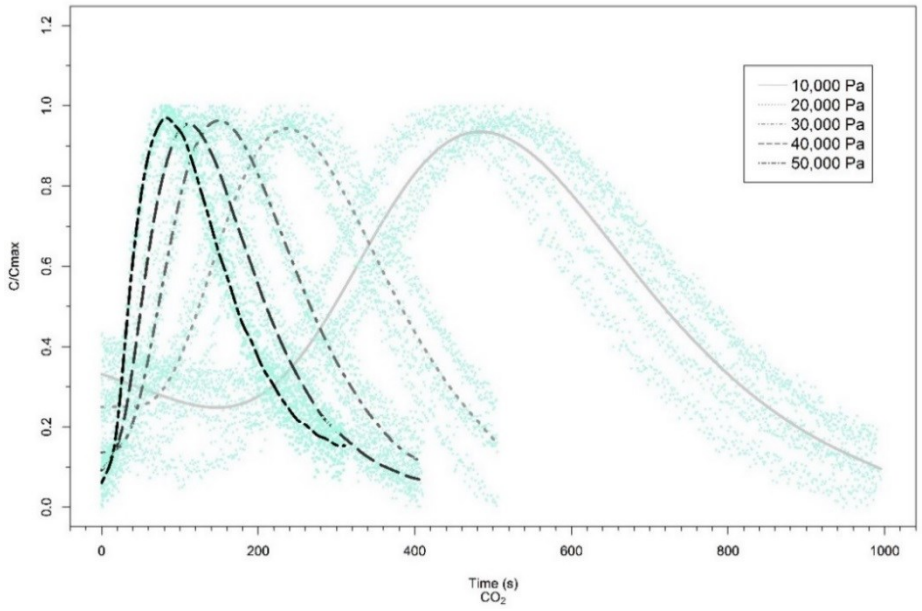

Figure 57: Results of flow experiments of CO_2 through the flow cell. Results are plotted as scatter plots. Smoothed lines have been plotted for the gas concentrations (C/C_{max}) over time (s) as an average of the five experiments.

The results from these experiments show variation in the number of sampling points as well as the fit to the smoothed line depending on the tracer gas. Helium, argon and CO_2 flow experiments were done using the QGA Professional software. This software allows for a higher level of accuracy and sampling intervals. The MASsoft software package was used for the neon, krypton, xenon and SF_6 flow experiments. Although this also provides real-time continuous analysis, the sampling intervals are longer. This difference in software has led to fewer data points. Additionally, the helium values have a wider scatter compared to the average line fit at each pressure gradient. It is likely that the cause of this is the high ionisation energy needed to pull an electron away from the attraction of the nucleus (Section 3.2). Because noble gases are stable gases with filled shell configurations, it is difficult to remove an electron. Helium in particular has a very high ionisation energy value (Table 21). Due to this high value needed, the helium values do not plot as a smooth line and can appear as 'noisy'.

Table 21: Ionisation energies for gases sampled using QMS (NIST, 2002).

Gas Sample	Ionisation Energy (eV)
Helium	24.6
Neon	21.6
Argon	15.8
Krypton	14.0
Xenon	12.1
CO_2	13.8
SF_6	15.3
N_2	15.6

It is evident that the CO_2 tracer results do not have the same starting concentration values as the noble gases and SF_6. Despite the removal of the baseline values, the CO_2 curves have high C/C_{max} values prior to pulse release. This observation becomes more apparent with a decrease in pressure gradient. Unlike noble gases and SF_6, CO_2 can interact with the surrounding matrix and solution present that is referred to as sorption. The concept of sorption will be further described in the transport mechanism and modelling sections. However, before proceeding it was important to identify if there was a trend in the level of the starting and finishing ratio values in relation to the observations made. In addition, the values were investigated prior to the baseline removal, as this would be the true level of CO_2 in the system at the time of the experiment. Figure 58 shows a breakdown of the absolute start and finishing percentage values for the CO_2 experiments. There is a slight trend in the increase in initial CO_2 values on the days where the pressure gradient is reduced. It is also clear that the initial CO_2 values are higher for the lower pressure gradients; suggesting the effect is only observed with a decrease in pressure gradient. The changes in sampling pressure and dates make it difficult to identify any quantifiable trends between the start and end values of each CO_2 experiments.

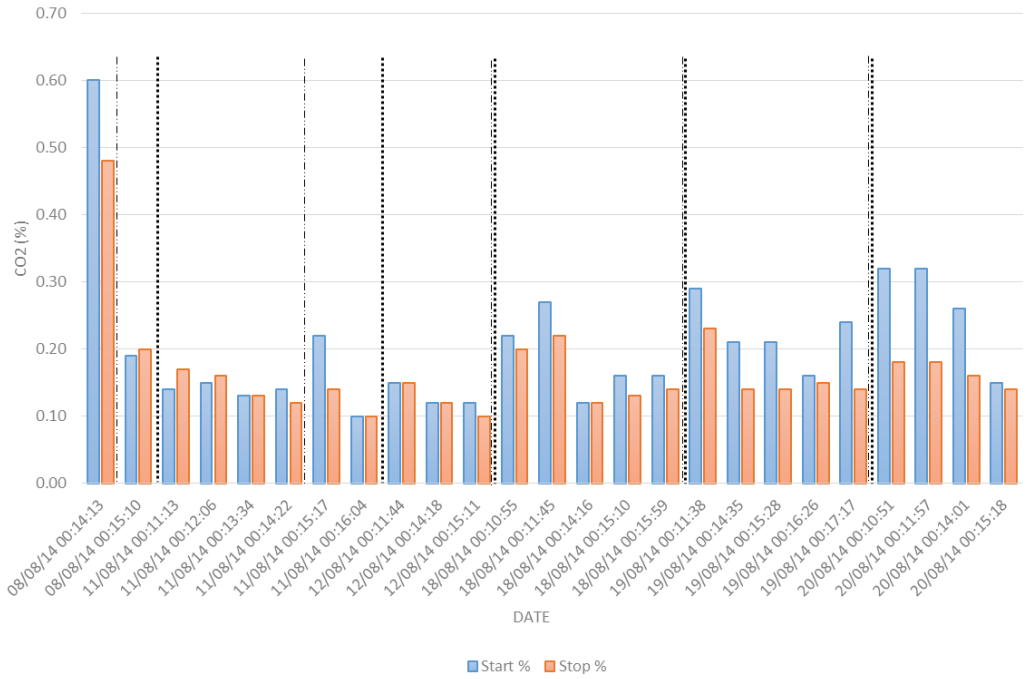

Figure 58: Bar chart of the raw start (blue) and finishing (orange) values of CO_2 (%) for each of the experiments. The dotted lines segregate experiments carried out on the same day. The dashed lines separate the changes in sampling pressure gradient. With the exception of a 10,000 Pa experiment as the first CO_2 values, the applied pressure gradient (10,000 -50,000 Pa) decreases from left to right with date of experiment. Shown here is the five repeat experiments for each pressure gradient.

5.3.3 Comparison of arrival times for tracer gases at different pressures

For ease of comparison, the shape of a breakthrough curve has been subdivided into 'concentration sectors' (Figure 59). Each of the curves can be considered using these divisions as presented in Table 22 where:

- Start – the time when the concentration rises 10% above the initial value post pulse release.
- T1 – the time when the concentration has contributed 25% towards the peak concentration.
- T2 – the time when the concentration has contributed 50% towards the peak concentration.

- T3 – the time when the concentration has contributed 75% towards the peak concentration.
- T4 – the time at which peak concentration occurs - where concentration is equal to Cmax (1).
- T5 – the time when the concentration persists at 75% of the peak concentration.
- T6 – the time when the concentration persists at 50% of the peak concentration.
- T7 – the time when the concentration persists at 25% of the peak concentration.
- End – the time by which the concentration has returned (as close as possible) to the initial starting concentration (Start).

The tracer experiments using the gases helium, neon, krypton, xenon and SF_6 are presented in this section in relation to the sampling pressure used. Figure 60 to Figure 64 show the decrease in upstream sampling pressure from 50,000 - 10,000 Pa in 10,000 Pa intervals; due to the complex behaviour and significantly longer travel times for CO_2 through N_2, it has been removed from these figures. The scatter plots for each of the five replicate experiments have been omitted for ease of identification; using the smoothed lines instead to show the existence of any variance in shapes of the different gases.

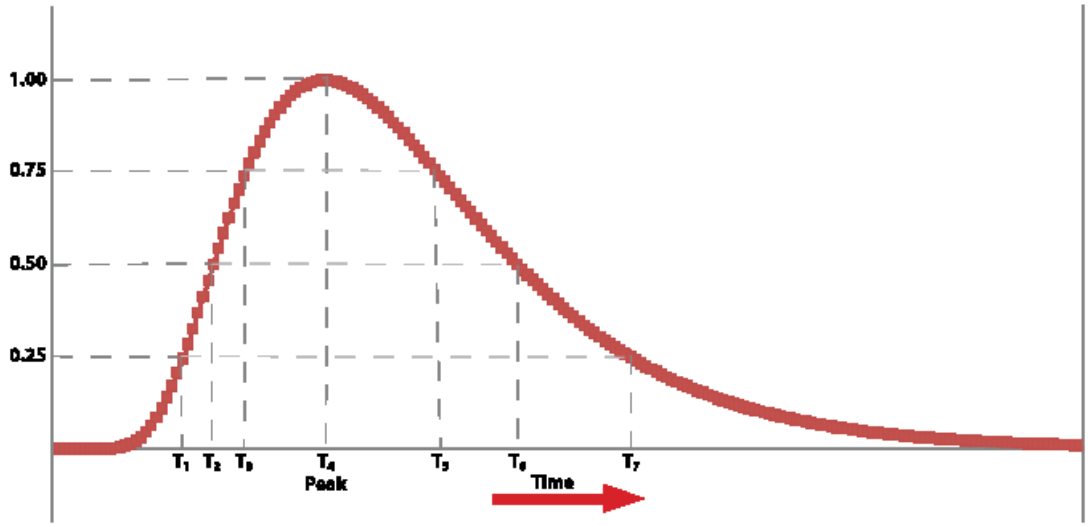

Figure 59: Illustration showing the concentration intervals used to record trends in the tracer experiments.

Table 22: Timings (s) of the different sampled gases at set concentration intervals as shown in Figure 59. Also included where possible is the time of first arrival and completion of tracer; these times vary depending on the pressure and gas used. The first arrival is determined by a 10% increase in the baseline value and the completion is determined when the concentration falls beneath that same value.

50,000 Pa	**Start**	**T1**	**T2**	**T3**	**T4**	**T5**	**T6**	**T7**	**End**
Helium	13	24	32	38	53	71	81	97	123
Neon	3	9	16	23	40	64	75	92	132
Argon	3	14	20	27	45	69	87	110	196
Krypton	-	6	14	21	40	66	84	109	185
Xenon	-	5	19	23	40	70	89	119	208
SF_6	-	-	20	22	38	69	88	118	234
CO_2	-	23	34	48	79	132	172	237	-
40,000 Pa	**Start**	**T1**	**T2**	**T3**	**T4**	**T5**	**T6**	**T7**	**End**
Helium	19	33	42	50	65	84	95	112	155
Neon	4	16	22	32	55	76	90	109	163
Argon	5	18	25	34	55	81	101	126	232
Krypton	3	19	25	29	51	84	103	131	189
Xenon	-	20	25	28	53	86	109	141	245
SF_6	-	5	21	27	49	84	109	142	264
CO_2	-	32	51	70	112	164	210	273	-
30,000 Pa	**Start**	**T1**	**T2**	**T3**	**T4**	**T5**	**T6**	**T7**	**End**
Helium	30	48	59	69	88	110	123	140	195
Neon	9	30	40	50	70	102	118	139	211
Argon	10	28	38	50	75	107	129	157	245
Krypton	7	25	36	46	73	110	133	166	260
Xenon	-	22	35	47	75	115	143	180	290
SF_6	4	18	30	39	69	111	140	180	330
CO_2	-	46	73	98	150	216	266	335	-
20,000 Pa	**Start**	**T1**	**T2**	**T3**	**T4**	**T5**	**T6**	**T7**	**End**
Helium	49	76	90	102	126	152	168	192	270
Neon	20	56	70	84	120	148	171	196	280
Argon	19	49	64	80	113	152	179	213	309
Krypton	6	45	60	76	113	159	189	228	400
Xenon	10	45	60	77	113	159	189	229	401

SF_6	-	35	50	67	108	165	203	254	445
CO_2	-	10	124	168	237	318	382	464	-
10,000 Pa	**Start**	**T1**	**T2**	**T3**	**T4**	**T5**	**T6**	**T7**	**End**
Helium	123	165	188	208	247	289	315	352	438
Neon	80	138	164	188	234	286	315	353	496
Argon	64	122	149	174	226	285	323	370	482
Krypton	49	116	145	173	230	300	344	399	575
Xenon	40	113	145	178	243	322	373	439	630
SF_6	11	99	133	167	237	326	385	462	710
CO_2	-	-	296	371	483	613	717	850	-

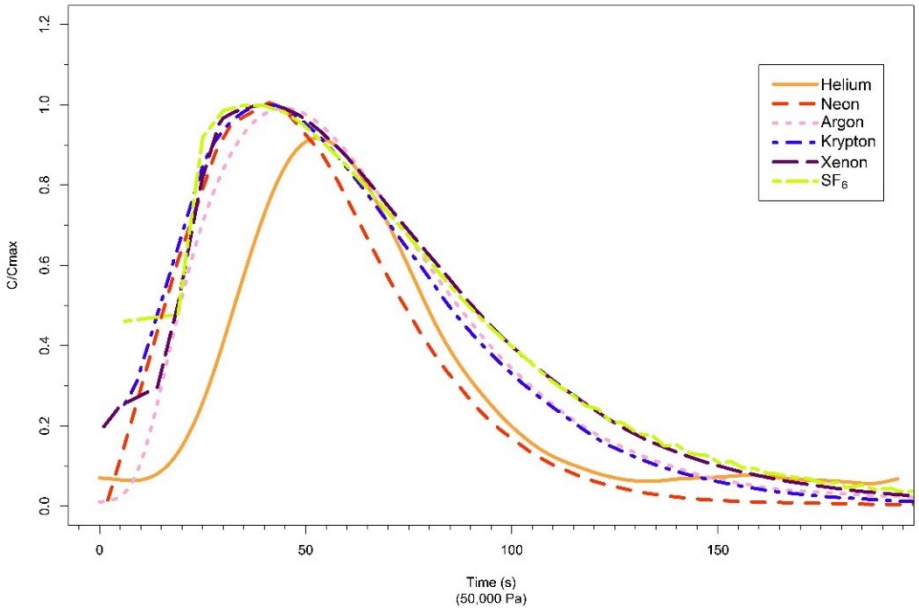

*Figure 60: Smoothed lines obtained from results of tracer flow experiments for all gases through the flow cell. Experiments shown were carried out at **50,000 Pa.** All gases were passed through using CO_2 as a feeder gas. CO_2 results are not included in this figure.*

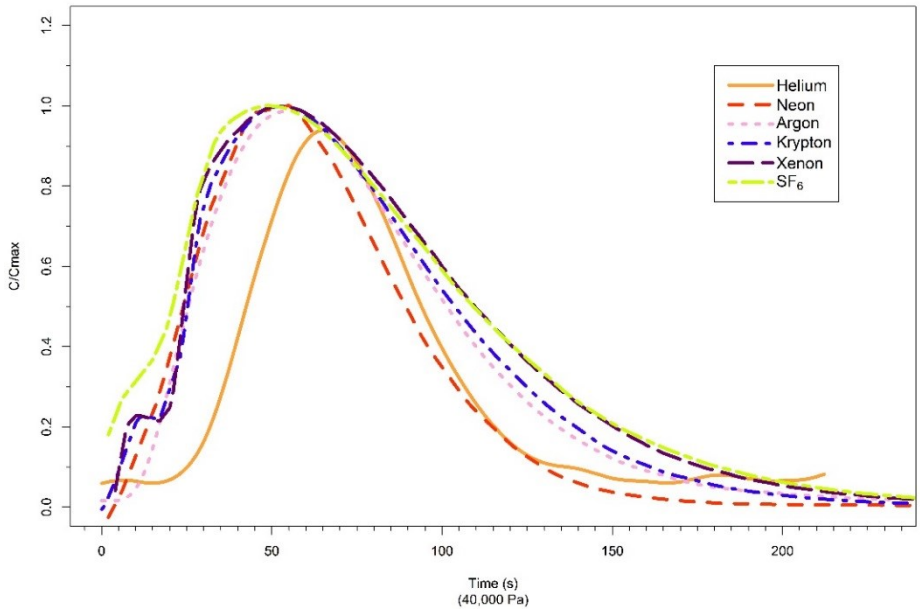

*Figure 61: Smoothed lines obtained from results of tracer flow experiments for all gases through the flow cell. Experiments shown were carried out at **40,000 Pa**. All gases were passed through using CO_2 as a feeder gas. CO_2 results are not included in this figure.*

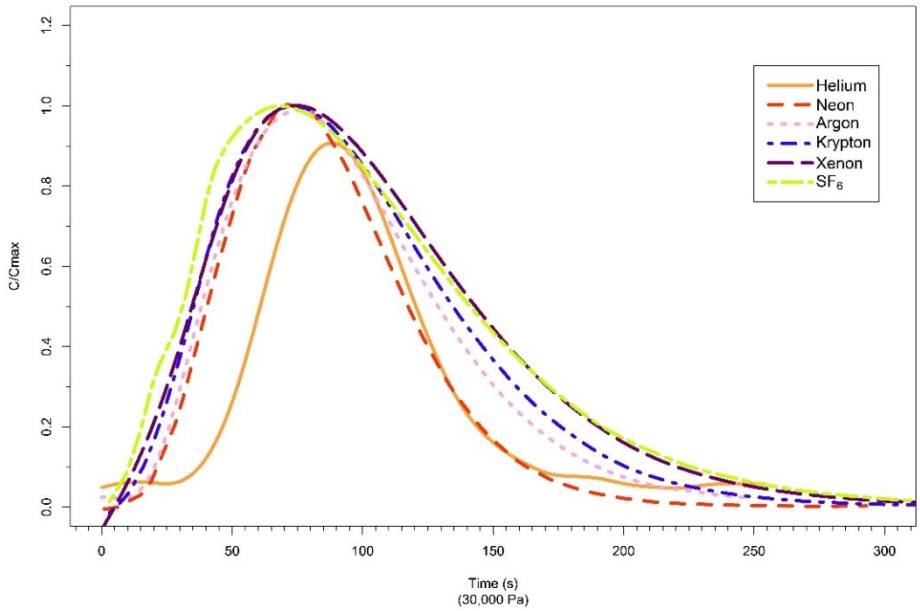

*Figure 62: Smoothed lines obtained from results of tracer flow experiments for all gases through the flow cell. Experiments shown were carried out at **30,000 Pa**. All gases were passed through using CO_2 as a feeder gas. CO_2 results are not included in this figure.*

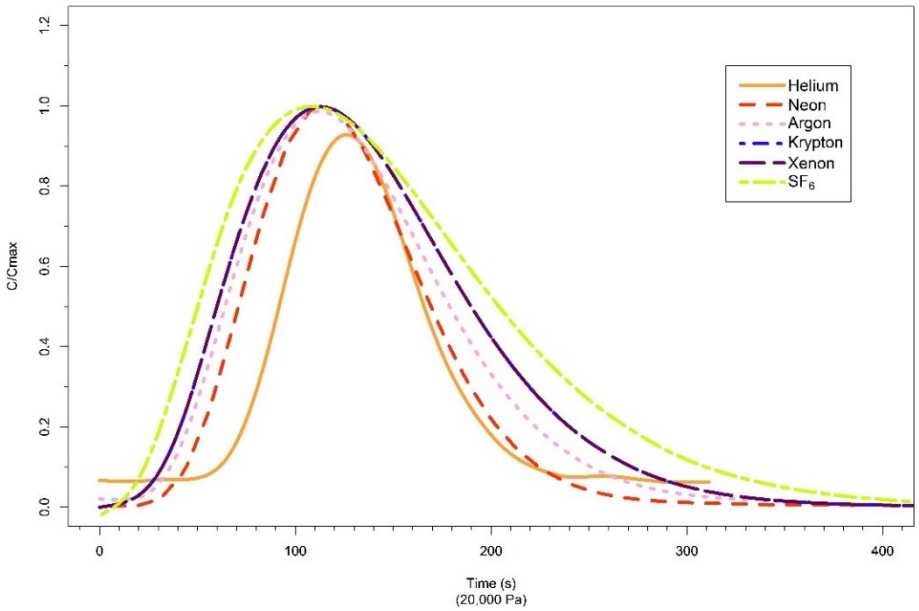

Figure 63: Smoothed lines obtained from results of tracer flow experiments for all gases through the flow cell. Experiments shown were carried out at ***20,000 Pa****. All gases were passed through using CO_2 as a feeder gas. CO_2 results are not included in this figure.*

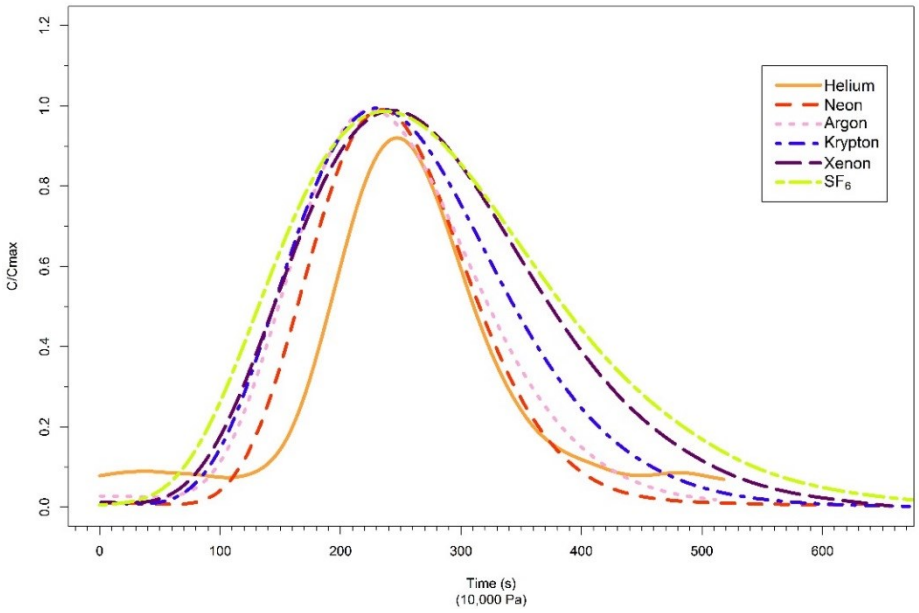

Figure 64: Smoothed lines obtained from results of tracer flow experiments for all gases through the flow cell. Experiments shown were carried out at ***10,000 Pa****. All gases were passed through using CO_2 as a feeder gas. CO_2 results are not included in this figure.*

5.3.4 Overall trends from experimental results

The following section illustrates the behaviour of the individual tracers. These trends are described using the smoothed line for each of the five replicate experiments at each of the sampling pressures. For ease of comparison, the smoothed line for all seven tracer experiments sets at each of the sampling pressures, have been depicted as colour contour plots in Figure 65 to Figure 69. C/C_{max} has been converted to a colour gradient with 0.2 intervals from 0.0 to the peak value of 1.0. Time is the principal axis where release starts at the moment of tracer release upstream of the flow cell (0 s). The observations are based on the recorded timings noted in Table 22 and should be considered as semi-quantitative. The timings will be discussed under first arrival time (Start), pre-peak concentration ($T_1 – T_3$), peak concentration of C/C_{max} (T_4), post-peak concentration ($T_5 – T_7$) and cessation of tracer detection (End).

- 50,000 Pa sampling pressure

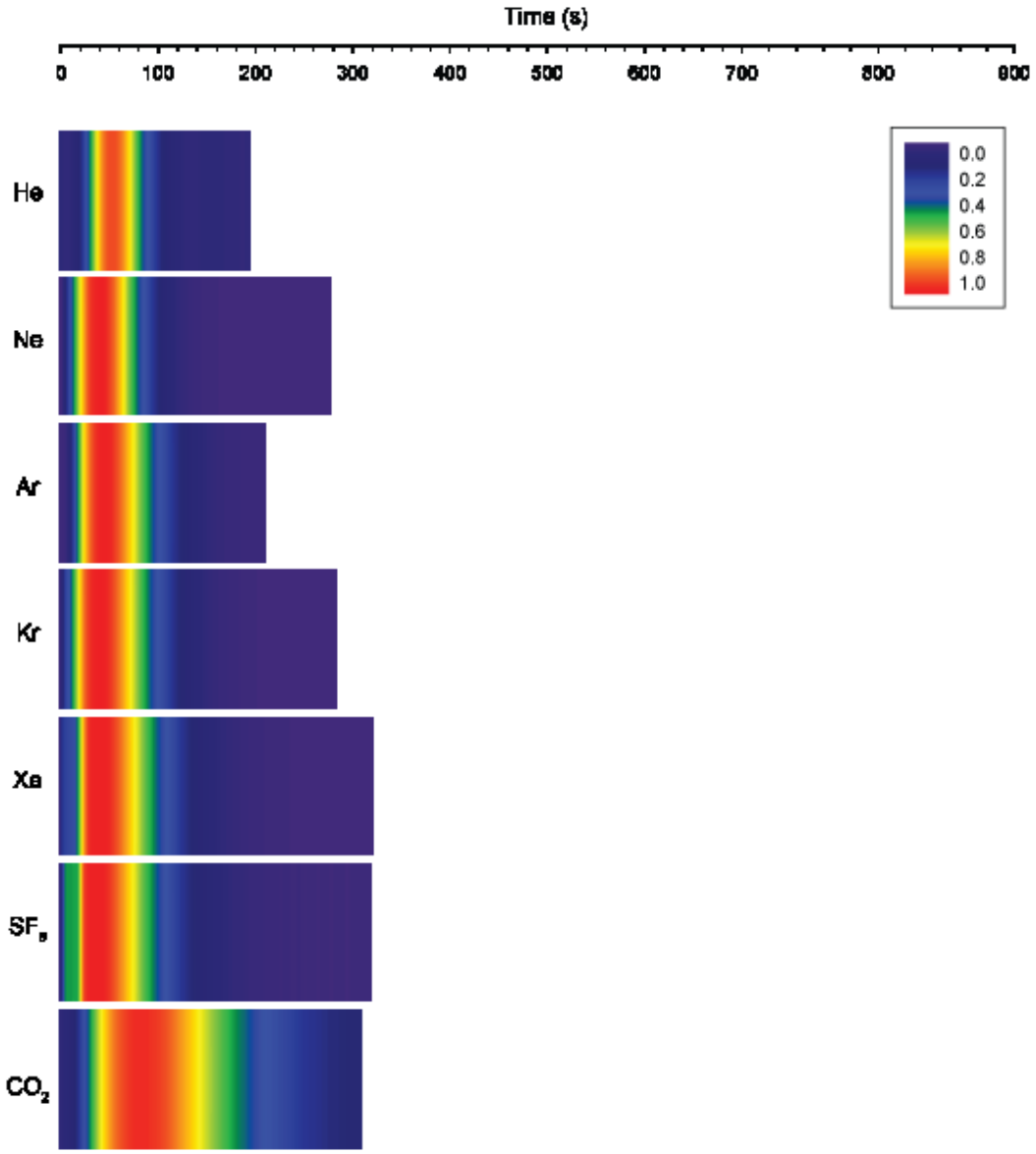

Figure 65: Colour contour plots of breakthrough curves from gas experiments. Values shown are the representative values developed from repeat experiments for C/C_{max}. Sampling pressure was set at 50,000 Pa.

At a sampling pressure of 50,000 Pa, due to the sampling intervals there is great difficulty is determining the true first arrival times, with the exception of helium (Figure 65). The pre-peak timing of the gases is greatly varied with helium and CO_2 being the slowest to reach the same concentration. At $C/C_{max,}$ helium has the slowest peak time (52 s) of the noble gases. The rest

of the noble gases have a similar arrival time (41 ± 3 s), which is within error for the SF_6 peak time; CO_2 remains the slowest tracer to reach peak value (48 s). Post-peak concentration, the quickest tracer to complete the experiment is neon (92 s) followed closely by helium after 97 s. SF_6 returns to pre-release values at a similar timeframe to the remainder noble gases. CO_2 remains the slowest gas to return to pre-release values, although the value fails to return to the baseline concentration level, unlike the other tracers tested.

- 40,000 Pa sampling pressure

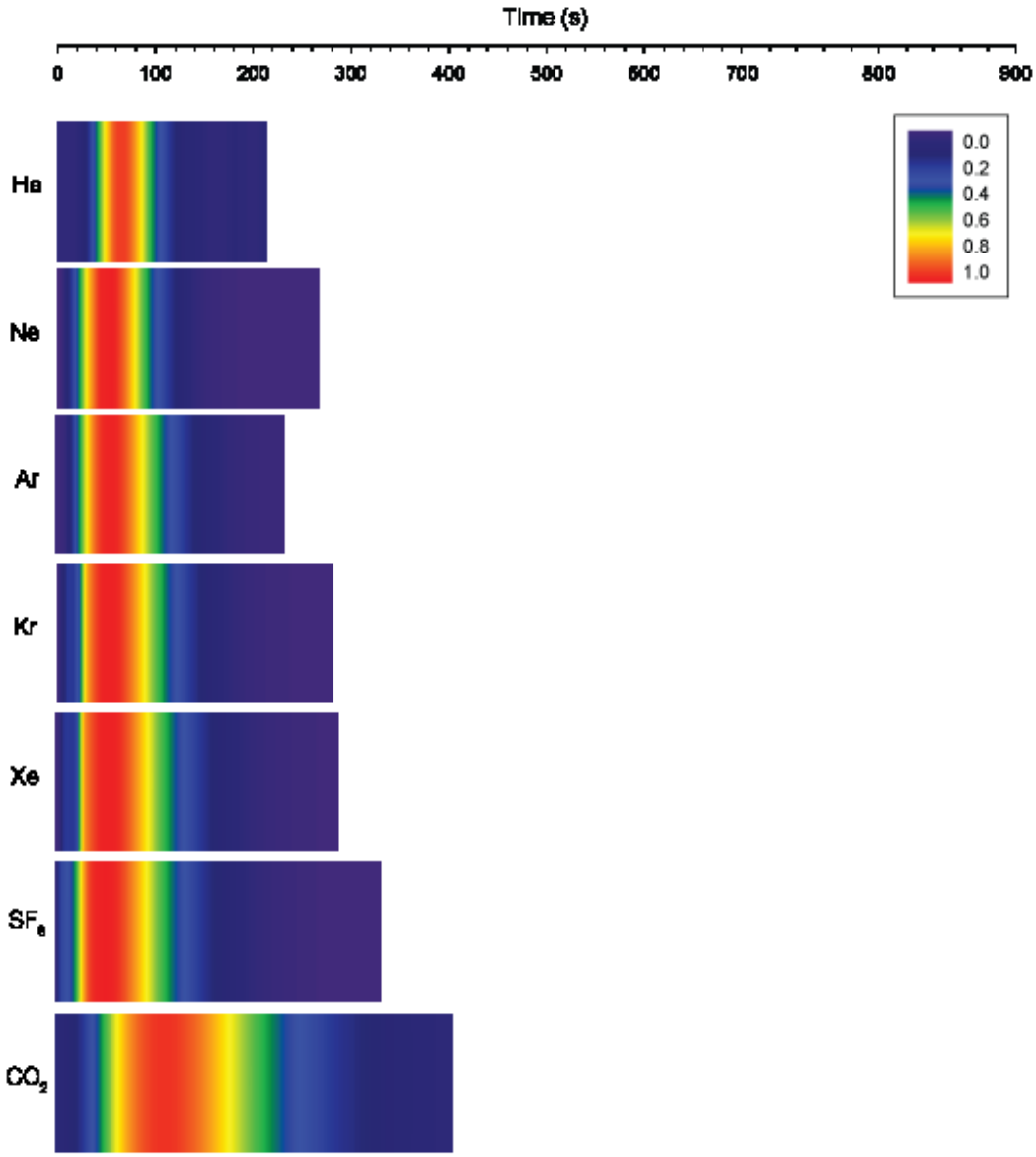

Figure 66: Colour contour plots of breakthrough curves from gas experiments. Values shown are the representative values developed from repeat experiments for C/C_{max}. Sampling pressure was set at 40,000 Pa.

At a sampling pressure of 40,000 Pa, the trends become easier to distinguish (Figure 66). Helium is still the last tracer to appear after initial release. Pre-peak values for all the tracers are similar in timing with the exception of helium and CO_2; neon, argon, krypton, xenon and

SF_6 show a similar build up to the maximum tracer value (53 ± 3 s). By C_{max}, the time it has taken for CO_2 to arrive (112 s) has nearly doubled in comparison to helium. Post-peak values for the tracers show a similar relationship for helium and neon. The remainder of the noble gases show a decrease with time, as there is a decrease in atomic mass. Cessation of tracer flow is the slowest for SF_6; lasting nearly 20 s longer than xenon. Helium was the fastest of the noble gases to complete the tracer pathway. Detecting the completion of CO_2 flow was not possible.

- 30,000 Pa sampling pressure

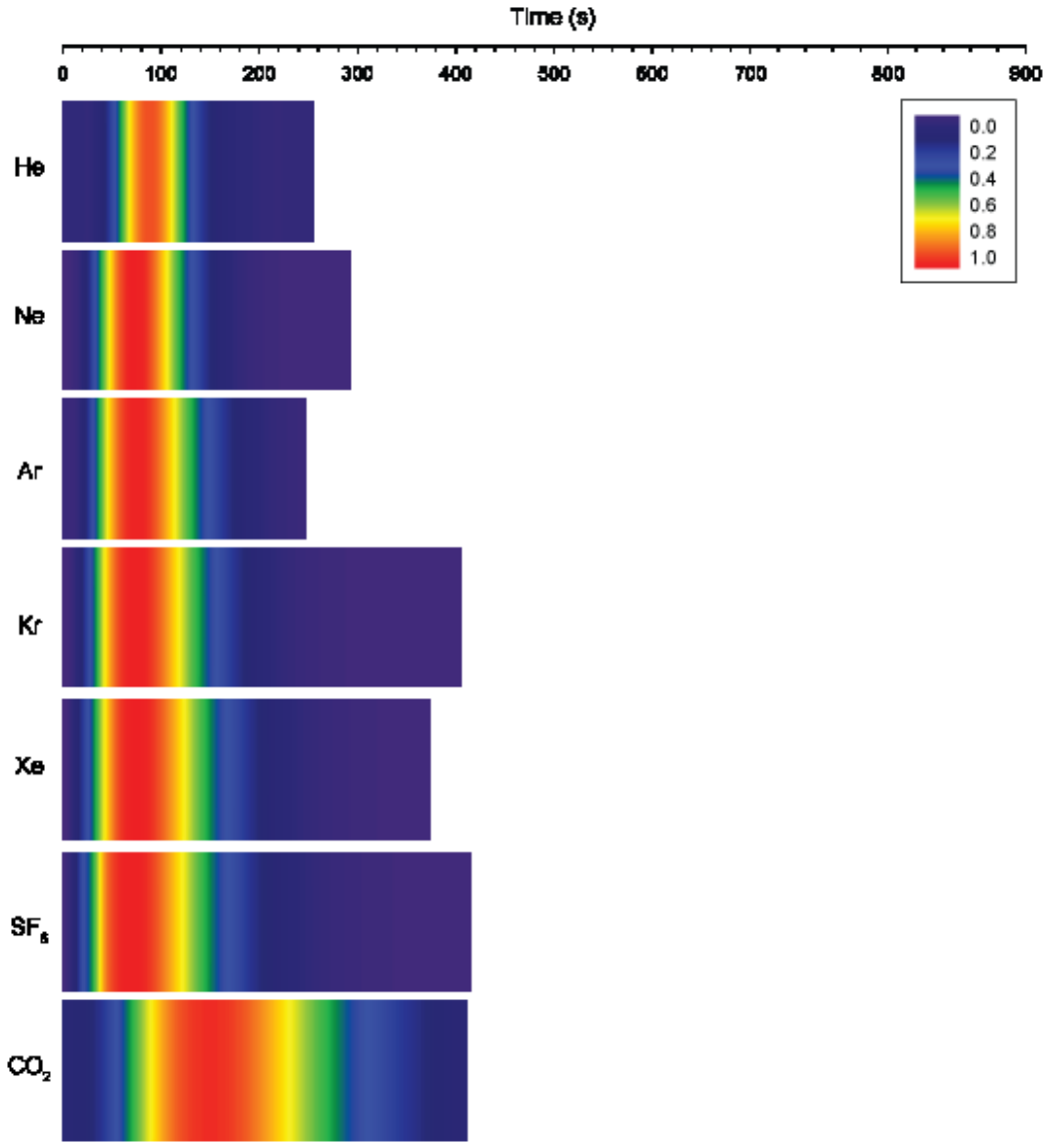

Figure 67: Colour contour plots of breakthrough curves from gas experiments. Values shown are the representative values developed from repeat experiments for C/C_{max}. Sampling pressure was set at 30,000 Pa.

Helium is again the slowest of all the noble gases to arrive and reach peak concentration (Figure 67). Software detection issues make determining the first arrival of the other gases subjective. Travel times for the noble gases pre-peak concentrations towards C/C_{max} are quicker as atomic mass increases. The pre-peak travel times are similar for krypton and xenon

in particular. At C_{max}, argon, krypton and xenon all fall within a range of ± 1 s; SF_6 and neon show a similar time of 70 ± 1 s. Overall, helium is the second slowest tracer to arrive (88 s) with CO_2 remaining the slowest (150 s). Post-peak concentration times continue for longer as there is an increase in size. Helium is the fastest tracer of the noble gases to complete the travel time. The SF_6 pulse persists for 40 s longer than all of the noble gases (xenon pulse took 290 s).

- 20,000 Pa sampling pressure

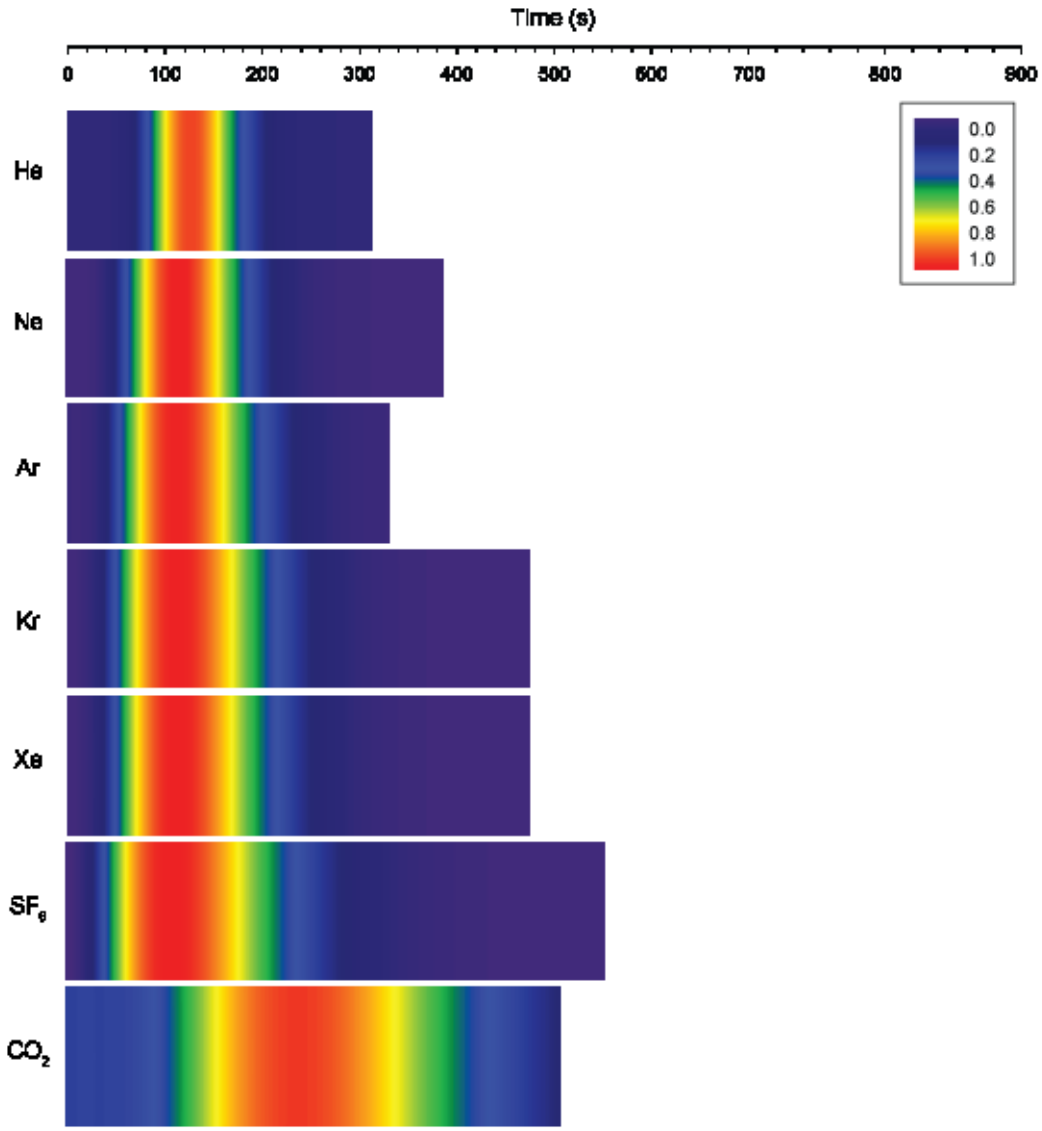

Figure 68 Colour contour plots of breakthrough curves from gas experiments. Values shown are the representative values developed from repeat experiments for C/C_{max}. Sampling pressure was set at 20,000 Pa.

Helium was detected 49 s after pulse release, making it the slowest tracer to arrive (neon was the second slowest at 20 s) (Figure 68). For pre-peak concentration, there is a clear trend in atomic mass, as the mass increases, the timing toward peak concentration is faster. Krypton and xenon display a similar timing range of less than 1 s time difference. By $C/C_{max,}$ helium is the slowest of the noble gases to reach peak concentration. Argon, krypton and xenon all show the same arrival time (113 s) and CO_2 is twice as slow to arrive (237 s). Post-peak

concentration, there is a trend in atomic mass, as the mass increases the timing towards completion is slower. Again, krypton and xenon show similar transport timings; CO_2 is twice as slow as helium. Cessation of detectable readings for the noble gases continue to show the trend of increase in time with an increase in atomic mass. SF_6 continues to be detected for 44 s longer than xenon.

- 10,000 Pa sampling pressure

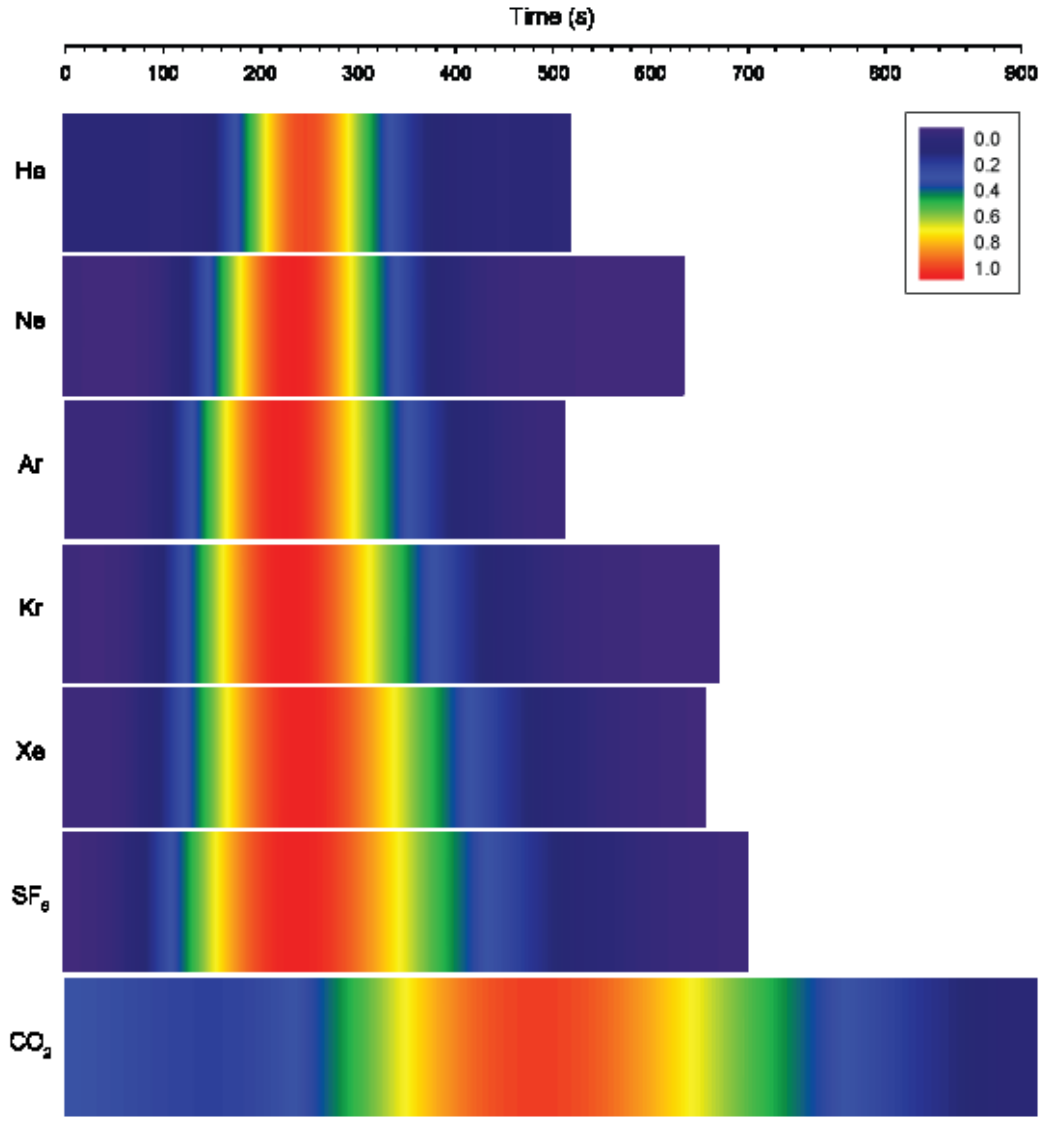

Figure 69: Colour contour plots of breakthrough curves from gas experiments. Values shown are the representative values developed from repeat experiments for C/C_{max}. Sampling pressure was set at 10,000 Pa.

At 10,000 Pa, the first arrival of the tracers is quicker, the larger the atomic mass (Figure 69). Helium takes three times as long to appear as xenon. SF_6 shows a significantly shorter first arrival time relation to the noble gases (11 s). At this sampling pressure, background CO_2 readings were too high to detect initial arrival of the new CO_2 pulse. Pre-peak concentrations of the noble gases show a clear trend in faster travel times for higher atomic mass. SF_6 remains the faster tracer prior to reach peak concentration. C_{max} values for helium and xenon show similar arrival times (245 ± 3 s) and the rest of the noble gases and SF_6 arrive sooner. CO_2 takes the longest to reach C_{max} at 483 s. Post-peak concentrations show a shift in timing between argon and krypton. Helium takes longer to reduce than neon and argon, although neon is very similar to helium. SF_6 is then slower than xenon and krypton to dissipate. CO_2 appears twice as slow as the next slowest tracer (SF_6). Cessation of tracer timing is fastest for helium with the heavier noble gases taking longer to complete. The SF_6 pulses continues for 80 s longer than xenon. CO_2 completion was not possible to detect, due to CO_2 concentrations not returning to baseline values.

5.3.4.1 Summary of overall trends from experimental results

Several behavioural trends can be seen for the different tracer gases. Helium is the last of the noble gases to reach C_{max} for all the pressure ranges and it is the quickest tracer to cease detection. Neon shows quicker pre-peak concentration values but has similar post-peak times to helium with a decrease in pressure gradient. Argon, krypton and xenon show similar C/C_{max} timings at lower sampling pressure. As there is a decrease in sampling pressure, krypton and xenon continue to have similar pre-peak, C_{max} and post-peak timings. At all sampling pressures, a pulse of SF_6 tends to be quickest to reach C_{max} but takes longer to complete the experiment than any of the noble gases. CO_2 behaves very differently compared to the noble gases and SF_6. The CO_2 values never drop to 0.0 when plotted as C/C_{max} and takes nearly twice as long as the noble gases to reach the C_{max}.

The following section introduces the laws that control the flow of a fluid from one point to another. The inputs and processes involved with the transport of a tracer through a porous medium will then be explained. The observed trends from the experimental results will be analysed and discussed in detail combining these processes.

5.4 Analysis of breakthrough curves for tracer transport in homogenous porous media

5.4.1 Introduction

A solution is a homogenous mixture made up of two or more substances. A fluid solution may refer to a gas or liquid that is made up of solute and solvent components. The amount of solute (tracer) in a solution tends to be lower than that of the solvent (carrier gas). For this research, the transport of a tracer through a system consists of two aspects, the movement of the tracer with the fluid and within the solution itself. Movement of the tracer with the movement of the fluid is governed by physical properties; the geometry and physiochemical behaviour of the surrounding body can affect the pathway migration. This process is known as advective transport (Fetter, 2008). Movement of the tracer within the solution itself is the result of thermal motion and is known as hydrodynamic dispersion. Hydrodynamic dispersion itself is further classified into molecular diffusion and mechanical dispersion (Fetter, 2008). In addition to this, sorption processes may be involved for the reactive tracers used.

Several laws control the flow of a fluid from one point to another. These conservation laws include the conservation of mass, the conservation of momentum and the equation of state. These laws are first applied to a system and then extended to regions in space called control volumes.

5.4.2 Conservation of mass

The conservation of mass means that mass is neither created nor destroyed. Hence, in a steady state system the mass must remain constant over time. In terms of fluid dynamics, this means that within a control volume of porous media, the difference between the mass of the fluid entering and the mass of the fluid leaving the system must be balanced by a change in mass of the fluid within the fixed volume. For a tracer within a fluid system:

$$\frac{dm}{dt} = 0 \qquad (4)$$

m = mass

t = time (no sources or sinks involved)

So that (De Marsily, 1986):

$$\frac{\partial \rho}{\partial t} + \nabla(\rho v) = 0 \quad (5)$$

ρ = the density of the fluid

v = velocity vector

t = time

This is known as the equation of continuity (or mass conservation) for the fluid (Bear, 1972).

5.4.3 Conservation of momentum

The momentum of a fluid is the product of mass and velocity. The conservation of momentum states that the momentum of a system is constant if there are no external forces acting on the system. Thus, momentum can be changed by the action of forces external and internal to the fluid (McDermott, 1999):

$$\frac{d(mv)}{dt} = \sum f \quad (6)$$

f = the forces acting on and within the fluid

m = mass of fluid

v = velocity vector

Forces that can change the momentum of a fluid include the gradient of pressure, gravity and viscosity:

$$\sum \vec{f} = \vec{f}_{press} + \vec{f}_{grav} + \vec{f}_{visc} \quad (7)$$

By including these effects, the momentum balance equation for a Newtonian Fluid can be presented as the Navier-Stokes equation:

$$\rho\vec{a} = -\vec{\nabla}P + \rho\vec{g} + \mu\nabla^2\vec{v} \quad (8)$$

ρ = the density of the fluid

$\vec{a}$ = the vector of acceleration of the fluid mass

P = pressure

$\vec{g}$ = the acceleration due to gravity vector

$\vec{v}$ = the velocity vector

μ = dynamic viscosity

5.4.4 Equation of state

Equations of state are relations among intensive thermodynamic properties (Fox *et al.*, 2009). An equation of state provides a relationship between two or more state functions associated with the fluid. Although many fluids exhibit complex behaviours, at moderate temperature and pressure they can be represented by the ideal gas equation of state:

$$PV = nRT \quad (9)$$

P = pressure

V = volume

n = number of moles of substance

R = ideal gas constant

T = temperature

An ideal gas is a gas composed of randomly moving, non-interacting particles. Under normal conditions such as standard temperature and pressure (STP), noble gases and CO_2 can be treated like an ideal gas. For liquid phases and critical states, the Peng Robinson Equation (1976) is more suited:

$$P = \frac{RT}{v - b} - \frac{a(T)}{v(v + b) + b(v - b)} \tag{10}$$

P = pressure

R = ideal gas constant

T = temperature

v = molar volume (V/n)

a = measure of the intermolecular force

b = constant related to the size of the hard spheres

5.4.5 Darcy's Law

Darcy's Law is an equation that describes the flow of a fluid through a porous medium. Darcy established that the flux of water thorough a porous medium is directly related to the pressure gradient across the formation.

$$Q = KA\frac{\Delta h}{L} \tag{11}$$

Q =volumetric flow rate

K = hydraulic conductivity

A = cross-sectional area

Δh = head difference

L = length of pressure drop

Darcy's law is the proportional relationship between flow rate, viscosity and changes in pressure over a given distance. Linear flow paths are assumed in Darcy's Law – a flow regime characterised by parallel flow lines within a system. With Darcy's flow, it is assumed that the flow is inertialess. Thus, Darcy flow regime accounts for creeping flow and viscous forces prevail over inertial forces. Turbulent flow occurs when the path of the fluid flow is no longer smooth, this may be the results of low viscosity or increased pressure gradient. Long before a flow becomes turbulent, non-linear laminar comes into effect and deviations from Darcy's law occurs (Kolditz, 2001).

5.4.6 Porosity

Porosity refers the 'empty' spaces within a matrix. It is measured as a fraction such that:

$$n = \frac{V_v}{V_t} \tag{12}$$

n = porosity (0 – 1 or %)

V_v = volume of the void space

V_t = volume of matrix

The porosity of a matrix is dependent on the rock type, diagenetic history and level of sorting. Porosities in sandstones are almost entirely a function of the type of cementing material between the sand grains and the extent to which the larger grains interlock (Dullien, 2012). The effective porosity (n_e) refers to the sum of all the interconnected pore space. In a clean sandstone, the total porosity should be equal to the effective porosity. However, after deposition voids can become occupied by shale or clay. The effective porosity represents the pore space that contains free moving solution that is not clay-bound. The sandstone has an experimentally derived porosity of 20.3% (Chapter 4). However, analysis of the sample using PAMs, ImageJ analysis and physical information provided by the stonemasons have provided a porosity range of 13.10 – 19.78% (Hutton Stone Co. Ltd., 2013).

5.4.7 Tortuosity

Tortuosity defines the pathway complexity of a porous medium. The tortuosity factor (τ_f) is defined as the ratio of the real diffusive path length (l_e) to the direct diffusive path length (l) through the porous medium (Figure 70):

$$\tau_f = \frac{l_e}{l} \tag{13}$$

Tortuosity is related to porosity and it decreases slowly with an increase in porosity (Carman, 1956). Tortuosity can be defined as the relationship between the effective porosity (n_e) where m is determined experimentally (Grathwohl, 1998):

$$\tau_f = \frac{n_e}{{n_e}^m} \tag{14}$$

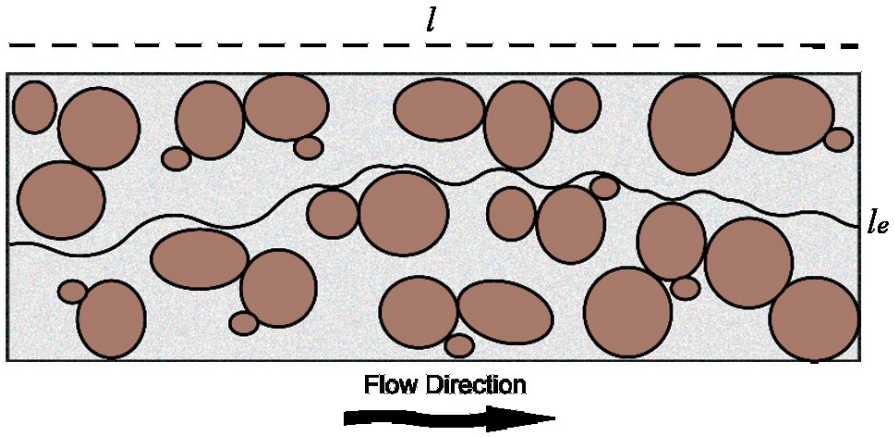

Figure 70: Diagram of flow in porous medium, showing relationship between the real diffusive path length (solid line) and the direct diffusive path length (dashed line).

5.4.8 Permeability

Permeability is a measure of the ease with which a system allows fluids to pass through it (m^2 or D). Permeability depends on the geometry and connectivity of the matrix media in addition to void volume. The intrinsic permeability refers to the function of the medium and is limited to single-phase flow. Relative permeability is a more suitable method of representing a porous medium where more than one phase exists and the ratio fluctuates; the relative permeability is

a dimensionless function and it is an adaption of the Darcy equation for multiphase flow conditions. It is described as:

$$k_r = \frac{k_e}{k_i} \quad (15)$$

k_r = relative permeability (ratio 0 -1)

k_e = effective permeability of a particular fluid when other fluids are present

k_i = intrinsic permeability of the system in single phase flow

The relative permeability of a rock is controlled by the fluid saturation and the fluid history (hysteresis) (Aminu and Ardo, 2015). The experiments carried out are in 'dry' porous media and use gas-gas interactions thus the relative permeability is equal to 1. For this reason, the intrinsic permeability is considered a suitable value for the experimental conditions of this research. The intrinsic permeability of this sandstone has been experimentally derived on a smaller plug as 2.18 x 10^{-13} m^2 (Table 16). The intrinsic permeability of the system from experimental conditions ranged from 9.31 × 10^{-13} - 1.16 × 10^{-12} m^2 (Table 15).

5.4.9 Wettability

Wettability refers to the tendency of one fluid to adhere to the matrix surface in the presence of other immiscible fluids. It is defined by the contact angle of a fluid with the matrix surface. Within a reservoir rock, the fluid may be water, oil or gas; a preferentially wetting fluid is likely to replace another existing fluid. The wettability of a matrix is dependent on the shape, size and rounding of the surface. The wettability of a system can directly affect the mass transport of a solution within a system by retardation or contribution. The injection of CO_2 into a reservoir is affected by the wettability of a system through imbibition and drainage processes (hysteresis) (Lyons and Plisga, 2011). This in turn can lead to residual trapping, whereby solutes become disconnected. While this is an important interaction within a system, it requires immiscible fluids. In the experimental system used, it is entirely gas-gas interactions; thus, the process of wettability will not be considered in further detail.

5.4.10 Pore network and connectivity

The pore network of a system is controlled by the spatial correlation and geometry of the spaces. A pore network of a system can be used to understand the effects of wettability, hysteresis, permeability and mass transport. Although porosity and permeability can be experimentally measured, it is important to understand how these values relate to the complex geometry of a pore space. Chapter 4 described the acquisition of BS and OM images to identify pore networks using ImageJ and construct PAMs. The analysis of these images provide important information on the connectivity of the Fell sandstone. Analysis of pore geometry suggests there are some simple pore spaces present as well as some highly branching pathways. In addition, PAM analysis shows that during drainage the injected oil does not equally invade all the pore spaces, suggesting that there may be preferential pathways. A potential reason for this is the oil is unable to overcome the capillary threshold pressure.

5.4.11 Advection

Fluids move with an average linear velocity within a porous medium using Darcy's Law. This is dependent on the effective porosity of the medium as well as the hydraulic conductivity and the prevailing hydraulic gradient (Fetter, 2008). Darcy's Law describes the flow a fluid through a porous medium such that the flux is directly related to the pressure gradient across a system. If there is no pressure gradient, no flow will occur within the system; otherwise the flow will occur from high to lower pressure. Advection is the transport of fluids due to the fluid's bulk motion. In a one dimensional context, advection has no effect on the shape of a breakthrough curve, rather shifts the tracer plume in time by a distance. Advection is dependent on the permeability and porosity of the porous medium. The average linear velocity can be shown as (Fetter, 2008):

$$v_x = \frac{K}{n_e}\frac{dh}{dl} \tag{16}$$

v_x = average linear velocity

K = hydraulic conductivity

n_e = effective porosity

$\frac{dh}{dl}$ = hydraulic gradient

In a one dimensional, advective transport equation for a concentration gradient ($\partial C/\partial x$) is written as:

$$\frac{\partial C}{\partial t} = -v_x \frac{\partial C}{\partial x} \tag{17}$$

Under advection, a solute is unable to move across flow lines. To account for deviations from the average linear velocity calculated by Darcy's Law, other mechanisms must be at play; this is hydrodynamic dispersion and is a combination of molecular diffusion and mechanical dispersion.

5.4.12 Molecular diffusion

Diffusion refers to the process by which particles intermingle as a result of their kinetic energy of random motion. The particles mix due to the random velocities of their atoms. After a specific time, a solute and solvent would become a uniform mixture – a solution. Diffusion is likely to happen due to the high molecular velocities associated with the thermal energy of the particles (Domenico and Schwartz, 1990). For an ideal monatomic gas, thermal energy is entirely kinetic energy. In other solutions, where some of thermal energy is stored in atomic vibration or by increased separation of particles having mutual forces of attraction, the thermal energy is equally partitioned between potential energy and kinetic energy. The rate of diffusive movement is a function of temperature, viscosity of the fluid and the mass of the particles involved (Lyman, 1982). At thermal equilibrium, all particles of different masses have the same average kinetic energy; the average molecular diffusion rate is dependent on the different average velocities. The mean free path is inversely proportional to the density of the gas. Molecular diffusion drives the movement of a solute from an area of higher concentration to an area where it is less concentrated. Diffusion is a second order mechanism in most transport systems where advection and mechanical dispersion dominates. Diffusion in porous media is controlled by the porosity, tortuosity and any chemical reaction with the matrix (McDermott, 1999).

When the pressure is high, molecule-molecule collisions dominate and the system behaves as normal and follows a Fickian regime:

$$F = -D_e\left(\frac{\partial C}{\partial x}\right) \quad (18)$$

F = mass flux of solute

D_e = molecular diffusion coefficient

C = concentration of the diffusing material

x = length over which the diffusion occurs

$\partial C/\partial x$ = concentration gradient

The negative symbol indicates that the movement is from areas of high concentration to areas of lower concentration. For systems in which diffusion happens over time, Fick's second law describes diffusion as:

$$\frac{\partial C}{\partial t} = D_e \frac{\partial^2 C}{\partial x^2} \quad (19)$$

$\delta C/\delta t$ = change in concentration with time ($M.L^{-3}.T^{-1}$)

In addition to molecular diffusion, if the pressure is low, frequent collisions occur between molecules and the surrounding matrix. The mean free path is restricted by the geometry of the void space - the diffusion through the scale length of the system is comparable to or smaller than the free mean path; this is known as Knudsen diffusion. The presence of other gases no longer affects the transport and the transport over time is dependent on the density gradient of the solution. The molecular flux of a solute due to the Knudsen diffusion is given by:

$$J_{iK} = -D_{iK}\frac{\partial c_i}{\partial x} \quad (20)$$

D_{iK} = Knudsen Diffusivity

5.4.13 Mechanical dispersion

Within a porous media, a solute moves at rates that are greater and less than the average linear velocity. The dispersivity in the direction of flow is typically larger than the dispersivity in the direction perpendicular to the flow direction. There are three main mechanisms that drive dispersion - friction within pores, various path lengths and pore size (Fetter, 2008). Mechanical dispersion dilutes the solute front in the flow direction. Mechanical dispersion depends on flow; it is expected to increase with an increase in velocity. Mechanical dispersion is commonly referred to as a 'fudge factor' to account for deviations within a system; it is solute and medium specific and commonly derived via experimental tests. It is also scale dependent, mainly due to changes in heterogeneity in regional systems compared to on core samples. In one dimension, longitudinal dispersion can be written as:

$$-D_L \frac{\partial C}{\partial x} \tag{21}$$

D_L = hydrodynamic dispersion coefficient

The coefficient of longitudinal dispersion is proportional to the magnitude of the solution velocity (Fetter, 2008).

5.4.14 Sorption

When a solute is not conservative (such as CO_2 and slightly with SF_6), it may interact with matrix. This may be by adsorbing on to the surface of the matrix or absorbed into the structure itself. Sorption encompasses both of these terms (as well as chemisorption and ion exchange). In a porous media, the extent of the sorption is controlled by the electrostatic surface of the minerals present. The retardation of tracers' lead to a delay in detection time as well as a prolonged tail off if desorption is also simultaneously occurring. This is commonly recorded as a direct linear relationship between the amount of a solute sorbed onto the solid and the concentration of the solute; this assumes that there is no limit to the amount of solute that can be sorbed onto the matrix. The amount of retardation caused by sorption is derived empirically from the slope of the Freundlich linear sorption isotherm:

$$C_s = K_d C^N \tag{22}$$

C_s = concentration of the chemical in the sorbed state

K_d = partition/distribution coefficient

C^N = concentration exponent for each solution and matrix (where N is the sorption intensity)

5.4.15 Discussion of how transport processes have governed the breakthrough curves

A breakthrough curve is described by its steepness and shape. It is apparent from the results that the gas breakthrough curves for the different gases are not symmetrical and that not all the tracers behave in the same manner. It is important to understand the processes that affect the mass transport of tracers and their individual contributions to the system. Figure 71 shows the inputs and processes affecting the spreading of a tracer through the flow cell. While this list is not exhaustive, the aim is to highlight what processes are involved in mass transport.

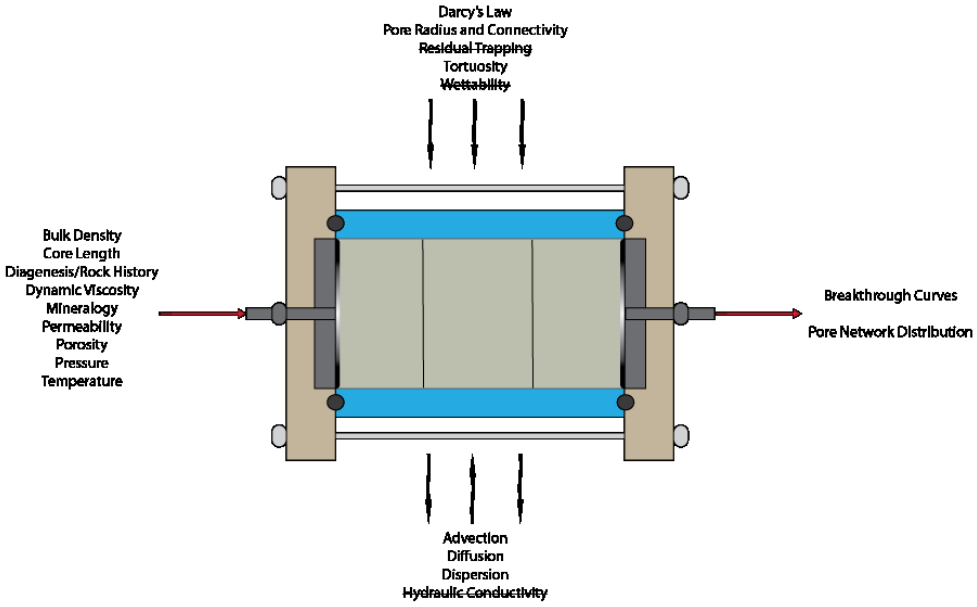

Figure 71: Illustration showing the inputs and processes affecting the spreading of a tracer through the flow cell. On the upstream end of the flow cell, are the inputs needed to understand and complete the experiments. Downstream of the flow cell, are the outputs; these are the physical data and information that are produced because of the experiments. To achieve this, it is important to understand the processes that affect the mass transport and their contribution to the system. In the case of the research specific parameters, some processes have been considered but omitted.

Overall, the breakthrough curves arrived sooner than would be expected based on the initially calculated permeability (221 mD) and porosity values (20.3%) from plug analysis. Sometimes permeability to gases can be different to liquids in the same media. Results from permeability analysis from Heriot Watt, suggest that this is not the case for this flow cell core (Figure 31). PAM values of permeability were much lower than expected. If the permeability were as low as PAM results suggest, then the samples would take longer than they actually did. This suggests that the output from the PAM readings are imperfect and should be observed with caution. Table 15 summarised the calculated permeability range for the sandstone core as 943 – 1,179 mD using the flow rates recorded. The flow cell is an artificially created system and it is possible for variations in permeability to occur. The calculated permeability range for the sandstone core should reflect the 'true' permeability for the system. In addition, further analysis of the porosity of the sample has shown a lower porosity range (as low as 14.65% from ImageJ and PAM analysis), suggesting that the travel times of the breakthrough curves may be faster due to this lower porosity value (Table 16).

Advection involves mass transport due to the flow of the solution. When only advection processes are occurring, a solute is unable to move across flow lines. Advective velocity increases with a decrease in porosity. If advective processes were only occurring, the breakthrough curves would present as sharp tight peaks. Variation in the spreading of the tracers must be occurring as the curves vary in shape and length. Molecular diffusion drives the movement of a solute from an area of higher concentration to an area where it is less concentrated. The spreading of molecules is analogous to a Gaussian normal distribution (Einstein, 1905b, Einstein, 1905a, Grathwohl, 1998). The diffusion of a solute causes the spread of a tracer with time even with the absence of flow (Figure 72).

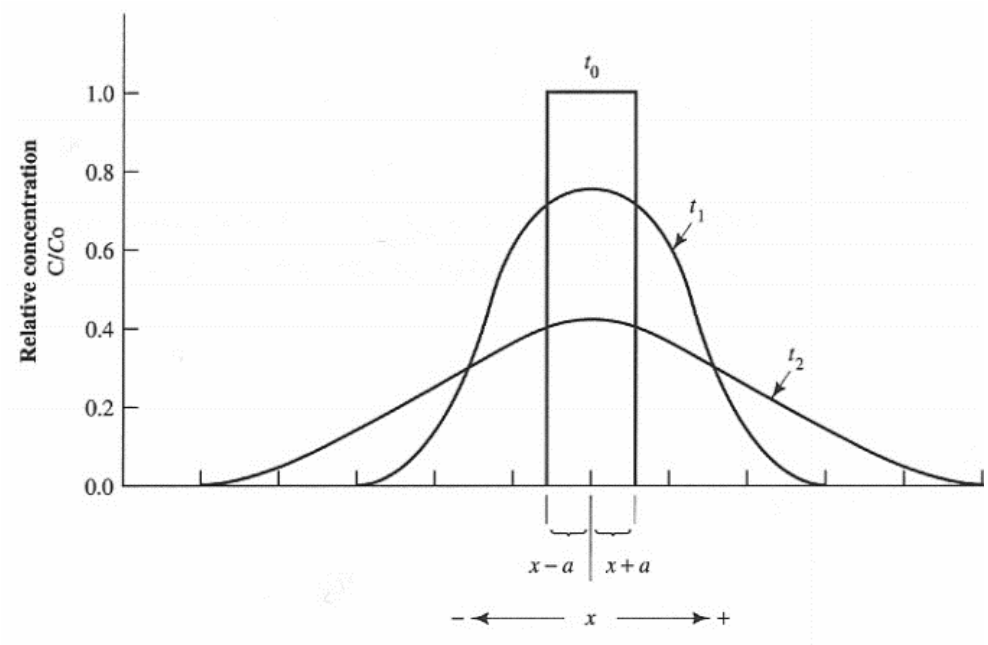

Figure 72: Spreading of a solute pulse with time due to diffusion. A slug of solute was injected into the aquidfer at time t_0 with a resulting concentration of C_0 (Fetter, 2008).

Mechanical dispersion is the mixing caused by local variations around the mean velocity of flow (Domenico and Schwartz, 1990). On the scale of the flow cell, these variations are pore-to-pore heterogeneities. Where a mass spreads in one direction, the dispersion is expressed as longitudinal. The advective velocity and grain size are the main controls on the longitudinal dispersion in a column. With an increase in time, the spread becomes Gaussian and the mean defines the position due to advective velocity and the spread is the result of hydrodynamic dispersion (Figure 73).

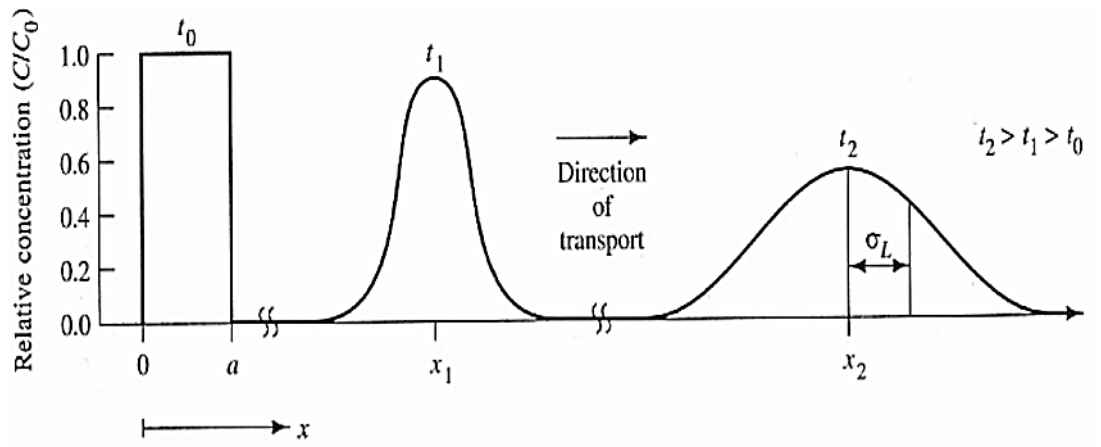

Figure 73: Variation in concentration of a tracer spreading in one dimension in a constant velicity flow system where σ_L is the longitudinal spread of the data about the mean (Domenico and Schwartz, 1990).

The contribution of molecular diffusion and mechanical dispersion to the spreading of a tracer depends on the nature of the solute (tracer) and the solution. At high flow rates, advection dominates and the C/C_{max} follows a parabolic flow velocity profile. This is because of friction between the fluid and the matrix. For gases, the velocity of the solution in contact with the matrix is significant and leads to slip flow, which could result in a higher flux. In the case of these experiments, the sandstone has a semi-pervious permeability and medium grain size; it is unlikely that the mean free path length of a tracer is of the same length as the pore diameters (Klinkenberg effect). The superimposition of hydrodynamic dispersion with the advective profile can skew the breakthrough curve profile. This is apparent in all of the results but particularly at the high pressure gradients (50,000 Pa) where the pre-peak concentrations side of the curves have a steeper slope than the post-peak values. At lower flow rates, hydrodynamic dispersion is important, as the concentration gradient at the tracer front will be high. During advective transport in porous media, the longitudinal dispersion causes more spreading of a solute plume than molecular diffusion (Grathwohl, 1998). The experimental breakthrough curves for all of the tracers have the same advective velocity values for each of the sampling pressures. Therefore, the spreading of the curves is due to dispersion values and must be different for each tracer. At 10,000 Pa, helium has the least amount of spreading over time and must be primarily from advective velocity and molecular diffusion (Figure 51). As the atomic radius increases towards xenon (and SF_6), the amount of spreading increases. This suggests that there is a higher level of dispersion with an increase in size. CO_2 results show

increased spreads that may be the result of high dispersivity but also appears to show some retardation effects.

Retardation occurs where some tracers move slower through the porous medium than the carrier gas caused by adsorbing on to the surface of the matrix or absorbed into the structure itself. Retardation can shift the breakthrough curves further along the time axis. Additionally if there is already some of the retarded species in the system, it can affect the next pulse that is released. Sorption has affected the shape of the CO_2 breakthrough curves (Figure 58). The results show that despite purging the system (all the experiments followed the same procedure), there is CO_2 retardation occurring. The level of CO_2 does not drop below detectable levels and these sorption processes mask the breakthrough curves.

5.5 Summary

This chapter presented the breakthrough curves for noble gases, SF_6 and CO_2 through the Fell sandstone. Several behavioural trends can be seen for the different tracer gases. Helium is the last of the noble gases to reach C_{max} for all the pressure ranges and it is also the quickest tracer to cease detection. Neon shows quicker pre-peak concentration values but has similar post-peak times to helium with a decrease in pressure gradient. Argon, krypton and xenon show similar C/C_{max} timings at lower sampling pressure. At all sampling pressures, a pulse of SF_6 tends to be quickest to reach C_{max} but takes longer to complete the experiment than any of the noble gases. CO_2 C_{max} takes the longest and behaves very differently compared to the noble gases and SF_6. The observed trends from the experimental results were described with the mechanisms involved in the mass transport of tracers through porous media. The experimental breakthrough curves for all of the tracers have the same advective velocity values due to bulk movement for each of the sampling pressures. Therefore, the spreading of the curves is due to hydrodynamic dispersion and must be different for each individual tracer. The contribution of molecular diffusion and mechanical dispersion to the spreading of a tracer depends on the nature of the solute (tracer) and the solution. The significance of the breakthrough curves produced for each tracer will now be considered in further detail in Chapter 6 using analytical and statistical modelling observations.

Chapter 6 - Analysis of experimental flow results using a one dimensional advection dispersion model

6.1 Introduction

Models describing the transport of a tracer in homogeneous porous media can be formulated using a one dimensional advection dispersion transport equation with distance or time dependent transport coefficients. The aim of this chapter is to provide modelled data, which can be compared to tracer results from the core flow experiments previously presented and discussed in Chapter 5. This chapter will use the one dimensional advective dispersion transport equation to fit curves to the experimental outputs using two different modelling approaches. The first part of this chapter will describe the processes involved and the necessary equations used to calculate the transport behaviour of the different tracers. These equations will produce model curves fitted to the experimental data using statistical and analytical approaches. The outputs from the two modelling approaches will provide values for the transport of the noble gases, SF_6 and CO_2 through porous media. Subsequently, the resulting modelled data and experimental breakthrough curves will be compared in order to understand the mechanisms involved in transporting CO_2 and noble gases.

6.2 The advective dispersion equation for one dimensional pulse injection

The fundamental processes involved in the transport of a solute have already been described and summarised in detail in Chapter 5. The objective of this section is to incorporate these processes into a mass transport equation that can be used for fitting curves to experimental data. As previously mentioned, a solution is a fluid that is made up of solute and solvent components. The amount of solute (tracer) in a solution (carrier gas) tends to be lower than that of the solvent. For this research, the transport of a tracer through a system consists of two aspects, the movement of the tracer with the fluid and within the solution itself. Movement of the solute with the movement of the fluid is governed by physical properties is known as advective transport. Movement of the solute within the solution itself is the result of thermal motion and is known as hydrodynamic dispersion. Diffusion itself is further classified into molecular diffusion and mechanical dispersion. The processes affecting mass transport through a porous system will now be considered in further detail.

6.2.1 Advective velocity

Fluids move with an average linear velocity within a porous medium. This is dependent on the effective porosity of the medium as well as the hydraulic conductivity and the prevailing hydraulic gradient (Fetter, 2008). This means that the amount of tracer being transported through the flow rig is a function of its concentration in the solvent and the quantity of solvent flowing. According to Carmen (1956), Darcy's law for compressible one dimensional flow conditions can be written as:

$$Q = A\frac{k}{\mu_a}\left(\frac{{P_1}^2 - {P_2}^2}{2P_2 x}\right) \tag{23}$$

Q = volumetric flow rate ($m^3\ s^{-1}$)

A = cross sectional area (m^2)

k = intrinsic permeability (m^2)

μ_a = dynamic viscosity of the gas ($Pa\ s^{-1}$)

P_1 = pressure input (Pa)

P_2 = pressure output (Pa)

x = length of the flow path (m)

For incompressible flow, the change in pressure over distance can be described as:

$$Q = A\frac{k}{\mu_a}\left(\frac{P_1 - P_2}{x}\right) \quad (24)$$

Linear flow paths are assumed in Darcy's Law. For one dimensional flow normal to a unit cross-sectional area of the porous media, the average linear velocity is equal to the quantity of fluid flowing divided by the effective porosity (Fetter, 2008):

$$q = \left(\frac{Q}{A}\right) \quad (25)$$

q = specific discharge (m s^{-1})

Q = volumetric flow rate (m^3 s^{-1})

A = cross sectional area (m^2)

$$v = \left(\frac{q}{n_e}\right) \quad (26)$$

v = advective velocity (m s^{-1})

q = specific discharge (m s^{-1})

n_e = effective porosity (%)

The effective porosity excludes isolated pores and only accounts for the porosity of the rock that is available for fluid flow.

6.2.2 Molecular diffusion

Molecular diffusion is the transfer of mass from an area of high concentration to an area of lower concentration. The mass of a fluid diffusing is proportional to the concentration gradient, which can be expressed in one dimension using Fick's first law. The diffusion coefficient can

be determined using the analytical formula from the Fuller, Schettler and Giddings (FSG) method (Lyman, 1982):

$$D = \frac{0.001T^{1.75}\left(\frac{1}{m_g}+\frac{1}{m}\right)^{0.5}}{P\left(V_g{}^{1/3}+V^{1/3}\right)^2} \quad (27)$$

D = pore diffusion coefficient of tracer in solvent ($cm^2\ s^{-1}$)

T = temperature (K)

P = atmospheric pressure (atm)

m_g = molecular weight of air ($g\ mol^{-1}$)

m = molecular weight of the diffusing gas ($g\ mol^{-1}$)

V_g = atomic diffusion volume of air ($cm^3\ mol^{-1}$)

V = atomic diffusion volume of the diffusing gas ($cm^3\ mol^{-1}$)

Table 23 shows the diffusion volumes for the tracers tested under the experimental conditions. These are based on the FSG method as outlined by Lyman (1982) and are diffusivities from structure. These diffusion volumes have been used to calculate the pore diffusion coefficient for all the tracers over the sampling pressure gradients and will be used in the advective dispersion transport equation (Table 24).

Table 23: Diffusion volumes for atomic and simple molecules used in calculated diffusion coefficients based on the FSG method using Equation (27).

Atomic Diffusion Volumes (V) ($cm^3\ mol^{-1}$)	
Helium	2.88
Neon	5.59
Argon	16.1
Krypton	22.8
Xenon	37.9
SF_6	69.7
CO_2	26.9
N_2	17.9

Table 24: Diffusion coefficients calculated for the different tracers over the sampling pressures used (T = 293.15 K). These are part of the mass balance formulation for solute transport.

Tracer **D ($m^2\ s^{-1}$)** **Solvent**	CO_2 N_2	He	Ne	Ar	Kr	Xe	SF_6
	(CO_2)						
	($\times 10^{-5}$)						
151,325 Pa	1.2784	4.4539	1.9675	1.1941	0.9118	0.7184	0.5664
141,325 Pa	1.3310	4.6374	2.0486	1.2433	0.9494	0.7480	0.5897
131,325 Pa	1.3882	4.8368	2.1366	1.2968	0.9902	0.7801	0.6151
121,325 Pa	1.4506	5.0540	2.2326	1.3550	1.0347	0.8152	0.6427
111,325 Pa	1.5188	5.2917	2.3376	1.4187	1.0833	0.8535	0.6729

6.2.3 Mechanical dispersion

Within a porous media, a solute moves at rates that are greater and less than the average advective velocity (Fetter, 2008). Mechanical dispersion describes when a solute does not travel at the same velocity through the porous media and mixing occurs. At the scale of the

experimental layout, three major processes may affect the travel time of the tracer. (1) Different pore size along the flow paths allows tracer particles to move faster through some pores; (2) tortuosity of the pore channels mean some of the tracer will travel through longer flow paths over the same linear distance; (3) different velocity profiles in the pore channels allow the tracer to move faster in the centre of the pores than along the edges (Fetter, 2008, McDermott, 1999) (Figure 74).

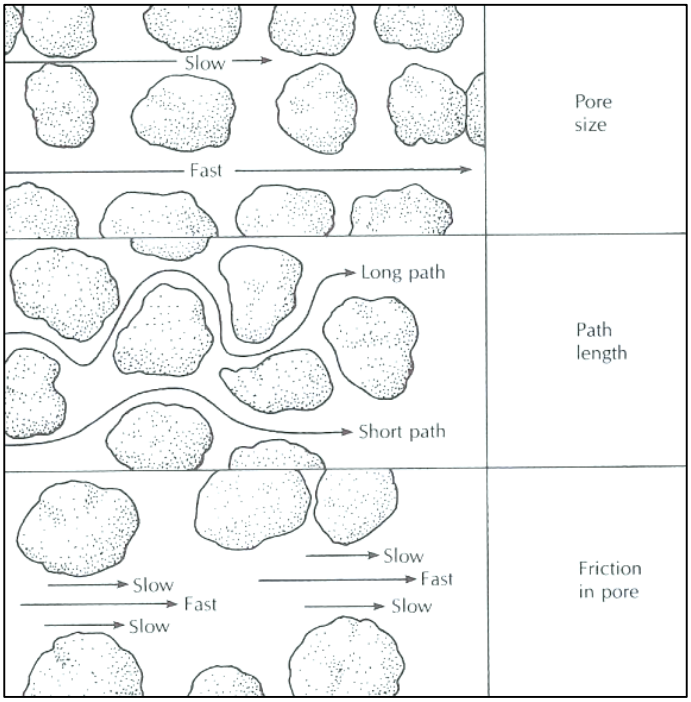

Figure 74: Factors causing longitudinal dispersion at the scale of individual pores (Fetter, 2008, Fetter, 1994).

For the type of experimental set up involved, only longitudinal dispersion is considered – that is dispersion in the direction of flow. In one dimension, contribution of longitudinal dispersion (α_L) can be written as:

$$-D_L \frac{dC}{dx} \tag{28}$$

D_L = hydrodynamic dispersion coefficient

The coefficient of longitudinal dispersion is proportional to the magnitude of the advective velocity (Fetter, 2008):

$$D_L = \alpha|v| \tag{29}$$

α = dispersivity (m)

v = advective velocity (m s^{-1})

6.2.4 Sorption

Sorption is the process by which a substrate attaches to another. Sorption in porous media can be classified as adsorption or absorption. Adsorption occurs when the substance is physically adhered to an interface. Absorption is a process by which the substance is incorporated into the sorbent. These two processes can take place simultaneously within porous media. Sorption can be expressed as (Kosakowski and McDermott, 2008):

$$R_f = 1 + \frac{\rho_b K_d\ (1 - n_e)}{n_e} \tag{30}$$

R_f = retardation factor

ρ_b = bulk density (mass of aquifer material per unit volume of porous medium) (kg m^3)

K_d = solid-water distribution ratio (ml g^{-1})

n_e = effective porosity (%)

The K_d value is usually measured using data from experiments. It is a unit of measurement that is used to describe the extent to which a substrate has sorbed to the porous media. The partition coefficient K_d is defined as:

$$K_d = \frac{C_{Solid}}{C_{Solution}} \tag{31}$$

K_d = solid-water distribution ratio

C_{Solid} = solute concentration on the solid at equilibrium

$C_{Solution}$ = solute concentration remaining in solution at equilibrium

6.2.5 Hydrodynamic dispersion coefficient

To apply the diffusion coefficient to the Fell sandstone, it is necessary to consider the porosity, tortuosity and chemical interaction of the matrix with the diffusing gas. In the case of a transient non-reactive pulse of tracer (noble gas) through the system, Fick's second law may be applied to include a sink term due to sorption and provide an effective diffusion coefficient, given by Grathwohl (1998) as:

$$n_e \frac{\partial C}{\partial t} = D_e \frac{\partial^2 C}{\partial x^2} - \rho \frac{\partial q}{\partial t} \tag{32}$$

The effective diffusion coefficient accounts for the geometry of the system and is described using the pore diffusion coefficient by Grathwohl (1998) as:

$$D_e = \frac{D n_e \delta}{\tau_f} \tag{33}$$

δ is a dimensionless factor that accounts for constrictivity of the pore pathways (≤ 1). In most cases, only the overall porosity can be determined and D_e is often defined by n_e alone ($\delta = 1$) (Grathwohl, 1998).

Combining a linear sorption to Fick's second law gives the following relationship:

$$\frac{\partial C}{\partial t}(n_e + K_d \rho) = D_e \frac{\partial^2 C}{\partial x^2} \tag{34}$$

The capacity factor ($n_e + K_d\rho$) relates to the amount of adsorption of the diffusing gas in the porous medium. Using this, the apparent diffusion coefficient for transient conditions can be described as:

$$D_a = \frac{D n_e}{(n_e + K_d \rho)\tau_f} \tag{35}$$

As the tracer gases behave conservatively, there is no adsorption of the gas to the matrix particles. The capacity factor is reduced to n_e. Additionally, τ has been previously described as a relationship between the effective porosity and the experimentally derived component m (Section 5.4.7). When m is assumed to be approximately 2 (common value for sandstones) (McDermott, 1999), D_a is identical to the pore diffusion coefficient:

$$D_a = Dn_e \tag{36}$$

The process of molecular diffusion cannot be separated from mechanical dispersion. The two are combined are the hydrodynamic dispersion coefficient and is defined using the following equation:

$$D_l = n_e D + \alpha_l |v| \tag{37}$$

D_l = longitudinal apparent diffusion constant ($m^2\ s^{-1}$)

n_e = effective porosity (%)

D = pore diffusion coefficient of that gas in air at a certain temperature and pressure ($m^2\ s^{-1}$)

α_l = longitudinal dispersion (m)

v = advective velocity ($m\ s^{-1}$)

The contribution of mechanical dispersion and molecular diffusion to the spreading of the tracer varies according to the nature of the solvent and the solute. In terms of the experimental equipment, the solute is a noble gas and the solvent will be CO_2 (or N_2 for the CO_2 tracer equations).

6.2.6 Advective dispersion equation for one dimensional transport

In a one dimensional flow field the basic advective dispersion equation for the transport of a tracer can be written as:

$$\frac{\partial C}{\partial t} = D\frac{\partial^2 C}{\partial x^2} - v\frac{\partial C}{\partial x} \quad (38)$$

C = concentration of the solute

v = advective velocity

x = flow path length

D = diffusion coefficient

Including the transformation process sorption, this can be written as (Kosakowski and McDermott, 2008):

$$\frac{\partial C}{\partial t} = \frac{D}{R_f}\frac{\partial^2 C}{\partial x^2} - \frac{v}{R_f}\frac{\partial C}{\partial x} \quad (39)$$

In the cases of a non-reactive (conservative) tracer, such as a noble gases used in the experimental equipment, there is no sorption of the gas into or onto the matrix particles. This means that the pore diffusion coefficient can be used and the retardation factor can be neglected (Grathwohl, 1998). This is not the case for CO_2 and needs to be accounted for in the modelling.

The analytical solution of the basic advective dispersion equation used for modelling comparison of the experimental results is:

$$C(x,t) = \frac{M_0}{2\sqrt{\pi D_x t}} \times exp\left[-\left(\frac{(x-vt)^2}{4D_x t}\right)\right] \quad (40)$$

$C(x,t)$ = advective-dispersion equation for one dimensional pulse injection (g m^{-2})

M_0 = mass injected (g)

D_x = longitudinal apparent diffusion constant (m^2 s^{-1})

t = time (s) (Kinzelbach, 1992)

x = flow path length (m)

v = advective velocity (m s^{-1})

For this system, the one dimensional advective transport equation is sufficient. However, this can also be present for two and three dimensional transport such that:

$$C(x,y,t) = \frac{M_0}{4\pi t\sqrt{D_x D_y}} \times exp\left[-\left(\frac{(x-vt)^2}{4D_x t}\right) - \left(\frac{y^2}{4D_y t}\right)\right] \quad (41)$$

$$C(x,y,z,t) = \frac{M_0}{8(\pi t)^{3/2}\sqrt{D_x D_y D_z}} \times exp\left[-\left(\frac{(x-vt)^2}{4D_x t}\right) - \left(\frac{y^2}{4D_y t}\right) - \left(\frac{z^2}{4D_z t}\right)\right] \quad (42)$$

D_y = Transverse apparent diffusion constant

D_z = Vertical apparent diffusion constant (Kinzelbach, 1992)

6.3 Two modelling approaches for mass transport using the advective dispersion transport equation

6.3.1 Methodology

The advective-dispersion equation for a one dimensional pulse injection, described in the theory section of this chapter was calculated by two approaches – analytically and statistically. These two approaches will be referred as 'the statistically derived transport model' and the 'analytically derived transport model'. These methods will be explained individually in the following sections before being compared and assessed for how accurate they are to the experimental results. Table 25 is a summary of the experimental values and modelling inputs used to construct modelled breakthrough curves. These were the initial values intended to be guidelines. However, the inputs are subject to change as the model fitting progresses.

Table 25: Initial modelling inputs for mass transport equation.

Initial Modelling Inputs	
Average bulk density	2063 kg m^3
Cross sectional area of rock	~ 0.001 m^2
Dynamic viscosity (CO_2)	1.48 x 10^{-5} Pa s^{-1}
Dynamic viscosity (N_2)	1.75 x 10^{-5} Pa s^{-1}
Flow path length (core)	0.96 m
Intrinsic permeability (experimentally measured)	2.184 x 10^{-13} m^2
Porosity (experimentally measured)	20.3 %
Porosity (OM and PAM)	14.65 – 18.03%
Pressure downstream	~ 100,000 Pa
Pressure upstream	~ 150,000 – 110,000 Pa
Temperature (average)	293.15 K

6.3.2 Compressible or incompressible flow?

When calculating the advective velocity of a system, it is important to determine whether the incompressible or compressible form for pressure change over distance should be used. In fluid dynamics, the compressibility of a fluid deals with flows in which there are variations in density – it addresses the fractional change in volume. Flows in which variation in density are negligible are termed incompressible; where density variations within a flow are not

negligible, it is termed as compressible. For most fluids, density is only a weak function of temperature (Fox *et al.*, 2009), but a fluid is prone to volume variation per unit change in pressure. The one dimensional mass transport equation used, refers to the flow of a tracer through a cell where the parameters are expected to change in only one spatial direction; in this case, it is the core length (approximately 27 times longer than the core diameter).

While most ideal liquids can be referred to as incompressible, the density of a gas is subject to change. The compressibility of a gas is a measure of the relative change in volume in response to changes in pressure. At the low sampling pressure of this system (50,000 to 10,000 Pa gradient), it is unlikely that any significant compressibility of the solution should occur. To identify if this statement is true and to determine which form of the advective velocity equation would be best suited to use, a velocity profile was investigated for the flow cell system. Derivation of the velocity profile for compressible fluid flow can be found in the Appendix I. Using argon as the representative tracer due to its good behaviour during sampling, Figure 75 and Figure 76 show the pressure and advective velocity profile for incompressible and compressible flow at the end ranges of sampling (50,000 and 10,000 Pa pressure gradient). As expected, for an incompressible flow, the advective velocity remains at a constant value depending on the pressure gradient (1.99×10^{-2} m s^{-1} for 50,000 Pa and 3.98×10^{-3} m s^{-1} for 10,000 Pa), with a linear trend for the pressure profile gradient. The pressure profile for compressible flow has a near linear trend with a slight concave shape where the pressure profile is higher mid-way through the core length. When there is a 10,000 Pa pressure gradient, there is a slight difference in pressure along the core length between incompressible and compressible flow. For compressible flow, the advective velocity profile diverges from the incompressible value (that is the average of the compressible flow system). For 10,000 Pa, the advective velocity diverges by $\pm 1.12 \times 10^{-4}$ m s^{-1} from 3.98×10^{-3} m s^{-1}; and $\pm 2.38 \times 10^{-3}$ m s^{-1} from 1.99×10^{-2} m $s^{-1}$for 50,000 Pa.

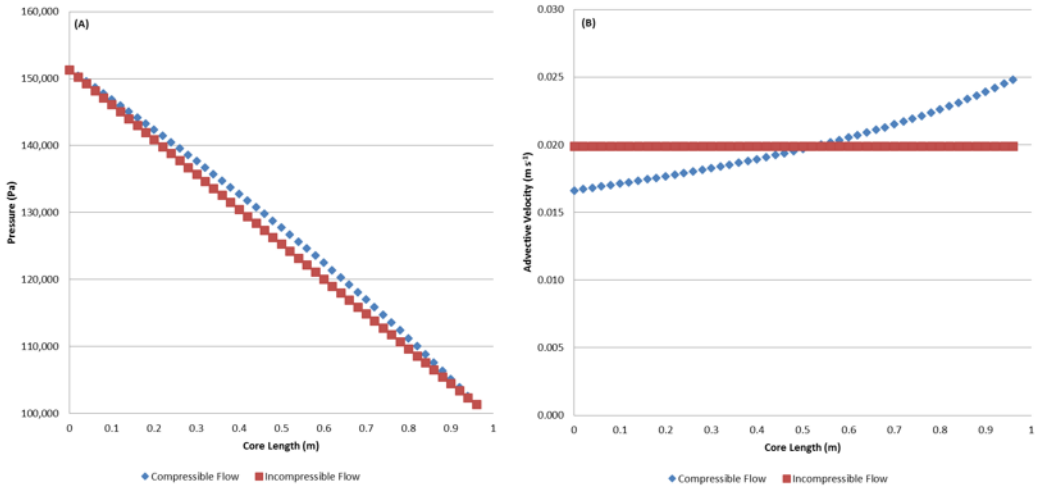

Figure 75: (A) Pressure profile for argon at 50,000 Pa gradient across the core length using compressible and an incompressible flow. (B) Velocity profile for argon at 50,000 Pa gradient across the core length using compressible and an incompressible flow.

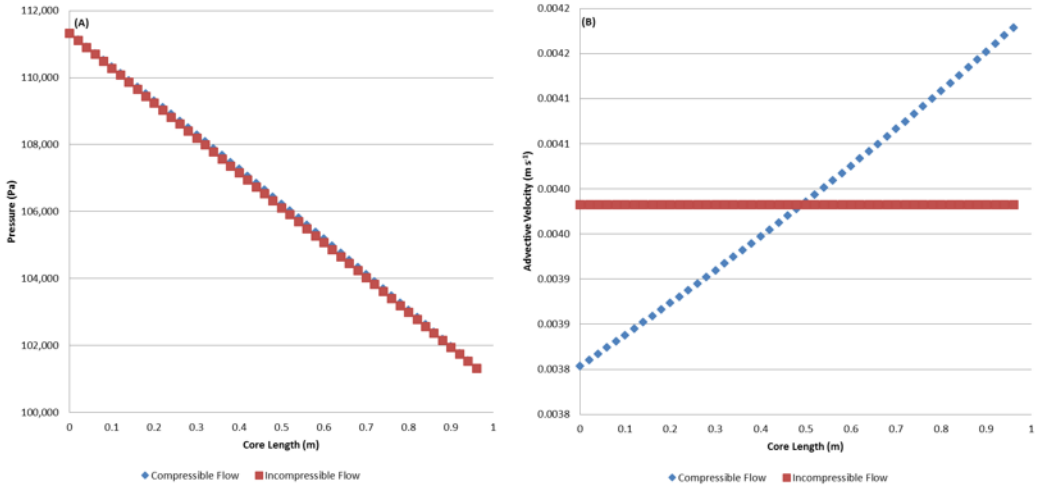

Figure 76: (A) Pressure profile for argon at 10,000 Pa gradient across the core length using compressible and an incompressible flow. (B) Velocity profile for argon at 10,000 Pa gradient across the core length using compressible and an incompressible flow.

These outputs can be used to explore the effects of transport in compressible and incompressible flow. Figure 77 and Figure 78 compare compressible and incompressible flow at the end ranges of sampling (50,000 and 10,000 Pa pressure gradient) using the flow cell. The cell has been divided into three equal sections (0.32 m), identified as S1, S2 and S3. Each

of the sections are assigned a predicted advective velocity at the selected distance along the core (using values from Figure 75(B) and Figure 76(B)). Using the one dimensional advective dispersion transport equation, where the advective velocity and core length is changeable, the tracer is a point input superimposed cumulatively through the solution. The output from S1 is used as the input for S2; the output from S2 is then used as the input for S3. Figure 77 and Figure 78 show the compressible flow for the end of S2 (0.64 m) and S3 (0.96 m). This is then compared to the control curves for the same distance if the incompressible (linear) advective velocity had been used (presented in Section 6.2.1). The slight inaccuracy is due to rounding errors and the resolution of the system depending on the timing intervals chosen.

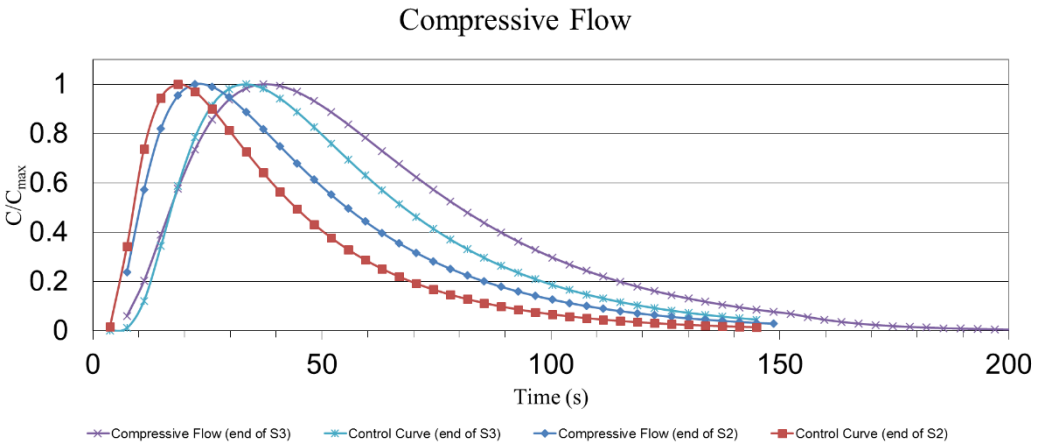

Figure 77: Effects of compressible gas flow through the experimental flow cell for argon at ***50,000 Pa****. Control curves show incompressible flow under same conditions.*

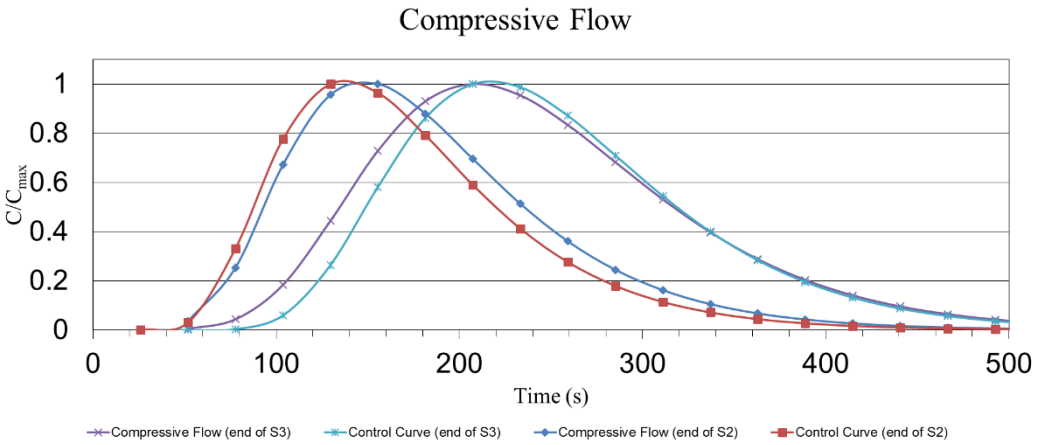

Figure 78: Effects of compressible gas flow through the experimental flow cell for argon at ***10,000 Pa****. Control curves show incompressible flow under same conditions.*

At such low sampling pressure gradients, there is a slight difference between a compressive and an incompressive flow system. Some error may arise from the allocation of a 'fixed' dispersivity value for a tracer; as dispersivity is scale dependent this would be an over simplification of the fit of the curve for each section division. Due to the low sampling pressures, all modelling approaches described in the following sections will be carried out assuming incompressible flow.

6.3.3 Statistically derived transport model

A Gaussian function is an equation that follows the form:

$$f(x) = a.exp\left(-\frac{(x-b)^2}{2c^2}\right) \tag{43}$$

a = height of the curve's peak

b = x-axis value for the curve's peak

c = the standard deviation/the width of the curve

A graph of a Gaussian function has the 'bell curve' shape and is commonly used in statistical evaluations. The spreading of molecules is analogous to a Gaussian normal distribution

(Einstein, 1905b, Einstein, 1905a, Grathwohl, 1998). Based on the similarity of the two processes, a mean square displacement as a measure for the diffusion distance can be used (Grathwohl, 1998), such that:

$$c^2 = 2D_x t \tag{44}$$

This mean square displacement represents the distance travelled by a solute along the x-axis over a given time in the one dimensional advection dispersion equation Equation (40).

In order to analyse the experimental data and appropriately fit a curve to the results, it is necessary to transform the function into a format that can be easily used. The one dimensional advection dispersion equation can be considered as a function composed of a concave quadratic function with an exponential function (a Gaussian function). Thus, the logarithm of a Gaussian function is a concave quadratic equation. The most efficient manner in which to analyse the data, which is not in an ideal format, is to linearise the data. By doing so, it is achievable to perform an analysis on the equation. After obtaining this function, it is then possible to transform it back into its original form to obtain the model.

The one dimensional advection dispersion equation can be expanded to a linear function using the basic rules of logarithms to obtain (Appendix II):

$$log(y) = log(M_0) + \frac{xv}{2D_x} - \log(2\sqrt{\pi D_x}) - {}^1/_2 \log(t) - \frac{x^2}{4D_x t} - \frac{v^2 t}{4D_x} \tag{45}$$

From this equation, there are three coefficients to be determined. As the first coefficient is already known from expansion, this can be set so that:

$$Coeffcient\ A = -{}^1/_2 \tag{46}$$

$$Coeffcient\ B = -\frac{x^2}{4D_x} \tag{47}$$

$$Coeffcient\ C = -\frac{v^2}{4D_x} \tag{48}$$

Equation (45) can then be rearranged to the form:

$$log(y) + {}^{1}/_{2}\log(t) = -\frac{x^2}{4D_x t} - \frac{v^2 t}{4D_x} + \left[\frac{xv}{2D_x} - \log(2\sqrt{\pi D_x}) + log(M_0)\right] \tag{49}$$

By rearranging coefficients from Equations (47) and (48), the advective velocity and hydrodynamic dispersion for each example can be solved as:

$$v = \sqrt{\frac{Cx^2}{B}} \tag{50}$$

$$D_x = -\frac{x^2}{4B} \tag{51}$$

Analysis of Equation (49) was completed in RStudio – an open source integrated development environment for R, a programming language and software environment for statistical computing and graphics.

6.3.3.1 Results

Error propagation values

As individual error values were supplied as part of the statistical model, it was possible to combine these values and propagate the error through system for this approach; these are summarised in Table 26, Table 27 and Table 28. Due to the high values obtained, these have been numerically presented rather than attached to the resulting graphs. All ranges presented graphically with the statistical results are the averaged propagated error values for standard deviations from the average values. The results from the CO_2 experiments show particularly high error values due the high sampling number of varying graphs used.

Table 26: Averaged propagated error values for standard deviations (±) for advective velocity and permeability, calculated using the statistical model coefficients. Values are the standard deviation of all the gases (including CO_2 sorption values but neglecting without sorption results) for each of the pressures.

(Pa)	Advective Velocity ($m\ s^{-1}$)	Permeability (m^2)
50,000	0.465	2.774×10^{-11}
40,000	0.325	2.321×10^{-11}
30,000	0.288	3.038×10^{-11}
20,000	0.446	5.525×10^{-11}
10,000	0.376	9.272×10^{-11}

Table 27: Averaged propagated error values for standard deviations (±) for dispersivity, calculated using the statistical model coefficients. Values are the standard deviation of all the noble gases and SF_6 for each of the pressures.

(Pa)	Dispersivity (m)					
	He	Ne	Ar	Kr	Xe	SF_6
50,000	3.265	3.559	1.172	10.276	2.737	1.117
40,000	3.635	2.614	1.305	1.851	0.955	2.393
30,000	3.538	2.848	1.282	1.481	1.259	1.415
20,000	7.105	4.741	1.131	3.242	1.105	1.509
10,000	4.112	25.125	2.028	1.129	1.609	4.345

Table 28: Averaged propagated error values for standard deviations (±) calculated using the statistical model coefficients. Values are the standard deviation of CO_2 with and without sorption effects accounted for at each of the sampling pressures.

	CO_2 (no sorption)			CO_2 (with sorption)		
(Pa)	*va* (m s^{-1})	*k* (m^2)	*α* (m)	*va* (m s^{-1})	*k* (m^2)	*α* (m)
50,000	0.102	6.096×10^{-12}	3.849	0.315	4.500×10^{-11}	3.849
40,000	0.101	7.539×10^{-12}	3.986	0.311	3.801×10^{-11}	3.986
30,000	0.111	1.105×10^{-11}	3.445	0.342	7.143×10^{-11}	3.445
20,000	0.082	1.228×10^{-11}	2.615	0.254	2.334×10^{-11}	2.615
10,000	0.048	1.453×10^{-11}	2.855	0.150	1.887×10^{-11}	2.855

Noble gases and SF_6

Using the linearised Equation (49) with RStudio, the coefficients could be statistically determined to fit a curve to the experimental data. The results from these models are in the Appendix III. Argon has been presented here as an example of the quality of the curves produced when the solute is passing through CO_2.

- Argon

To successfully model the breakthrough curves for each of the gases through the pressure values, the x-axis values were selected using the timings for T1 as described in Chapter 5. Where this initial limit did not provide sufficient data to perform the model fitting, the x-axis values were increased or decreased accordingly. For the noble gases and SF_6 models, a single experiment at each of the sampling pressures was chosen to represent that particular system. Figure 79 to Figure 83 show the results of the curve fitting for argon over the five sampling pressure gradients. The circles represent the experimental data and the red line shows the curve fitting by the model for that particular data.

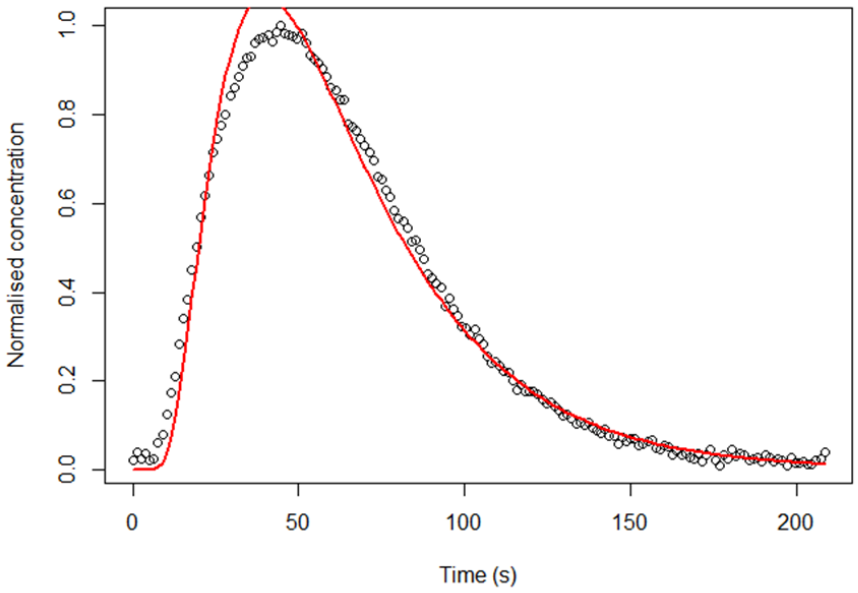

*Figure 79: Results of argon modelling for **50,000 Pa** sampling conditions. The circle point represent the experimental data. The red line represents a model curve fitting of the data.*

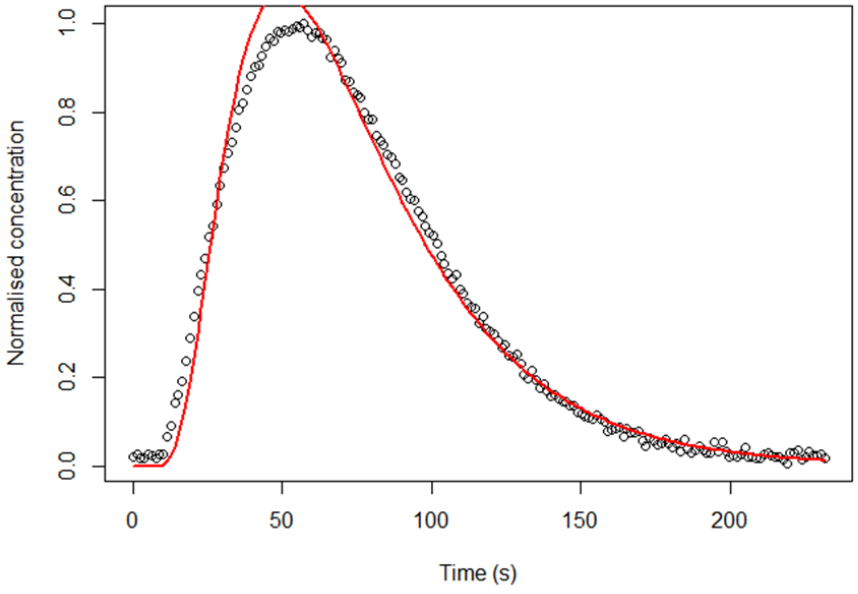

*Figure 80: Results of argon modelling for **40,000 Pa** sampling conditions. The circle point represent the experimental data. The red line represents a model curve fitting of the data.*

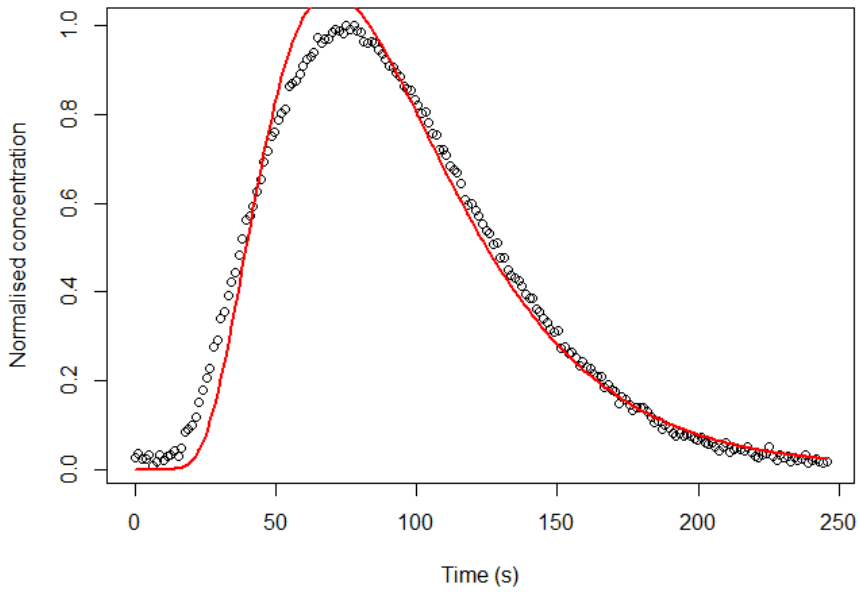

*Figure 81: Results of argon modelling for **30,000 Pa** sampling conditions. The circle point represent the experimental data. The red line represents a model curve fitting of the data.*

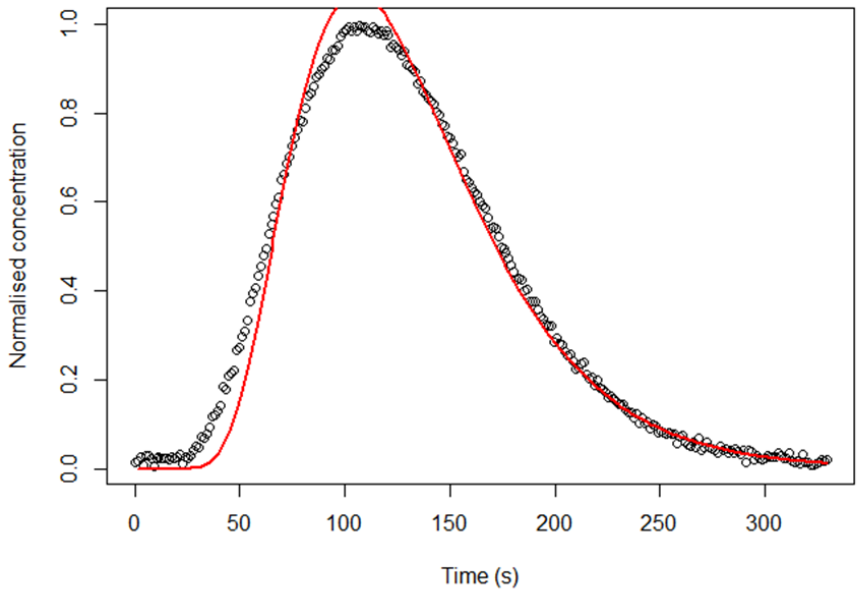

*Figure 82: Results of argon modelling for **20,000 Pa** sampling conditions. The circle point represent the experimental data. The red line represents a model curve fitting of the data.*

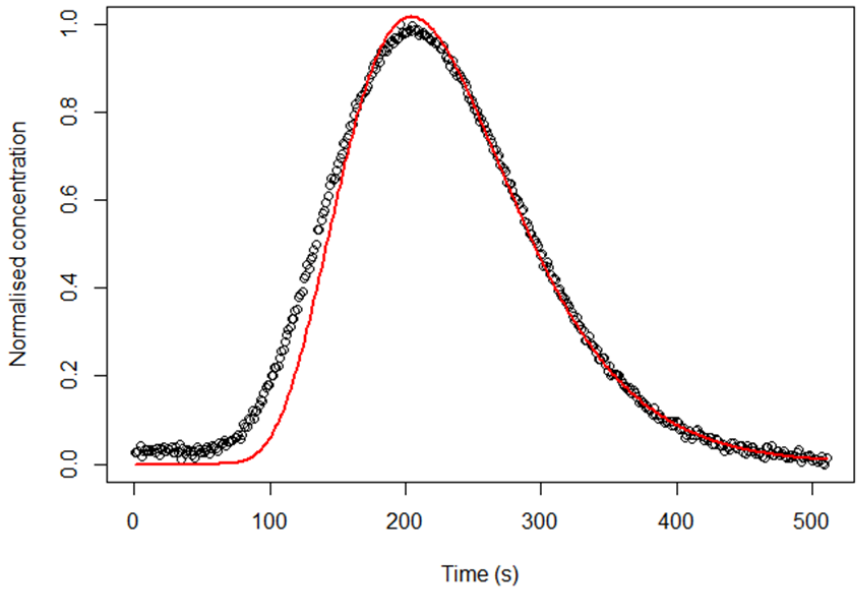

*Figure 83: Results of argon modelling for **10,000 Pa** sampling conditions. The circle point represent the experimental data. The red line represents a model curve fitting of the data.*

CO_2

Due to the complexity of the experimental data produced by the CO_2/N_2 experiments, it was necessary to tackle each of the results individually. To model the breakthrough curves for all of the replicated experiments successfully, the x-axis values were selected using the T1 values as described in Chapter 5. Where this initial limit did not provide sufficient data to perform the model fitting, the values were increased or decreased accordingly, as with the noble gases and SF_6 experiments. The results shown below are the fittings for the CO_2 experiments in two forms – with and without accounting for sorption effects (Figure 84 to Figure 86). The K_d value of 0.08 (ml g^{-1}) was chosen with a R_f of 1.76 for the sorption effects (Equation (30)). This R_f value was estimated using the analytical solution results and how similar the statistical results for advective velocity were to the noble gas and SF_6 permeability values.

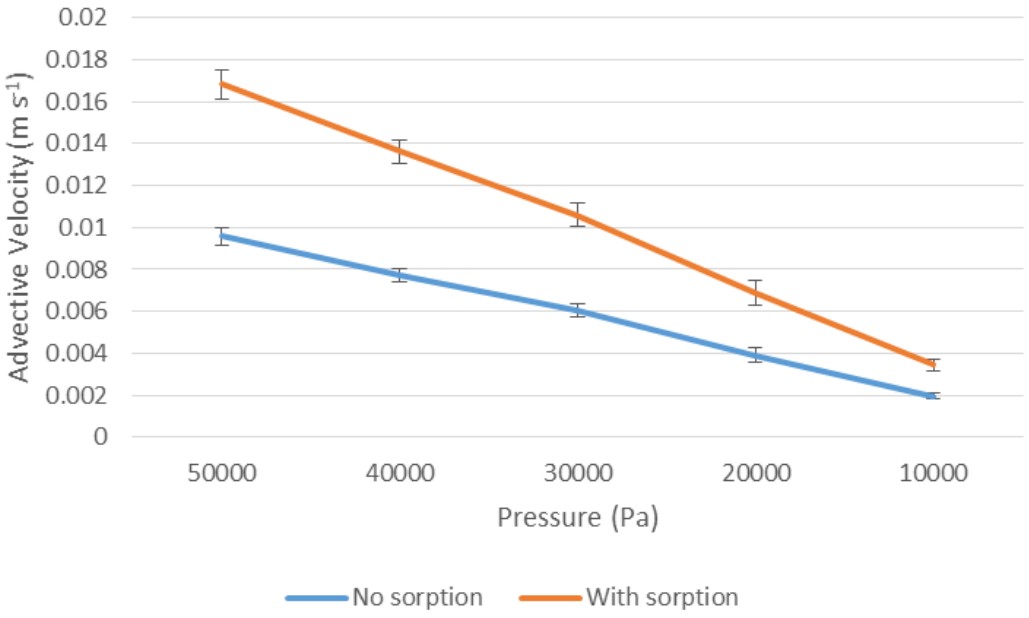

Figure 84: Advective velocity results for CO_2/N_2 experiments. Results show the average value of advective velocity at each for the pressures. The standard deviation represent the range difference in values for each for each of the five replicated experiments.

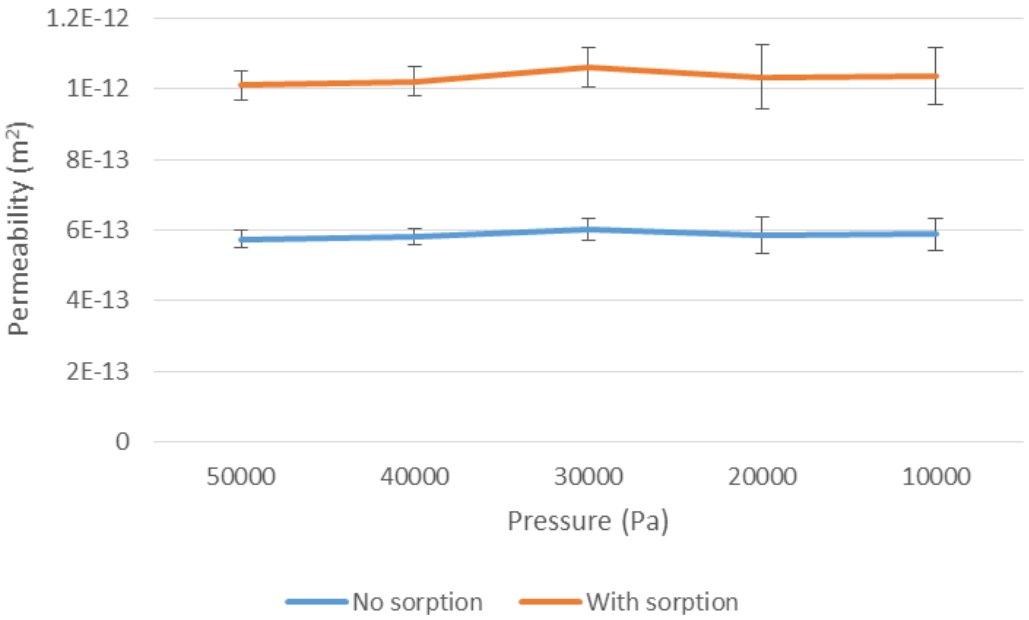

Figure 85: Permeability values calculated using the advective velocity values obtained from Figure 84. The standard deviation represent the range difference in values for each of the five replicated experiments.

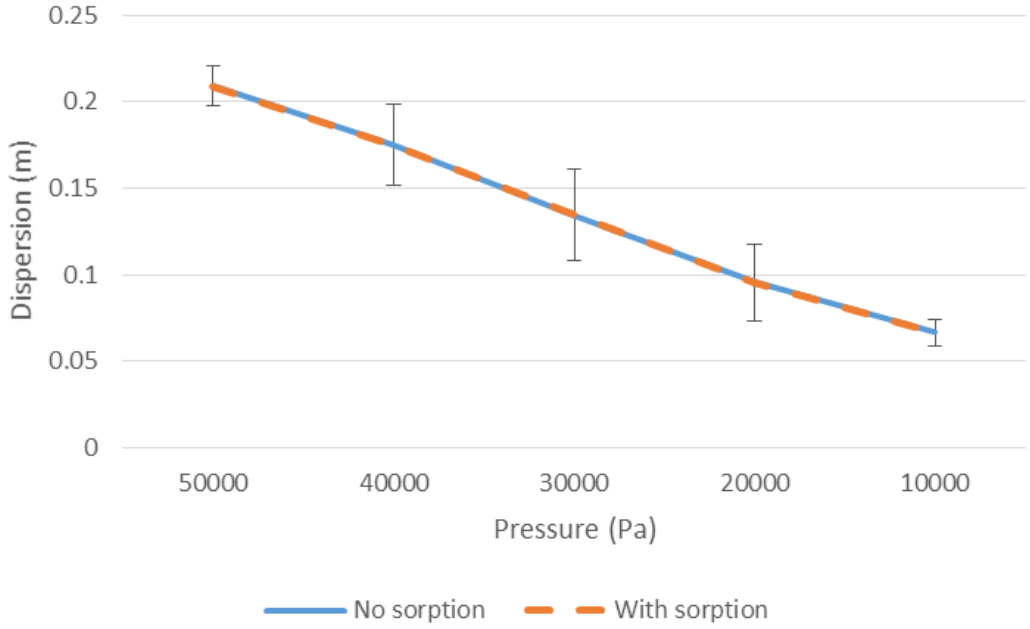

Figure 86: Dispersivity values for CO_2/N_2 experiment. The standard deviation represent the range difference in values for each for each of the five replicated experiments.

6.3.3.2 Discussion of results from statistical model outputs

R^2 measures how successful the fit is in explaining the variation of the data – the goodness-of-fit. It is the square of the correlation between the response values and the predicted response values. Overall the fitting of the linearised equation has produced high R-square (R^2) values for curve fitting all of the gases (Table 29). Argon, krypton, xenon and SF_6 have greater than 0.940 for all the pressure values. Neon and helium were less successful in matching the breakthrough curves, but still show highly significant results. Helium plots have a high signal to noise ratio due to a high ionisation energy value and a smooth curve fit can be difficult to produce. When weighting the number of sample points, many of the neon experiments had few data points for pre-peak concentration times due to sampling methods (without a calibration gas). Curves were fitted to all of the CO_2 experiments with varying degrees of accuracy, as the repeat experiments did not have similar pre-peak concentration values (Figure 58). Examples of limitations to the statistical model include influence of noise, number of sample points and the effect of repeat analyses. An additional factor to consider is the derived outputs are curve fitting a geostatistical model that allows $C/C_{max} \geq 1$.

Table 29: R^2 values derived for statistical models. Values for CO_2 using statistical model have not been included as each curve was derived individually.

(Pa)	Helium	Neon	Argon	Krypton	Xenon	SF_6	CO_2
50,000	0.795	0.910	0.985	0.985	0.997	0.998	NA
40,000	0.753	0.928	0.982	0.998	0.998	0.986	NA
30,000	0.822	0.895	0.983	0.991	0.995	0.998	NA
20,000	0.678	0.973	0.991	0.962	0.998	0.996	NA
10,000	0.875	0.914	0.991	0.995	0.995	0.949	NA

Advective velocity and permeability

Advective velocity for each of the gas models was derived directly from the output coefficients Equations (47) and (48). These outputs from the statistical modelling show similar values in terms of advective velocity (Figure 87) and permeability values (Figure 88). Permeability values were obtained using the advective velocity output values and core analysis data. The porosity value used was 17.85%, incorporating the original experimental porosity result and OM images. The value provided by Hutton Stone was omitted as it was an average of the entire sandstone formation and not calculated over the same scale of analysis (Table 30). Neon is the only one of the noble gases that shows significant disagreement from the advective velocity trend, as was also highlighted by its lower R^2 values. This lack of similarity is most likely due to difficulty in fitting the curve to the available data. As previously mentioned, many of the neon experiments had few data points for pre-peak concentration times.

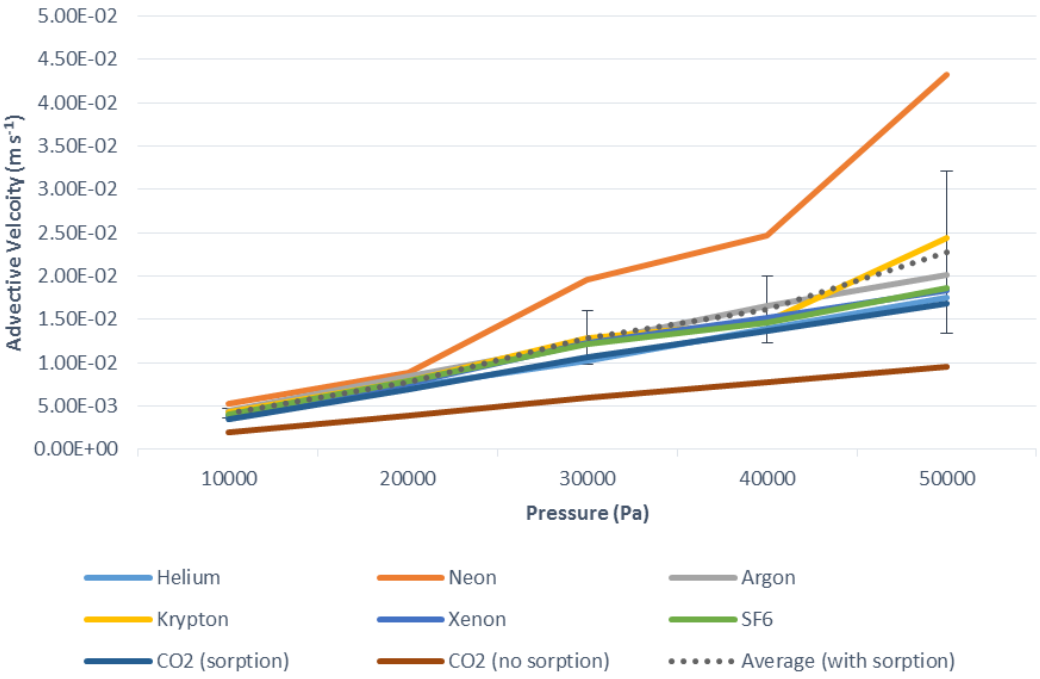

Figure 87: Combined results of calculated advective velocities for all the tracer gases. Included in the graph are the CO_2 results when there sorption is not accounted for. An average advective velocity has been calculated using all the noble gases, SF_6 and CO_2 when sorption has been accounted for. CO_2 without sorption values is omitted when calculating the average value.

From the advective velocity results (Figure 87), it can be seen that the CO_2 values are a closer fit when sorption has been accounted for. When a K_d value of 0.08 (ml g^{-1}) has been selected for in flow path calculations, the CO_2 advective velocity falls within the average range. As permeability is calculated using the advective velocity values, it has the same similar trends. The permeability range for the 0.96 m system was calculated using the noble gases, SF_6 and CO_2 results. Due to its poorly related outputs, the values for neon were not included and the values for CO_2 with sorption were used. An average permeability of 1.01 x 10^{-12} m^2 (± 2.91 x 10^{-14} m^2) was obtained. This value is necessary for determining the intrinsic permeability of the system by comparing it to the value obtained from experimental conditions (9.31 × 10^{-13} - 1.16 × 10^{-12} m^2) (Table 15) as well as the permeability test carried on a smaller plug (2.18 x 10^{-13} m^2) (Table 16).

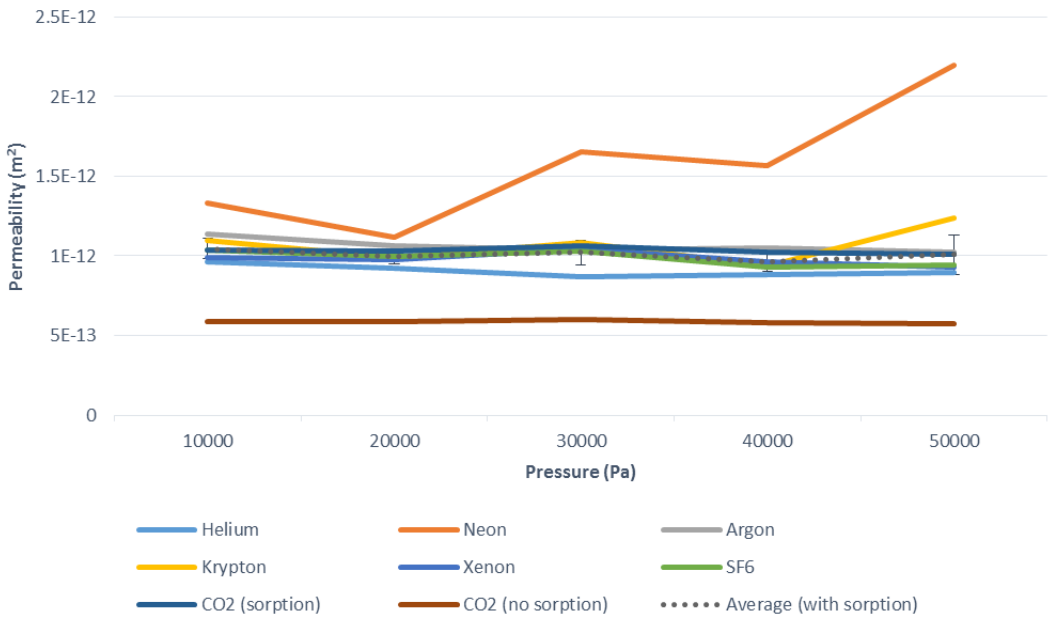

Figure 88: Combined results for the calculated permeability of the flow cell. Included in the graph are the CO_2 results when there sorption is not accounted for. Due to its poorly related outputs, the values for neon were not included and the values for CO_2 with sorption were used (CO_2 without sorption has been added to the plot as a reference) when calculating the average permeability value.

Table 30: Results of porosity analysis for the Fell sandstone using multiple approaches.

Porosity (%)	Source	Comments
(13.10)	Hutton Stone	Ignored as large scale value and bulk density not relevant
20.30	HW	Experimentally derived on core sample
16.51	OM (1mm)	ImageJ analysis
18.03	OM (1mm)	ImageJ analysis
14.65	BS (500 µm)	16.34% image, 14.49% PAM according to HW
19.78	BS (200 µm)	15.28% image, 15.28% PAM according to HW
17.85		***Suggested average value***

Hydrodynamic dispersion coefficient

The hydrodynamic dispersion coefficient (D_x) was calculated using the output coefficients from the statistical model. Dispersivity is calculated using Equation (37) and the advective velocity value used is from the modelling output coefficients.

The dispersion for all the gases follow a shallow, positive slope with an increase in pressure (Figure 89). Again, neon deviates from the general pattern of the other noble gases. In this case, CO_2 with and without sorption does not directly affect the dispersivity value. This is due to the allocation for R_f when calculating the advective velocity and hydrodynamic dispersion coefficient. Helium displays the lowest values for dispersivity. SF_6 and xenon have a similar range for dispersivity, which is expected, as they show very similar peak concentration behaviour during the experiments.

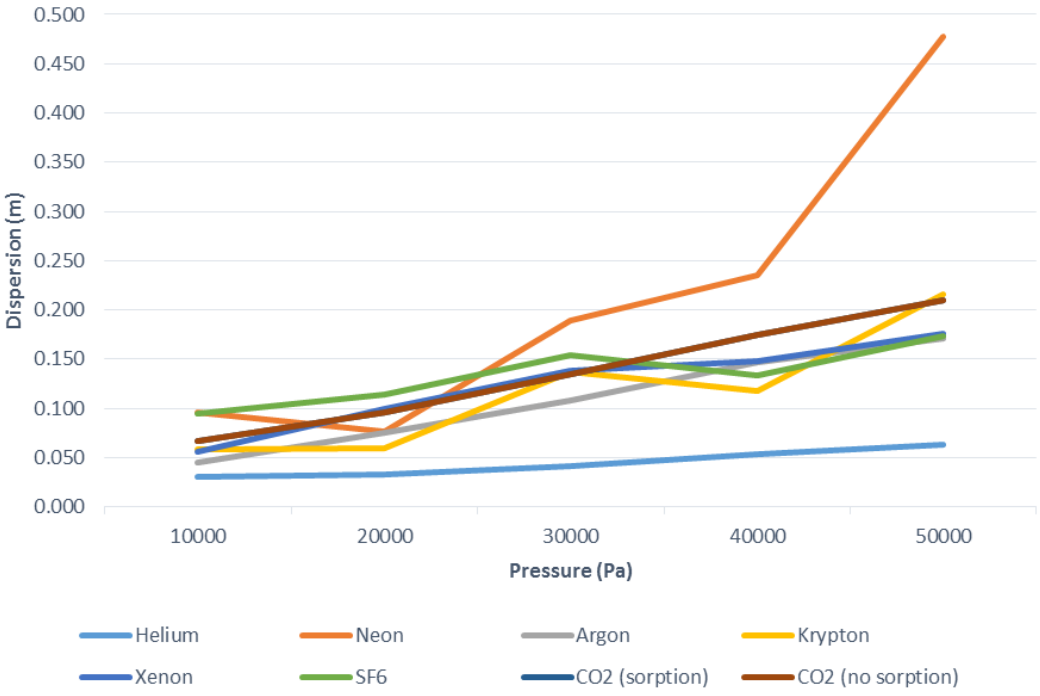

Figure 89: Dispersivity values (m) calculated from modelling coefficient values for each of the tracers at each pressure range. Dispersivity is calculated where $D_x = n_e D + \alpha|v|$.

The values for advective velocity and permeability were within the expected range for a permeable sample such as sandstone; however, the trend behaviour of the dispersion values is not. Dispersion is scale dependent and is the spatial separation of a solute within the matrix (m). As the core is 0.96 m long, the values determined are 'typical' of what would be anticipated for the core (range produced 0.03 – 0.48 m). Dispersion values are solute and matrix dependent. The cores initial input parameters identified it as a homogenous system with one permeability value associated with it. As such, the dispersivity value (α) should remain the same regardless of the pressure gradient in place and mechanical dispersion is proportional

to the magnitude of the advective velocity. It is possible that there are a number of reasons for this dispersivity pattern. The first possible case is that the modelling parameters set allow the $C/C_{max} \geq 1$; this could be sufficient to allow the dispersion factor to exceed expected ranges. The second may be the limitations of experimental set-up. Prior to the point of release, there is a 0.33 (ID) x 7.62 cm static mixer in place after the 20 cm long tracer loop to ensure complete mixing of the gases; it is possible that at lower pressure gradients this is contributing to a 'false' dispersion shape by delaying the tracer entering the core. It is also possible that the simplification of an average permeability for an artificial core is not sufficient and that there are preferential pathways being used depending on the pressure gradient. This concept will be addressed in further detail using the analytical model approach and will form part of the discussion section of this chapter.

6.3.4 Analytically derived transport model

Using the one dimensional advection dispersion equation (40), an analytical calculation was carried out using the initial experimentally derived parameters as starting values. A porosity of 20.3% and an intrinsic permeability of 2.184×10^{-13} m^2 using incompressible flow conditions were the initial input values. These inputs provided breakthrough curves with a first arrival appearance that was up to four times longer than the experimental results. A more appropriate set of values were required to satisfy the data sets obtained. Based on the output values from the statistical model, an average permeability was identified of 1.01×10^{-12} m^2 ($\pm$ 2.91×10^{-14} m^2); this value is an average of the all the permeability values for each of the gases and pressures (using CO_2 with sorption and excluding neon due to poor results). The permeability range estimated from the experimental flow values were not used due to high error associated with the flow rate meter (Table 15). However, these values served as a guide for confirming the range from the statistical modelling approach. Porosity was then amended to an average of 17.85% incorporating the original experimental porosity result and OM images (Table 30). The 13.1% value provided by Hutton Stone was omitted as it was an average of the entire sandstone formation and not calculated over the same scale of analysis. By allowing these new porosity and permeability values to be used, the breakthrough curves were closer in the time region to that of the experimental smoothed lines. As a result, mechanical dispersion and sorption were the only two unknown variables within the calculations.

6.3.4.1 Results

Key results are presented in the following section. For full results, please refer to the Appendix IV for details. Modelled curves were compared to the smoothed line (represented by a green line on Figure 90 - Figure 99,) calculated for each of the tracers over the different pressure ranges as shown in Chapter 5. A singular modelled curve was unable to match the experimental results for all the pressures using a singular dispersivity value. To successfully model the breakthrough curves using the analytical solution, a two-part flow model system was proposed. Although it is possible to continue to propose further division, a two-pathway flow model was sufficient and the least complicated approach. Previous studies of sub-core scale permeability distributions has identified heterogeneity within core samples with similar properties to the Fell sandstone (Krause *et al.*, 2013).

The term 'pathway' was chosen to describe the allocation of the different transport values. However, these two pathways are not independent of one another. Rather the term pathway refers to the regions of the matrix that is accessed depending on the pressure gradient applied. Using the statistically derived permeability value of 1.01×10^{-12} m^2 ($\pm$ 2.91×10^{-14} m^2), the two pathways were designated as 'fast' and 'slow' so that they are the end members of the permeability range using the deviations values. Where the pathway contribution is considered as trace amounts, this may be envisaged as ≤ 1. It has been recorded as 0 due to rounding of the pathway ratios.

Noble gases and SF_6

Using the one dimensional advective dispersion equation, it was possible to analytically develop breakthrough curves to match the experimental data. The results from these models are in the Appendix IV. Argon will be presented as the example of the quality of the curves produced when the solute is passing through CO_2.

- Argon

Figure 90 to Figure 94 shows the analytical results for argon over the sampled pressure ranges compared to the experimentally derived smoothed line C/C_{max} (green). Each pathway has the same porosity (17.85%) but is allocated a different permeability and dispersivity value. Pathways one ('fast') and two ('slow') are end members of the permeability range and are

represented respectively as the blue (1.04 x 10^{-12} m^2) and red (9.77 x 10^{-13} m^2) lines. From the results, it is clear that one pathway with a fixed dispersivity value is not enough to account for the breakthrough curves produced at the different pressure gradients. Dispersivity values were selected to fit the curves to the data for 50,000 and 10,000 Pa. A weighted system has been allocated for pressure gradient values for 40,000, 30,000 and 20,000 Pa using the end member dispersivity values. The dispersivity values are different for each pathway and for each tracer. However, the weighting at each pressure remained the same for all tracers (Table 31). The purple line is a conceptual model with a specific weighting of the two pathways. Although the sorption of SF_6 is possible, the addition of R_f made no difference to the improvement of the fit of the curve and so this was not accounted for in the curve fitting for it.

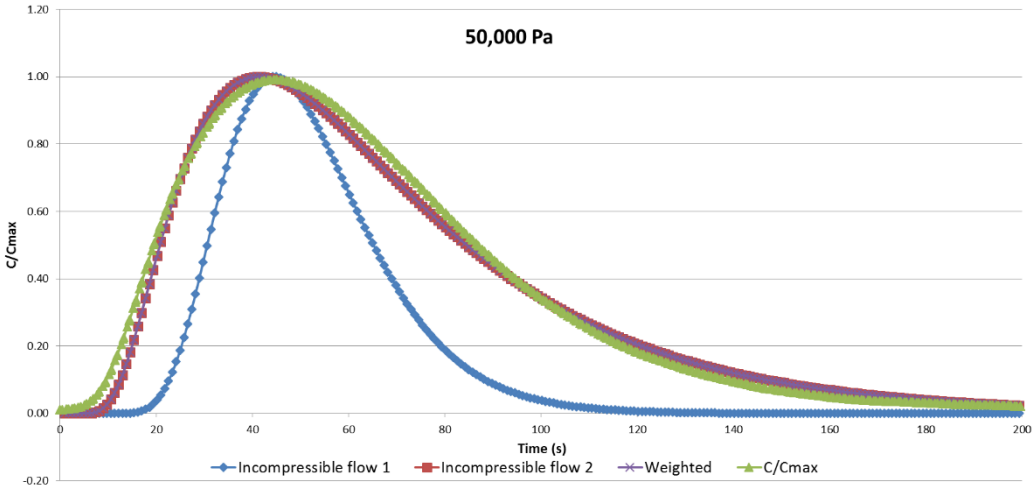

*Figure 90: Analytical modelling results for argon at **50,000 Pa**. Pathways one and two are represented as the blue (1.04 x 10^{-12} m^2) and red (9.77 x 10^{-13} m^2) lines. The purple line is a specific weighting of the two pathways - **0:100**.*

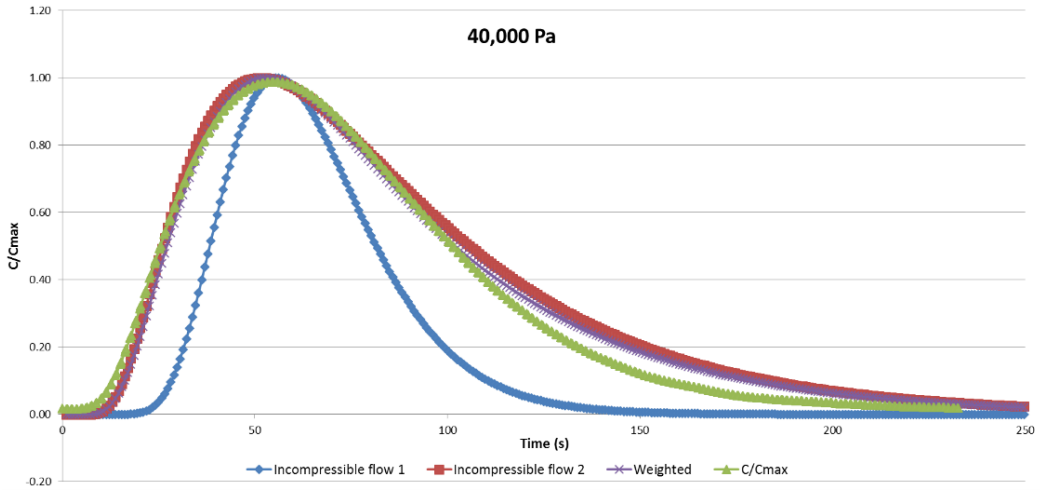

*Figure 91: Analytical modelling results for argon at **40,000 Pa**. Pathways one and two are represented as the blue (1.04 x 10^{-12} m^2) and red (9.77 x 10^{-13} m^2) lines. The purple line is a specific weighting of the two pathways - **10:90**.*

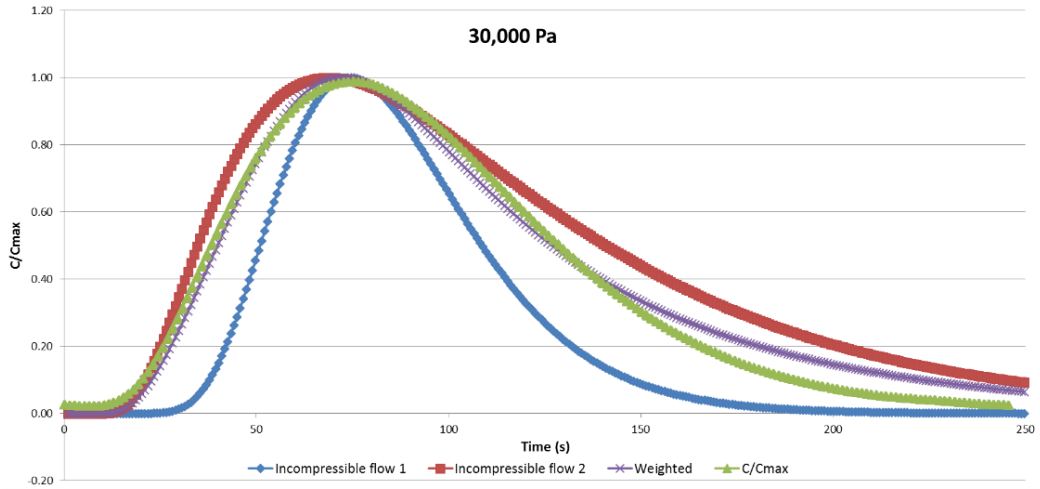

*Figure 92: Analytical modelling results for argon at **30,000 Pa**. Pathways one and two are represented as the blue (1.04 x 10^{-12} m^2) and red (9.77 x 10^{-13} m^2) lines. The purple line is a specific weighting of the two pathways - **30:70**.*

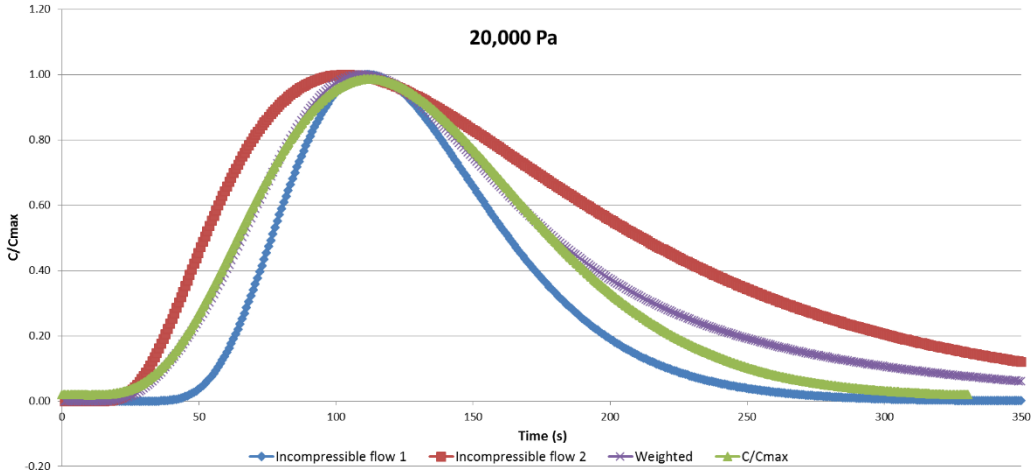

*Figure 93: Analytical modelling results for argon at **20,000 Pa**. Pathways one and two are represented as the blue (1.04 x 10^{-12} m^2) and red (9.77 x 10^{-13} m^2) lines. The purple line is a specific weighting of the two pathways - **50:50**.*

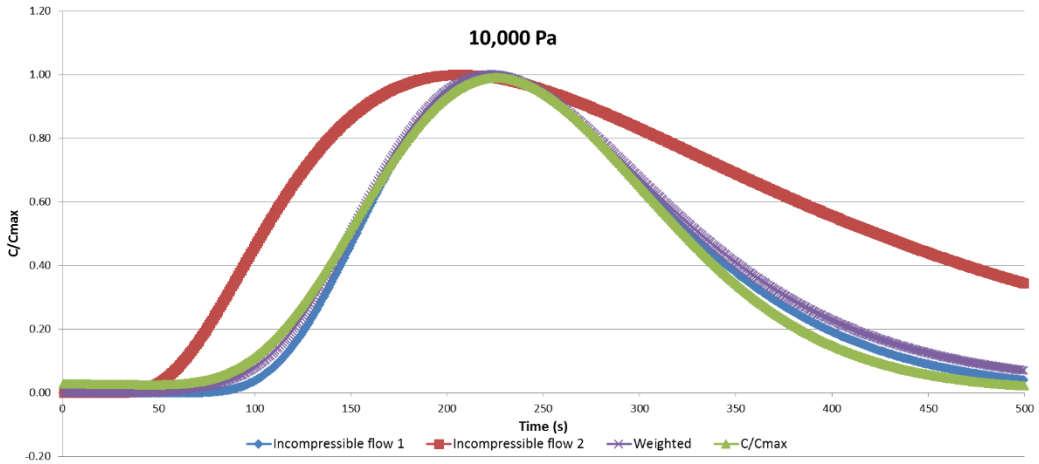

*Figure 94: Analytical modelling results for argon at **10,000 Pa**. Pathways one and two are represented as the blue (1.04 x 10^{-12} m^2) and red (9.77 x 10^{-13} m^2) lines. The purple line is a specific weighting of the two pathways - **90:10**.*

Table 31: Summary of weighting of the two pathways depending on the pressure gradient

Weighting	Pressure (Pa)
0:100	50,000
10:90	40,000
30:70	30,000
50:50	20,000
90:10	10,000

CO_2

The plotting of the CO_2/N_2 experiments using the analytical solution required further inputs to account for the breakthrough curve shapes. The addition of sorption using a K_d value of 0.08 (ml g^{-1}) has been accounted for in flow path calculations. Due to the higher than background concentrations at the commencement of the experiment, it was not possible to fit the curves as closely as those in the noble gases and SF_6 were. As with the noble gas and SF_6 experiments, the two pathways were designated as 'fast' and 'slow' using the end values of the permeability range and are compared to the experimentally derived smoothed line C/C_{max} (green).. Figure 95 to Figure 99 shows the analytical results for CO_2.

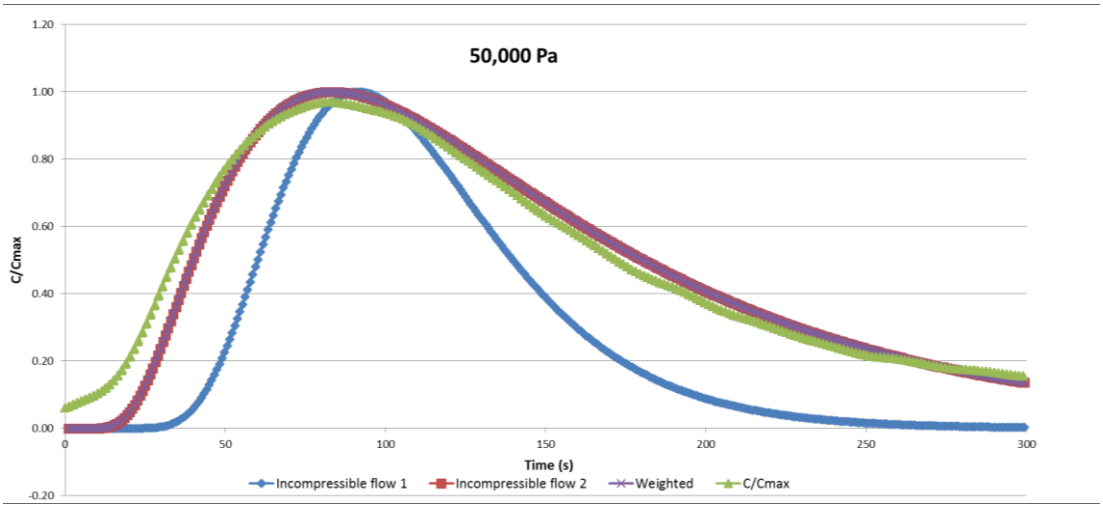

*Figure 95: Analytical modelling results for CO_2 at **50,000 Pa**. Pathways one and two are represented as the blue (1.04 x 10^{-12} m^2) and red (9.77 x 10^{-13} m^2) lines. The purple line is a specific weighting of the two pathways - **0:100**.*

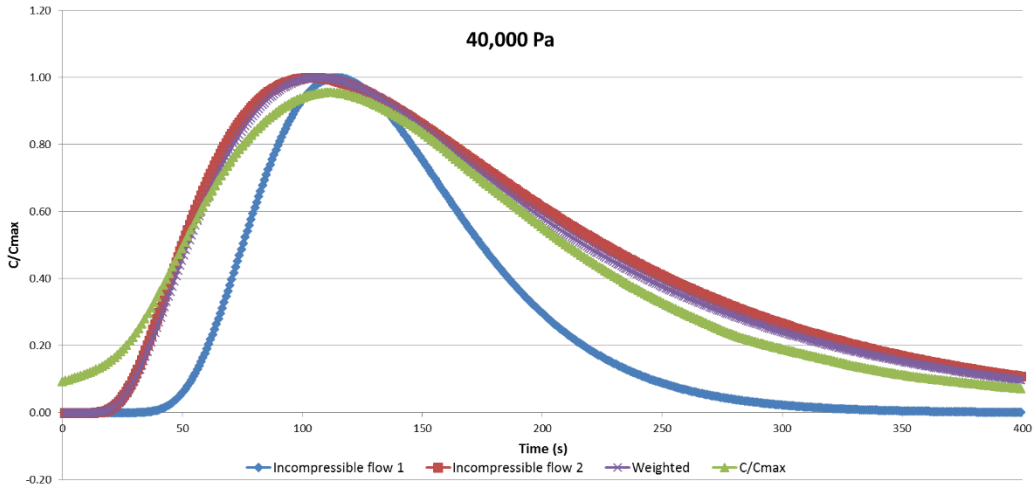

*Figure 96: Analytical modelling results for CO_2 at **40,000 Pa**. Pathways one and two are represented as the blue (1.04 x 10^{-12} m^2) and red (9.77 x 10^{-13} m^2) lines. The purple line is a specific weighting of the two pathways - **10:90**.*

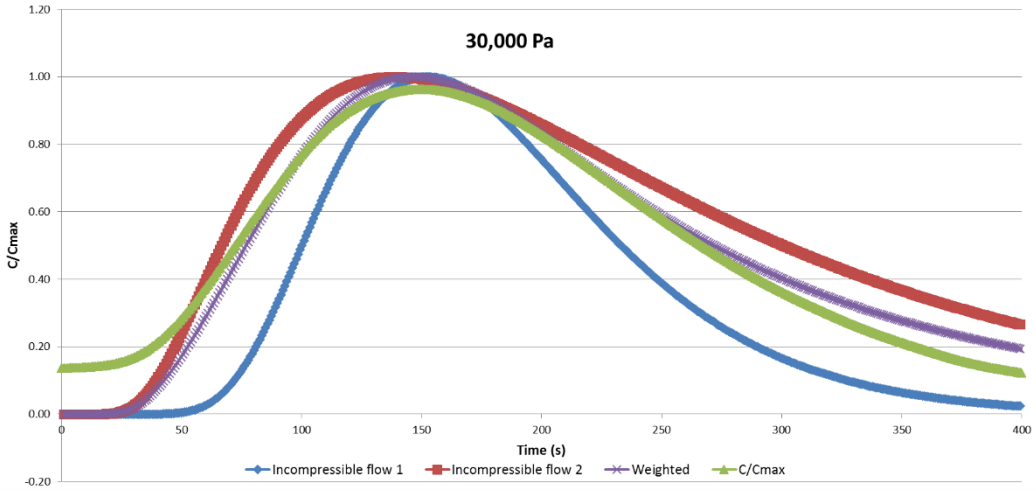

*Figure 97: Analytical modelling results for CO_2 at **30,000 Pa**. Pathways one and two are represented as the blue (1.04 x 10^{-12} m^2) and red (9.77 x 10^{-13} m^2) lines. The purple line is a specific weighting of the two pathways - **30:70**.*

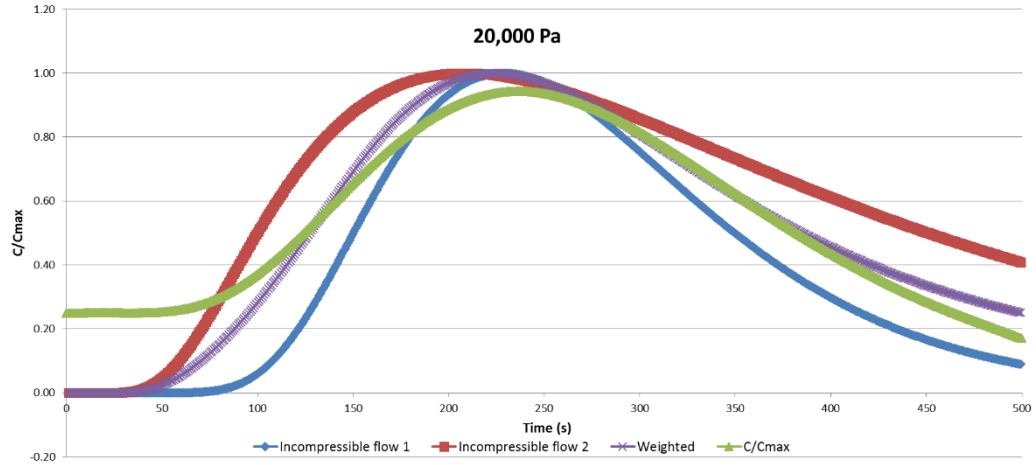

*Figure 98: Analytical modelling results for CO_2 at **20,000 Pa**. Pathways one and two are represented as the blue (1.04 x 10^{-12} m^2) and red (9.77 x 10^{-13} m^2) lines. The purple line is a specific weighting of the two pathways - **50:50**.*

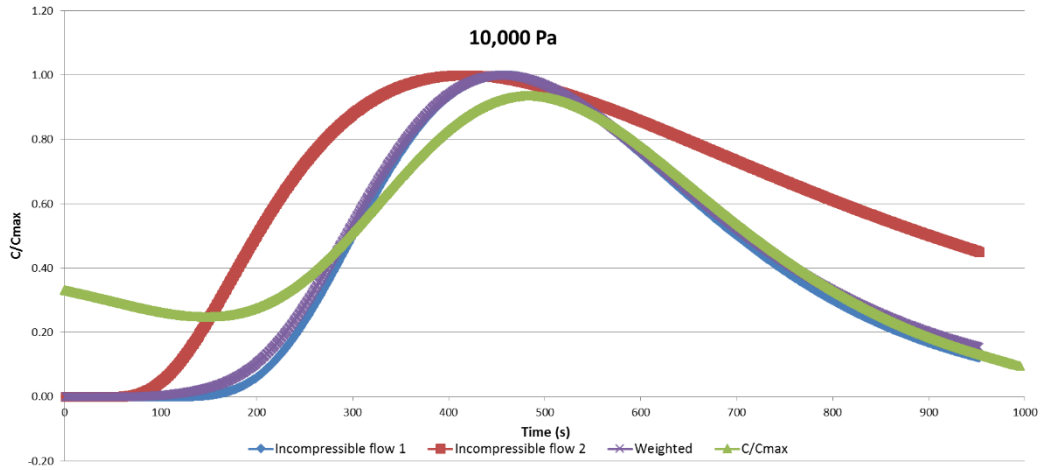

*Figure 99: Analytical modelling results for CO_2 at **10,000 Pa**. Pathways one and two are represented as the blue (1.04 x 10^{-12} m^2) and red (9.77 x 10^{-13} m^2) lines. The purple line is a specific weighting of the two pathways - **90:10**.*

These results show that the CO_2/N_2 experiments have a similar requirement to the noble gases and SF_6 values; one pathway with a fixed dispersivity value is not enough to account for the breakthrough curves produced at the different pressure gradients. A weighted system has been allocated in the same manner as shown in the argon results (Table 31).

6.3.4.2 Discussion

Overall curve fitting of an analytical solution to the smoothed lines has produced high R^2 values (how successful the fit is in explaining the variation of the data) for all the gases (Table 32 and Table 33). With the exception of helium, all the noble gases had values greater than 0.950; SF_6 also fell within this range. Although helium was harder to fit a modelled curve to, the results were still of significance. The CO_2 results were less reliable, with a decrease in fit, as the pressure gradient was smaller. This is most likely to due to the pre-peak concentration values as the model started off with no solute in the system and treating it as a single pulse; due to sorption effects, this was not the case. The improvement in most of the tracer gases is due to the multiple pathway model approach.

Table 32: R^2 values derived for analytical models.

(Pa)	Helium	Neon	Argon	Krypton	Xenon	SF_6	CO_2
50,000	0.916	0.954	0.991	0.976	0.981	0.974	0.964
40,000	0.918	0.960	0.988	0.980	0.982	0.988	0.974
30,000	0.888	0.967	0.983	0.982	0.975	0.985	0.957
20,000	0.921	0.959	0.979	0.984	0.980	0.984	0.846
10,000	0.897	0.986	0.984	0.984	0.948	0.970	0.639

Table 33: Difference in R^2 values derived for analytical model approach compared to statistical model. Brackets represents where the statistical model gave a better fit than the analytical model approach.

(Pa)	Helium	Neon	Argon	Krypton	Xenon	SF_6	CO_2
50,000	0.121	0.044	0.006	(0.009)	(0.016)	(0.024)	-
40,000	0.165	0.032	0.006	(0.018)	(0.016)	0.002	-
30,000	0.066	0.072	0.000	(0.009)	(0.020)	(0.013)	-
20,000	0.243	(0.014)	(0.012)	0.022	(0.018)	(0.012)	-
10,000	0.022	0.072	(0.007)	(0.011)	(0.047)	0.021	-

As the advective velocity was determined from the statistical model, this limited the number of variables to the dispersivity values and the weighting of the two pathways. To determine the values of the dispersivity, a value was selected that fulfilled the 50,000 Pa curve and a value was selected for the 10,000 Pa curve. As dispersivity is solute and matrix dependent, these values differ for each of the gases (Figure 100).

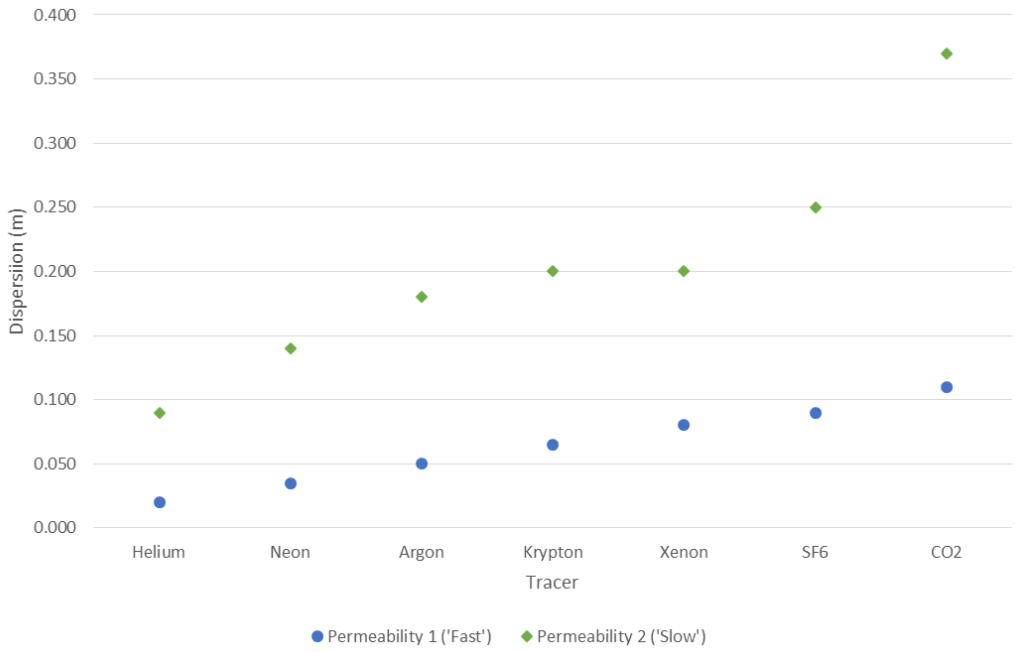

Figure 100: Dispersion values estimated for pathways with permeability 1 (1.04 x 10^{-12} m^2) and permeability 2 (9.77 x 10^{-13} m^2).

As permeability is inversely proportional to the tortuosity of a system, the dispersivity value for pathway one was set to be lower than that of pathway two (Nolen-Hoeksema, 2014). The weighting of the two dispersivity values for all the gases were set the same for each of the pressure gradients (Figure 101). The weighting was set after the end member dispersivity values were identified for all the gases. Thus, the weighting of the two pathways are the same regardless of the solute that is acting as the tracer.

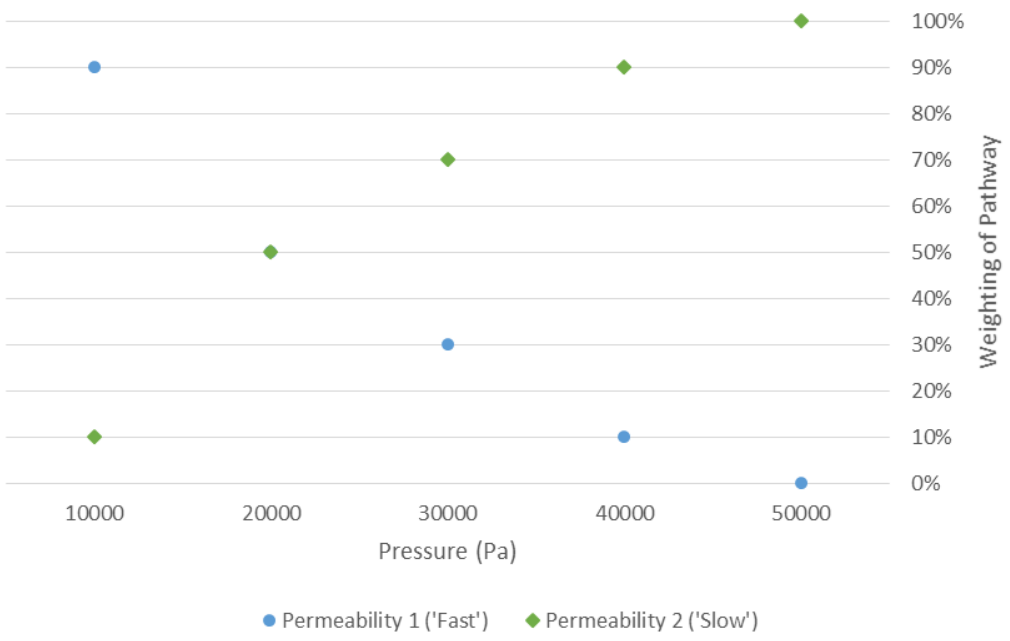

Figure 101: Weighting of the two permeability pathways depending on the pressure gradient.

Figure 102 shows the dispersivity as an average for the entire core for each of the tracers at each pressure using the weighting system. This shows a concave trend where there are lower dispersivity values for all of the tracers at lower pressure gradients. In addition, the trend for the dispersivity values increase moving down the periodic table for the noble gases; SF_6 and CO_2 show the largest dispersivity trends. This means that at high pressure, all the gases preferentially travel via pathway two, which has a higher dispersivity value, and a lower permeability – the tracer takes the longer, convoluted pathway. As the pressure gradient decreases, the gases preferentially travel via pathway one, with a lower dispersivity value but a higher permeability. This is a similar trend compared to the statistical model dispersion outputs. This will be discussed when comparing the modelling outputs of the two approaches in the following section.

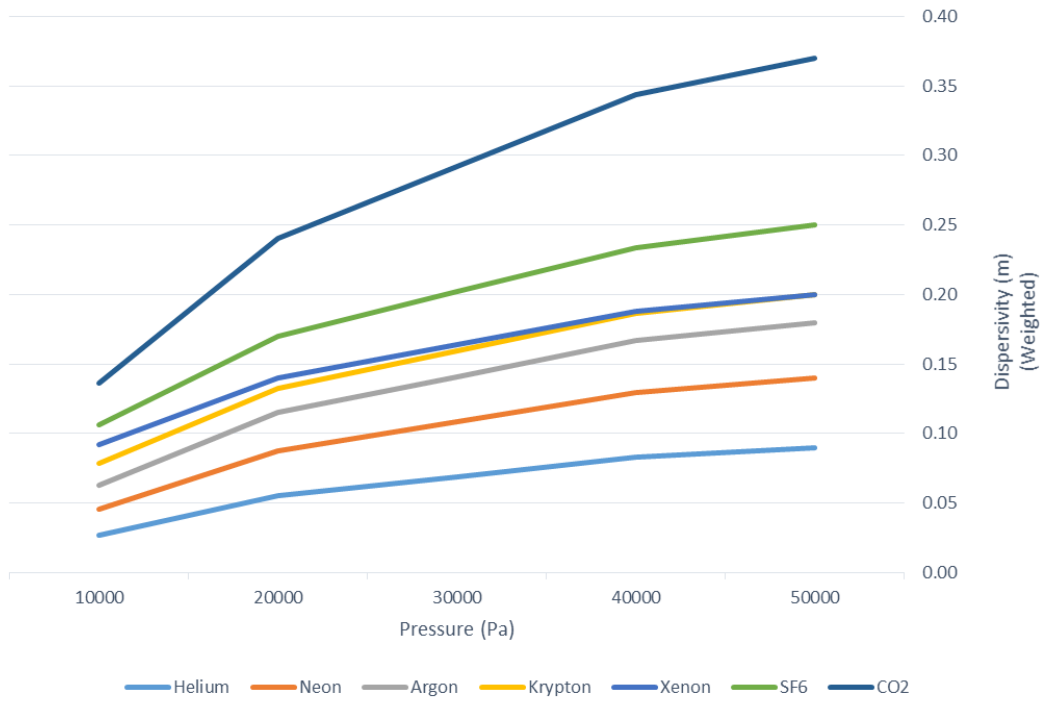

Figure 102: Average dispersion value for each tracer when weighted using values shown in Figure 101.

The dispersivity values obtained from the analytical model can be compared to the experimental observations made in Chapter 5. The analysis of the breakthrough curves for the tracers show that all of the tracers have the same advective velocity values over each of the sampling pressures. Therefore, the spreading of the curves is due to hydrodynamic dispersion and must differ for each tracer. With the noble gases, helium has the least amount of spreading over time and as the atomic radius gets larger towards xenon the amount of spreading increases (Figure 51). Since the calculated values for molecular diffusion are small (Table 24), mechanical dispersion must be the dominant factor in curve shape. This suggests that there is a higher level of dispersion with an increase in size and this is confirmed from the modelling results (Figure 100) (Warr *et al.*, 2015). SF_6 is not monatomic like the noble gases and is octahedral in shape. The size of the tracer is similar to that of xenon, which would explain the similar timings for C/C_{max}. However, the dispersivity values allocated for SF_6 and CO_2 are higher than that of the noble gases, which could be the result of the complex molecular shapes in their stable electronic configuration. Other studies have observed this behaviour where noble gases travel patterns have been studied (Torgerson *et al.,* 2004, Wacker *et al.,* 1985). On an angstrom scale, noble gases have physical properties that are strong functions of atomic mass and radii, which may impede heavy noble gases such as Xe (Torgerson *et al.,* 2004). The

heavier noble gases must migrate by 'random walk' to enter and leave constricted pores (/pore throats) (Wacker *et al.,* 1985).

6.3.5 Comparison of outputs from two modelling approaches

This chapter has presented the results of a statistical model and an analytical model to fit curves to experimental data using a one dimensional advection dispersion equation. For each of the modelling approaches, the goodness of fit and the outputs have been discussed. The following section compares and contrasts the outputs for both of these models to one another and identifies the strengths and weaknesses of the difference approaches.

Overall, both the modelling approaches have been extremely successful at curve fitting the experimental data. The goodness-of-fit using the analytical model is higher for helium, neon an argon but there is a slightly better fit for krypton, xenon and SF_6 with the statistical model. Both models are difficult to use to fit the CO_2 results; this is most likely due to the high concentrations of CO_2 already present prior to the commencement of the experiment. The one dimensional transport equation is designed for a pulse release of a tracer and so would not account for already existing values. Due to the complexity of each CO_2 replicate, the statistical model was used to determine each of the experiments individually which still provided similar outputs to the noble gases for a linear advective velocity trend.

Using the statistical model, the advective velocity is calculated as a direct output from the coefficients (Figure 87). A clear trend has been identified that highlights the increase in advective velocity, as there is an increase in pressure gradient. This follows the fundamental mechanisms involved in Darcy's Law such that the flow of a fluid through a porous medium is directly related to the pressure gradient. This bulk motion for all of the fluids modelled using the statistical method displays a linear trend negative slope towards the intercept; this uniform trend suggests that the experimental setup has ensured that all the gas is travelling through the core, rather than along any unintentional routes, such as between the core and the resin. If it was travelling outside the intended area, it is likely that the advective velocity would presents as a convex shape. In addition, the calculated volumetric flow rates through the core are comparative to the statistical advective velocity when under the same pressure gradient. This

can be further examined by comparing the permeability outputs from that of the statistical model to the predicted advective velocity from laboratory readings.

The permeability from the statistical model is derived from the advective velocity outputs by rearranging Darcy's law for incompressible one dimensional flow. The average of permeability output from the tracers (except for neon and accounting for sorption in CO_2) provided a range of 1.01×10^{-12} m^2 ± 2.91×10^{-14} m^2 (Figure 88). This value provided a component for the analytical model, which was a prior unknown limitation. Prior to this, the original experimental value of 2.18×10^{-13} m^2 was used from plug tests carried out by Heriot Watt. It was clear from using this value along with the porosity of 20.3% from the same plug, that the model curve inputs would not provide the same value range as that from experimental work. The permeability value output from the statistical model provided a more reasonable and limited range to use; prior to this there was too many variables to apply to the analytical model without introducing bias. In addition, the permeability value range from the statistical model was similar to the experimental conditions (9.31×10^{-13} - 1.16×10^{-12} m^2) (Table 15).

Using the standard deviation from the mean as the end members of the average permeability range, the two pathways that were proposed can be addressed via the analytical method. Following the trend that permeability is inversely proportional to the tortuosity of a system, the two pathways could then be identified as a 'slow'/lower permeability route with a high dispersivity value, and a 'fast'/higher permeability route with a low dispersivity value. This means the system has a 9.77×10^{-13} m^2 to 1.04×10^{-12} m^2 range.

Using the values estimated from the OM images, SEM images and the calculated porosity test, an average porosity for the system of 17.85% was used. This porosity value was fixed in the statistical model and so the same value was used in the analytical model. Pathway one and pathway two had the same porosity value. By using the permeability outputs of the statistical model and constraining the porosity values within the region of the actual core values, it is possible to only alter the dispersivity value within the analytical model.

When comparing the two modelling methods using the same one dimensional transport equation, there is a strong agreement for the advective velocity profile (and thus the intrinsic permeability), compared to the experimental results. The statistical model confirmed the advective velocity inputs needed to constrain the number of variables present within the analytical model. Within a more appropriate range for permeability and porosity chosen, the remaining transport mechanism to be assessed by the model is the hydrodynamic dispersion coefficient. As the porosity, molecular diffusivity and advective velocity are known, the final factor is the dispersivity. The dispersivity will then act as a 'fudge factor' when fitting a model to any of the experimental data. The dispersivity values from the statistical model attempted to fit the shape of the curve to the data irrespective of the basic laws of transport.

Dispersivity is solute and matrix dependent; it is also scale dependent. Thus, as the input values show, the outputs changed over pressure. Helium showed the lowest dispersivity values and there was a general trend of increase in dispersion moving down the periodic table (again neon shows unusual results reflected in goodness-of-fit). As with the statistical model, one dispersivity value did not satisfy all the pressure ranges using the analytical modelling approach. However, it is possible with the analytical model, to apply more than one dispersivity to each of the tracers and allow a weighting system. Each tracer was allocated two dispersivity values, using the two permeability pathways as a means of applying them (Figure 100 and Figure 101). Although the dispersivity values were different for every tracer, the weighting for each of the pressure gradients remained the same. When comparing the two modelling outputs for the dispersivity, the values chosen for the analytical model are well within the expected range for such a system; with the weighting system in place, these values fit the modelling data and are similar to the statistically derived values (Figure 103). When applying the weighting system and assessing the 'average' dispersivity trend of the gases over the pressures, disregarding the scale, the shape of the trend is concave.

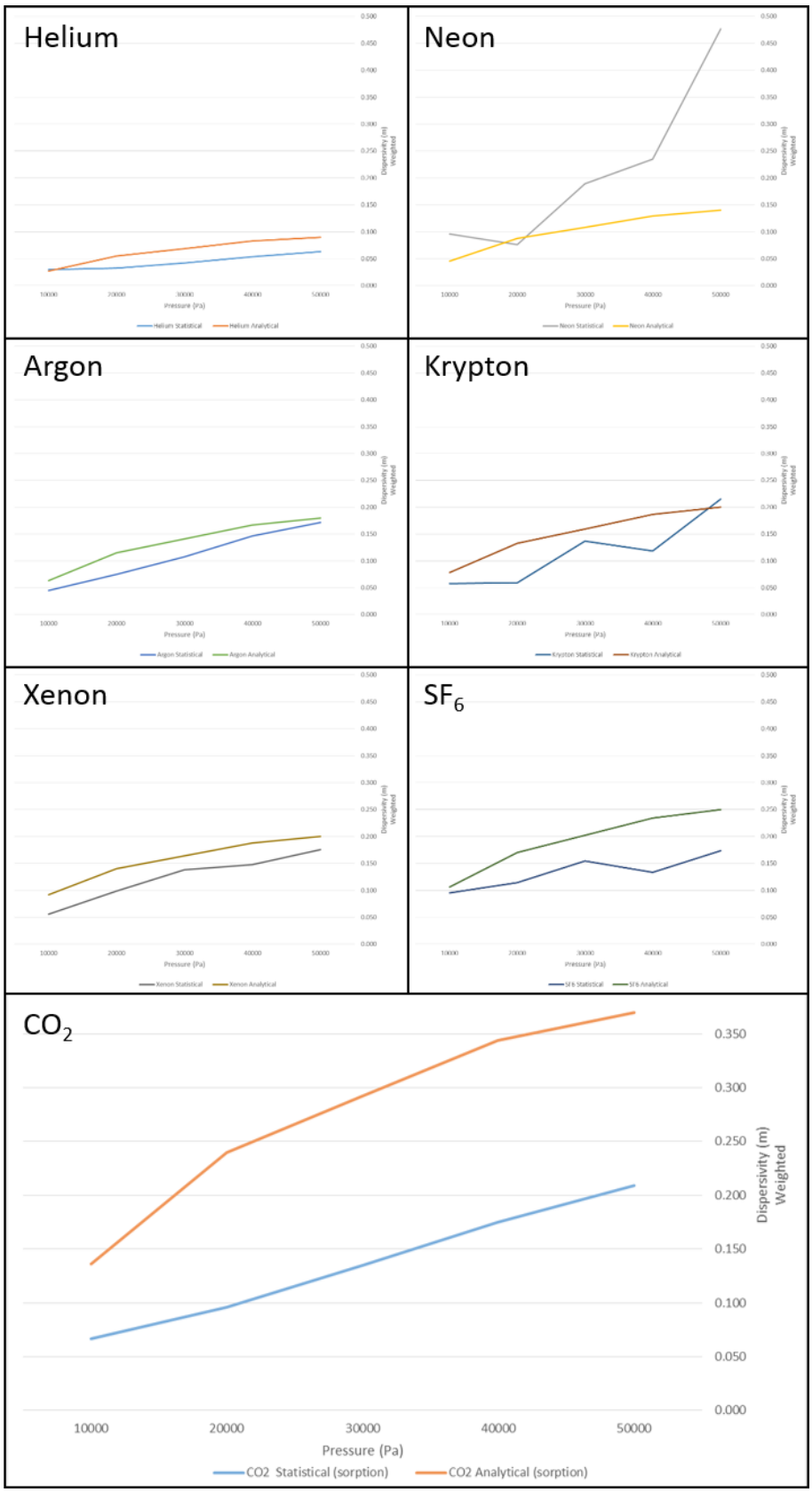

Figure 103: Comparision of dispersivity values obtained from two modelling approaches.

Noble gases are conservative tracers but it was necessary to account for retardation effects from the CO_2. It is evident from the CO_2 curves that there were some residual traces of CO_2 left despite the purging regime (Figure 58). In addition, the levels of background CO_2 become more evident at the lower pressures. Due to this, both of the models struggled to fit the pre-peak concentration profile. To determine the sorption value, the analytical model was formulated with the new porosity values and the (noble gas) permeability range determined from the statistical modelling approach. Once a K_d value had been selected, this was applied to the results for CO_2 in the statistical method; the advective velocity and permeability values were evaluated and remained within the average values of the other tracers.

6.3.6 Summary

From this discussion, it is clear that the statistical and analytical modelling approaches were both necessary to constrain the values of the transport mechanism involved. Neither would have been sufficient on its own. The analytical model provided the initial investigation into how applicable the experimentally obtained porosity and permeability would be and that one dispersivity value would not suffice; however it was limited by the number of variables that could be altered and prone to unintentional bias. The statistical model, allowed the identification of a permeability range with the correction of a new porosity value. However, it was limited by single dispersivity values as it tried to fit the breakthrough curves of the experimental data. With the amended permeability and porosity values, the analytical approach could provide realistic values for dispersivity and introduce a pathway weighting system within the core, explaining why the statistical model showed a change in dispersivity with pressure.

6.4 Discussion of the transport mechanisms involved in fluid flow in the Fell sandstone

Based on the modelling curves fitted to the experimental breakthrough data, a two pathway flow regime is the proposed explanation for the observed trends in the sandstone core. These two pathways or routes are through the sandstone core, but appear to deviate from a fixed pathway depending on the pressure gradient applied. Using the experimental breakthrough profiles and the output from both the statistical and analytical models, this information will now be used to discuss the flow mechanisms involved in the sandstone cell. Prior to doing so, a summary of these two pathways will be outlined.

6.4.1 Pathway one

Pathway one is described as the 'fast pathway'. It has a higher permeability value of 1.04 x 10^{-12} m^2 with a porosity of 17.85%. However, the dispersivity value for the pathway is always lower than that of the second proposed pathway (Figure 100). Pathway one is the dominant pathway used when the pressure gradient is low. There is a slight convex trend for the contribution of the pathway as the pressure increases (Figure 101).

6.4.2 Pathway two

Pathway two is described as the 'slow pathway'. It has a lower permeability value of 9.77 x 10^{-13} m^2 with a porosity of 17.85%. The dispersivity value of this pathway is higher and is the dominant pathway for the higher pressure gradient. The contribution of the pathway shows a slight concave trend for the contribution of the pathway as the pressure decreases. This is expected as it is the reverse trend to that of pathway one.

6.4.3 Fluid flow in the Fell sandstone

6.4.3.1 Darcy Flow – linear laminar flow

Darcy's law describes the flow of fluid through a porous medium. It is the proportional relationship between flow rate, viscosity and changes in pressure over a given distance. Linear flow paths are assumed in Darcy's Law – a flow regime characterised by parallel flow lines within a system. Linear flow is plotted as a positive ½ slope when time is calculated against pressure (log-log). With Darcy's flow it is assumed that the flow is inertialess. Thus, Darcy

flow is described as linear, where it accounts for creeping flow and viscous forces prevail over inertial forces.

The Reynolds number (*Re*) can be used to predict similar flow patterns in different flow scenarios. The dimensionless number can be described as the ratio of inertial forces to viscous forces and be presented as:

$$Re = \frac{g_f v_f L}{\mu} \quad (52)$$

Re = Reynolds number (dimensionless)

g_f = density of the fluid (kg m^3)

v_f = velocity of the fluid (m s^{-1})

L = characteristic length (m)

μ = dynamic viscosity of the fluid (Pa s^{-1})

Using Reynolds numbers, a departure from Darcy regime occurs at order unity ($Re >> 1$) (Dukhan *et al.*, 2014, Kolditz, 2001). The order of critical Reynolds numbers, when non-linear effects become evident is 1-10 based on previously conducted experiments (Barenblatt *et al.*, 1990). According to Scheidegger (1963), there appear to be two critical Reynolds numbers at which the flow regime changes. The first indicates when the flow conditions are affected by inertia effects and then when true turbulence flow sets in (Dullien, 2012).

6.4.3.2 Forchheimer - non-linear laminar flow

Before a flow becomes turbulent, non-linear laminar effects occur and flow deviates from a Darcy regime (Kolditz, 2001). Non-linear laminar flow becomes the dominant method of flow as inertial effects become important. Causes of non-linear effects can be high advective velocity, molecular/ionic effects, non-Newtonian behaviour of the fluid itself as well as pore geometry (Kolditz, 2001, Dullien, 2012, Scheidegger, 1963). Forchheimer' Law includes the

inertial effect as a function of the kinetic energy in the relationship between the pressure gradient and the flow velocity such that:

$$-\frac{dP}{dx} = \frac{\mu}{k}\, v + \beta \rho v^2 \qquad (53)$$

k = intrinsic permeability (m^2)

μ = dynamic viscosity of the fluid (Pa s^{-1})

v = velocity of the fluid (m s^{-1})

ρ = fluid density (kg m^3)

β = turbulence factor (Forchheimer coefficient) (m^{-1})

As flow velocity increase, the kinetic energy term becomes more important and the linear relationship breaks down. The determination of the Forchheimer coefficient tends to be calculated using the best-fit information from experimental data. The Forchheimer coefficient is strongly dependent on the internal structure of the porous medium (Dukhan *et al.*, 2014). Previous work has shown that for the same porous medium, different values of permeability exist in different flow regimes (Dukhan *et al.*, 2014).

Kolditz (1997, 2001) based on the Forchheimer equation, represents this breakdown of linear behaviour as:

$$q = K|\Delta i|^{(\alpha-1)} = K_0 K_{rel} \qquad (54)$$

q = specific discharge (m s^{-1})

K = hydraulic conductivity (m s^{-1})

i = hydraulic head/gradient

α = non-linear flow parameter

> 1 pre-linear

= 1 linear (Darcy Law)

< 1 post-linear (= 1/2 turbulent friction)

This equation highlights that the hydraulic resistance increases for smaller pressure gradients in pre-linear situations as well as for larger pressure gradients in post-linear situations.

6.4.3.3 Turbulent regimes

Turbulent flow is the case after non-linear laminar flow, when the flow pattern becomes transient due to velocity fluctuations. At this point, turbulent flow fully develops. The pressure and the inertial forces dominate the flow. In porous media, the transition from laminar flow to turbulent flow is gradual (Dullien, 2012). Turbulence can be triggered by non-uniformity of pore size distribution and internal surface roughness (Dukhan *et al.*, 2014). The pressure drop for turbulent flow in porous media is a power 2 term in velocity (Skjetne and Auriault, 1999).

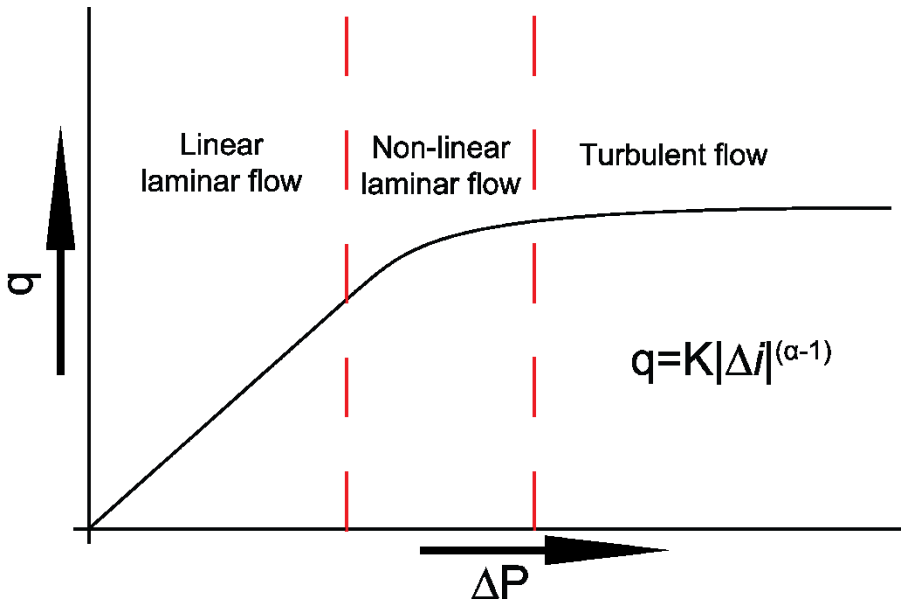

Figure 104: Not-to-scale illustration representing the different flow regimes found as a relationship between pressure (ΔP) and flow rate (q), using the non-linear flow parameter.

6.4.3.4 Discussion of results

As previously summarised, using the artificially constructed Fell sandstone system, two pathways were identified. Pathway one, is a higher permeability flow system with a low dispersivity value; a route which is dominant during low pressure gradients. Pathway two is a lower permeability system with a high dispersivity value, a route that is dominant during high pressure gradients. This trend of pathway use is the same for all the tracers. Figure 105 shows the average permeability range and pressure gradient values for each of the experimental advective velocities. During Darcy linear laminar flow, the plot of pressure to specific discharge should produce a ½ slope trend. Figure 105 suggests that a 3rd order polynomial regression fit ($R^2 = 0.997$) is slightly better than a linear fit ($R^2 = 0.993$). Similarly, in a Darcy regime the permeability should be constant, while in the Forchheimer regime, it should decrease with increasing velocity. Figure 105 shows a very slight decrease in average permeability with an increase in velocity but an increase in the standard error associated with the lower permeability values. It would be difficult to identify this as evidence for a Forchheimer regime for the overall core.

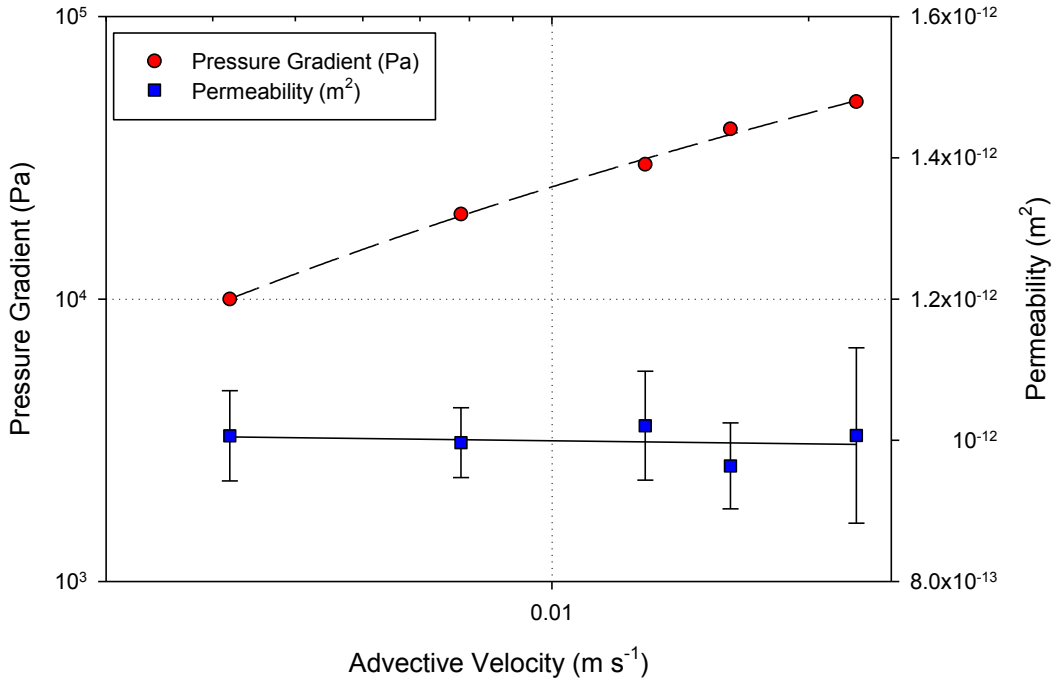

Figure 105: Plot of advective velocity and pressure gradient as a log-log relationship. Plot of advective velocity and permeability as a log-linear relationship.

Thus, these results suggest that a Darcy flow regime should be observed. However, the pathways used suggest this is not the case. It is necessary to look at closer at the pathway functions and contributions. Table 34 shows the estimated *Re* values for the Fell sandstone system. Values were calculated using the average advective velocity for the system over the sampling pressure gradients. The characteristic length scale for porous media is based on grain boundary diameters. *Re* numbers were calculated for two pore space diameters (450 and 150 μm). Pathway one was allocated the maximum detected pore diameter range of 450 μm due to the higher permeability value and lower dispersivity trend – permeability is directly related to pore space/grain size. Similarly, pathway two was allocated diameter value of 150 μm as this was calculated as the most dominant size for diameter. For comparative purposes, the weighting allocated to both pathways during modelling are included.

Table 34: Reynolds number for CO_2 transport through the Fell sandstone under experimental conditions. For comparative purposes, the weighting allocated to both pathways during modelling are included.

Pressure Gradient	(Pa)	Pathway One (%)	Pathway One (*Re*)	Pathway Two (%)	Pathway Two (*Re*)
High Pressure	50,000	≤1	1.92	100	0.64
	40,000	10	1.27	90	0.42
Medium Pressure	30,000	30	0.94	70	0.31
	20,000	50	0.52	50	0.17
Low Pressure	10,000	90	0.26	10	0.09

Any flow with a *Re* approaching 1 suggests a transition into non-linear laminar flow. Reynolds numbers for turbulent flow are much higher than anything that are produced during the experimental conditions. The results suggested in Table 34 are described in the subheadings below.

a) Low pressure (10,000 Pa)

At low sampling pressure gradients, the flow is primarily via pathway one (Table 31). The flow passes through the higher permeability portions of the system with greater ease and these are the areas of higher pore diameter. At the low sampling pressure gradient, the *Re* values suggest that the flow is following the Darcy regime and as such is pure linear laminar flow. At this pressure gradient level, there appears to be little or no contribution flow through the higher dispersivity routes (pathway two).

b) Medium pressure (20,000 - 30,000 Pa)

With an increase in pressure gradient, there is a distinct increase in *Re* numbers for pathway one and approaches the value of unity. The contribution from both pathways has become 50:50 at 20,000 Pa. Within the 30,000 Pa pressure gradient, the pathway one approaches non-linear laminar flow. Pathway two remains within the region of linear laminar flow. As such, the medium pressure gradient range is a transition of areas with linear and non-linear laminar flow.

c) High pressure (40,000 Pa to 50,000 Pa)

When the pressure gradient reaches 40,000 Pa, the contribution of flow is predominately through pathway two (Table 31). The lower permeability pathway two is providing 90% of the tracer route contribution through a more dispersive manner, reducing the contribution from the higher permeability regions. By 50,000 Pa, the contribution of the pathway one has drastically reduced and according to the *Re* is well into the non-linear laminar flow region. At this pressure, the linear flow is approaching unity but accounts for 90% of the flow.

As suggested in Dukhan *et al.* (2014) permeability within a Darcy regime is considered constant, while in the Forchheimer regime, it decreases with increasing velocity. This observation agrees with the modelling output descriptions when compared to the *Re* numbers of those areas. Thus, it appears that within this Fell sandstone core, the transition from linear to non-linear flow on the micro-scale (no turbulent regions), is the reason for identifying multiple pathways or routes that are taken by the tracer as the velocity increases. Figure 106 summarises the different areas of the flow cell, which are accessed depending on the advective velocity. These areas have been classified as pathway one and two but Figure 106 emphasises that these regions are not isolated.

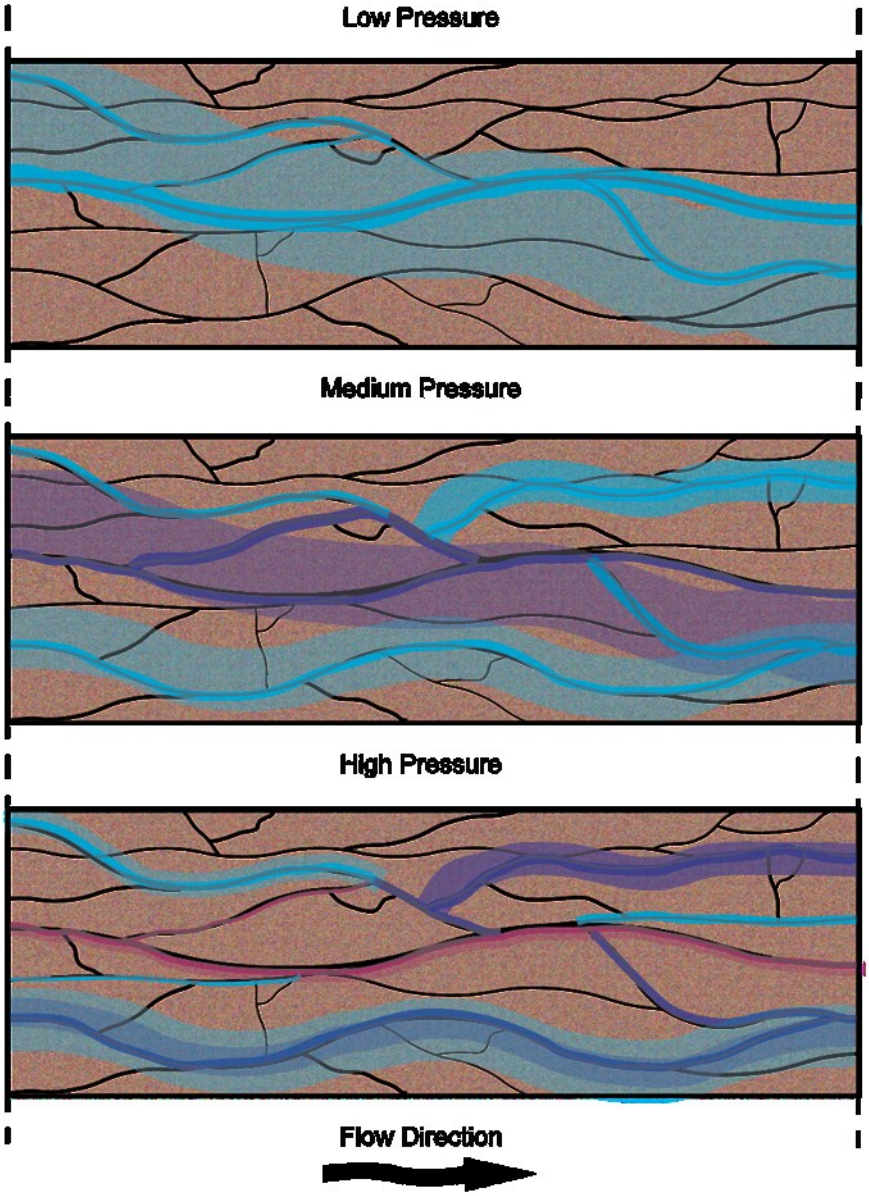

Figure 106: Schematic diagram illustrating the different areas of the flow cell accessed, as there is an increase in advective velocity. The blue areas represent linear laminar flow, the purple areas represent a transition to non-linear laminar flow and the red areas are non-linear laminar flow.

6.4.3.5 Summary

During the experiments, the core has experienced a pressure gradient range of 10,000 to 50,000 Pa. Although on a larger scale there appears to be no deviation from Darcy regime when the

micro-scale fluctuations were investigated, it is apparent that this statement is not entirely true. At low pressures, the system follows Darcy regime and tracers travel along a higher permeability route. With an increase in pressure, *Re* values suggest a partial migration from a linear regime and into a non-linear regime, as identified using the Forchheimer regime at the pore diameter scale. At this time, the tracer is prone to travelling along linear low permeability routes and non-linear high permeability routes. By 50,000 Pa, the high permeability routes are experiencing non-linear laminar flow but contribute significantly less to the overall route. The low permeability regimes with a higher dispersivity are the dominant route. These low permeability regimes are not fully within the non-linear regime but are vastly approaching it. This appears to suggest that an increase in *Re* number leads to a non-linear laminar flow, which is 'slower' to contribute than a true linear laminar flow to the Fell sandstone system.

Acknowledgments

The author wishes to acknowledge the contribution and support from Dr. Mark Naylor for the derivation of the statistical model used in this chapter. The author also wishes to acknowledge the contribution from Dr. Christopher McDermott for the development of the velocity profile for compressible fluid flow.

Chapter 7 - Discussion and synthesis of work

7.1 Discussion of experimental results in comparison to existing tracer research

Whilst the sampling of the experiments were carried out in low pressure and in an air-dried core sample, it is important that the results be compared to existing observations and trends from related research. There are few studies of noble gas tracers as the sole method of tracing migration. In most cases, the selection of tracers used include noble gases as well as SF_6 and isotopes. This section refers to and discusses these examples where artificially introduced noble gases and SF_6 are used as tracers for transport monitoring and how they relate to the experimental results from this research. It will also briefly approach any results of breakthrough curve trends produced during CO_2 transport.

7.1.1 Noble gases and SF_6 as tracers

The research of Carrigan *et al.* (1996) presented the transport of trace gases flow along faults and fractures, resulting from barometric pressure variations. These fractures may be considered preferential pathways during transport. The tracer gases used were helium and SF_6; from these results, SF_6 was quicker to arrive than the helium although the initial detection location was the same for both tracers (Figure 107). In a diffusively dominated transport environment, the helium should have arrived before the SF_6 based on atomic size. The paper suggests the speed of transport along the fractures is much greater than the diffusion rate driven by deeper 'low' barometric pressure variations. They also suggest that the high diffusion coefficient of helium compared to SF_6 actually impedes its transport along a fracture by allowing it to diffuse out of the main flow path more effectively than SF_6. This observation made by the paper is worth comparing to the results of this research, as helium is one of the slowest tracers to arrive during all pressure gradients; it is also the quickest to drop below detection levels post-peak concentration. This observation is in contrast to research by Cohen *et al.* (2013) where the helium peaked before the krypton pulse in a near-surface environment. However, the results did suggest that this was due to the higher molecular diffusion rate of helium, which has been discussed in this research as a reason why it completes the experiments faster. Additionally, the work confirms that CO_2 is delayed by the complexity and heterogeneity of the medium, including possible sorption effects (Cohen *et al.*, 2013).

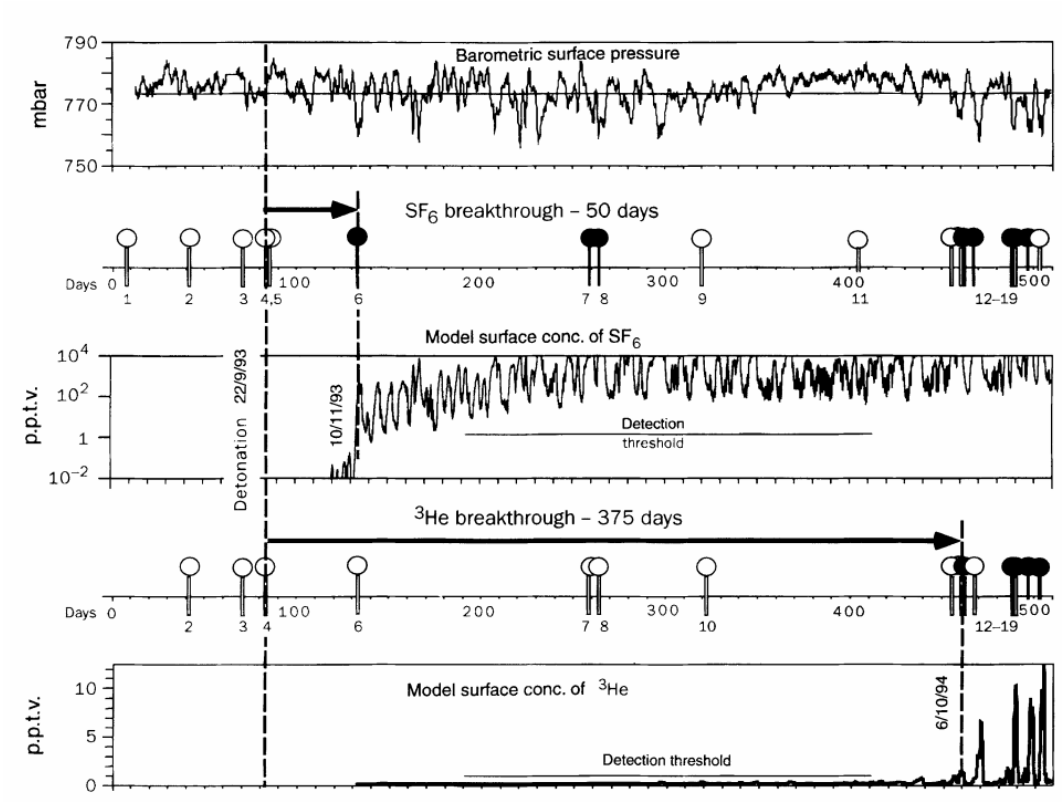

Figure 107: Summary of SF_6 and helium readings for trace gas emissions as indicators of underground nuclear testing (Carrigan et al., 1996).

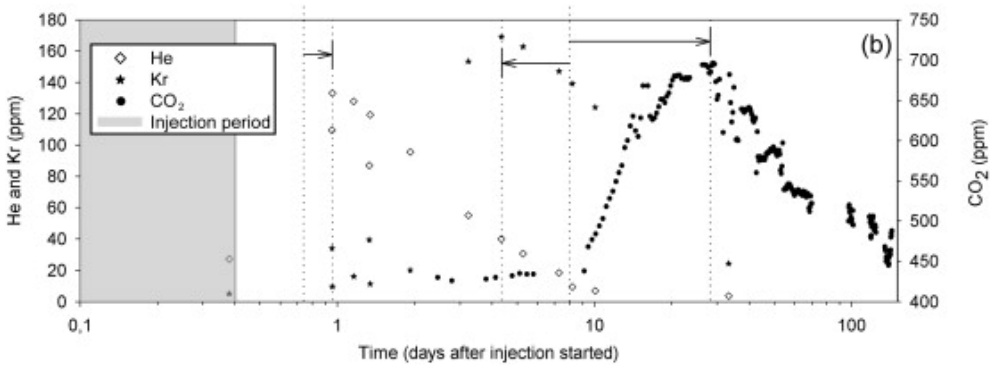

Figure 108: Experimental results from tracer gas releases (helium, krypton and CO_2) carried out by Cohen et al. (2013).

Little research could be identified where neon or argon have been directly injected into a reservoir as an artificial tracer. Although they have been used as natural tracers for subsurface CO_2 origin and migration (Wilkinson *et al.*, 2010) with isotopic ratios, to discern these tracers

from atmospheric or background signals would require large quantities of the tracer to be added (Stalker *et al.*, 2009). Carrigan and Sun (2014) suggest that ^{37}Ar (and ^{133}Xe) be used for detecting an underground nuclear testing location as they are not produced in high concentrations in the natural environment and they have relatively short half-lives. This might be something worth considering when using tracers to monitor initial CO_2 injection sites by sampling soils via mass spectrometry.

The choice of using krypton with SF_6 has proven to be popular for monitoring CO_2 pathways. Cranfield, Mississippi is home to a large-scale CO_2 injection and observation survey from a natural source (Jackson Dome), which has been used for data collection and monitoring (Hovorka *et al.*, 2013). Lu *et al.* (2012) carried out continual fluid sampling during the first month of injection in 2009 when injection began. SF_6 and krypton were the artificial tracers used (Figure 109). Their research highlights that flow evolves through time and injection rate by monitoring fluid from the observation wells. The paper highlights the importance of internal heterogeneity and the effects it would have on CO_2-flow behaviour.

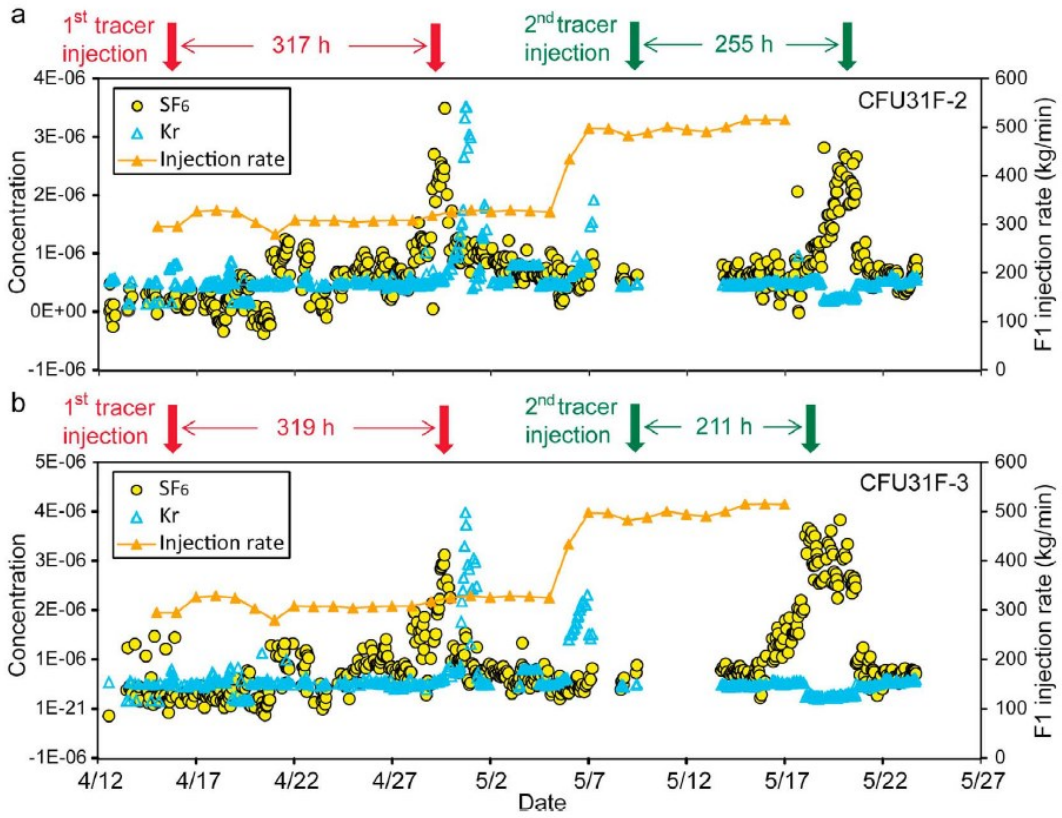

Figure 109: Data from Lu et al. (2012) during 2010. (a) Measured concentrations of SF_6 and krypton of first observation well (65 m east of injection well). (b) Measured concentrations of SF_6 and krypton of second observation well (112 m east of injection well). SF_6 was introduced twice, but krypton was only injected during the first injection period.

Some interesting results from these experiments are that for the first tracer injection, SF_6 arrived quicker than krypton to both observation wells. As expected, the tracers arrived at the closest well first. An increase in injection rate, led to a second pulse of krypton arriving but not SF_6 – perhaps the result of their physical or chemical properties. During the second injection of tracer (only SF_6), with an increase in fluid flow velocity, the SF_6 arrived at the more-distant observation well earlier than the closer one. These results highlight the possibility of separate flow pathways between wells and that travel time is not proportional to the distance between the wells; fluid velocity is different along different flow pathways. When the papers findings for krypton and SF_6 results are compared to the results from this project, there are some similarities. In terms of peak concentration times where C/C_{max} is 1, the krypton arrives later than the SF_6 at the sampling pressure gradients (10,000 to 50,000 Pa). Something that is more evident in the experimental results is that the krypton signal also ceases sooner than the

SF_6. Similar to the results from Cranfield, the flow velocities of the tracers depend non-linearly on the density/viscosity and that preferential flow paths can exist. Although in the case of Cranfield, they consider these paths as separate and distinct, most likely due to the larger scale of the system.

The Frio brine aquifer in Texas was part of pilot study based on two small volume CO_2 injections in 2004 and 2006. The work of Freifeld *et al.* (2005) carried out detailed sample monitoring with tracers, also with SF_6 and krypton (as well as perfluorocarbon (PFT)). Samples were collected downhole from an observation well (1.5 km deep) using a U-tube sampling system. Tracers were added to the CO_2 injection stream to indicate the formation CO_2 saturation and the different travel times between them (Figure 110). The results from these tracers show that SF_6 arrives faster than the krypton tracer as well as peaking sooner. This is similar and supporting of the results from this research and from the findings of the more recent Lu *et al.* (2012) study at Cranfield, Mississippi.

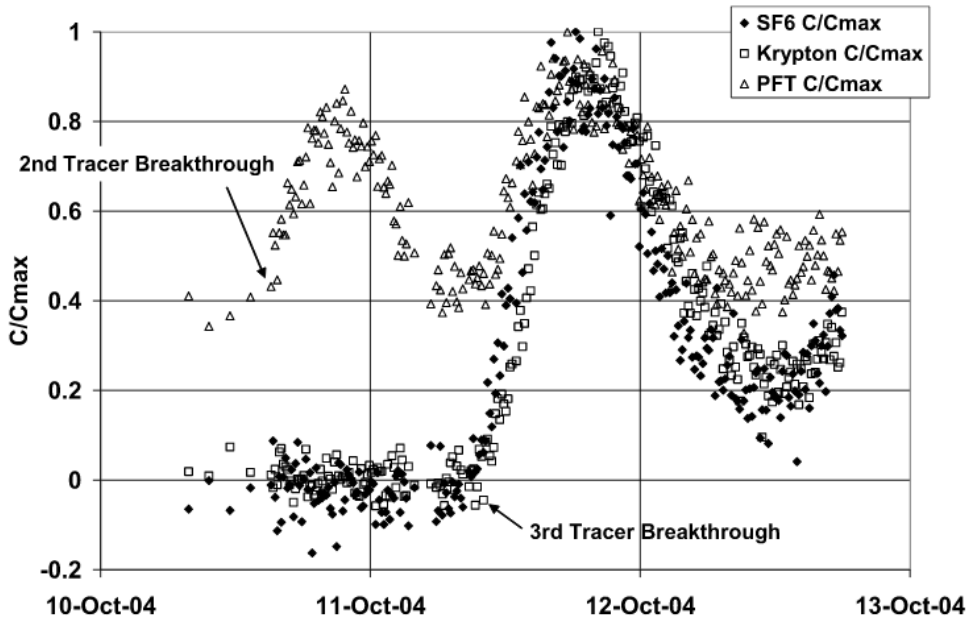

Figure 110: Tracer results from Freifeld et al. (2005). Tracers were injected over three batches. The results from SF_6 and krypton were the third batch to be injected (09/10/04).

Much work has been carried out in Victoria, Australia as part of the CO2RC Otway Project, a project that involved the injection of CO_2 into a depleted gas reservoir (Boreham *et al.*, 2011). Like the Cranfield and Frio aquifer research, ongoing monitoring projects have used krypton and SF_6 as tracers, as well as perdeuterated CH_4 (CD_4) (Boreham *et al.*, 2011, Stalker *et al.*, 2015). Figure 111 shows the results from some of the tracer experiments. The results are recovered from the similar method as that in Boreham *et al.* (2011) and Jenkins *et al.* (2012), where the monitoring well was used to measure the arrival of the tracers at different depths significant to fluid contacts using a purpose built bottom hole assembly.

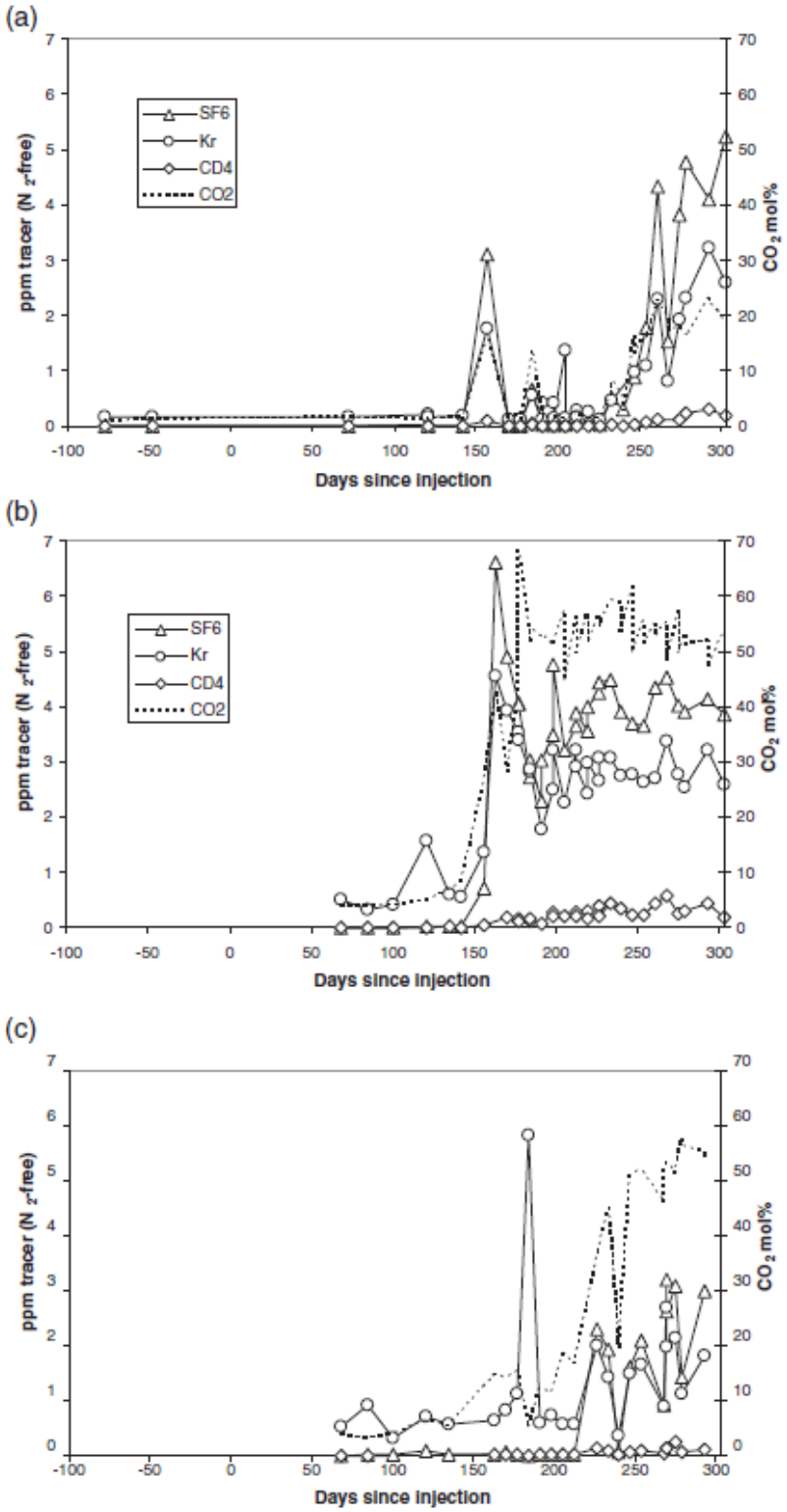

Figure 111: Results from study by Stalker et al. (2015) using tracers to verify breakthrough of CO_2 down the monitoring well. (a) Sampling time from within methane gas cap (2028.8 – 2029.4 m). (b) Sampling from just below the post-production gas-water contact (2041.8 – 2042.4 m). (c) Sampling of the deepest region (2046.3 – 2046.9 m).

Results from the post-production gas-water contact show that krypton, SF_6 and CD_4 all behaved as successful tracers for detecting initial breakthrough arrivals. Both the SF_6 and krypton reach maximum peaks prior to the CO_2, as is the case seen in the experimental research of this project. The research highlights the concept of different discrete pathways for migration, although it also highlights the difficulty of identifying detailed differences in arrival between CO_2 and tracers when the sampling times are on a larger scale.

Tracer work using SF_6 and krypton has also been used as part of the investigations in Ketzin (Martens *et al.*, 2012). SF_6 and krypton were artificially injected as part of the monitoring process to compare CO_2 from the oxyfuel pilot plant Schwarze Pumpe, to food grade CO_2 from hydrogen by-product (Linde AG) as they are alternated by injection (Figure 112).

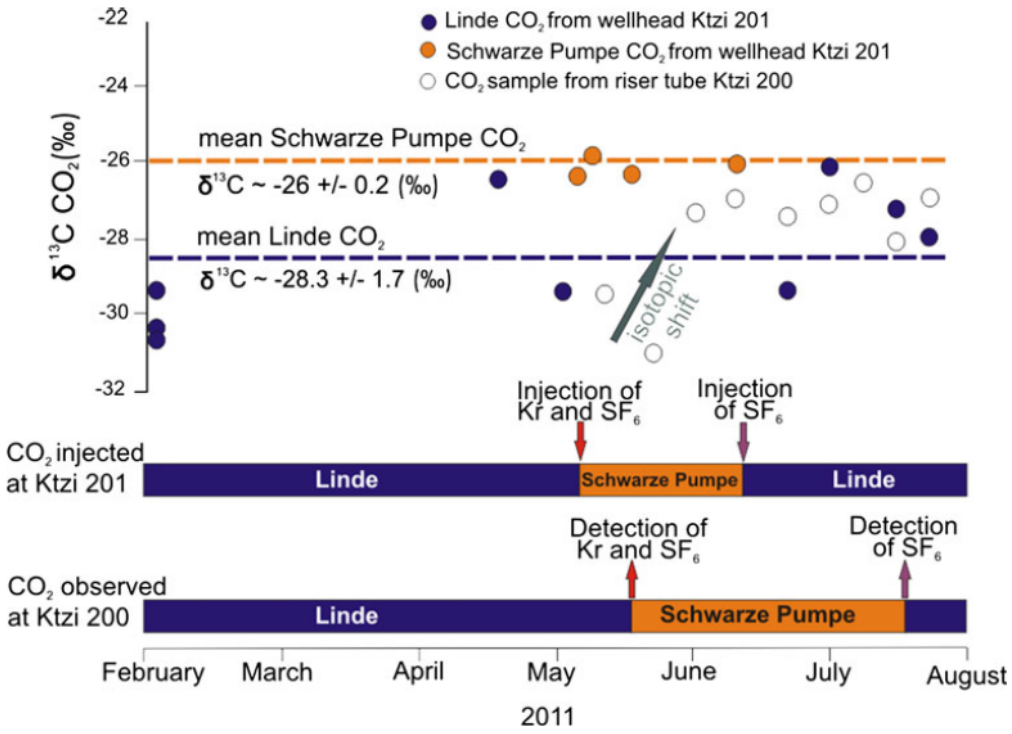

Figure 112: Results from study at Ketzin (Martens et al., 2012). Ktzi 201 is the injection well/well head. Ktzi 200 is an observation well at 640 m depth approximately 40 m away from the Ktzi 201.

Although this work fails to do a comparison between the two tracers, it does show how they can be used to differentiate on a short-term scale by the introduction of different sources of CO_2. Figure 112 also highlights the effect of injection rate on the appearance of a tracer as shown by the second injection of SF_6 to highlight the change back to Linde source. This is most likely due to the change in transport driving mechanisms, something that is clearly seen in the pressure gradient range of this studies result.

Nimz and Hudson (2005) have carried out monitoring of CO_2 storage sites using noble gas isotopes, with particular emphasis on the use of xenon over SF_6 and $^{14}CO_2$ due to the high number of different xenon isotopic compositions. Work focuses in particular with the Mabee EOR field in West Texas that uses existing CO_2 from natural deposits. The amount of any tracer required is a function of the type of system to be monitored (groundwater, deep soil, formation gases, ground surface emissions). Research suggests that $^{14}CO_2$ as a tracer may be considered the best due to the low volume needed compared to cost. However, due to its radioactive behaviour, it may be considered an unsavoury choice of tracer. Similarly, SF_6 has been a popular tracer presented in the other studies but it is a far more potent greenhouse gas than CO_2. There are strict laws in place for the licence to procure this gas in the UK (and EU) (Department for Environment Food and Rural Affairs and Environment Agency, 2014); this will limit the access to using it as well as increasing the costs involved. The choice of noble gas tracer depends on how much is needed to make it distinct but also based on the volatile nature of the cost. ^{3}He was once a cheaper solution but since the publishing of the Nimz and Hudson (2005) paper, the cost has continued to increase. Nimz and Hudson (2005) research looked at helium, neon, argon and xenon concentration and isotopic data for Mabee EOR field. Since the injected CO_2 is already enriched in the noble gases, the results are from a 'matured' monitoring project, which means there would be no breakthrough curve analysis available for comparative purposes with this research.

7.1.2 Tracing of CO_2 behaviour using isotopic signatures

Additional work in carbon isotopes highlight the use of detecting CO_2 using breakthrough curves in field and laboratory conditions using a one dimensional transport model to interpret the results (Newell *et al.*, 2014, Liu *et al.*, 2014, Larson and Breecker, 2014). Experiments carried out by Larson and Breecker (2014) using packed column experiments show how sorption effects may significantly affect $^{12}CO_2$ to $^{13}CO_2$ ratios even in dry geological media

where certain minerals are present, something that is important to take into account when conducting monitoring studies using isotopes. In the experiments carried out for this research, it was apparent that unintended sorption effects were occurring despite the core being predominately quartz. Although there was no use of isotopes, it would be interesting to carry out this experiment again using them to quantify the effect of sorption. This is something that should be considered under future work.

What many of these upscaled experiments are lacking is the access to real-time analysis. Although this research is limited by low pressure and single-phase flow, it allows the user to develop the understanding of the fundamental transport mechanisms behind tracer transport with delays in sampling. By identifying any similarities in the results from this research to real world environments, it can help answer some of the uncertainties raised in the larger scale experiments.

7.2 Discussion of noble gases as tracers for CO_2 migration in porous media

One of the primary aims of the research was to investigate how noble gases could be used as early warning tracers for CO_2 migration in CCS sites. As part of this work, experimental breakthrough curves were generated over a low pressure range (10,000 – 50,000 Pa). This section explores the trend of the arrivals, how they relate to CO_2, and whether they could be used as early warning tracers for unplanned migration.

7.2.1 Noble gases as early warning tracers for CO_2 migration

Figure 113 shows a summary of the timings for all the tracers to reach C/C_{max} as a pulse through the Fell sandstone from the experiments. As previously summarised in Chapter 5, helium is the last noble gas to reach C_{max} for all the pressure ranges. Neon, argon, krypton and xenon show relatively similar C/C_{max} times. SF_6 tends to be quicker than all the noble gases at all the sampling pressures to reach C_{max}. CO_2 takes longer to reach C/C_{max} but displays a similar trend over all the pressure ranges due to retardation effects.

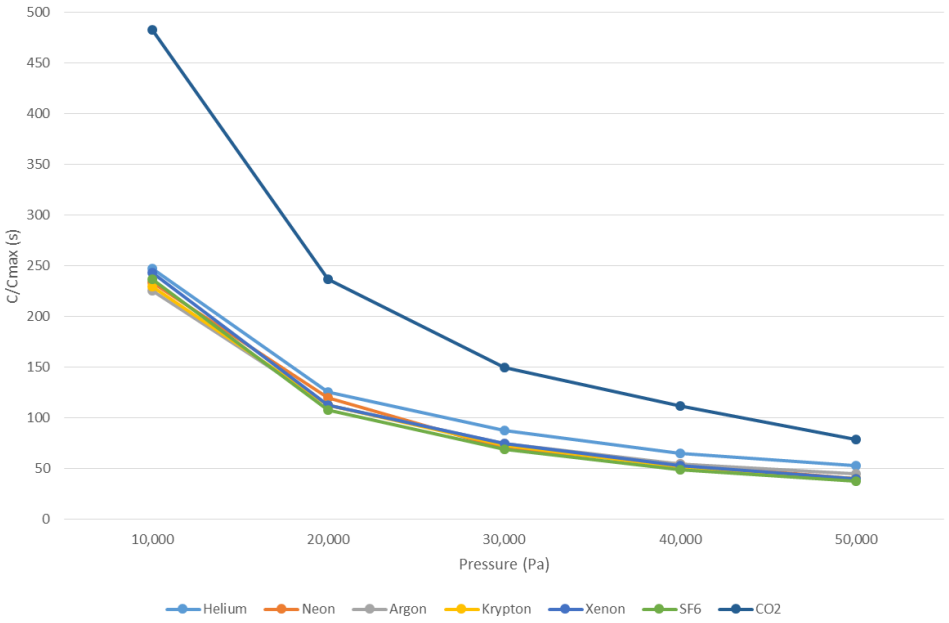

Figure 113: Summary of C/C_{max} values obtained from smoothed lines for noble gases, SF_6 and CO_2 breakthrough curves at each sampling pressure gradient.

Using the concentration intervals (s) described in Chapter 5, Figure 114 and Figure 115 show the end-member pressure gradients for the breakthrough curve profiles.

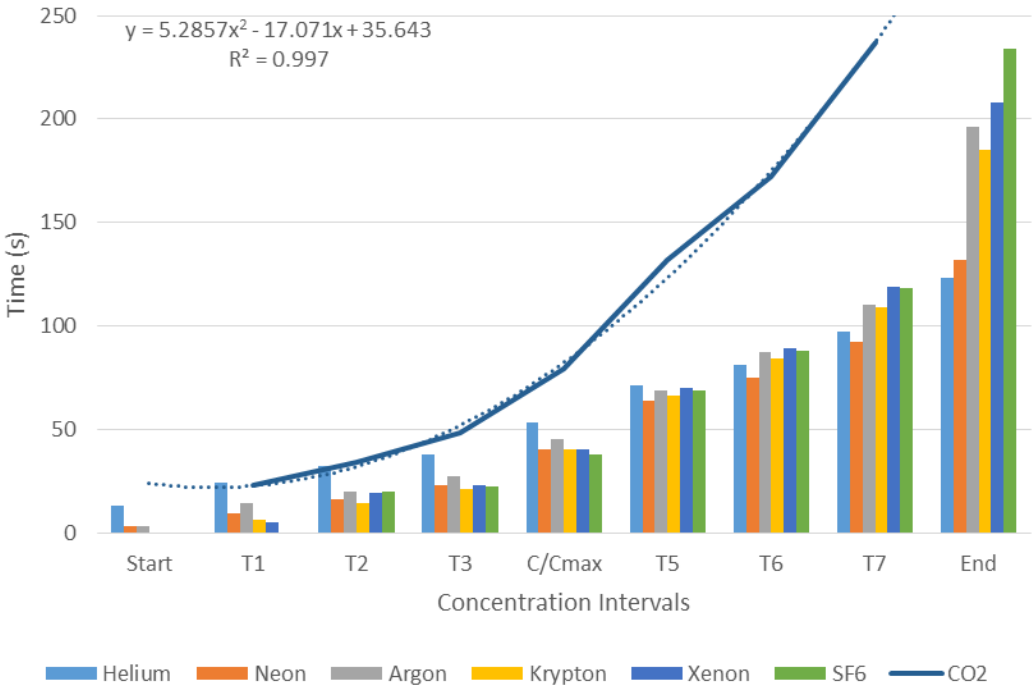

Figure 114: Timings of the different sampled gases at set concentration intervals at 50,000 Pa. A polynominal trendline for CO_2 was applied, as background readings were too high to detect initial arrival times.

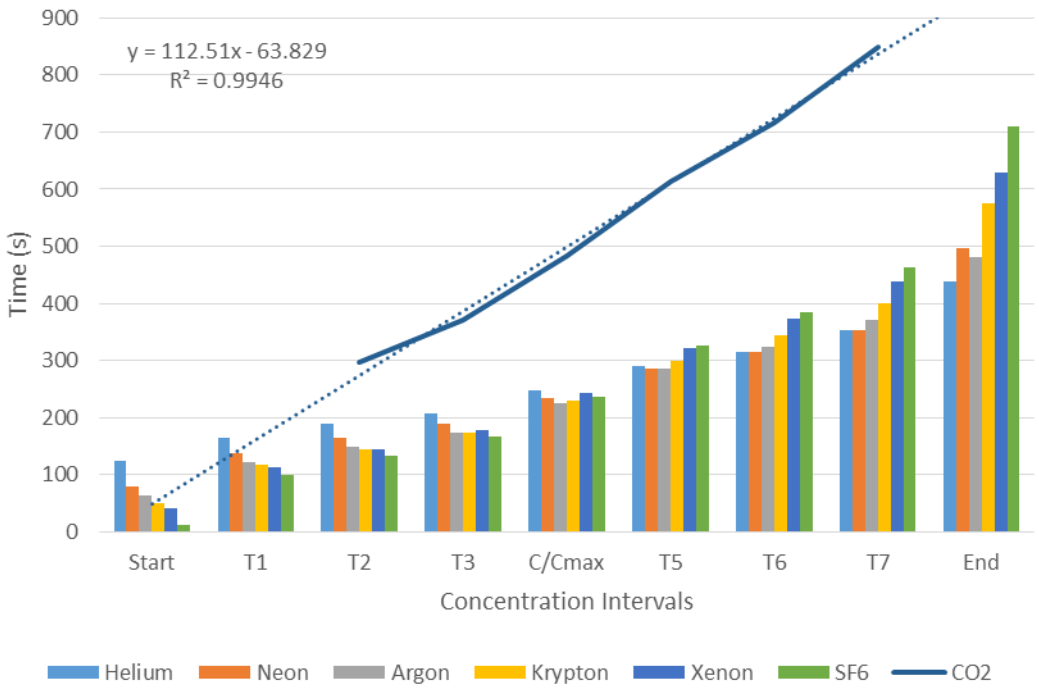

Figure 115: Timings of the different sampled gases at set concertation intervals at 10,000 Pa. A linear trendline for CO_2 was applied as background readings were too high to detect initial arrival times.

There are two approaches to deciding how these tracers could be used as an early warning tracer for CO_2 migration. Firstly, using these timings, it is evident that all the noble gases and SF_6 reach C_{max} before CO_2 does (Figure 113). This suggests that all the noble gases and SF_6 can be successful tracers for identifying the early migration of CO_2 under the experimental conditions. The trends from these experiments compare to other research at larger scale test sites (Section 1), which implies the order in which the tracers arrive (or a combination) at C_{max} could act as a means of understanding the transport timings of any unplanned CO_2 migration through porous media.

Alternatively, when a baseline has been identified prior to injection, the initial arrival of certain tracers could be used as early warning indicators for possible CO_2 migration. Background CO_2 readings were too high to detect initial arrival of a new CO_2 pulse at lower pressures. Trendlines have been applied as a guide to determine which tracers may not be suitable as they arrive after the initial detection of CO_2 (Figure 114 and Figure 115). From these results, it is

apparent that helium, neon and argon may not be suitable as early warning tracers for CO_2 migration. Krypton and xenon arrival times are quicker and could be used as a means of detecting CO_2 migration. The results suggest that SF_6 is the fastest travelling tracer for pre-peak concentration values.

7.2.2 Noble gases as a method of fingerprinting CO_2 storage sites

While helium, neon and argon appear to be unsuitable as early warning tracers for initial detection of CO_2, this suggests that they can be used as part of mixture to fingerprint individual CO_2 storage sites that may be in close proximity to one another. Noble gases and their isotopes are able to provide unique constraints on certain geological processes (Burnard *et al.*, 2013, Wilkinson *et al.*, 2010, Gilfillan *et al.*, 2008). Understanding their predicted arrival times in relation to each other can help determine ownership of CO_2 storage sites and thus the party responsible to rectify any unplanned effects.

7.3 Discussion for upscaling experimental results

When designing and conducting the experiments needed for this project the topic of commercial relevance and upscaling was regularly considered. Upscaling is a method of applying parameter values and transport processes to a larger scale environment. The spatial distribution increases from pore, formation, and to regional scale. At the pore scale, physical variables are defined in terms of averages over a volume containing many molecules; these variables change by orders of magnitude as the scale increases (Sanchez-Vila *et al.*, 2006). The experiments for this research were carried out under a low range of pressure gradients, single-phase conditions and through an air-dried sample. Comparing these conditions directly to real world environments where CO_2 storage is carried out in underground environments with multiphase flow and high-pressure conditions is restricted. The fundamental aim of the project was to understand the mechanisms involved for the transport of tracers in porous media. By doing so, the results of this research have uncovered new and original data about 'conservative' noble gases as tracers and contributed to the understanding of transport at the micro-pore scale. These results have been compared to existing research at larger and more complicated sampling environments and yet, show the same patterns in terms of travel times and behaviour. These results demonstrate that whilst the large-scale experiments need a sophisticated methodology and larger budgets, the research conducted lacks what this research could provide – real-time analysis of tracers. From this research, descriptions of the breakthrough curves have been provided and show the complex geometry of each of the tracers as they pass through porous media.

The issue of scaling is highlighted in the work of Sanchez-Vila *et al.* (2006) looking at the behaviour of groundwater flow within an aquifer. The research highlights the fundamental questions that should be asked when establishing how valid results are at different scales. Does the structure of the transport equation remain the same? If not, how should flow processes be defined at a different scale? It is necessary to decide what different input parameters are to be used depending on the scale and how to bridge the input and output parameters across different scales (Sanchez-Vila *et al.*, 2006). From comparison with other research carried out under reservoir conditions, it is possible to make some similarities in behaviour of the tracers in relation to another, as well as some possible reasons for the arrival times. The following section will now discuss in what form could the parameters, transport mechanisms and outputs used be considered for upscaling of flow and transport in porous media.

7.3.1 Input parameters

In order to carry out the experiments for the research, fundamental input parameters needed to be determined and defined. Some of the input parameters were average values and as such would remain the same with the changing of conditions. The calculated bulk density of 2063 kg m^3 was the average of the core samples taken; based on the average value provided by Hutton Stone for the entire formation it was 2240 kg m^3. The scale of the sampling area would need change to accommodate the dimensions of the reservoir region from sampling to observation well. In civil engineering, hydraulic conductivity is often termed permeability and is the most variable parameter for upscaling; even in seemingly homogenous aquifers, measured values may range over some orders of magnitude (Sanchez-Vila *et al.*, 2006). The permeability and porosity of a rock as it is upscaled will depend on the type of formation. An average intrinsic permeability may be selected to reduce the level of variability within the formation. However, from the experimental results presented in this research, it is apparent that there is a permeability range even within a rock that was selected for its supposed homogenous behaviour. Similarly, the constraints of heterogeneity will increase as the scale of observation is increased. For porosity, with an increase in scale, the heterogeneity flattens out and appear to show less variability. It has also been proposed that the influence of micro-scale porosity heterogeneity is reduced as the flow rate increases (Shi *et al.*, 2011).

With upscaling of the conditions, the input pressure and temperature range would be extended appropriately, which means a change in the viscosity and physical properties of the CO_2 as it transitions into a supercritical fluid. Projecting values obtained at five low sampling pressure gradients with a temperature that is in gaseous phases would prove problematic. Clearly, the results for this research do not account for multiphase flow; to continue to compare these values to real test sites, the introduction of two-phase flow (for saturated systems) and multiphase flow (transition of CO_2 phase behaviour) would need to be applied for reservoir conditions, leading to fractionation of the noble gases. Although a liquid may be considered an incompressible fluid and a gas primarily as a compressible fluid, supercritical CO_2 has both liquid and gaseous properties (the density of a liquid, but the viscosity of a gas). It is also known that supercritical CO_2 is compressible, and has pressure and temperature dependent density and viscosity functions. Thus, it would make it difficult to compare noble gas properties to it. Although as with the Carrigan *et al.* (1996) research where it was observing the pressure fluctuations as the driving force, these experiments would relate better to systems

where the CO_2 has already phased into gas and is migrating above the injection/storage area. This would remove the issue of comparing any results to supercritical CO_2 conditions. The conceptual and technical difficulties of upscaling described here, highlight the need for measurement devices that could acquire data at a predefined scale in order to avoid these upscaling issues (Sanchez-Vila *et al.*, 2006).

7.3.2 Transport mechanisms and outputs

The output results from the experiments provide values for the conditions. Using the described modelling inputs for the mass transport equation, the breakthrough curves produced a set of values for the transport mechanism, advective velocity and the hydrodynamic dispersion coefficient as well as sorption effects over a pressure range of 10,000 – 50,000 Pa gradient.

The advective velocity of the system describes the movement of fluid due to bulk motion. This flow is dependent on the effective porosity, the hydraulic conductivity and the hydraulic gradient. A fluid follows Darcy's Law for flow under certain conditions, where the fluid is 'creeping'. Above this velocity, non-Darcy behaviour occurs and an amended description of the fluid must be considered. A fluid may transition from linear laminar flow to non-linear laminar flow before it reaches true 'turbulent' flow. It is not possible to use five experimental points to predict the flow behaviour when this is the case. Similarly, dispersion is scale dependent, gas dependent and matrix dependent and to a degree, time dependent. Dispersion is not suitable in comparative examples, and is best calculated at a predefined scale. Sorption is solute and matrix dependent but could be compared in the absence of another phase.

It is apparent that the parameters from this research are unique, developed under the conditions of a controlled laboratory environment, which means that the values are specific to the spatial distributions applied and it is not possible to extrapolate the data beyond this research. When the flow pattern is not simple, it is not possible to describe its complex nature by means of a single effective equivalent parameter (Sanchez-Vila *et al.*, 2006). It is not possible to neglect transport mechanisms such as sorption, hydrodynamic dispersion and channel heterogeneity. However, the results provide previously unknown breakthrough curves and transport values for noble gases, SF_6 and CO_2 through porous media. These results provide further insight into the transport mechanisms involved as conservative gaseous tracers travel through homogenous

media. This is supposedly a simplistic process but the results have shown that there are micro-scale processes occurring that determine the pathways taken. Additionally, the breakthrough curves have provided real-time analysis of the pre-peak and post-peak profile produced during a pulse injection. Previous research on larger scales are limited to batch analysis and sampling delays and can lose this type of information. Largely, the results have been successfully compared to overall trends seen in other research. The relative arrival times and patterns are relatable, allowing this research to support and even present reasons as to why the behaviour of the tracers have been observed. Thus, this research forms a distinct contribution to the existing knowledge on transport in porous media.

7.4 Summary of main findings from research

7.4.1 Pipeline odourisation and monitoring

CCS research has shown that monitoring is a necessity of any technology. One of the most efficient means of transporting fluids over large distances is via pipeline. Pipeline leaks can be problematic, especially when transporting colourless and odourless gases such as natural gas and CO_2. Compulsory odourisation was introduced into pipelines as an additional inherent safety measure of detection of a potentially hazardous gas that may have been unintentionally released. It is one of the current methods of risk mitigation for natural gas transport. Natural gas in the United Kingdom is odourised in only the lower pressure distribution pipelines. Existing technologies for monitoring are already well established for high pressure natural gas pipelines as well as for CO_2 pipelines without using odourisation as a detection method. As CO_2 pipeline networks are established into regions which are not familiar with CO_2 transport (i.e. outside of North America), then for public reassurance it may well be beneficial to odourise the gas phase, low pressure, CO_2 pipelines during the first projects developed. Thus the odourisation of CO_2 pipelines may be a societal requirement rather than a technical one.

7.4.2 Noble gases as conservative tracers through porous media

It is apparent from the results that the gas breakthrough curves for the different tested tracers are not symmetrical and have distinct behaviours. Although noble gases are described as conservative tracers, comparing the breakthrough curves over a range of pressure gradients show that they do not behave as simply as previously assumed. If advective processes were only occurring, the breakthrough curves would be sharp tight peaks (Gaussian in nature due to pulse). Variation in the spreading of the tracers must be occurring as the curves vary in shape and length. These experimental flow results can be modelled using a one dimensional advection dispersion model, which identifies the impact of mechanical dispersivity. Mechanical dispersion is directly related to the heterogeneity of the porous media and is scale dependent.

The tracer experiments allow for the predictive behaviour trends of the noble gases through porous media. These results are compared to a popular tracer, SF_6, which has been used in many upscaled projects. SF_6 shows very similar trends to that of krypton and xenon. As SF_6 is an extremely potent greenhouse gas and will potentially be difficult to obtain for use in the

UK, it is suggested that noble gases could be a positive replacement tracer for future monitoring projects. Results from experimental curves also highlighted the impact of CO_2 sorption even through a dried system.

7.4.3 Experimental results modelled using a one dimensional advection dispersion equation

It was possible to successfully model the experimental results using a one dimensional advection dispersion model. A statistical approach for this model can constrain the advective velocity, permeability and porosity for an analytical approach, which is needed to develop the dispersivity behaviour of the tracers. With these results, a conceptual model has been proposed for the experimental system whereby preferential paths exist depending on the flow velocity. The model requires multiple weighting of these pathways to match the experimental data. At low pressures, the system follows a Darcy flow regime and tracers travel preferentially along a higher permeability route. With an increase in pressure, *Re* values suggest a partial migration from a linear regime and into a non-linear regime as identified using the Forchheimer regime at the pore diameter scale. At this time, the tracer is travelling along linear low permeability routes and non-linear high permeability pathways. By 50,000 Pa, the high permeability pathways are experiencing non-linear laminar flow but contribute significantly less to the overall route. The low permeability regimes with a higher dispersivity are the dominant pathway. These low permeability regimes are not fully within the non-linear regime but are approaching it. This appears to suggest that an increase in *Re* number leads to a non-linear laminar flow, which is 'slower' to contribute than a true linear laminar flow to the Fell sandstone system. These results can be used to explain patterns observed with tracers in large-scale reservoirs but the value outputs obtained are scale-dependent and would not be suitable for direct upscaling.

Chapter 8 - Future work and conclusions

8.1 Scope for future work and applications

The experiments for this research were carried out using a specially constructed tracer loop and flow cell. Prior to construction of this flow cell, initial research aims for this project consisted of altering and using an existing rig that could be used to expose a core sample to supercritical CO_2 under reservoir temperatures and pressures. When the use of the equipment was critically assessed it was determined that to use the high pressure/temperature rig would provide data that would associate it with existing environments targeted for CCS. However, the use of the rig limited the length of the core used (~10 cm). The length of piping needed to connect the tracer to the system was greater than the calculated pore volume of the standard core plug. Additionally, it was not feasible to connect the QMS safely due to the high pressure and temperature conditions of the rig.

A significant aspect of this project was the design, purchase and construction of a purpose-built flow cell to fulfil this part of this project. This led to a restricted amount of time to test and carry experimental procedures using noble gases. With access to larger budget and time, the following sections are potential future projects that could be carried out using the experimental layout.

8.1.1 Saturated core system and X-ray CT scanning

There is potential to saturate the sandstone core and re-run the experiments through a saturated medium. The saturation would need to be carried out with water rather than brine, as the QMS in its current setup would become damaged with a highly saline sample. This experiment would offer a one-off opportunity to compare the transport behaviour of the noble gases, SF_6 and CO_2 to the original unsaturated core sample. It would require a calibrated mixture of the tracers and CO_2 in a single tracer pulse. In theory, the experiment may be repeated but due to the mineralogy of the rock there would be some chemical interaction between the matrix surface, the water and the CO_2. In addition, it would be difficult to ensure that all the tracers from prior experiments were removed. A strict and extensive purging regime would allow for replication but may prove to be timely.

In conjunction with this experiment, it would be beneficial to carry out pre and post flooding analysis of the core sample using X-ray CT scanning. It is rapidly becoming an attractive method to determine how the geometry and mineralogy of a core system affects mobility of CO_2 (Krause *et al.*, 2013, Jiang *et al.*, 2015). A computed tomography instrument has been constructed at the University of Edinburgh that could aid in the understanding of fluid flow in porous media (Pak *et al.*, 2015).

8.1.2 Mixtures of noble gas pulses and use of isotopes

One of the objectives of this research was to understand the behaviour of the noble gases in relation to CO_2. It was important to the research to understand the behaviour of each of the noble gases individually through the same system. This work has been presented here. With a greater budget and access to mixtures rather than individual cylinders of tracers, it would be highly worthwhile to carry out the same pressure gradients using this mixture of noble gases (and SF_6) through a CO_2 system. A limitation of this project was the CO_2/N_2; it would be conducive to the project if this experiment could be improved upon by the introduction of isotopic signatures. The use of $^{13}CO_2$ tracers would be a more suitable comparison by completing $^{13}CO_2/^{12}CO_2$ experiments. The $^{13}CO_2$ could then be added to the noble gas and SF_6 mixture.

8.1.3 Tracer system with low permeability 'cap rock'

It would be appealing to carry out the same type of tracer experiments using the same flow cell, but replacing the sandstone with a fractured 'cap rock' sample. Some extensive work within the department has looked at the transport of supercritical CO_2 versus gaseous CO_2 through fractured shales. It would be interesting to investigate this dimension of fracture transport as well the mass transport through a low permeability material.

8.1.4 Further applications for research

In addition to monitoring CO_2 migration in CCS projects, there are further opportunities to investigate the role of noble gases in other subsurface energy activities.

- Nuclear waste

Currently, nuclear regulatory agencies generally require that radionuclides in a buried waste repository remain isolated from the surface for at least 10^6 years (Hendry *et al.*, 2015). During geological disposal, monitoring of unintended release of hydrogen and ^{14}C during long-term storage is important as well as the buried radioactive waste. Nuclear power reactors generate radioactive fission products during their operation. Noble gases are released as part of the decay of the 'enriched' uranium fuel, including ^{85}Kr (half-life: 4.4 h), ^{87}Kr (78 min), ^{88}Kr (2.77 h), ^{133}Xe (5.27 d), ^{133}Xe (2.3 d), ^{135}Xe (9.13 h) and ^{138}Xe (17 min) (Okoshi and Nakayama, 2015). There is considerable interest in the use of thick argillaceous geologic formations to contain nuclear waste, where diffusion is the controlling transport process (Hendry *et al.*, 2015). Noble gases could be used to demonstrate that solute or radionuclide transport away from the proposed repository is slower than the necessary storage time.

- Nuclear testing

In a similar manner to nuclear waste monitoring, radioactive noble gases could be used to identify recently conducted subsurface nuclear explosions that violate the Comprehensive Nuclear Test Ban Treaty. This concept has been previously investigated by Carrigan *et al.* (1996) and Carrigan and Sun (2014) where ^{137}Xe, ^{133}Xe and ^{37}Ar could act as indicators of a recent underground nuclear explosion.

- Hydraulic fracturing

Hydraulic fracturing is the high pressure injection of fluid into a wellbore to create fractures. These fractures release natural gas or petroleum from shale gas, tight gas/oil and unconventional coal seams. This practice has been commercially applied since 1950 but has become more prominent to increase production as sources of fossil fuels deplete. It is considered highly controversial due to the increase in seismic activity along faults and the environmental impacts of the fluids used during the process. In the same manner as CCS, noble gases could be used as artificial tracers to monitor for any unplanned migration of injection fluids in surrounding groundwater (Darrah *et al.*, 2014).

8.2 Conclusions

Geological CO_2 capture and storage technology has the potential to a make a significant contribution to a low carbon technology future. Monitoring the CCS chain is vital, it minimises the risk of leakage of CO_2 as well improving the opportunity to mitigate any changes that may occur over time. In addition, it provides public reassurance that any risks are being managed.

Based on experience from natural gas, this research concluded that high pressure pipelines of CO_2 through sparsely populated areas could have odourant added, but will gain little safety benefit. Existing strategies are in place and are more effective at monitoring pipelines. However, adding odourant to CO_2 gas phase pipes could aid detection of leaks as well as improve public assurance. For management of odourisation of CO_2 pipelines, further investigation is needed into the interaction of specific impurities associated with captured CO_2 on the odourants, the transport of different phases of CO_2 and the result of intermittent operations; the financial costs involved for effective implementation must also considered.

Results were generated for noble gases, SF_6 and CO_2 using specially constructed experimental equipment that allowed for the determination of breakthrough curves of tracers in gaseous phase over a range of low pressure gradients (10,000 – 50,000 Pa) through air-dried porous media. As the atomic radius increases from helium to xenon, the amount of spreading also increases. The experimental breakthrough curves for all of the noble gases experience the same advective velocity values at each of the sampling pressures. Therefore, the spreading of the curves is due to hydrodynamic dispersion and must be unique for each tracer. During advective transport in porous media, the longitudinal dispersion causes more spreading of a solute plume than molecular diffusion. This suggests that there is a higher level of dispersion with an increase in size for noble gases. Tracers from the experimental flow results can be modelled using a one dimensional advection dispersion model. A statistical approach for this model can derive the parameters for an analytical approach, which is needed to understand the dispersivity behaviour of the tracers. A set of values for dispersion of noble gases, SF_6 and CO_2 through porous media has been presented in this research.

A conceptual model has been proposed to explain the experimental and modelling results for the system, whereby preferential paths exist depending on the flow velocity. At low pressures,

the system follows Darcy regime and tracers travel along a higher permeability route. With an increase in pressure, *Re* values suggest a partial migration from a linear regime and into a non-linear regime, as identified using the Forchheimer regime at the pore diameter scale. At this time, the tracer is prone to travelling along linear low permeability routes and non-linear high permeability routes. By 50,000 Pa, the high permeability routes are experiencing non-linear laminar flow but contribute significantly less to the overall route. The low permeability regimes with a higher dispersivity are the dominant route. These low permeability regimes are not fully within the non-linear regime but are vastly approaching it.

Using a baseline value approach, initial arrival times for krypton and xenon from this research suggest that they could be used as a means of detecting CO_2 migration. While helium, neon and argon appear to be unsuitable as early warning tracers for initial detection of CO_2, this suggests that they can be used as part of mixture to fingerprint individual CO_2 storage sites that may be in close proximity to one another. The results also imply that SF_6 is the fastest travelling tracer for pre-peak concentration values and initial detection. SF_6 has been a popular tracer presented in the other studies but it is a far more potent greenhouse gas than CO_2. Thus, krypton and xenon may act as suitable replacement.

The results presented here along with the propositions of pore scale heterogeneity, contribute to a better understanding of transport mechanisms involved in transporting tracers in porous media. The results can also be used to explain patterns observed with tracers in large-scale reservoirs but the output values obtained are limited by scale-dependence and would not be suitable for direct upscaling.

References

ALLIS, R., CHIDSEY, T., GWYNN, W., MORGAN, C., WHITE, S., ADAMS, M. & MOORE, J. Natural CO_2 reservoirs on the Colorado Plateau and southern Rocky Mountains: Candidates for CO_2 sequestration. Proceedings of the First National Conference on Carbon Sequestration, 2001. 14-17.

AMANN, R. 2010. A policy, legal, and regulatory evaluation of the feasibility of a national pipeline infrastructure for the transport and storage of carbon dioxide. *Topical Report.*

AMINU, M. & ARDO, B. 2015. A novel approach for determining permeability in porous media. *J Pet Environ Biotechnol,* 6**,** 2.

AMIRBEKYAN, D. 2013. Natural gas odorization monitoring for safety and consistency. *Pipeline and Gas Journal,* 240.

ANSELMETTI, F. S., LUTHI, S. & EBERLI, G. P. 1998. Quantitative characterization of carbonate pore systems by digital image analysis. *AAPG bulletin,* 82**,** 1815-1836.

ARAPOSTATHIS, S. 2011. Natural gas network development in the UK (1960-2010). *Case Study for Project: 'CCS-Realising the Potential'*.

ASHWORTH, P., BRADBURY, J., FEENSTRA, C. Y., GREENBERG, S., HUND, G., MIKUNDA, T. & WADE, S. 2010. Communication, project planning and management for carbon capture and storage projects: An international comparison. Queensland, Australia: CSIRO/GCCSI.

ASHWORTH, P., BRADBURY, J., WADE, S., FEENSTRA, C. Y., GREENBERG, S., HUND, G. & MIKUNDA, T. 2012. What's in store: Lessons from implementing CCS. *International Journal of Greenhouse Gas Control,* 9**,** 402-409.

ASHWORTH, P., DOWD, A., RODRIGUEZ, S., JEANNERET, T., MABON, L. & HOWELL, R. 2013. Synthesis of CCS social research: Reflections and current state of play in 2013. CSIRO EP134303, Australia.

BACHU, S. 2015. Review of CO_2 storage efficiency in deep saline aquifers. *International Journal of Greenhouse Gas Control*.

BALLENTINE, C. J., BURGESS, R. & MARTY, B. 2002. Tracing fluid origin, transport and interaction in the crust. *Reviews in mineralogy and geochemistry,* 47**,** 539-614.

BALLENTINE, C. J. & BURNARD, P. G. 2002. Production, release and transport of noble gases in the continental crust. *Reviews in mineralogy and geochemistry,* 47**,** 481-538.

BALLENTINE, C. J. & HOLLAND, G. 2008. What CO_2 well gases tell us about the origin of noble gases in the mantle and their relationship to the atmosphere. *Philosophical*

Transactions of the Royal Society A: Mathematical, Physical and Engineering Sciences, 366**,** 4183-4203.

BALLENTINE, C. J., MARTY, B., LOLLAR, B. S. & CASSIDY, M. 2005. Neon isotopes constrain convection and volatile origin in the Earth's mantle. *Nature,* 433**,** 33-38.

BAMBERG, J. 2000. *British Petroleum and Global Oil 1950-1975: The challenge of nationalism*, Cambridge University Press.

BARENBLATT, G., ENTOV, V. & RYZHIK, V. 1990. Theory of fluid flows through natural rocks. Kluwer Academic Publishers.

BARRIE, J., BROWN, K., HATCHER, P. & SCHELLHASE, H. 2004. Carbon dioxide pipelines: A preliminary review of design and risks. *Greenhouse Gas Control Technologies,* 7**,** 315-320.

BEAR, J. 1972. *Dynamics of fluids in porous media,* New York, American Elsevier Publishing Company Inc.

BELL, F. G. 1978. The physical and mechanical properties of the Fell sandstones, Northumberland, England. *Engineering Geology,* 12**,** 1-29.

BENSON, S., COOK, P., ANDERSON, J., BACHU, S., NIMIR, H., BASU, B., BRADSHAW, J., DEGUCHI, G., GALE, J. & VON GOERNE, G. 2005. Underground geological storage. *IPCC Special Report on carbon dioxide capture and storage***,** 195-276.

BLACKFORD, J., BULL, J. M., CEVATOGLU, M., CONNELLY, D., HAUTON, C., JAMES, R. H., LICHTSCHLAG, A., STAHL, H., WIDDICOMBE, S. & WRIGHT, I. C. 2015. Marine baseline and monitoring strategies for carbon dioxide capture and storage (CCS). *International Journal of Greenhouse Gas Control,* 38**,** 221-229.

BOREHAM, C., UNDERSCHULTZ, J., STALKER, L., KIRSTE, D., FREIFELD, B., JENKINS, C. & ENNIS-KING, J. 2011. Monitoring of CO_2 storage in a depleted natural gas reservoir: Gas geochemistry from the CO2CRC Otway Project, Australia. *International Journal of Greenhouse Gas Control,* 5**,** 1039-1054.

BOULOS, M. S. & MANUEL, O. K. 1971. The xenon record of extinct radioactivities in the earth. *Science,* 174**,** 1334-1336.

BRITISH GEOLOGICAL SURVEY. *Fell sandstone formation* [Online]. Available: http://www.bgs.ac.uk/lexicon/lexicon.cfm?pub=FELL 2015].

BURNARD, P., ZIMMERMANN, L. & SANO, Y. 2013. The noble gases as geochemical tracers: History and background. *The Noble Gases as Geochemical Tracers.* Springer.

BURNETT, W. C., PETERSON, R., MOORE, W. S. & DE OLIVEIRA, J. 2008. Radon and radium isotopes as tracers of submarine groundwater discharge – Results from the

Ubatuba, Brazil SGD assessment intercomparison. *Estuarine, Coastal and Shelf Science,* 76**,** 501-511.

CARMAN, P. C. 1956. *Flow of gases through porous media,* London, Butterworths Scientific Publications.

CARRIGAN, C. R., HEINLE, R. A., HUDSON, G. B., NITAO, J. J. & ZUCCA, J. J. 1996. Trace gas emissions on geological faults as indicators of underground nuclear testing. *Nature,* 383**,** 528-531.

CARRIGAN, C. R. & SUN, Y. 2014. Detection of noble gas radionuclides from an underground nuclear explosion during a CTBT on-site inspection. *Pure and Applied Geophysics,* 171**,** 717-734.

CEPA. 2015. *Types of pipelines* [Online]. Available: http://www.cepa.com/about-pipelines/types-of-pipelines [Accessed 21/02 2015].

CLEAVER, P. & HOPKINS, H. 2012. The application of individual and societal risk assessment to CO_2 pipelines. *Journal of Pipeline Engineering,* 11**,** 191-199.

COHEN, G., LOISY, C., LAVEUF, C., LE ROUX, O., DELAPLACE, P., MAGNIER, C., ROUCHON, V., GARCIA, B. & CEREPI, A. 2013. The CO_2-Vadose project: Experimental study and modelling of CO_2 induced leakage and tracers associated in the carbonate vadose zone. *International Journal of Greenhouse Gas Control,* 14**,** 128-140.

COSHAM, A. & EIBER, R. 2008. Fracture propagation in CO_2 pipelines. *Journal of Pipeline Engineering,* 7.

DAKOTA GASIFICATION COMPANY. 2008. *CO_2 pipeline* [Online]. Available: http://www.dakotagas.com/index.html [Accessed March 2011].

DARRAH, T. H., VENGOSH, A., JACKSON, R. B., WARNER, N. R. & POREDA, R. J. 2014. Noble gases identify the mechanisms of fugitive gas contamination in drinking-water wells overlying the Marcellus and Barnett Shales. *Proceedings of the National Academy of Sciences,* 111**,** 14076-14081.

DAVIS, T. L., TERRELL, M. J., BENSON, R. D., CARDONA, R., KENDALL, R. R. & WINARSKY, R. 2003. Multicomponent seismic characterization and monitoring of the CO_2 flood at Weyburn Field, Saskatchewan. *The Leading Edge,* 22**,** 696-697.

DE MARSILY, G. 1986. Quantitative hydrogeology. Paris School of Mines, Fontainebleau.

DEPARTMENT FOR ENVIRONMENT FOOD AND RURAL AFFAIRS & ENVIRONMENT AGENCY 2014. F gas: guidance for users, producers and traders. 31/12/2014 ed.

DET NORSKE VERITAS 2010a. DNV-RP-J202-2010 Design and operation of CO_2 pipelines. Oslo: DNV.

DET NORSKE VERITAS 2010b. Offshore standard. *DNV OS-F101, Submarine Pipeline Systems*.

DOCTOR, R., PALMER, A., COLEMAN, D. L., DAVISON, J., HENDRIKS, C., KAARSTAD, O., OZAKI, M. & AUSTELL, M. 2005. Transport of CO_2. *In:* IPCC (ed.) *IPCC Special Report on Carbon dioxide Capture and Storage.*

DOMENICO, P. & SCHWARTZ, F. 1990. *Physical and chemical hydrogeology*, Wiley.

DUKHAN, N., BAĞCı, Ö. & ÖZDEMIR, M. 2014. Experimental flow in various porous media and reconciliation of Forchheimer and Ergun relations. *Experimental Thermal and Fluid Science,* 57**,** 425-433.

DULLIEN, F. A. 2012. *Porous media: fluid transport and pore structure*, Academic press.

EDENHOFER, O., PICHS-MADRUGA, R., SOKONA, Y., FARAHANI, E., KADNER, S., SEYBOTH, K., ADLER, A., BAUM, I., BRUNNER, S. & EICKEMEIER, P. 2014. Climate change 2014: Mitigation of climate change. *Working group III contribution to the fifth assessment report of the Intergovernmental Panel on Climate Change. UK and New York*.

EDLMANN, K., HASZELDINE, S. & MCDERMOTT, C. 2013. Experimental investigation into the sealing capability of naturally fractured shale caprocks to supercritical carbon dioxide flow. *Environmental earth sciences,* 70**,** 3393-3409.

EIKEN, O., RINGROSE, P., HERMANRUD, C., NAZARIAN, B., TORP, T. A. & HØIER, L. 2011. Lessons learned from 14 years of CCS operations: Sleipner, In Salah and Snøhvit. *Energy Procedia,* 4**,** 5541-5548.

EINSTEIN, A. 1905a. *Eine neue bestimmung der moleküldimensionen.* Buchdruckerei KJ Wyss.

EINSTEIN, A. 1905b. Über die von der molekularkinetischen Theorie der Wärme geforderte Bewegung von in ruhenden Flüssigkeiten suspendierten Teilchen. *Annalen der physik,* 4.

ELSEVIER & IEA COAL RESEARCH 2013. *The problems of sulphur: Reviews in coal science*, Butterworth-Heinemann.

EPA. 2013. *An introduction to Indoor Air Quality (IAQ), Carbon Monoxide (CO)* [Online]. Available: http://www.epa.gov/iaq/co.html [Accessed 16/09 2014].

EU DIRECTIVE 2009. Directive 2009/31/EC Of The European Parliament And Of The Council of 23 April 2009 Directives 2000/60/EC, 2001/80/EC, 2004/35/EC,2006/12/EC, 2008/1/EC and Regulation (EC) No. 1013/2006. L140,

Official Journal of the European Union on the geological storage of carbon dioxide andamending Council Directive 85/337/EEC, European Parliament and Council.

EUROPEAN COMMISSION (EC) 2011. Energy roadmap 2050. *European Commission.*

FETTER, C. 1994. Applied hydrogeology: Macmillan College Publishing Company. *New York***,** 131-163.

FETTER, C. W. 2008. *Contaminant hydrogeology,* Long Grove, Waveland Press Inc.

FISCHER, C. & GAUPP, R. 2004. Multi-scale rock surface area quantification—a systematic method to evaluate the reactive surface area of rocks. *Chemie der Erde - Geochemistry,* 64**,** 241-256.

FOX, R. W., MCDONALD, A. T. & PRITCHARD, P. J. 2009. *Introduction to fluid mechanics*, John Wiley and Sons Canada Ltd.

FREIFELD, B. M., TRAUTZ, R. C., KHARAKA, Y. K., PHELPS, T. J., MYER, L. R., HOVORKA, S. D. & COLLINS, D. J. 2005. The U-tube: A novel system for acquiring borehole fluid samples from a deep geologic CO_2 sequestration experiment. *Journal of Geophysical Research: Solid Earth (1978–2012),* 110.

GALE, J. & DAVISON, J. 2004. Transmission of CO_2—safety and economic considerations. *Energy,* 29**,** 1319-1328.

GAMBLE, H. A. 1974. Leicester Gas Works. *The Industrial Railway Record***,** 161-169.

GILFILLAN, S. M., LOLLAR, B. S., HOLLAND, G., BLAGBURN, D., STEVENS, S., SCHOELL, M., CASSIDY, M., DING, Z., ZHOU, Z., LACRAMPE-COULOUME, G. & BALLENTINE, C. J. 2009. Solubility trapping in formation water as dominant CO_2 sink in natural gas fields. *Nature,* 458**,** 614-8.

GILFILLAN, S. M. V., BALLENTINE, C. J., HOLLAND, G., BLAGBURN, D., LOLLAR, B. S., STEVENS, S., SCHOELL, M. & CASSIDY, M. 2008. The noble gas geochemistry of natural CO_2 gas reservoirs from the Colorado Plateau and Rocky Mountain provinces, USA. *Geochimica et Cosmochimica Acta,* 72**,** 1174-1198.

GLEDHILL, D. 2008. *Gas lighting*, Osprey Publishing.

GLOBAL CCS INSTITUTE. 2015. *Large scale CCS projects* [Online]. Available: http://www.globalccsinstitute.com/projects/large-scale-ccs-projects.

GOUGH, C., O'KEEFE, L. & MANDER, S. 2014. Public perceptions of CO_2 transportation in pipelines. *Energy Policy,* 70**,** 106-114.

GRATHWOHL, P. 1998. *Diffusion in natural porous media: contaminant transport, sorption, desorption and dissolution kinetics,* Dordrecht, Kluwer Academic Publishers.

GROVE, C. & JERRAM, D. A. 2011. jPOR: An ImageJ macro to quantify total optical porosity from blue-stained thin sections. *Computers & Geosciences,* 37**,** 1850-1859.

HARPER, P., WILDAY, J. & BILIO, M. 2011. Assessment of the major hazard potential of carbon dioxide (CO_2). *Health and Safety Executive*.

HASZELDINE, R. S. 2009. Carbon capture and storage: how green can black be? *Science,* 325**,** 1647-52.

HEALTH AND SAFETY EXECUTIVE 2011. *EH40/2005 Workplace exposure limits*.

HEALTH AND SAFETY EXECUTIVE 2012/13. Major hazard safety performance indicators in Great Britain's onshore gas and pipelines industry

HEALTH AND SAFETY LABORATORY 2009. Comparison of risks from carbon dioxide and natural gas pipelines.

HEGGUM, G., WEYDAHL, T., ROALD, W., MØLNVIK, M. & AUSTEGARD, A. 2005. CO_2 conditioning and transportation. *Carbon dioxide capture for storage in deep geologic formations,* 2**,** 925-936.

HEINEMANN, N., WILKINSON, M., HASZELDINE, R. S., FALLICK, A. E. & PICKUP, G. E. 2013. CO_2 sequestration in a UK North Sea analogue for geological carbon storage. *Geology,* 41**,** 411-414.

HENDRY, M., SOLOMON, D., PERSON, M., WASSENAAR, L., GARDNER, W., CLARK, I., MAYER, K., KUNIMARU, T., NAKATA, K. & HASEGAWA, T. 2015. Can argillaceous formations isolate nuclear waste? Insights from isotopic, noble gas, and geochemical profiles. *Geofluids*.

HOLLAND, G. & GILFILLAN, S. 2013. Application of noble gases to the viability of CO_2 storage. *The Noble Gases as Geochemical Tracers.* Springer.

HOVORKA, S. D., MECKEL, T. A. & TREVINO, R. H. 2013. Monitoring a large-volume injection at Cranfield, Mississippi—Project design and recommendations. *International Journal of Greenhouse Gas Control,* 18**,** 345-360.

HUTTON STONE CO. LTD. 2013. *Hazeldean, technical information* [Online]. Available: http://www.huttonstone.co.uk/guides/hazeldean.pdf 2015].

IEAGHG 2004. Impact of impurities on CO_2 capture, transport and storage.

IEAGHG 2011. Effects of impurities on geological storage of CO_2.

IEAGHG 2013. UK FEED Studies 2011 - A summary.

IPCC 2007. Climate change 2007: The physical science basis. *Agenda,* 6**,** 333.

ITAOKA, K., SAITO, A., PAUKOVIC, M., DE BEST-WALDHOBER, M., DOWD, A., JEANNERET, T., ASHWORTH, P. & JAMES, M. 2012. Understanding how individuals perceive carbon dioxide: Implications for acceptance of carbon dioxide capture and storage. *Global CCS Institute Publications.*

IVANOV, I., STRMEN, J. & JONES, L. 2009. Pre-odorization or "pickling" of new natural gas pipe. *Pipeline and Gas Journal,* 236.

JEANDEL, E., BATTANI, A. & SARDA, P. 2010. Lessons learned from natural and industrial analogues for storage of carbon dioxide. *International Journal of Greenhouse Gas Control,* 4**,** 890-909.

JENDEN, P., HILTON, D., KAPLAN, I. & CRAIG, H. 1993. The future of energy gases. *US Geological Survey Professional Paper,* 1570**,** 31-56.

JENKINS, C. R., COOK, P. J., ENNIS-KING, J., UNDERSHULTZ, J., BOREHAM, C., DANCE, T., DE CARITAT, P., ETHERIDGE, D. M., FREIFELD, B. M. & HORTLE, A. 2012. Safe storage and effective monitoring of CO_2 in depleted gas fields. *Proceedings of the National Academy of Sciences,* 109**,** E35-E41.

JIANG, Z., WU, K., COUPLES, G., VAN DIJKE, M., SORBIE, K. & MA, J. 2007. Efficient extraction of networks from three-dimensional porous media. *Water resources research,* 43.

JIANG, L., LIU, Y., SONG, Y., YANG, M., XUE, Z., ZHAO, Y., ZHAO, J., ZHANG, Y., SUEKANE, T. & SHEN, Z. 2015. Application of X-ray CT investigation of CO2–brine flow in porous media. *Experiments in Fluids,* 56**,** 1-10.

JO, Y.-D. & CROWL, D. A. 2008. Individual risk analysis of high-pressure natural gas pipelines. *Journal of Loss Prevention in the Process Industries,* 21**,** 589-595.

KALLEL, W., VAN DIJKE, M. I. J., SORBIE, K. S., WOOD, R., JIANG, Z. & HARLAND, S. 2015. Modelling the effect of wettability distributions on oil recovery from microporous carbonate reservoirs. *Advances in Water Resources*.

KENDRICK, M. A. & BURNARD, P. 2013. Noble gases and halogens in fluid inclusions: a journey through the Earth's crust. *The Noble Gases as Geochemical Tracers.* Springer.

KINZELBACH, W. 1992. *Numerische Methoden zur Modellierung des Transports von Schadstoffen im Grundwasser,* München, Oldenbourg Verlag.

KNOOPE, M. M. J., RABEN, I. M. E., RAMÍREZ, A., SPRUIJT, M. P. N. & FAAIJ, A. P. C. 2014. The influence of risk mitigation measures on the risks, costs and routing of CO_2 pipelines. *International Journal of Greenhouse Gas Control,* 29**,** 104-124.

KNOOPE, M. M. J., RAMÍREZ, A. & FAAIJ, A. P. C. 2015. Investing in CO_2 transport infrastructure under uncertainty: A comparison between ships and pipelines. *International Journal of Greenhouse Gas Control,* 41**,** 174-193.

KOERS, P., DE LOOIJ, M., ENGBØ, A., BAKKER, M., SCHOUWENAARS, E., SNAPHAAN, P. & HELLE, K. 2010. Final public report: Safety study for liquid logistics shipping concept. Prepared by DNV for Vopak / Anthony Veder.

KOLDITZ, O. 1997. *Strömung, Stoff-und Wärmetransport im Kluftgestein*, Borntraeger Berlin, Stuttgart.

KOLDITZ, O. 2001. Non-linear flow in fractured rock. *International Journal of Numerical Methods for Heat & Fluid Flow,* 11**,** 547-575.

KOSAKOWSKI, G. & MCDERMOTT, C. 2008. Modelling matrix diffusion - Results of a bench mark study. *Journal of Environmental Science and Sustainable Society,* 2**,** 57-62.

KRAUSE, M., KREVOR, S. & BENSON, S. M. 2013. A procedure for the accurate determination of sub-core scale permeability distributions with error quantification. *Transport in porous media,* 98**,** 565-588.

LAFORTUNE, S., MOREIRA, M., AGRINIER, P., BONNEVILLE, A., SCHNEIDER, H. & CATALETTE, H. 2009. Noble gases as tools for subsurface monitoring of CO_2 leakage. *Energy Procedia,* 1**,** 2185-2192.

LARSON, T. E. & BREECKER, D. O. 2014. Adsorption isotope effects for carbon dioxide from illite- and quartz-packed column experiments. *Chemical Geology,* 370**,** 58-68.

LI, H., JAKOBSEN, J. P. & STANG, J. 2011. Hydrate formation during CO_2 transport: Predicting water content in the fluid phase in equilibrium with the CO_2-hydrate. *International Journal of Greenhouse Gas Control,* 5**,** 549-554.

LIU, Y., LARSON, T. E. & NICOT, J.-P. 2014. Theoretical and experimental study of controls on CO_2 DIssolution and CH4 outgassing rates. *Energy Procedia,* 63**,** 4773-4781.

LU, J., COOK, P. J., HOSSEINI, S. A., YANG, C., ROMANAK, K. D., ZHANG, T., FREIFELD, B. M., SMYTH, R. C., ZENG, H. & HOVORKA, S. D. 2012. Complex fluid flow revealed by monitoring CO_2 injection in a fluvial formation. *Journal of Geophysical Research: Solid Earth (1978–2012),* 117.

LYMAN, W. J. 1982. *Handbook of chemical property estimation methods*, American Chemical Society.

LYONS, W. C. & PLISGA, G. J. 2011. *Standard handbook of petroleum and natural gas engineering*, Gulf Professional Publishing.

MARCOGAZ. 2006. Odorisation of natural gas. Available: http://www.marcogaz.org/ [Accessed 23/01/2014].

MARCOGAZ. 2012. Natural gas odorisation practices in Europe. Available: http://www.marcogaz.org/ [Accessed 23/01/2014].

MARKUSSON, N., SHACKLEY, S. & EVAR, B. 2012. *The social dynamics of carbon capture and storage: understanding CCS representations, governance and innovation*, Routledge.

MARTENS, S., KEMPKA, T., LIEBSCHER, A., LÜTH, S., MÖLLER, F., MYRTTINEN, A., NORDEN, B., SCHMIDT-HATTENBERGER, C., ZIMMER, M. & KÜHN, M. 2012. Europe's longest-operating on-shore CO_2 storage site at Ketzin, Germany: a progress report after three years of injection. *Environmental Earth Sciences,* 67**,** 323-334.

MARTENS, S., MÖLLER, F., STREIBEL, M. & LIEBSCHER, A. 2014. Completion of five years of safe co_2 injection and transition to the post-closure phase at the Ketzin pilot site. *Energy Procedia,* 59**,** 190-197.

MAX MACHINERY INC. 2015. *Odorant meters for natural gas odorization* [Online]. Available: http://www.maxmachinery.com/industry-application/natural-gas-odorization 2015].

MAXFIELD, B. T., GINOSAR, D. M., MCMURTREY, R. D., ROLLINS, H. W. & SHOOK, G. M. 2005. The effect of moisture content on retention of fluorocarbon tracers on sand. *Geothermics,* 34**,** 47-60.

MAY JR, I. M. 2010. New London School explosion. *Handbook of Texas Online* [Online]. Available: http://www.tshaonline.org/handbook/online/articles/yqn01 [Accessed 23/01/2014].

MCCALLUM, S., RIESTENBERG, D., COLE, D., FREIFELD, B., TRAUTZ, R., HOVORKA, S. & PHELPS, T. Monitoring geologically sequestered CO_2 during the Frio Brine pilot test using perfluorocarbon tracers. Proceedings, Fourth Annual Conference on Carbon Capture and Sequestration DOE/NETL, 2005.

MCDERMOTT, C. I. 1999. *New experimental and modelling techniques to investigate the fractured porous system.* PhD, Eberhard Karls Universität Tübingen.

MILLER, C. & POULIOT, S. 2008. Dakota Gasification Company, an international energy venture. *INTERNATIONAL TECHNICAL CONFERENCE; 33rd, Coal utilization & fuel systems; Coal for the future.*

MOHITPOUR, M., JENKINS, A. & NAHAS, G. 2008. A generalized overview of requirements for the design, construction, and operation of new pipelines for CO_2 sequestration. *The Journal of Pipeline Engineering,* 7**,** 237-252.

MOREIRA, M. & KURZ, M. 2013. Noble gases as tracers of mantle processes and magmatic degassing. *The Noble Gases as Geochemical Tracers.* Springer.

MYERS, M., STALKER, L., PEJCIC, B. & ROSS, A. 2013. Tracers–Past, present and future applications in CO_2 geosequestration. *Applied Geochemistry,* 30**,** 125-135.

MYERS, M., WHITE, C., STALKER, L. & ROSS, A. 2012. Literature review of tracer partition coefficients.

MYHRE, G., SHINDELL, D., BRÉON, F., COLLINS, W., FUGLESTVEDT, J., HUANG, J., KOCH, D., LAMARQUE, J., LEE, D. & MENDOZA, B. 2013. Anthropogenic and natural radiative forcing. *Climate change*, 659-740.

NATIONAL ENERGY TECHNOLOGY LABORATORY 2013. Appendix B: Carbon dioxide capture technology sheets.

NATIONAL GRID 2006. Specification for equipment for odour intensity monitoring. *Gas Industry Standard.*

NATIONAL GRID 2014. Long term development plan.

NEWELL, D. L., LARSON, T. E., PERKINS, G., PUGH, J. D., STEWART, B. W., CAPO, R. C. & TRAUTZ, R. C. 2014. Tracing CO_2 leakage into groundwater using carbon and strontium isotopes during a controlled CO2 release field test. *International Journal of Greenhouse Gas Control,* 29, 200-208.

NIMZ, G. J. & HUDSON, G. B. 2005. The use of noble gas isotopes for monitoring leakage of geologically stored CO_2. *Carbon Dioxide Capture for Storage in Deep Geologic Formations,* 2, 1113-1128.

NIST. 2002. *Chemistry webbook* [Online]. Available: http://webbook.nist.gov/chemistry/.

NOAA. 2015. *Trends in atmospheric carbon dioxide* [Online]. Available: http://www.esrl.noaa.gov/gmd/ccgg/trends/weekly.html.

NOLEN-HOEKSEMA, R. 2014. Flow through pores. *Oilfield Review Autumn,* 26.

OECD/IEA 2015. Recent trends in OECD CO_2 emissions from fuel combustion - 2015 preliminary edition.

OKOSHI, M. & NAKAYAMA, S. 2015. Generation and characteristics of radioactive wastes. *Radioactive Waste Engineering and Management.* Springer.

OLAJIRE, A. A. 2010. CO_2 capture and separation technologies for end-of-pipe applications – A review. *Energy,* 35, 2610-2628.

ONUMA, T. & OHKAWA, S. 2009. Detection of surface deformation related with CO_2 injection by DInSAR at In Salah, Algeria. *Energy Procedia,* 1, 2177-2184.

OZIMA, M. & PODOSEK, F. A. 2002. *Noble gas geochemistry*, Cambridge University Press.

PAK, T., BUTLER, I. B., GEIGER, S., VAN DIJKE, M. I. & SORBIE, K. S. 2015. Droplet fragmentation: 3D imaging of a previously unidentified pore-scale process during multiphase flow in porous media. *Proceedings of the National Academy of Sciences,* 112, 1947-1952.

PARFOMAK, P. W. & FOLGER, P. Carbon dioxide (CO_2) pipelines for carbon sequestration: Emerging policy issues. 2007. Congressional Research Service, Library of Congress.

PARLIAMENT OF THE UNITED KINGDOM 1974. Health and safety at work etc. act 1974. London: HSMO.

PARLIAMENT OF THE UNITED KINGDOM 1996. Pipeline safety regulations (S.I. 1996/825). London: HSMO.

PENG, D.-Y. & ROBINSON, D. B. 1976. A new two-constant equation of state. *Industrial & Engineering Chemistry Fundamentals,* 15**,** 59-64.

PERRY, M. & ELIASON, D. 2004. CO_2 recovery and sequestration at Dakota Gasification Company

PORCELLI, D., BALLENTINE, C. J. & WIELER, R. 2002. An overview of noble gas geochemistry and cosmochemistry. *Reviews in mineralogy and geochemistry,* 47**,** 1-19.

REINER, D. M. & NUTTALL, W. J. 2011. Public acceptance of geological disposal of carbon dioxide and radioactive waste: similarities and differences. *Geological disposal of carbon dioxide and radioactive waste: A comparative assessment.* Springer.

RIDING, J. B. & ROCHELLE, C. A. 2005. The IEA Weyburn CO_2 monitoring and storage project final report of the European research team. RR/05/03 ed.

ROBERTS, J. J., WOOD, R. A. & HASZELDINE, R. S. 2011. Assessing the health risks of natural CO2 seeps in Italy. *Proceedings of the National Academy of Sciences,* 108**,** 16545-16548.

SANCHEZ-VILA, X., GUADAGNINI, A. & CARRERA, J. 2006. Representative hydraulic conductivities in saturated groundwater flow. *Reviews of Geophysics,* 44.

SANO, Y., MARTY, B. & BURNARD, P. 2013. Noble gases in the atmosphere. *The Noble Gases as Geochemical Tracers.* Springer.

SCHEIDEGGER, A. E. 1963. Physics of flow through porous media. *Physics of flow through porous media.* University of Toronto.

SCHMIDT-HATTENBERGER, C., BERGMANN, P., BÖSING, D., LABITZKE, T., MÖLLER, M., SCHRÖDER, S., WAGNER, F. & SCHÜTT, H. 2013. Electrical Resistivity Tomography (ERT) for monitoring of CO_2 migration - from tool development to reservoir surveillance at the Ketzin pilot site. *Energy Procedia,* 37**,** 4268-4275.

SCOTTISH CARBON CAPTURE & STORAGE. 2015. *Global CCS map* [Online]. Available: www.sccs.org.uk/map.

SCOTTISHPOWER CCS CONSORTIUM 2011a. ScottishPower consortium UKCCS demonstration competition: Goldeneye CO_2 store environmental statement.

SCOTTISHPOWER CCS CONSORTIUM 2011b. UK carbon capture and storage demonstration competition.

SEIERSTEN, M. 2001. Materials selection for separation, transportation and disposal of CO_2. *CORROSION 2001*. Houston, Texas: NACA International.

SERPA, J., MORBEE, J. & TZIMAS, E. 2011. Technical and economic characteristics of a CO_2 transmission pipeline infrastructure. European Commission, Joint Research Centre. *Institute for Energy*.

SHI, J.-Q., XUE, Z. & DURUCAN, S. 2011. Supercritical CO_2 core flooding and imbibition in Tako sandstone—Influence of sub-core scale heterogeneity. *International Journal of Greenhouse Gas Control,* 5**,** 75-87.

SKJETNE, E. & AURIAULT, J.-L. 1999. High-velocity laminar and turbulent flow in porous media. *Transport in Porous Media,* 36**,** 131-147.

SLOVIC, P. 1987. Perception of risk. *Science,* 236**,** 280-285.

SONLEY, J. M. 2012. Tales from the odourisary. *Historic Gas Times* [Online], 71-74.

STAFFORD, M. & WILLIAMS, N. 1996. *Pipeline leak detection study*, HSE Books.

STALKER, L., BOREHAM, C. & PERKINS, E. 2009. A review of tracers in monitoring CO_2 breakthrough: properties, uses, case studies, and novel tracers.

STALKER, L., BOREHAM, C., UNDERSCHULTZ, J., FREIFELD, B., PERKINS, E., SCHACHT, U. & SHARMA, S. 2015. Application of tracers to measure, monitor and verify breakthrough of sequestered CO_2 at the CO2CRC Otway Project, Victoria, Australia. *Chemical Geology*.

STEVENS, J. C., CAIN, W. S., WEINSTEIN, D. E. & PIERCE, J. B. 1987. Aging impairs the ability to detect gas odor. *Fire Technology,* 23**,** 198-204.

STEWART, R., SCOTT, V., HASZELDINE, R. S., AINGER, D. & ARGENT, S. 2014. The feasibility of a European-wide integrated CO_2 transport network. *Greenhouse Gases: Science and Technology,* 4**,** 481-494.

STORK, A. L., VERDON, J. P. & KENDALL, J. M. 2015. The microseismic response at the In Salah Carbon Capture and Storage (CCS) site. *International Journal of Greenhouse Gas Control,* 32**,** 159-171.

SVENSSON, R., ODENBERGER, M., JOHNSSON, F. & STRÖMBERG, L. 2004. Transportation systems for CO_2—application to carbon capture and storage. *Energy Conversion and Management,* 45**,** 2343-2353.

TENKRAT, D., PROKES, O. & HLINCIK, T. 2010. *Natural gas odorization*, INTECH Open Access Publisher.

TEXAS STATE LIBRARY AND ARCHIVES COMMISSION. 2006. *Texas board of professional engineers: An inventory of board of professional engineers records at the Texas State archives, 1937, 1952, 1972-2001, 2005-2006, undated* [Online]. Available: http://www.lib.utexas.edu/taro/tslac/50009/tsl-50009.html#did [Accessed 28/02/2014.

TEXAS STATE LIBRARY AND ARCHIVES COMMISSION. 2011. *The disaster scene at New London, March 18, 1937* [Online]. Available: https://www.tsl.texas.gov/exhibits/railroad/other/newlondon.html.

THE NORTH AMERICAN COAL CORPORATION. 2006. *Lignite coal...Powering America's heartland* [Online]. Available: http://www.nacoal.com/operations/Coteau_freedomfacts_b1FD0.pdf#1FD0.pdf [Accessed 20/01 2013].

TORGERSEN, T. 1989. Terrestrial helium degassing fluxes and the atmospheric helium budget: implications with respect to the degassing processes of continental crust. *Chemical Geology: Isotope Geoscience section,* 79**,** 1-14.

TORGERSEN, T., KENNEDY, B. M. & VAN SOEST, M. C. 2004. Diffusive separation of noble gases and noble gas abundance patterns in sedimentary rocks. *Earth and Planetary Science Letters,* 226**,** 477-489.

US GOVERNMENT 2012. Code of Federal Regulations, 49 CFR 192.625 - Odorization of gas. Federal Register: Office of the Federal Register.

USHER, M. 1999. Odor fade–Possible causes and remedies. Elf Atochem North America. *Inc., USA***,** 12.

VAN DER LAND, C., WOOD, R., WU, K., VAN DIJKE, M. I. J., JIANG, Z., CORBETT, P. W. M. & COUPLES, G. 2013. Modelling the permeability evolution of carbonate rocks. *Marine and Petroleum Geology,* 48**,** 1-7.

WACKER, J. F., ZADNIK, M. G. & ANDERS, E. 1985. Laboratory simulation of meteoritic noble gases. I. Sorption of xenon on carbon: Trapping experiments. *Geochimica et Cosmochimica Acta,* 49**,** 1035-1048.

WADE, S. & GREENBERG, S. 2011. Social site characterisation: From concept to application. A re-view of relevant social science literature and a toolkit for social site characterisation. CSIRO, Australia. Online: www. globalccsinstitute. com/publications/social-site-characterisation-concept-application.

WALLQUIST, L., SEIGO, S. L. O., VISSCHERS, V. H. M. & SIEGRIST, M. 2012. Public acceptance of CCS system elements: A conjoint measurement. *International Journal of Greenhouse Gas Control,* 6**,** 77-83.

WARR, O., ROCHELLE, C. A., MASTERS, A. & BALLENTINE, C. J. 2015. Determining noble gas partitioning within a CO_2–H_2O system at elevated temperatures and pressures. *Geochimica et Cosmochimica Acta,* 159**,** 112-125.

WHITE, D. J., ROACH, L. A. & ROBERTS, B. 2015. Time-lapse seismic performance of a sparse permanent array: Experience from the Aquistore CO_2 storage site. *Geophysics,* 80**,** WA35-WA48.

WILKINSON, M., GILFILLAN, S. V. M., HASZELDINE, R. S. & BALLENTINE, C. J. 2010. Plumbing the depths: Testing natural tracers of subsurface CO_2 origin and migration, Utah. *Carbon Dioxide Sequestration in Geological Media State of the Science (Aapg Studies in Geology).*

WU, K., NUNAN, N., CRAWFORD, J. W., YOUNG, I. M. & RITZ, K. 2004. An efficient Markov chain model for the simulation of heterogeneous soil structure. *Soil Science Society of America Journal,* 68**,** 346-351.

WU, K., VAN DIJKE, M. I., COUPLES, G. D., JIANG, Z., MA, J., SORBIE, K. S., CRAWFORD, J., YOUNG, I. & ZHANG, X. 2006. 3D stochastic modelling of heterogeneous porous media–applications to reservoir rocks. *Transport in Porous Media,* 65**,** 443-467.

YANG, H., XU, Z., FAN, M., GUPTA, R., SLIMANE, R. B., BLAND, A. E. & WRIGHT, I. 2008. Progress in carbon dioxide separation and capture: A review. *Journal of Environmental Sciences,* 20**,** 14-27.

ZEP 2010. CO_2 transport costs. Post-demonstration CCS in the EU.

ZHANG, R., VASCO, D., DALEY, T. M. & HARBERT, W. 2015. Characterization of a fracture zone using seismic attributes at the In Salah CO_2 storage project. *Interpretation,* 3**,** SM37-SM46.

ZHU, C., ZHANG, G., LU, P., MENG, L. & JI, X. 2015. Benchmark modeling of the Sleipner CO_2 plume: Calibration to seismic data for the uppermost layer and model sensitivity analysis. *International Journal of Greenhouse Gas Control*.

Appendix I

Derivation of the velocity profile for compressible fluid flow

$$Q = \rho_1 v_1 A_1 = \rho_2 v_2 A_2 \tag{55}$$

Isothermal flow, constant mass.

Using Darcy's law:

$$Q = \frac{k}{\mu}\frac{dP}{dx}\rho A \tag{56}$$

We want to derive an expression for $\frac{dP}{dx}$ as a function of distance. We need to write density in terms of pressure, so using the perfect gas law:

$$PV = nRT \tag{57}$$

Then:

$$PV = \frac{m}{M}RT \tag{58}$$

$$P = \frac{m}{V}\frac{RT}{M} = \rho\frac{RT}{M} \tag{59}$$

So:

$$Q = \frac{k}{\mu}\frac{dP}{dx}\frac{M}{RT}PA \tag{60}$$

$$Q\frac{\mu RT}{kMA} = C = P\frac{dP}{dx} \tag{61}$$

$$\int Cdx = \int PdP \tag{62}$$

So:

$$Cx = \frac{P^2}{2} + ic \tag{63}$$

$$P^2 = 2Cx - 2ic \tag{64}$$

At x = 0, Pressure = P_1:

$$\therefore \qquad P_1^2 = -2ic \tag{65}$$

$$ic = -\frac{P_1^2}{2} \tag{66}$$

$$P^2 = 2Cx + P_1^2 \tag{67}$$

At x=L, Pressure = P_2:

$$C = \frac{P_2^2 - P_1^2}{2L} \tag{68}$$

So:

$$P = \sqrt{\frac{P_2^2 - P_1^2}{L} x + P_1^2} \tag{69}$$

$$\frac{d\left(P^2\right)}{dx} = \frac{d\left(2Cx\right)}{dx} + \frac{d\left(P_1^2\right)}{dx} \tag{70}$$

$$2P\frac{dP}{dx} = 2C \tag{71}$$

$$\frac{dP}{dx} = \frac{C}{P} \tag{72}$$

Appendix II

Expansion of one dimensional advection dispersion equation to a linear function

$$\boldsymbol{C(x,t) = \frac{M_0}{2\sqrt{\pi D_x t}} \times exp\left[-\left(\frac{(x-vt)^2}{4D_x t}\right)\right]} \tag{73}$$

$$log(y) = log\left(\frac{M_0}{2\sqrt{\pi D_x t}}\right) + log\left(exp\left[-\left(\frac{(x-vt)^2}{4D_x t}\right)\right]\right) \tag{74}$$

$$log(y) = log(M_0) - log\left(2\sqrt{\pi D_x t}\right) - \left(\frac{(x-vt)^2}{4D_x t}\right) \tag{75}$$

$$log(y) = log(M_0) - \left(log\left(2\sqrt{\pi D_x}\right) + {}^1\!/_2 \log(t)\right) - \left(\frac{(x^2 - 2xvt + v^2t^2)}{4D_x t}\right) \tag{76}$$

$$log(y) = log(M_0) + \frac{xv}{2D_x} - \log(2\sqrt{\pi D_x}) - {}^1\!/_2 \log(t) - \frac{x^2}{4D_x t} - \frac{v^2 t}{4D_x} \tag{77}$$

$$Coeffcient\ A = -{}^1\!/_2 \tag{78}$$

$$Coeffcient\ B = -\frac{x^2}{4D_x} \tag{79}$$

$$Coeffcient\ C = -\frac{v^2}{4D_x} \tag{80}$$

$$log(y) + {}^1\!/_2 \log(t) = -\frac{x^2}{4D_x t} - \frac{v^2 t}{4D_x} + \left[\frac{xv}{2D_x} - \log(2\sqrt{\pi D_x}) + log(M_0)\right] \tag{81}$$

$$v = \sqrt{\frac{Cx^2}{B}} \tag{82}$$

$$D_x = -\frac{x^2}{4B} \tag{83}$$

Appendix III

Statistical model outputs

Helium results

50,000 Pa

Here are the outputs for helium at pressure 50,000 Pa.

```
i<-5

if(i==1){ t <-  data1[,4] ; y <-  data1[,3]
        } else if (i==2){ t <-  data2[,4]   ; y <-  data2[,3]
        } else if (i==3){ t <-  data3[,4]   ; y <-  data3[,3]
        } else if (i==4){ t <-  data4[,4]   ; y <-  data4[,3]
        } else if (i==5){ t <-  data5[,4]   ; y <-  data5[,3]
   }

recT =  1/t

n<-length(y)
n<-97
nStart<-  24
```

```
fit <-  lm( log(y[nStart:n]) ~    log(t[nStart:n]) +  recT[nStart:n] +  t[nSt
art:n]  )
summary(fit)

##
## Call:
## lm(formula = log(y[nStart:n]) ~ log(t[nStart:n]) + recT[nStart:n] +
##     t[nStart:n])
##
## Residuals:
##      Min       1Q   Median       3Q      Max
## -2.21169 -0.06110  0.02162  0.09229  0.97614
##
## Coefficients:
##                  Estimate Std. Error t value Pr(>|t|)
## (Intercept)      -14.94066   28.81696  -0.518   0.6058
## log(t[nStart:n])   5.31415    6.85696   0.775   0.4409
## recT[nStart:n]   -20.41242  219.83372  -0.093   0.9263
## t[nStart:n]       -0.11070    0.04943  -2.239   0.0283 *
## ---
## Signif. codes:  0 '***' 0.001 '**' 0.01 '*' 0.05 '.' 0.1 ' ' 1
##
## Residual standard error: 0.4406 on 70 degrees of freedom
## Multiple R-squared:  0.8455, Adjusted R-squared:  0.8389
## F-statistic: 127.7 on 3 and 70 DF,  p-value: < 2.2e-16

#plot(fit)
```

```
par(mfrow=c(1,1))

yOut <- exp(fit$coeff[1] + fit$coeff[2]*log(t) + fit$coeff[3]*recT +
fit$coeff[4]*t)
#plot(t,y)
#points( t, yOut, col=2, type="l", lwd=2)

yOut <- fit$coeff[1] + fit$coeff[2]*log(t) + fit$coeff[3]*recT + fit$c
oeff[4]*t
#plot(t,log(y))
#points( t, yOut, col=2, type="l", lwd=2)


y2 = log(y[nStart:n]) + 0.5*log(t[nStart:n])
fit2 <- lm( y2 ~      recT[nStart:n] + t[nStart:n] )

yOut <- exp(fit2$coeff[1] - 0.5*log(t) + fit2$coeff[2]*recT + fit2$c
oeff[3]*t)
plot(t,y, xlab="Time (s)", ylab="Normalised concentration")
points( t, yOut, col=2, type="l", lwd=2)
```

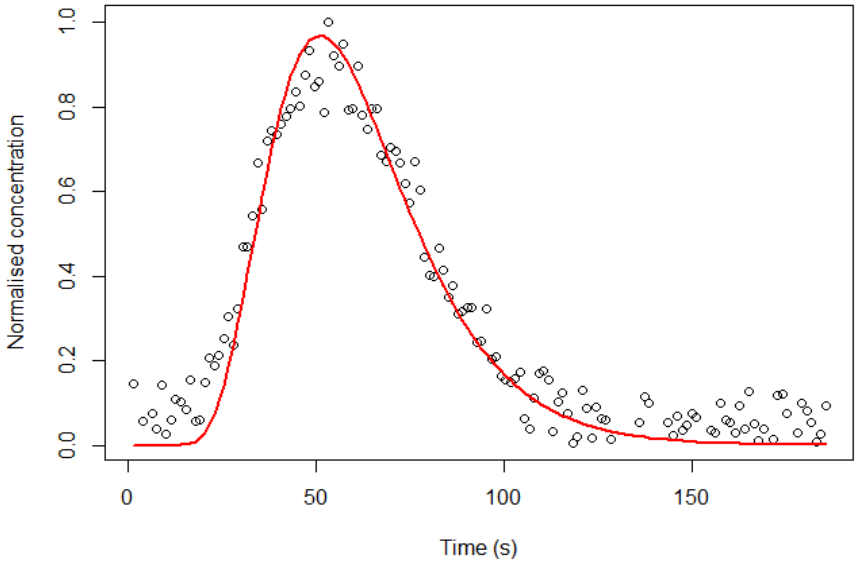


```
yOut <- fit2$coeff[1] - 0.5*log(t) + fit2$coeff[2]*recT + fit2$coeff[
3]*t
plot(t,log(y),xlab="Time (s)")
points( t, yOut, col=2, type="l", lwd=2)

summary(fit2)
```

```
##
## Call:
## lm(formula = y2 ~ recT[nStart:n] + t[nStart:n])
##
## Residuals:
##      Min       1Q   Median       3Q      Max
## -2.24652 -0.07052  0.02595  0.12927  0.92612
##
## Coefficients:
##                  Estimate Std. Error t value Pr(>|t|)
## (Intercept)     9.484e+00  8.042e-01  11.793  < 2e-16 ***
## recT[nStart:n] -2.055e+02  2.578e+01  -7.972 1.88e-11 ***
## t[nStart:n]    -6.905e-02  5.557e-03 -12.426  < 2e-16 ***
## ---
## Signif. codes:  0 '***' 0.001 '**' 0.01 '*' 0.05 '.' 0.1 ' ' 1
##
## Residual standard error: 0.4397 on 71 degrees of freedom
## Multiple R-squared:  0.7949, Adjusted R-squared:  0.7891
## F-statistic: 137.6 on 2 and 71 DF,  p-value: < 2.2e-16
```

```
plot(fit2)
```

Calculated values using coefficents from model.

```
# Output pressure
P <-  i *  10000

# Sample Length
x <-  0.96

# Dynamic viscosity
mu <-  1.48E-5

# Mass injection
M0 <-  1

# Effective porosity
ne <-  0.1785

#Diffusion
Dg_List_Helium<-c(5.2917E-5, 5.0540E-5, 4.8368E-5, 4.6374E-5, 4.4
539E-5)
Dg<-Dg_List_Helium[i]

#B = -(x^2/4*D)
B <-  coef(summary(fit2))["recT[nStart:n]","Estimate"]
#C =  -(v^2/4*D)
C <-  coef(summary(fit2))["t[nStart:n]","Estimate"]

#Calculate the following:

#Advective Velocity
v <-  sqrt((C*(x)^2)/B)

#Permeability
K <-  v*ne*x*mu/P

#Hydrodynamic Dispersion Coeffcient
```

```
D <-  -((x^2)/(4*B)

#Mechanical Dispersion
Ds <-  ((D -  (ne *  Dg)) /  v)



#Resulting Outputs
v; K; D; Ds
```

```
## [1] 0.0175967
```

```
## [1] 8.925495e-13
```

```
## [1] 0.001121168
```

```
## [1] 0.063
```

40,000 Pa

Here are the outputs for helium at pressure 40,000 Pa.

```
i<-4

if(i==1){ t <- data1[,4] ; y <- data1[,3]
        } else if (i==2){ t <- data2[,4]   ; y <- data2[,3]
        } else if (i==3){ t <- data3[,4]   ; y <- data3[,3]
        } else if (i==4){ t <- data4[,4]   ; y <- data4[,3]
        } else if (i==5){ t <- data5[,4]   ; y <- data5[,3]
   }

recT = 1/t

n<-length(y)
n<-112
nStart<- 33


fit <- lm( log(y[nStart:n]) ~  log(t[nStart:n]) + recT[nStart:n] + t[nStart:
n]  )
summary(fit)

##
## Call:
## lm(formula = log(y[nStart:n]) ~ log(t[nStart:n]) + recT[nStart:n] +
##     t[nStart:n])
##
## Residuals:
##      Min       1Q   Median       3Q      Max
## -2.77307 -0.07076  0.01861  0.11829  1.32631
##
## Coefficients:
##                   Estimate Std. Error t value Pr(>|t|)
## (Intercept)        2.58949   39.15328   0.066    0.947
## log(t[nStart:n])   1.38807    8.90009   0.156    0.876
## recT[nStart:n]   -231.24472  350.02184  -0.661    0.511
## t[nStart:n]        -0.07577    0.05305  -1.428    0.157
##
## Residual standard error: 0.4527 on 76 degrees of freedom
## Multiple R-squared:  0.8081, Adjusted R-squared:  0.8005
## F-statistic: 106.7 on 3 and 76 DF,  p-value: < 2.2e-16

#plot(fit)


par(mfrow=c(1,1))

yOut <- exp(fit$coeff[1]  + fit$coeff[2]*log(t) + fit$coeff[3]*recT + fit
$coeff[4]*t)
#plot(t,y)
#points( t, yOut, col=2, type="l", lwd=2)

yOut <- fit$coeff[1]  + fit$coeff[2]*log(t) + fit$coeff[3]*recT + fit$coef
f[4]*t
#plot(t,log(y))
#points( t, yOut, col=2, type="l", lwd=2)
```

```
y2 = log(y[nStart:n]) + 0.5*log(t[nStart:n])
fit2 <- lm( y2 ~   recT[nStart:n] + t[nStart:n]  )

yOut <- exp(fit2$coeff[1]  - 0.5*log(t) + fit2$coeff[2]*recT + fit2$coeff
[3]*t)
plot(t,y, xlab="Time (s)", ylab="Normalised concentration")
points( t, yOut, col=2, type="l", lwd=2)
```

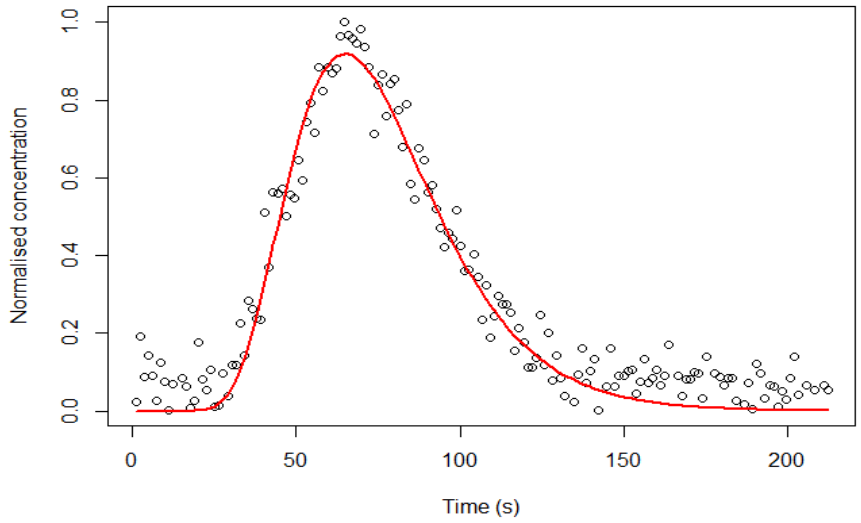


```
yOut <- fit2$coeff[1]  - 0.5*log(t) + fit2$coeff[2]*recT + fit2$coeff[3]*
t
plot(t,log(y),xlab="Time (s)")
points( t, yOut, col=2, type="l", lwd=2)
```

```
summary(fit2)

##
## Call:
## lm(formula = y2 ~ recT[nStart:n] + t[nStart:n])
##
## Residuals:
##      Min       1Q   Median       3Q      Max
## -2.78972 -0.06562  0.02046  0.11765  1.30335
##
## Coefficients:
##                  Estimate Std. Error t value Pr(>|t|)
## (Intercept)     1.089e+01  9.472e-01  11.501  < 2e-16 ***
## recT[nStart:n] -3.051e+02  3.717e+01  -8.206 4.07e-12 ***
## t[nStart:n]    -6.457e-02  5.468e-03 -11.811  < 2e-16 ***
## ---
## Signif. codes:  0 '***' 0.001 '**' 0.01 '*' 0.05 '.' 0.1 ' ' 1
##
## Residual standard error: 0.4499 on 77 degrees of freedom
## Multiple R-squared:  0.7527, Adjusted R-squared:  0.7462
## F-statistic: 117.2 on 2 and 77 DF,  p-value: < 2.2e-16

plot(fit2)
```

Calculated values using coefficents from model.

```
#Resulting Outputs
v; K; D; Ds

## [1] 0.01396688

## [1] 8.855452e-13

## [1] 0.000755162

## [1] 0.053
```

30,000 Pa

Here are the outputs for helium at pressure 30,000 Pa.

```
i<-3

if(i==1){ t <-  data1[,4] ; y <-  data1[,3]
        } else if (i==2){ t <-  data2[,4]   ; y <-  data2[,3]
        } else if (i==3){ t <-  data3[,4]   ; y <-  data3[,3]
        } else if (i==4){ t <-  data4[,4]   ; y <-  data4[,3]
        } else if (i==5){ t <-  data5[,4]   ; y <-  data5[,3]
   }

recT =  1/t

n<-length(y)
n<-140
nStart<-  48


fit <-  lm( log(y[nStart:n]) ~    log(t[nStart:n]) +  recT[nStart:n] +  t[nSt
art:n]  )
summary(fit)

##
## Call:
## lm(formula = log(y[nStart:n]) ~ log(t[nStart:n]) + recT[nStart:n] +
##     t[nStart:n])
##
## Residuals:
##      Min       1Q   Median       3Q      Max
## -2.38758 -0.06221  0.01742  0.09989  0.92559
##
## Coefficients:
##                   Estimate Std. Error t value Pr(>|t|)
## (Intercept)       34.48288   51.65718   0.668    0.506
## log(t[nStart:n])  -4.97112   10.96028  -0.454    0.651
## recT[nStart:n]   -766.81272  595.60755  -1.287    0.201
## t[nStart:n]       -0.04050    0.04811  -0.842    0.402
##
## Residual standard error: 0.3747 on 89 degrees of freedom
## Multiple R-squared:  0.861,  Adjusted R-squared:  0.8563
## F-statistic: 183.7 on 3 and 89 DF,  p-value: < 2.2e-16

#plot(fit)


par(mfrow=c(1,1))

yOut <-  exp(fit$coeff[1]  +  fit$coeff[2]*log(t) +  fit$coeff[3]*recT +
fit$coeff[4]*t)
#plot(t,y)
#points( t, yOut, col=2, type="l", lwd=2)

yOut <-  fit$coeff[1]  +  fit$coeff[2]*log(t) +  fit$coeff[3]*recT +  fit$c
oeff[4]*t
#plot(t,log(y))
#points( t, yOut, col=2, type="l", lwd=2)
```

```
y2 =  log(y[nStart:n]) +  0.5*log(t[nStart:n])
fit2 <-  lm( y2 ~      recT[nStart:n] +  t[nStart:n]  )

yOut <-  exp(fit2$coeff[1]  -  0.5*log(t) +  fit2$coeff[2]*recT +  fit2$c
oeff[3]*t)
plot(t,y, xlab="Time (s)", ylab="Normalised concentration")
points( t, yOut, col=2, type="l", lwd=2)
```

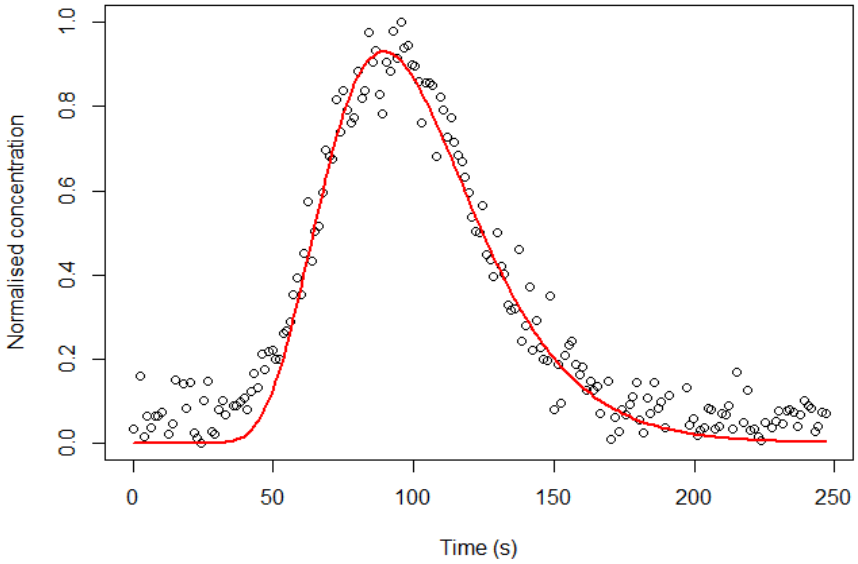


```
yOut <-  fit2$coeff[1]  -  0.5*log(t) +  fit2$coeff[2]*recT +  fit2$coeff[
3]*t
plot(t,log(y),xlab="Time (s)")
points( t, yOut, col=2, type="l", lwd=2)

summary(fit2)
```

```
##
## Call:
## lm(formula = y2 ~ recT[nStart:n] + t[nStart:n])
##
## Residuals:
##      Min       1Q   Median       3Q      Max
## -2.38047 -0.06998  0.02690  0.10384  0.94958
##
## Coefficients:
##                  Estimate Std. Error t value Pr(>|t|)
## (Intercept)     1.341e+01  9.855e-01   13.61  < 2e-16 ***
## recT[nStart:n] -5.248e+02  5.350e+01   -9.81 7.08e-16 ***
## t[nStart:n]    -6.005e-02  4.223e-03  -14.22  < 2e-16 ***
## ---
## Signif. codes:  0 '***' 0.001 '**' 0.01 '*' 0.05 '.' 0.1 ' ' 1
##
## Residual standard error: 0.373 on 90 degrees of freedom
## Multiple R-squared:  0.8223, Adjusted R-squared:  0.8183
## F-statistic: 208.2 on 2 and 90 DF,  p-value: < 2.2e-16
```

```
plot(fit2)
```

Calculated values using coefficents from model.

```
#Resulting Outputs
v; K; D; Ds
```

```
## [1] 0.01026852
```

```
## [1] 8.680764e-13
```

```
## [1] 0.000439024
```

```
## [1] 0.042
```

20,000 Pa

Here are the outputs for helium at pressure 20,000 Pa.

```
i<-2

if(i==1){ t <-  data1[,4] ; y <-  data1[,3]
        } else if (i==2){ t <-  data2[,4]   ; y <-  data2[,3]
        } else if (i==3){ t <-  data3[,4]   ; y <-  data3[,3]
        } else if (i==4){ t <-  data4[,4]   ; y <-  data4[,3]
        } else if (i==5){ t <-  data5[,4]   ; y <-  data5[,3]
   }

recT =  1/t

n<-length(y)
n<-192
nStart<-  76


fit <-  lm( log(y[nStart:n]) ~    log(t[nStart:n]) +  recT[nStart:n] +  t[nSt
art:n]  )
summary(fit)

##
## Call:
## lm(formula = log(y[nStart:n]) ~ log(t[nStart:n]) + recT[nStart:n] +
##     t[nStart:n])
##
## Residuals:
##     Min      1Q  Median      3Q     Max
## -6.1414 -0.0374  0.0132  0.1236  1.1516
##
## Coefficients:
##                   Estimate Std. Error t value Pr(>|t|)
## (Intercept)       1.556e+02  1.284e+02   1.211    0.228
## log(t[nStart:n]) -2.781e+01  2.522e+01  -1.103    0.272
## recT[nStart:n]   -3.108e+03  2.014e+03  -1.543    0.126
## t[nStart:n]       2.890e-02  7.617e-02   0.379    0.705
##
## Residual standard error: 0.6462 on 113 degrees of freedom
## Multiple R-squared:   0.73,  Adjusted R-squared:  0.7228
## F-statistic: 101.8 on 3 and 113 DF,  p-value: < 2.2e-16

#plot(fit)


par(mfrow=c(1,1))

yOut <-  exp(fit$coeff[1]  +  fit$coeff[2]*log(t) +  fit$coeff[3]*recT +
fit$coeff[4]*t)
#plot(t,y)
#points( t, yOut, col=2, type="l", lwd=2)

yOut <-  fit$coeff[1]  +  fit$coeff[2]*log(t) +  fit$coeff[3]*recT +  fit$c
oeff[4]*t
#plot(t,log(y))
#points( t, yOut, col=2, type="l", lwd=2)
```

```
y2 =  log(y[nStart:n]) +  0.5*log(t[nStart:n])
fit2 <-  lm( y2 ~      recT[nStart:n] +  t[nStart:n]  )

yOut <-  exp(fit2$coeff[1]  -  0.5*log(t) +  fit2$coeff[2]*recT +  fit2$c
oeff[3]*t)
plot(t,y, xlab="Time (s)", ylab="Normalised concentration")
points( t, yOut, col=2, type="l", lwd=2)
```

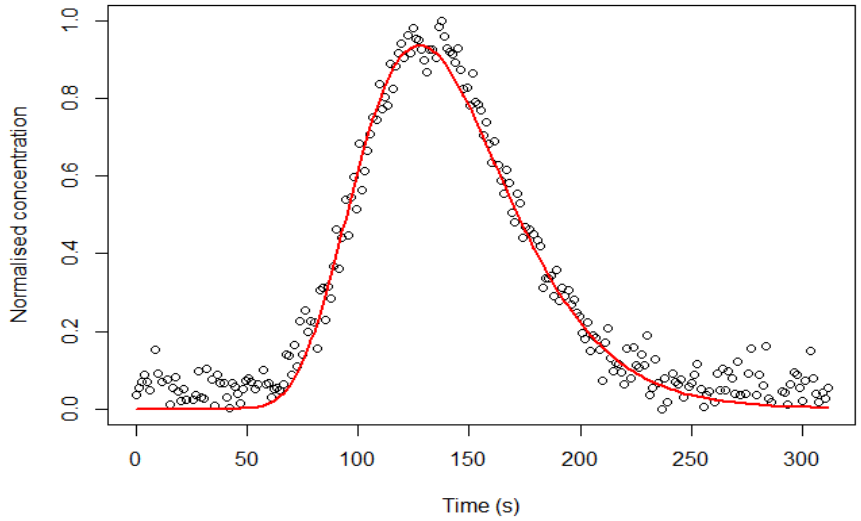


```
yOut <-  fit2$coeff[1]  -  0.5*log(t) +  fit2$coeff[2]*recT +  fit2$coeff[
3]*t
plot(t,log(y),xlab="Time (s)")
points( t, yOut, col=2, type="l", lwd=2)

summary(fit2)

##
## Call:
## lm(formula = y2 ~ recT[nStart:n] + t[nStart:n])
##
## Residuals:
##     Min      1Q  Median      3Q     Max
## -6.1100 -0.0511  0.0337  0.0859  1.2964
##
## Coefficients:
##                  Estimate Std. Error t value Pr(>|t|)
## (Intercept)     1.648e+01  1.991e+00   8.276 2.70e-13 ***
## recT[nStart:n] -9.328e+02  1.589e+02  -5.871 4.36e-08 ***
## t[nStart:n]    -5.337e-02  5.903e-03  -9.040 4.75e-15 ***
## ---
## Signif. codes:  0 '***' 0.001 '**' 0.01 '*' 0.05 '.' 0.1 ' ' 1
##
## Residual standard error: 0.6467 on 114 degrees of freedom
## Multiple R-squared:  0.6783, Adjusted R-squared:  0.6726
## F-statistic: 120.2 on 2 and 114 DF,  p-value: < 2.2e-16

plot(fit2)
```

Calculated values using coefficents from model.

```
#Resulting Outputs
v; K; D; Ds
```

```
## [1] 0.007261367
```

```
## [1] 9.207878e-13
```

```
## [1] 0.000246998
```

```
## [1] 0.033
```

10,000 Pa

Here are the outputs for helium at pressure 10,000 Pa.

```
i<-1

if(i==1){ t <-  data1[,4] ; y <-  data1[,3]
        } else if (i==2){ t <-  data2[,4]   ; y <-  data2[,3]
        } else if (i==3){ t <-  data3[,4]   ; y <-  data3[,3]
        } else if (i==4){ t <-  data4[,4]   ; y <-  data4[,3]
        } else if (i==5){ t <-  data5[,4]   ; y <-  data5[,3]
   }

recT =  1/t

n<-length(y)
n<-352
nStart<-  130


fit <-  lm( log(y[nStart:n]) ~    log(t[nStart:n]) +  recT[nStart:n] +  t[nSt
art:n]  )
summary(fit)

##
## Call:
## lm(formula = log(y[nStart:n]) ~ log(t[nStart:n]) + recT[nStart:n] +
##     t[nStart:n])
##
## Residuals:
##      Min       1Q   Median       3Q      Max
## -1.39676 -0.10060  0.01522  0.12367  0.89819
##
## Coefficients:
##                   Estimate Std. Error t value Pr(>|t|)
## (Intercept)       2.923e+02  3.208e+01   9.111  < 2e-16 ***
## log(t[nStart:n]) -4.922e+01  5.682e+00  -8.662 1.03e-15 ***
## recT[nStart:n]   -8.589e+03  7.878e+02 -10.902  < 2e-16 ***
## t[nStart:n]       5.472e-02  9.828e-03   5.567 7.53e-08 ***
## ---
## Signif. codes:  0 '***' 0.001 '**' 0.01 '*' 0.05 '.' 0.1 ' ' 1
##
## Residual standard error: 0.2507 on 219 degrees of freedom
## Multiple R-squared:  0.9253, Adjusted R-squared:  0.9243
## F-statistic: 904.4 on 3 and 219 DF,  p-value: < 2.2e-16

#plot(fit)


par(mfrow=c(1,1))

yOut <-  exp(fit$coeff[1]  +  fit$coeff[2]*log(t) +  fit$coeff[3]*recT +
fit$coeff[4]*t)
#plot(t,y)
#points( t, yOut, col=2, type="l", lwd=2)

yOut <-  fit$coeff[1]  +  fit$coeff[2]*log(t) +  fit$coeff[3]*recT +  fit$c
oeff[4]*t
```

```
#plot(t,log(y))
#points( t, yOut, col=2, type="l", lwd=2)


y2 =  log(y[nStart:n]) +  0.5*log(t[nStart:n])
fit2 <-  lm( y2 ~      recT[nStart:n] +  t[nStart:n]  )

yOut <-  exp(fit2$coeff[1]  -  0.5*log(t) +  fit2$coeff[2]*recT +  fit2$c
oeff[3]*t)
plot(t,y, xlab="Time (s)", ylab="Normalised concentration")
points( t, yOut, col=2, type="l", lwd=2)
```

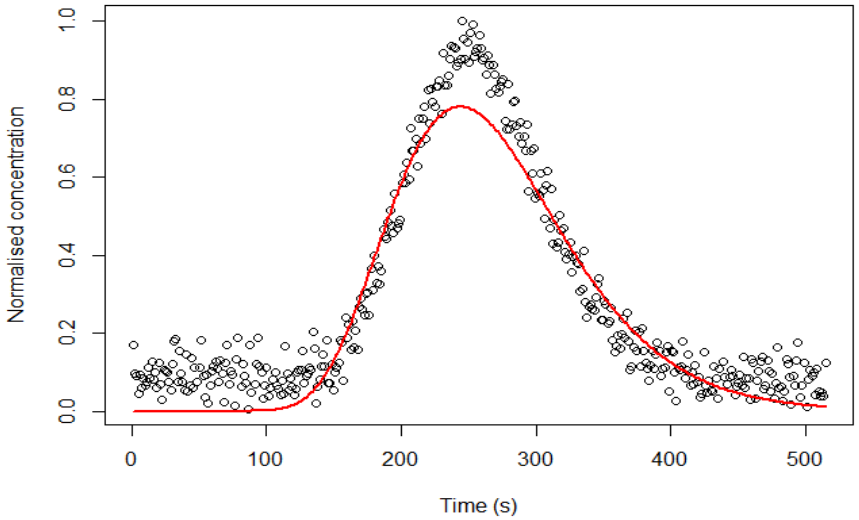


```
yOut <-  fit2$coeff[1]  -  0.5*log(t) +  fit2$coeff[2]*recT +  fit2$coeff[
3]*t
plot(t,log(y),xlab="Time (s)")
points( t, yOut, col=2, type="l", lwd=2)

summary(fit2)

##
## Call:
```

```
## lm(formula = y2 ~ recT[nStart:n] + t[nStart:n])
##
## Residuals:
##      Min       1Q   Median       3Q      Max
## -1.43706 -0.15464  0.02719  0.14515  1.20325
##
## Coefficients:
##                  Estimate Std. Error t value Pr(>|t|)
## (Intercept)     1.726e+01  5.562e-01   31.03   <2e-16 ***
## recT[nStart:n] -1.858e+03  7.706e+01  -24.11   <2e-16 ***
## t[nStart:n]    -2.926e-02  9.414e-04  -31.08   <2e-16 ***
## ---
## Signif. codes:  0 '***' 0.001 '**' 0.01 '*' 0.05 '.' 0.1 ' ' 1
##
## Residual standard error: 0.2891 on 220 degrees of freedom
## Multiple R-squared:  0.8747, Adjusted R-squared:  0.8736
## F-statistic: 767.9 on 2 and 220 DF,  p-value: < 2.2e-16
```

```
plot(fit2)
```

Calculated values using coefficents from model.

```
#Resulting Outputs
v; K; D; Ds

## [1] 0.003809375

## [1] 9.661063e-13

## [1] 0.000124004

## [1] 0.030
```

Neon results

50,000 Pa

Here are the outputs for neon at pressure 50,000 Pa.

```
i<-5


if(i==1){ t <-  data1[,4] ; y <-  data1[,3]
        } else if (i==2){ t <-  data2[,2]   ; y <-  data2[,1]
        } else if (i==3){ t <-  data3[,4]   ; y <-  data3[,3]
        } else if (i==4){ t <-  data4[,4]   ; y <-  data4[,3]
        } else if (i==5){ t <-  data5[,4]   ; y <-  data5[,3]
        }


recT =  1/t

n<-length(y)
n<-92
nStart<-0


fit <-  lm( log(y[nStart:n]) ~    log(t[nStart:n]) +  recT[nStart:n] +  t[nSt
art:n]  )
summary(fit)
```

```
##
## Call:
## lm(formula = log(y[nStart:n]) ~ log(t[nStart:n]) + recT[nStart:n] +
##     t[nStart:n])
##
## Residuals:
##      Min       1Q   Median       3Q      Max
## -0.86749 -0.43492  0.05457  0.42584  0.97756
##
## Coefficients:
##                   Estimate Std. Error t value Pr(>|t|)
## (Intercept)       1.831566   2.185521   0.838   0.4136
## log(t[nStart:n]) -0.276055   0.601107  -0.459   0.6519
## recT[nStart:n]   -9.803923   3.860199  -2.540   0.0212 *
## t[nStart:n]      -0.024600   0.005438  -4.524   0.0003 ***
## ---
## Signif. codes:  0 '***' 0.001 '**' 0.01 '*' 0.05 '.' 0.1 ' ' 1
##
## Residual standard error: 0.5695 on 17 degrees of freedom
##   (71 observations deleted due to missingness)
## Multiple R-squared:  0.9324, Adjusted R-squared:  0.9204
## F-statistic: 78.11 on 3 and 17 DF,  p-value: 3.79e-10

#plot(fit)


par(mfrow=c(1,1))

yOut <-  exp(fit$coeff[1]  +  fit$coeff[2]*log(t) +  fit$coeff[3]*recT +
```

```
fit$coeff[4]*t)
#plot(t,y)
#points( t, yOut, col=2, type="l", lwd=2)

yOut <-  fit$coeff[1]  +  fit$coeff[2]*log(t) +  fit$coeff[3]*recT +  fit$c
oeff[4]*t
#plot(t,log(y))
#points( t, yOut, col=2, type="l", lwd=2)


y2 =  log(y[nStart:n]) +  0.5*log(t[nStart:n])
fit2 <-  lm( y2 ~      recT[nStart:n] +  t[nStart:n]  )

yOut <-  exp(fit2$coeff[1]  -  0.5*log(t) +  fit2$coeff[2]*recT +  fit2$c
oeff[3]*t)
plot(t,y, xlab="Time (s)", ylab="Normalised concentration")
points( t, yOut, col=2, type="l", lwd=2)
```

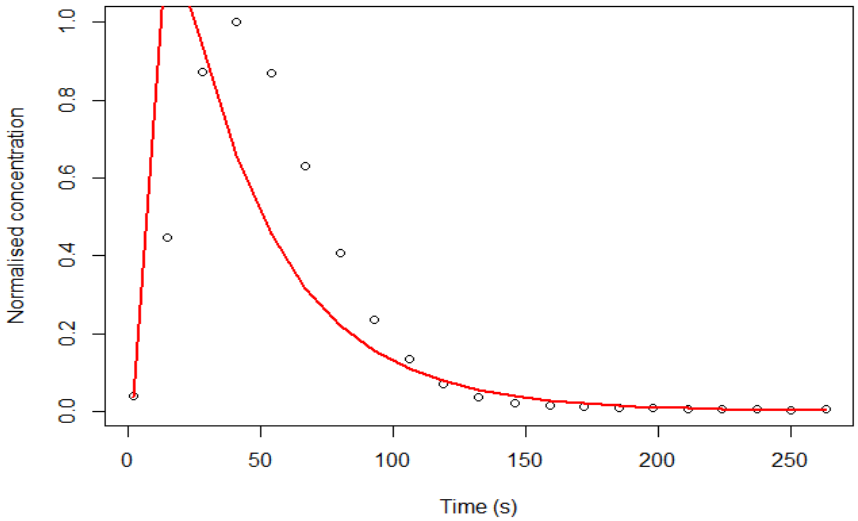


```
yOut <-  fit2$coeff[1]  -  0.5*log(t) +  fit2$coeff[2]*recT +  fit2$coeff[
3]*t
plot(t,log(y),xlab="Time (s)")
points( t, yOut, col=2, type="l", lwd=2)

summary(fit2)

##
## Call:
```

```
## lm(formula = y2 ~ recT[nStart:n] + t[nStart:n])
##
## Residuals:
##      Min       1Q   Median       3Q      Max
## -1.00695 -0.39128  0.03616  0.41705  0.91947
##
## Coefficients:
##                  Estimate Std. Error t value Pr(>|t|)
## (Intercept)      2.638700   0.280851   9.395 2.31e-08 ***
## recT[nStart:n] -11.153303   1.302759  -8.561 9.21e-08 ***
## t[nStart:n]     -0.022684   0.001723 -13.165 1.12e-10 ***
## ---
## Signif. codes:  0 '***' 0.001 '**' 0.01 '*' 0.05 '.' 0.1 ' ' 1
##
## Residual standard error: 0.5558 on 18 degrees of freedom
##   (71 observations deleted due to missingness)
## Multiple R-squared:  0.9098, Adjusted R-squared:  0.8997
## F-statistic: 90.73 on 2 and 18 DF,  p-value: 3.97e-10
```

```
plot(fit2)
```

Calculated values using coefficents from model.

```
#Resulting Outputs
v; K; D; Ds
```

```
## [1] 0.04329444
```

```
## [1] 2.196005e-12
```

```
## [1] 0.0207
```

```
## [1] 0.477
```

40,000 Pa

Here are the outputs for neon at pressure 40,000 Pa.

```
i<-4



if(i==1){ t <-  data1[,4] ; y <-  data1[,3]
        } else if (i==2){ t <-  data2[,2]   ; y <-  data2[,1]
        } else if (i==3){ t <-  data3[,4]   ; y <-  data3[,3]
        } else if (i==4){ t <-  data4[,4]   ; y <-  data4[,3]
        } else if (i==5){ t <-  data5[,4]   ; y <-  data5[,3]
        }


recT =  1/t

n<-length(y)
n<-109
nStart<-0


fit <-  lm( log(y[nStart:n]) ~    log(t[nStart:n]) +  recT[nStart:n] +  t[nSt
art:n]  )
summary(fit)

##
## Call:
## lm(formula = log(y[nStart:n]) ~ log(t[nStart:n]) + recT[nStart:n] +
##     t[nStart:n])
##
## Residuals:
##      Min       1Q   Median       3Q      Max
## -0.80345 -0.30889  0.07156  0.40220  1.02104
##
## Coefficients:
##                   Estimate Std. Error t value Pr(>|t|)
## (Intercept)        0.918869   3.163331   0.290   0.7750
## log(t[nStart:n])   0.252499   0.808188   0.312   0.7585
## recT[nStart:n]   -29.427297  11.744251  -2.506   0.0227 *
## t[nStart:n]       -0.031706   0.006083  -5.212 7.05e-05 ***
## ---
## Signif. codes:  0 '***' 0.001 '**' 0.01 '*' 0.05 '.' 0.1 ' ' 1
##
## Residual standard error: 0.5129 on 17 degrees of freedom
##   (88 observations deleted due to missingness)
## Multiple R-squared:  0.9465, Adjusted R-squared:  0.937
## F-statistic: 100.2 on 3 and 17 DF,  p-value: 5.239e-11

#plot(fit)


par(mfrow=c(1,1))

yOut <-  exp(fit$coeff[1]  +  fit$coeff[2]*log(t) +  fit$coeff[3]*recT +
fit$coeff[4]*t)
#plot(t,y)
```

```
#points( t, yOut, col=2, type="l", lwd=2)

yOut <-  fit$coeff[1]  +  fit$coeff[2]*log(t) +  fit$coeff[3]*recT +  fit$c
oeff[4]*t
#plot(t,log(y))
#points( t, yOut, col=2, type="l", lwd=2)


y2 =  log(y[nStart:n]) +  0.5*log(t[nStart:n])
fit2 <-  lm( y2 ~      recT[nStart:n] +  t[nStart:n]  )

yOut <-  exp(fit2$coeff[1]  -  0.5*log(t) +  fit2$coeff[2]*recT +  fit2$c
oeff[3]*t)
plot(t,y, xlab="Time (s)", ylab="Normalised concentration")
points( t, yOut, col=2, type="l", lwd=2)
```

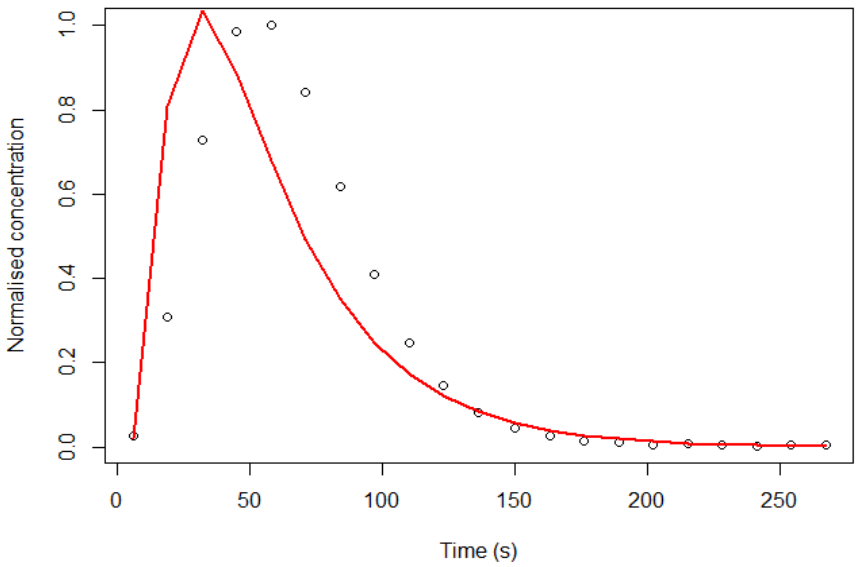


```
yOut <-  fit2$coeff[1]  -  0.5*log(t) +  fit2$coeff[2]*recT +  fit2$coeff[
3]*t
plot(t,log(y),xlab="Time (s)")
points( t, yOut, col=2, type="l", lwd=2)

summary(fit2)
```

```
##
## Call:
## lm(formula = y2 ~ recT[nStart:n] + t[nStart:n])
##
## Residuals:
##      Min       1Q   Median       3Q      Max
## -0.96600 -0.35360  0.03332  0.38911  0.88332
##
## Coefficients:
##                 Estimate Std. Error t value Pr(>|t|)
## (Intercept)      3.85022    0.30697   12.54 2.47e-10 ***
## recT[nStart:n] -39.72961    3.92229  -10.13 7.33e-09 ***
## t[nStart:n]     -0.02628    0.00173  -15.19 1.04e-11 ***
## ---
## Signif. codes:  0 '***' 0.001 '**' 0.01 '*' 0.05 '.' 0.1 ' ' 1
##
## Residual standard error: 0.511 on 18 degrees of freedom
##   (88 observations deleted due to missingness)
## Multiple R-squared:  0.9284, Adjusted R-squared:  0.9205
## F-statistic: 116.7 on 2 and 18 DF,  p-value: 4.937e-11
```

```
plot(fit2)
```

Calculated values using coefficents from model.

```
#Resulting Outputs
v; K; D; Ds
```

```
## [1] 0.02468931
```

```
## [1] 1.565381e-12
```

```
## [1] 0.0058
```

```
## [1] 0.235
```

30,000 Pa

Here are the outputs for neon at pressure 30,000 Pa.

```
i<-3



if(i==1){ t <-  data1[,4] ; y <-  data1[,3]
        } else if (i==2){ t <-  data2[,2]   ; y <-  data2[,1]
        } else if (i==3){ t <-  data3[,4]   ; y <-  data3[,3]
        } else if (i==4){ t <-  data4[,4]   ; y <-  data4[,3]
        } else if (i==5){ t <-  data5[,4]   ; y <-  data5[,3]
        }


recT =  1/t

n<-length(y)
n<-139
nStart<-0


fit <-  lm( log(y[nStart:n]) ~    log(t[nStart:n]) +  recT[nStart:n] +  t[nSt
art:n]  )
summary(fit)

##
## Call:
## lm(formula = log(y[nStart:n]) ~ log(t[nStart:n]) + recT[nStart:n] +
##     t[nStart:n])
##
## Residuals:
##      Min       1Q   Median       3Q      Max
## -0.51638 -0.26724  0.04643  0.22546  0.59815
##
## Coefficients:
##                   Estimate Std. Error t value Pr(>|t|)
## (Intercept)      -12.624153   1.791201  -7.048 1.04e-06 ***
## log(t[nStart:n])   3.828669   0.450950   8.490 6.85e-08 ***
## recT[nStart:n]    -1.179108   6.788149  -0.174    0.864
## t[nStart:n]       -0.055034   0.003177 -17.324 4.26e-13 ***
## ---
## Signif. codes:  0 '***' 0.001 '**' 0.01 '*' 0.05 '.' 0.1 ' ' 1
##
## Residual standard error: 0.3134 on 19 degrees of freedom
##   (116 observations deleted due to missingness)
## Multiple R-squared:  0.9833, Adjusted R-squared:  0.9807
## F-statistic: 373.5 on 3 and 19 DF,  p-value: < 2.2e-16

#plot(fit)


par(mfrow=c(1,1))

yOut <-  exp(fit$coeff[1]  +  fit$coeff[2]*log(t) +  fit$coeff[3]*recT +
fit$coeff[4]*t)
#plot(t,y)
```

```
#points( t, yOut, col=2, type="l", lwd=2)

yOut <-  fit$coeff[1]  +  fit$coeff[2]*log(t) +  fit$coeff[3]*recT +  fit$c
oeff[4]*t
#plot(t,log(y))
#points( t, yOut, col=2, type="l", lwd=2)


y2 =  log(y[nStart:n]) +  0.5*log(t[nStart:n])
fit2 <-  lm( y2 ~      recT[nStart:n] +  t[nStart:n]  )

yOut <-  exp(fit2$coeff[1]  -  0.5*log(t) +  fit2$coeff[2]*recT +  fit2$c
oeff[3]*t)
plot(t,y, xlab="Time (s)", ylab="Normalised concentration")
points( t, yOut, col=2, type="l", lwd=2)
```

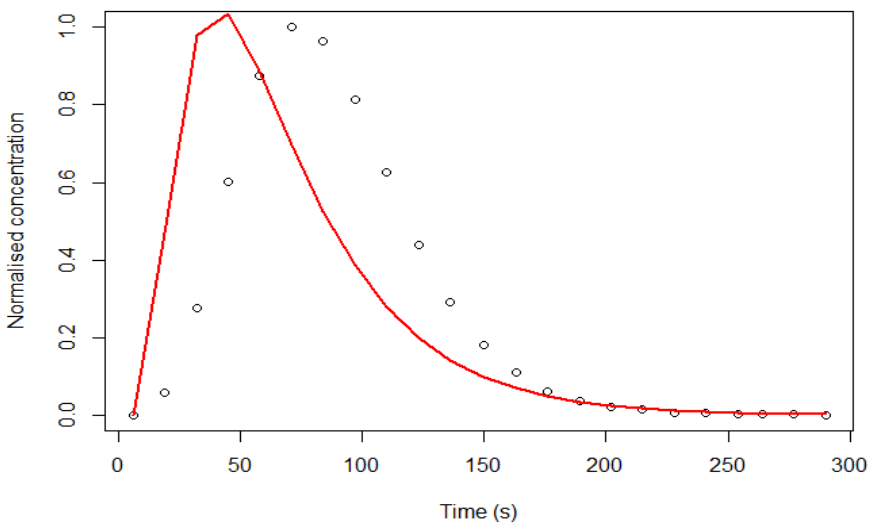


```
yOut <-  fit2$coeff[1]  -  0.5*log(t) +  fit2$coeff[2]*recT +  fit2$coeff[
3]*t
plot(t,log(y),xlab="Time (s)")
points( t, yOut, col=2, type="l", lwd=2)
```

```
summary(fit2)
```

```
##
## Call:
## lm(formula = y2 ~ recT[nStart:n] + t[nStart:n])
##
## Residuals:
##      Min       1Q   Median       3Q      Max
## -2.05908 -0.28363 -0.01393  0.60553  0.80608
##
## Coefficients:
##                  Estimate Std. Error t value Pr(>|t|)
## (Intercept)      4.485150   0.417968   10.73 9.54e-10 ***
## recT[nStart:n] -62.277068   5.561181  -11.20 4.57e-10 ***
## t[nStart:n]     -0.025852   0.002173  -11.90 1.58e-10 ***
## ---
## Signif. codes:  0 '***' 0.001 '**' 0.01 '*' 0.05 '.' 0.1 ' ' 1
##
## Residual standard error: 0.7387 on 20 degrees of freedom
##   (116 observations deleted due to missingness)
## Multiple R-squared:  0.8951, Adjusted R-squared:  0.8846
## F-statistic: 85.36 on 2 and 20 DF,  p-value: 1.608e-10
```

```
plot(fit2)
```

Calculated values using coefficents from model.

```
#Resulting Outputs
v; K; D; Ds
```

```
## [1] 0.01955935
```

```
## [1] 1.6535e-12
```

```
## [1] 0.0037
```

```
## [1] 0.189
```

20,000 Pa

Here are the outputs for neon at pressure 20,000 Pa.

```
i<-2



if(i==1){ t <-  data1[,4] ; y <-  data1[,3]
        } else if (i==2){ t <-  data2[,2]   ; y <-  data2[,1]
        } else if (i==3){ t <-  data3[,4]   ; y <-  data3[,3]
        } else if (i==4){ t <-  data4[,4]   ; y <-  data4[,3]
        } else if (i==5){ t <-  data5[,4]   ; y <-  data5[,3]
        }


recT =  1/t

n<-length(y)
n<-196
nStart<-7


fit <-  lm( log(y[nStart:n]) ~    log(t[nStart:n]) +  recT[nStart:n] +  t[nSt
art:n]  )
summary(fit)

##
## Call:
## lm(formula = log(y[nStart:n]) ~ log(t[nStart:n]) + recT[nStart:n] +
##     t[nStart:n])
##
## Residuals:
##      Min       1Q   Median       3Q      Max
## -0.34024 -0.18008 -0.01889  0.18671  0.30304
##
## Coefficients:
##                   Estimate Std. Error t value Pr(>|t|)
## (Intercept)       1.051e+02  1.824e+01   5.761 1.23e-05 ***
## log(t[nStart:n]) -1.907e+01  3.508e+00  -5.437 2.54e-05 ***
## recT[nStart:n]   -1.908e+03  2.992e+02  -6.376 3.20e-06 ***
## t[nStart:n]       1.945e-02  9.175e-03   2.120   0.0467 *
## ---
## Signif. codes:  0 '***' 0.001 '**' 0.01 '*' 0.05 '.' 0.1 ' ' 1
##
## Residual standard error: 0.2144 on 20 degrees of freedom
##   (166 observations deleted due to missingness)
## Multiple R-squared:  0.9908, Adjusted R-squared:  0.9895
## F-statistic: 720.3 on 3 and 20 DF,  p-value: < 2.2e-16

#plot(fit)


par(mfrow=c(1,1))

yOut <-  exp(fit$coeff[1]  +  fit$coeff[2]*log(t) +  fit$coeff[3]*recT +
fit$coeff[4]*t)
#plot(t,y)
```

```
#points( t, yOut, col=2, type="l", lwd=2)

yOut <-  fit$coeff[1]  +  fit$coeff[2]*log(t) +  fit$coeff[3]*recT +  fit$c
oeff[4]*t
#plot(t,log(y))
#points( t, yOut, col=2, type="l", lwd=2)


y2 =  log(y[nStart:n]) +  0.5*log(t[nStart:n])
fit2 <-  lm( y2 ~      recT[nStart:n] +  t[nStart:n]  )

yOut <-  exp(fit2$coeff[1]  -  0.5*log(t) +  fit2$coeff[2]*recT +  fit2$c
oeff[3]*t)
plot(t,y, xlab="Time (s)", ylab="Normalised concentration")
points( t, yOut, col=2, type="l", lwd=2)
```

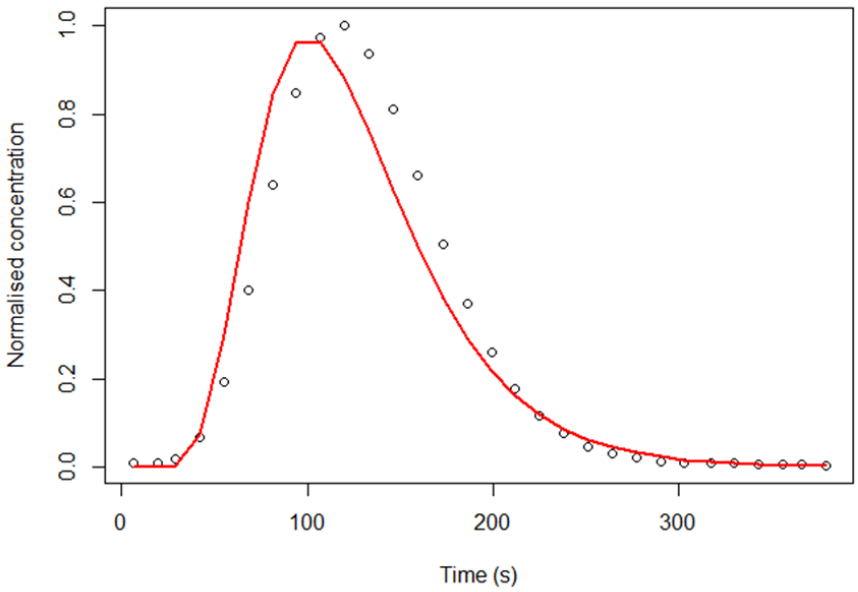


```
yOut <-  fit2$coeff[1]  -  0.5*log(t) +  fit2$coeff[2]*recT +  fit2$coeff[
3]*t
plot(t,log(y),xlab="Time (s)")
points( t, yOut, col=2, type="l", lwd=2)

summary(fit2)
```

```
##
## Call:
## lm(formula = y2 ~ recT[nStart:n] + t[nStart:n])
##
## Residuals:
##      Min       1Q   Median       3Q      Max
## -0.54627 -0.19668  0.04759  0.21733  0.68125
##
## Coefficients:
##                 Estimate Std. Error t value Pr(>|t|)
## (Intercept)     8.540e+00  7.454e-01  11.457 1.70e-10 ***
## recT[nStart:n] -3.392e+02  6.339e+01  -5.351 2.63e-05 ***
## t[nStart:n]    -2.871e-02  1.837e-03 -15.630 4.86e-13 ***
## ---
## Signif. codes:  0 '***' 0.001 '**' 0.01 '*' 0.05 '.' 0.1 ' ' 1
##
## Residual standard error: 0.3242 on 21 degrees of freedom
##   (166 observations deleted due to missingness)
## Multiple R-squared:  0.9728, Adjusted R-squared:  0.9702
## F-statistic: 375.2 on 2 and 21 DF,  p-value: < 2.2e-16
```

```
plot(fit2)
```

Calculated values using coefficents from model.

```
#Resulting Outputs
v; K; D; Ds
```

```
## [1] 0.008830866
```

```
## [1] 1.11981e-12
```

```
## [1] 0.0007
```

```
## [1] 0.076
```

10,000 Pa

Here are the outputs for neon at pressure 10,000 Pa.

```
i<-1



if(i==1){ t <-  data1[,4] ; y <-  data1[,3]
        } else if (i==2){ t <-  data2[,2]   ; y <-  data2[,1]
        } else if (i==3){ t <-  data3[,4]   ; y <-  data3[,3]
        } else if (i==4){ t <-  data4[,4]   ; y <-  data4[,3]
        } else if (i==5){ t <-  data5[,4]   ; y <-  data5[,3]
        }


recT =  1/t

n<-length(y)
n<-353
nStart<-13


fit <-  lm( log(y[nStart:n]) ~    log(t[nStart:n]) +  recT[nStart:n] +  t[nSt
art:n]  )
summary(fit)

##
## Call:
## lm(formula = log(y[nStart:n]) ~ log(t[nStart:n]) + recT[nStart:n] +
##     t[nStart:n])
##
## Residuals:
##      Min       1Q   Median       3Q      Max
## -0.24192 -0.14033  0.00533  0.10594  0.35165
##
## Coefficients:
##                   Estimate Std. Error t value Pr(>|t|)
## (Intercept)       2.870e+02  2.049e+01   14.00 3.38e-15 ***
## log(t[nStart:n]) -4.877e+01  3.539e+00  -13.78 5.25e-15 ***
## recT[nStart:n]   -7.970e+03  5.549e+02  -14.36 1.68e-15 ***
## t[nStart:n]       5.687e-02  5.200e-03   10.94 2.42e-12 ***
## ---
## Signif. codes:  0 '***' 0.001 '**' 0.01 '*' 0.05 '.' 0.1 ' ' 1
##
## Residual standard error: 0.1665 on 32 degrees of freedom
##   (305 observations deleted due to missingness)
## Multiple R-squared:  0.9901, Adjusted R-squared:  0.9892
## F-statistic:  1067 on 3 and 32 DF,  p-value: < 2.2e-16

#plot(fit)


par(mfrow=c(1,1))

yOut <-  exp(fit$coeff[1]  +  fit$coeff[2]*log(t) +  fit$coeff[3]*recT +
fit$coeff[4]*t)
#plot(t,y)
```

```
#points( t, yOut, col=2, type="l", lwd=2)

yOut <-  fit$coeff[1]  +  fit$coeff[2]*log(t) +  fit$coeff[3]*recT +  fit$c
oeff[4]*t
#plot(t,log(y))
#points( t, yOut, col=2, type="l", lwd=2)


y2 =  log(y[nStart:n]) +  0.5*log(t[nStart:n])
fit2 <-  lm( y2 ~      recT[nStart:n] +  t[nStart:n]  )

yOut <-  exp(fit2$coeff[1]  -  0.5*log(t) +  fit2$coeff[2]*recT +  fit2$c
oeff[3]*t)
plot(t,y, xlab="Time (s)", ylab="Normalised concentration")
points( t, yOut, col=2, type="l", lwd=2)
```

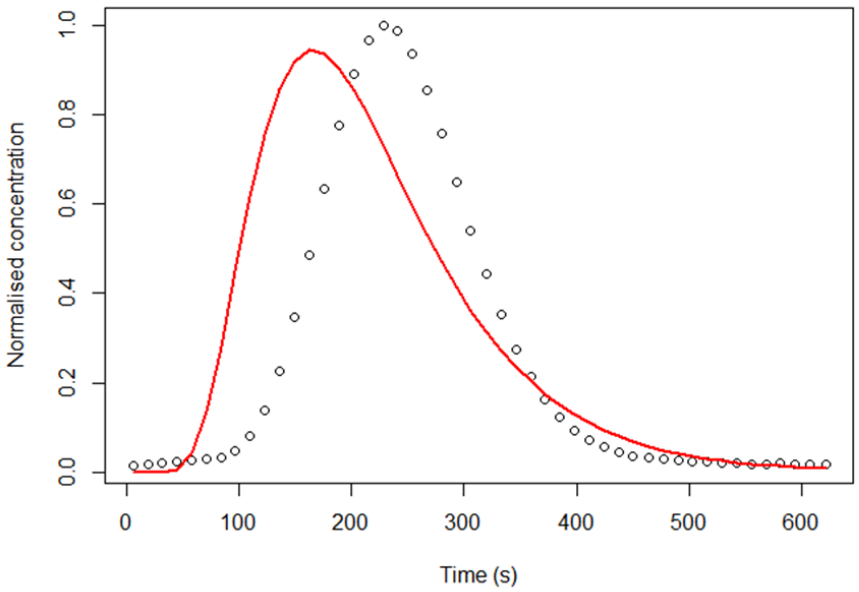


```
yOut <-  fit2$coeff[1]  -  0.5*log(t) +  fit2$coeff[2]*recT +  fit2$coeff[
3]*t
plot(t,log(y),xlab="Time (s)")
points( t, yOut, col=2, type="l", lwd=2)

summary(fit2)
```

```
##
## Call:
## lm(formula = y2 ~ recT[nStart:n] + t[nStart:n])
##
## Residuals:
##      Min       1Q   Median       3Q      Max
## -0.66324 -0.39095  0.03691  0.39678  0.77810
##
## Coefficients:
##                 Estimate Std. Error t value Pr(>|t|)
## (Intercept)     7.494e+00  1.086e+00   6.902 6.98e-08 ***
## recT[nStart:n] -4.545e+02  1.701e+02  -2.672   0.0116 *
## t[nStart:n]    -1.359e-02  1.528e-03  -8.897 2.78e-10 ***
## ---
## Signif. codes:  0 '***' 0.001 '**' 0.01 '*' 0.05 '.' 0.1 ' ' 1
##
## Residual standard error: 0.4281 on 33 degrees of freedom
##   (305 observations deleted due to missingness)
## Multiple R-squared:  0.9144, Adjusted R-squared:  0.9092
## F-statistic: 176.3 on 2 and 33 DF,  p-value: < 2.2e-16
```

```
plot(fit2)
```

Calculated values using coefficents from model.

```
#Resulting Outputs
v; K; D; Ds
```

```
## [1] 0.005250427
```

```
## [1] 1.331576e-12
```

```
## [1] 0.0005
```

```
## [1] 0.096
```

Argon results

50,000 Pa

Here are the outputs for argon at pressure 50,000 Pa.

```
i<-5

if(i==1){ t <-  data1[,4] ; y <-  data1[,3]
        } else if (i==2){ t <-  data2[,4]   ; y <-  data2[,3]
        } else if (i==3){ t <-  data3[,4]   ; y <-  data3[,3]
        } else if (i==4){ t <-  data4[,4]   ; y <-  data4[,3]
        } else if (i==5){ t <-  data5[,4]   ; y <-  data5[,3]
   }

recT =  1/t

n<-length(y)
n<-110
nStart<-14


fit <-  lm( log(y[nStart:n]) ~    log(t[nStart:n]) +  recT[nStart:n] +  t[nSt
art:n]  )
summary(fit)

##
## Call:
## lm(formula = log(y[nStart:n]) ~ log(t[nStart:n]) + recT[nStart:n] +
##     t[nStart:n])
##
## Residuals:
##       Min        1Q    Median        3Q       Max
## -0.109925 -0.013610 -0.000814  0.018403  0.089851
##
## Coefficients:
##                   Estimate Std. Error t value Pr(>|t|)
## (Intercept)      -4.155e+00  4.066e-01 -10.219  < 2e-16 ***
## log(t[nStart:n])  1.751e+00  1.026e-01  17.062  < 2e-16 ***
## recT[nStart:n]   -1.467e+01  2.419e+00  -6.064 2.82e-08 ***
## t[nStart:n]      -4.870e-02  8.944e-04 -54.450  < 2e-16 ***
## ---
## Signif. codes:  0 '***' 0.001 '**' 0.01 '*' 0.05 '.' 0.1 ' ' 1
##
## Residual standard error: 0.028 on 93 degrees of freedom
## Multiple R-squared:  0.9986, Adjusted R-squared:  0.9985
## F-statistic: 2.139e+04 on 3 and 93 DF,  p-value: < 2.2e-16

#plot(fit)


par(mfrow=c(1,1))

yOut <-  exp(fit$coeff[1]  +  fit$coeff[2]*log(t) +  fit$coeff[3]*recT +
fit$coeff[4]*t)
#plot(t,y)
#points( t, yOut, col=2, type="l", lwd=2)
```

```
yOut <-  fit$coeff[1]  +  fit$coeff[2]*log(t) +  fit$coeff[3]*recT +  fit$coeff[4]*t
#plot(t,log(y))
#points( t, yOut, col=2, type="l", lwd=2)


y2 =  log(y[nStart:n]) +  0.5*log(t[nStart:n])
fit2 <-  lm( y2 ~      recT[nStart:n] +  t[nStart:n]  )

yOut <-  exp(fit2$coeff[1]  -  0.5*log(t) +  fit2$coeff[2]*recT +  fit2$coeff[3]*t)
plot(t,y, xlab="Time (s)", ylab="Normalised concentration")
points( t, yOut, col=2, type="l", lwd=2)
```

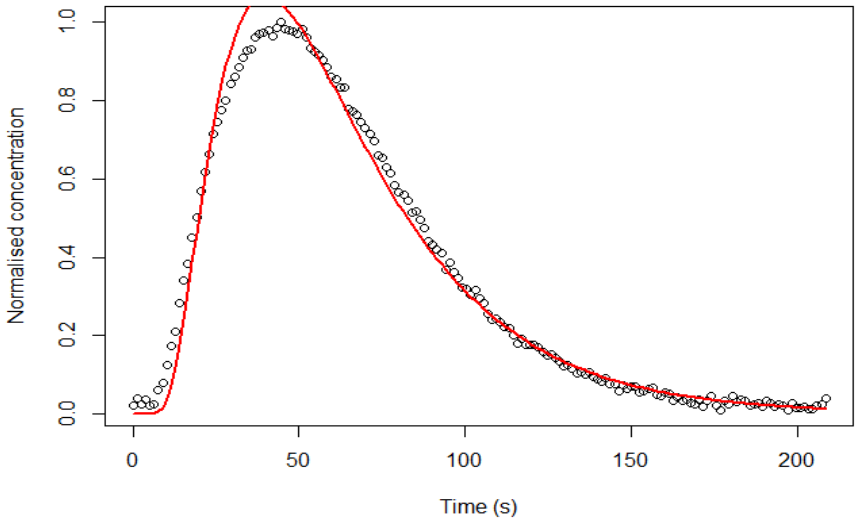


```
yOut <-  fit2$coeff[1]  -  0.5*log(t) +  fit2$coeff[2]*recT +  fit2$coeff[3]*t
plot(t,log(y),xlab="Time (s)")
points( t, yOut, col=2, type="l", lwd=2)

summary(fit2)

##
## Call:
```

```
## lm(formula = y2 ~ recT[nStart:n] + t[nStart:n])
##
## Residuals:
##       Min        1Q    Median        3Q       Max
## -0.135923 -0.047293  0.005075  0.054787  0.207726
##
## Coefficients:
##                  Estimate Std. Error t value Pr(>|t|)
## (Intercept)     4.752e+00  4.900e-02   96.98   <2e-16 ***
## recT[nStart:n] -6.672e+01  1.154e+00  -57.80   <2e-16 ***
## t[nStart:n]    -2.938e-02  3.857e-04  -76.18   <2e-16 ***
## ---
## Signif. codes:  0 '***' 0.001 '**' 0.01 '*' 0.05 '.' 0.1 ' ' 1
##
## Residual standard error: 0.06921 on 94 degrees of freedom
## Multiple R-squared:  0.9846, Adjusted R-squared:  0.9843
## F-statistic:  3014 on 2 and 94 DF,  p-value: < 2.2e-16

plot(fit2)

#Resulting Outputs
v; K; D; Ds

## [1] 0.0201461

## [1] 1.021862e-12

## [1] 3.4532E-03

## [1] 0.171
```

40,000 Pa

Here are the outputs for argon at pressure 40,000 Pa.

```
i<-4

if(i==1){ t <-  data1[,4] ; y <-  data1[,3]
        } else if (i==2){ t <-  data2[,4]   ; y <-  data2[,3]
        } else if (i==3){ t <-  data3[,4]   ; y <-  data3[,3]
        } else if (i==4){ t <-  data4[,4]   ; y <-  data4[,3]
        } else if (i==5){ t <-  data5[,4]   ; y <-  data5[,3]
   }

recT =  1/t

n<-length(y)
n<-126
nStart<-18


fit <-  lm( log(y[nStart:n]) ~    log(t[nStart:n]) +  recT[nStart:n] +  t[nSt
art:n]  )
summary(fit)

##
## Call:
## lm(formula = log(y[nStart:n]) ~ log(t[nStart:n]) + recT[nStart:n] +
##     t[nStart:n])
##
## Residuals:
##       Min        1Q    Median        3Q       Max
## -0.129338 -0.010375 -0.000201  0.010590  0.114797
##
## Coefficients:
##                   Estimate Std. Error t value Pr(>|t|)
## (Intercept)      -7.2877275  0.5084629 -14.333   <2e-16 ***
## log(t[nStart:n])  2.5426759  0.1224013  20.773   <2e-16 ***
## recT[nStart:n]   -8.4818624  3.5467287  -2.391   0.0186 *
## t[nStart:n]      -0.0500354  0.0008889 -56.290   <2e-16 ***
## ---
## Signif. codes:  0 '***' 0.001 '**' 0.01 '*' 0.05 '.' 0.1 ' ' 1
##
## Residual standard error: 0.02948 on 105 degrees of freedom
## Multiple R-squared:  0.9984, Adjusted R-squared:  0.9984
## F-statistic: 2.179e+04 on 3 and 105 DF,  p-value: < 2.2e-16

#plot(fit)


par(mfrow=c(1,1))

yOut <-  exp(fit$coeff[1]  +  fit$coeff[2]*log(t) +  fit$coeff[3]*recT +
fit$coeff[4]*t)
#plot(t,y)
#points( t, yOut, col=2, type="l", lwd=2)

yOut <-  fit$coeff[1]  +  fit$coeff[2]*log(t) +  fit$coeff[3]*recT +  fit$c
oeff[4]*t
```

```
#plot(t,log(y))
#points( t, yOut, col=2, type="l", lwd=2)


y2 =  log(y[nStart:n]) +  0.5*log(t[nStart:n])
fit2 <-  lm( y2 ~      recT[nStart:n] +  t[nStart:n]  )

yOut <-  exp(fit2$coeff[1]  -  0.5*log(t) +  fit2$coeff[2]*recT +  fit2$c
oeff[3]*t)
plot(t,y, xlab="Time (s)", ylab="Normalised concentration")
points( t, yOut, col=2, type="l", lwd=2)
```

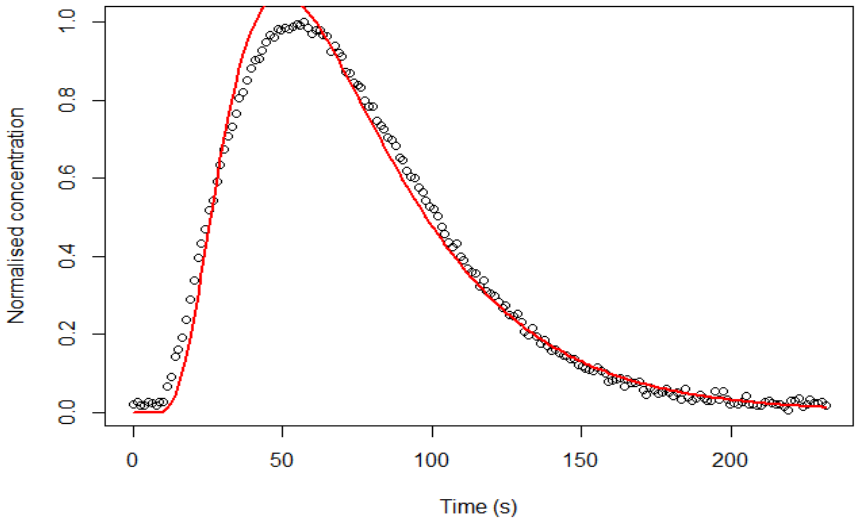


```
yOut <-  fit2$coeff[1]  -  0.5*log(t) +  fit2$coeff[2]*recT +  fit2$coeff[
3]*t
plot(t,log(y),xlab="Time (s)")
points( t, yOut, col=2, type="l", lwd=2)

summary(fit2)

##
## Call:
```

```
## lm(formula = y2 ~ recT[nStart:n] + t[nStart:n])
##
## Residuals:
##       Min        1Q    Median        3Q       Max
## -0.254228 -0.059117  0.008266  0.058269  0.282233
##
## Coefficients:
##                  Estimate Std. Error t value Pr(>|t|)
## (Intercept)     5.340e+00  5.743e-02   92.98   <2e-16 ***
## recT[nStart:n] -9.521e+01  1.664e+00  -57.23   <2e-16 ***
## t[nStart:n]    -2.824e-02  3.811e-04  -74.10   <2e-16 ***
## ---
## Signif. codes:  0 '***' 0.001 '**' 0.01 '*' 0.05 '.' 0.1 ' ' 1
##
## Residual standard error: 0.077 on 106 degrees of freedom
## Multiple R-squared:  0.9819, Adjusted R-squared:  0.9815
## F-statistic:  2870 on 2 and 106 DF,  p-value: < 2.2e-16

plot(fit2)

#Resulting Outputs
v; K; D; Ds

## [1] 0.01653287

## [1] 1.048237e-12

## [1] 2.4199E-03

## [1] 0.146
```

30,000 Pa

Here are the outputs for argon at pressure 30,000 Pa.

```
i<-3

if(i==1){ t <-  data1[,4] ; y <-  data1[,3]
        } else if (i==2){ t <-  data2[,4]   ; y <-  data2[,3]
        } else if (i==3){ t <-  data3[,4]   ; y <-  data3[,3]
        } else if (i==4){ t <-  data4[,4]   ; y <-  data4[,3]
        } else if (i==5){ t <-  data5[,4]   ; y <-  data5[,3]
   }

recT =  1/t

n<-length(y)
n<-157
nStart<-28


fit <-  lm( log(y[nStart:n]) ~    log(t[nStart:n]) +  recT[nStart:n] +  t[nSt
art:n]  )
summary(fit)

##
## Call:
## lm(formula = log(y[nStart:n]) ~ log(t[nStart:n]) + recT[nStart:n] +
##     t[nStart:n])
##
## Residuals:
##       Min        1Q    Median        3Q       Max
## -0.164167 -0.008762 -0.000790  0.011551  0.118356
##
## Coefficients:
##                   Estimate Std. Error t value Pr(>|t|)
## (Intercept)     -1.501e+01  8.118e-01  -18.50  < 2e-16 ***
## log(t[nStart:n])  4.347e+00  1.813e-01   23.98  < 2e-16 ***
## recT[nStart:n]    2.237e+01  7.429e+00    3.01  0.00315 **
## t[nStart:n]      -5.417e-02  9.683e-04  -55.94  < 2e-16 ***
## ---
## Signif. codes:  0 '***' 0.001 '**' 0.01 '*' 0.05 '.' 0.1 ' ' 1
##
## Residual standard error: 0.03297 on 126 degrees of freedom
## Multiple R-squared:  0.9983, Adjusted R-squared:  0.9983
## F-statistic: 2.478e+04 on 3 and 126 DF,  p-value: < 2.2e-16

#plot(fit)


par(mfrow=c(1,1))

yOut <-  exp(fit$coeff[1]  +  fit$coeff[2]*log(t) +  fit$coeff[3]*recT +
fit$coeff[4]*t)
#plot(t,y)
#points( t, yOut, col=2, type="l", lwd=2)

yOut <-  fit$coeff[1]  +  fit$coeff[2]*log(t) +  fit$coeff[3]*recT +  fit$c
oeff[4]*t
```

```
#plot(t,log(y))
#points( t, yOut, col=2, type="l", lwd=2)


y2 =  log(y[nStart:n]) +  0.5*log(t[nStart:n])
fit2 <-  lm( y2 ~      recT[nStart:n] +  t[nStart:n]  )

yOut <-  exp(fit2$coeff[1]  -  0.5*log(t) +  fit2$coeff[2]*recT +  fit2$c
oeff[3]*t)
plot(t,y, xlab="Time (s)", ylab="Normalised concentration")
points( t, yOut, col=2, type="l", lwd=2)
```

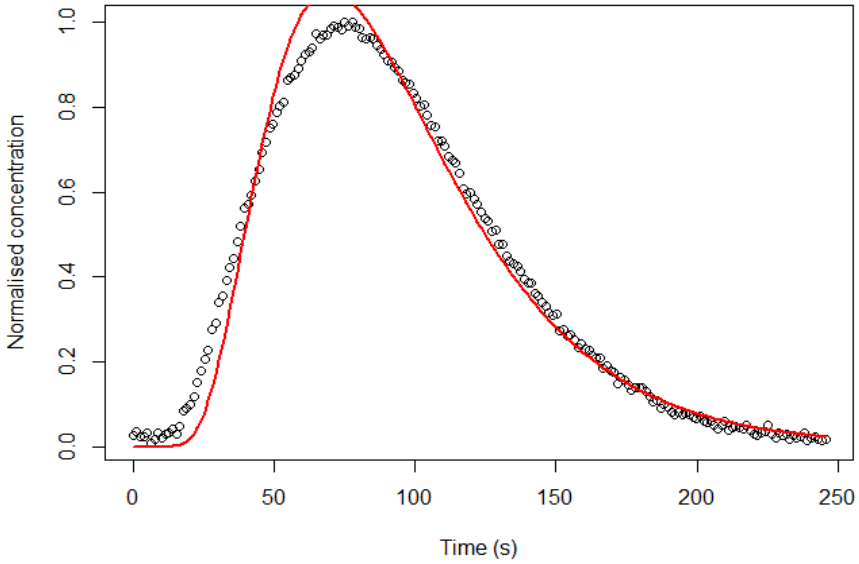


```
yOut <-  fit2$coeff[1]  -  0.5*log(t) +  fit2$coeff[2]*recT +  fit2$coeff[
3]*t
plot(t,log(y),xlab="Time (s)")
points( t, yOut, col=2, type="l", lwd=2)

summary(fit2)
```

```
##
## Call:
## lm(formula = y2 ~ recT[nStart:n] + t[nStart:n])
##
## Residuals:
##      Min       1Q   Median       3Q      Max
## -0.26981 -0.06237  0.01681  0.06316  0.26890
##
## Coefficients:
##                  Estimate Std. Error t value Pr(>|t|)
## (Intercept)     6.678e+00  7.266e-02   91.92   <2e-16 ***
## recT[nStart:n] -1.739e+02  2.977e+00  -58.40   <2e-16 ***
## t[nStart:n]    -2.855e-02  3.617e-04  -78.94   <2e-16 ***
## ---
## Signif. codes:  0 '***' 0.001 '**' 0.01 '*' 0.05 '.' 0.1 ' ' 1
##
## Residual standard error: 0.08484 on 127 degrees of freedom
## Multiple R-squared:  0.9825, Adjusted R-squared:  0.9822
## F-statistic:  3559 on 2 and 127 DF,  p-value: < 2.2e-16
```

```
plot(fit2)
```

#Resulting Outputs

v; K; D; Ds

```
## [1] 0.01230245
```

```
## [1] 1.3249E-03
```

```
## [1] 0.108
```

```
## [1] 3256.126
```

20,000 Pa

Here are the outputs for argon at pressure 20,000 Pa.

```
i<-2

if(i==1){ t <-  data1[,4] ; y <-  data1[,3]
        } else if (i==2){ t <-  data2[,4]   ; y <-  data2[,3]
        } else if (i==3){ t <-  data3[,4]   ; y <-  data3[,3]
        } else if (i==4){ t <-  data4[,4]   ; y <-  data4[,3]
        } else if (i==5){ t <-  data5[,4]   ; y <-  data5[,3]
   }

recT =  1/t

n<-length(y)
n<-213
nStart<-49


fit <-  lm( log(y[nStart:n]) ~    log(t[nStart:n]) +  recT[nStart:n] +  t[nSt
art:n]  )
summary(fit)

##
## Call:
## lm(formula = log(y[nStart:n]) ~ log(t[nStart:n]) + recT[nStart:n] +
##     t[nStart:n])
##
## Residuals:
##       Min        1Q    Median        3Q       Max
## -0.173413 -0.010044  0.000316  0.009393  0.294733
##
## Coefficients:
##                   Estimate Std. Error t value Pr(>|t|)
## (Intercept)     -19.696979   1.705404 -11.550   <2e-16 ***
## log(t[nStart:n])   5.316000   0.347966  15.277   <2e-16 ***
## recT[nStart:n]     3.822452  22.235636   0.172    0.864
## t[nStart:n]       -0.048450   0.001238 -39.138   <2e-16 ***
## ---
## Signif. codes:  0 '***' 0.001 '**' 0.01 '*' 0.05 '.' 0.1 ' ' 1
##
## Residual standard error: 0.04409 on 161 degrees of freedom
## Multiple R-squared:  0.9977, Adjusted R-squared:  0.9976
## F-statistic: 2.291e+04 on 3 and 161 DF,  p-value: < 2.2e-16

#plot(fit)


par(mfrow=c(1,1))

yOut <-  exp(fit$coeff[1]  +  fit$coeff[2]*log(t) +  fit$coeff[3]*recT +
fit$coeff[4]*t)
#plot(t,y)
#points( t, yOut, col=2, type="l", lwd=2)

yOut <-  fit$coeff[1]  +  fit$coeff[2]*log(t) +  fit$coeff[3]*recT +  fit$c
oeff[4]*t
```

```
#plot(t,log(y))
#points( t, yOut, col=2, type="l", lwd=2)


y2 =  log(y[nStart:n]) +  0.5*log(t[nStart:n])
fit2 <-  lm( y2 ~      recT[nStart:n] +  t[nStart:n]  )

yOut <-  exp(fit2$coeff[1]  -  0.5*log(t) +  fit2$coeff[2]*recT +  fit2$c
oeff[3]*t)
plot(t,y, xlab="Time (s)", ylab="Normalised concentration")
points( t, yOut, col=2, type="l", lwd=2)
```

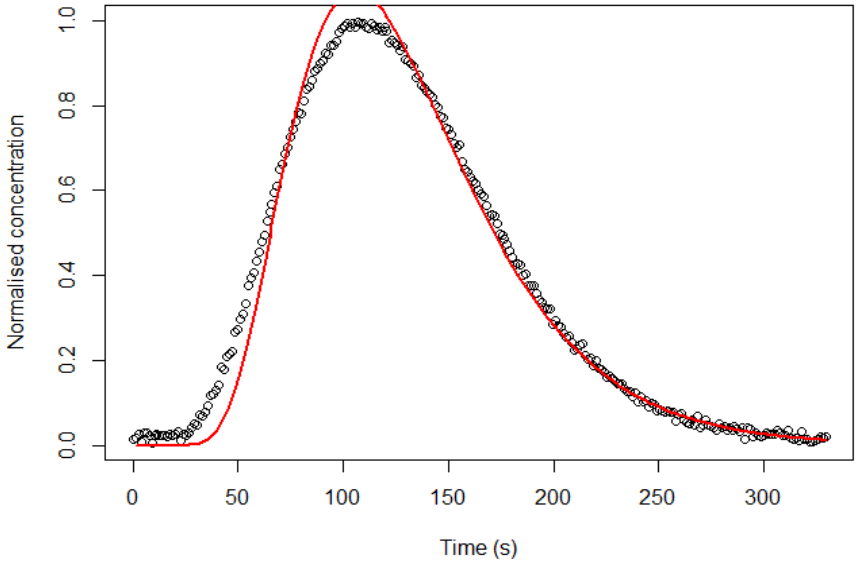


```
yOut <-  fit2$coeff[1]  -  0.5*log(t) +  fit2$coeff[2]*recT +  fit2$coeff[
3]*t
plot(t,log(y),xlab="Time (s)")
points( t, yOut, col=2, type="l", lwd=2)

summary(fit2)
```

```
##
## Call:
## lm(formula = y2 ~ recT[nStart:n] + t[nStart:n])
##
## Residuals:
##      Min       1Q   Median       3Q      Max
## -0.26253 -0.05095  0.01392  0.04981  0.19853
##
## Coefficients:
##                  Estimate Std. Error t value Pr(>|t|)
## (Intercept)     8.798e+00  7.466e-02  117.83   <2e-16 ***
## recT[nStart:n] -3.647e+02  4.771e+00  -76.44   <2e-16 ***
## t[nStart:n]    -2.792e-02  2.524e-04 -110.61   <2e-16 ***
## ---
## Signif. codes:  0 '***' 0.001 '**' 0.01 '*' 0.05 '.' 0.1 ' ' 1
##
## Residual standard error: 0.07269 on 162 degrees of freedom
## Multiple R-squared:  0.9907, Adjusted R-squared:  0.9906
## F-statistic:  8647 on 2 and 162 DF,  p-value: < 2.2e-16
```

```
plot(fit2)
```

#Resulting Outputs

v; K; D; Ds

```
## [1] 0.008399689
```

```
## [1] 1.065134e-12
```

```
## [1] 6.3175E-04
```

```
## [1] 0.075
```

10,000 Pa

Here are the outputs for argon at pressure 20,000 Pa.

```
i<-2

if(i==1){ t <-  data1[,4] ; y <-  data1[,3]
        } else if (i==2){ t <-  data2[,4]   ; y <-  data2[,3]
        } else if (i==3){ t <-  data3[,4]   ; y <-  data3[,3]
        } else if (i==4){ t <-  data4[,4]   ; y <-  data4[,3]
        } else if (i==5){ t <-  data5[,4]   ; y <-  data5[,3]
   }

recT =  1/t

n<-length(y)
n<-213
nStart<-49


fit <-  lm( log(y[nStart:n]) ~    log(t[nStart:n]) +  recT[nStart:n] +  t[nSt
art:n]  )
summary(fit)

##
## Call:
## lm(formula = log(y[nStart:n]) ~ log(t[nStart:n]) + recT[nStart:n] +
##     t[nStart:n])
##
## Residuals:
##       Min        1Q    Median        3Q       Max
## -0.173413 -0.010044  0.000316  0.009393  0.294733
##
## Coefficients:
##                   Estimate Std. Error t value Pr(>|t|)
## (Intercept)     -19.696979   1.705404 -11.550   <2e-16 ***
## log(t[nStart:n])   5.316000   0.347966  15.277   <2e-16 ***
## recT[nStart:n]     3.822452  22.235636   0.172    0.864
## t[nStart:n]       -0.048450   0.001238 -39.138   <2e-16 ***
## ---
## Signif. codes:  0 '***' 0.001 '**' 0.01 '*' 0.05 '.' 0.1 ' ' 1
##
## Residual standard error: 0.04409 on 161 degrees of freedom
## Multiple R-squared:  0.9977, Adjusted R-squared:  0.9976
## F-statistic: 2.291e+04 on 3 and 161 DF,  p-value: < 2.2e-16

#plot(fit)


par(mfrow=c(1,1))

yOut <-  exp(fit$coeff[1]  +  fit$coeff[2]*log(t) +  fit$coeff[3]*recT +
fit$coeff[4]*t)
#plot(t,y)
#points( t, yOut, col=2, type="l", lwd=2)

yOut <-  fit$coeff[1]  +  fit$coeff[2]*log(t) +  fit$coeff[3]*recT +  fit$c
oeff[4]*t
```

```
#plot(t,log(y))
#points( t, yOut, col=2, type="l", lwd=2)


y2 =  log(y[nStart:n]) +  0.5*log(t[nStart:n])
fit2 <-  lm( y2 ~      recT[nStart:n] +  t[nStart:n]  )

yOut <-  exp(fit2$coeff[1]  -  0.5*log(t) +  fit2$coeff[2]*recT +  fit2$c
oeff[3]*t)
plot(t,y, xlab="Time (s)", ylab="Normalised concentration")
points( t, yOut, col=2, type="l", lwd=2)
```

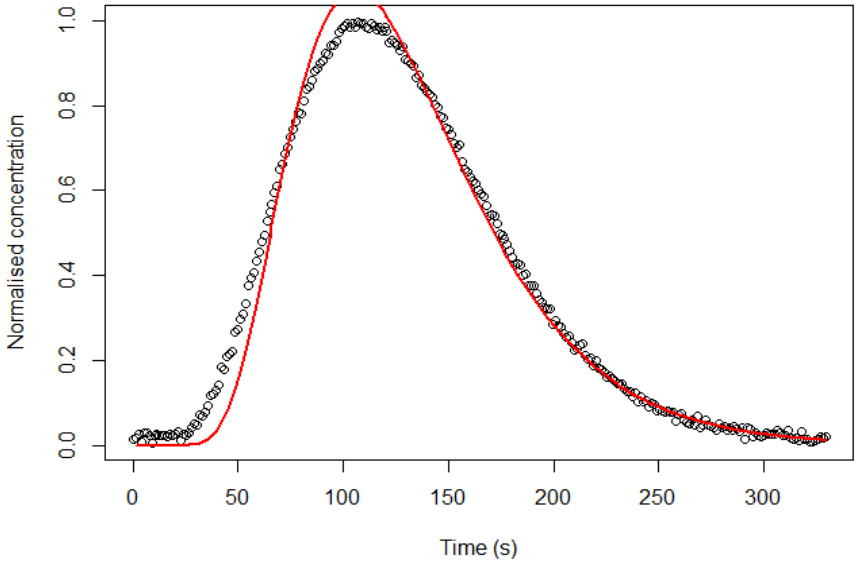


```
yOut <-  fit2$coeff[1]  -  0.5*log(t) +  fit2$coeff[2]*recT +  fit2$coeff[
3]*t
plot(t,log(y),xlab="Time (s)")
points( t, yOut, col=2, type="l", lwd=2)

summary(fit2)
```

```
##
## Call:
## lm(formula = y2 ~ recT[nStart:n] + t[nStart:n])
##
## Residuals:
##      Min       1Q   Median       3Q      Max
## -0.26253 -0.05095  0.01392  0.04981  0.19853
##
## Coefficients:
##                  Estimate Std. Error t value Pr(>|t|)
## (Intercept)     8.798e+00  7.466e-02  117.83   <2e-16 ***
## recT[nStart:n] -3.647e+02  4.771e+00  -76.44   <2e-16 ***
## t[nStart:n]    -2.792e-02  2.524e-04 -110.61   <2e-16 ***
## ---
## Signif. codes:  0 '***' 0.001 '**' 0.01 '*' 0.05 '.' 0.1 ' ' 1
##
## Residual standard error: 0.07269 on 162 degrees of freedom
## Multiple R-squared:  0.9907, Adjusted R-squared:  0.9906
## F-statistic:  8647 on 2 and 162 DF,  p-value: < 2.2e-16

plot(fit2)

#Resulting Outputs
v; K; D; Ds

## [1] 0.008399689

## [1] 1.065134e-12

## [1] 2.0462E-04

## [1] 0.045
```

Krypton results

50,000 Pa

Here are the outputs for krypton at pressure 50,000 Pa.

```
i<-5

if(i==1){ t <- data1[,4] ; y <- data1[,3]
        } else if (i==2){ t <- data2[,4]   ; y <- data2[,3]
        } else if (i==3){ t <- data3[,4]   ; y <- data3[,3]
        } else if (i==4){ t <- data4[,4]   ; y <- data4[,3]
        } else if (i==5){ t <- data5[,4]   ; y <- data5[,3]
   }

recT = 1/t

n<-length(y)
n<-109
nStart<-6


fit <- lm( log(y[nStart:n]) ~  log(t[nStart:n]) + recT[nStart:n] + t[nStart:
n]  )
summary(fit)

##
## Call:
## lm(formula = log(y[nStart:n]) ~ log(t[nStart:n]) + recT[nStart:n] +
##     t[nStart:n])
##
## Residuals:
##      Min       1Q   Median       3Q      Max
## -0.33190 -0.08712  0.01441  0.08462  0.23580
##
## Coefficients:
##                   Estimate Std. Error t value Pr(>|t|)
## (Intercept)       4.186e+01  5.801e+00   7.216 4.08e-08 ***
## log(t[nStart:n]) -8.446e+00  1.227e+00  -6.883 1.02e-07 ***
## recT[nStart:n]   -4.546e+02  6.430e+01  -7.069 6.12e-08 ***
## t[nStart:n]       4.159e-03  5.087e-03   0.818     0.42
## ---
## Signif. codes:  0 '***' 0.001 '**' 0.01 '*' 0.05 '.' 0.1 ' ' 1
##
## Residual standard error: 0.1378 on 31 degrees of freedom
##   (69 observations deleted due to missingness)
## Multiple R-squared:  0.9951, Adjusted R-squared:  0.9946
## F-statistic:  2093 on 3 and 31 DF,  p-value: < 2.2e-16

#plot(fit)



par(mfrow=c(1,1))

yOut <- exp(fit$coeff[1]  + fit$coeff[2]*log(t) + fit$coeff[3]*recT + fit
$coeff[4]*t)
#plot(t,y)
```

```
#points( t, yOut, col=2, type="l", lwd=2)

yOut <- fit$coeff[1]  + fit$coeff[2]*log(t) + fit$coeff[3]*recT + fit$coeff[4]*t
#plot(t,log(y))
#points( t, yOut, col=2, type="l", lwd=2)


y2 = log(y[nStart:n]) + 0.5*log(t[nStart:n])
fit2 <- lm( y2 ~   recT[nStart:n] + t[nStart:n]  )

yOut <- exp(fit2$coeff[1]  - 0.5*log(t) + fit2$coeff[2]*recT + fit2$coeff[3]*t)
plot(t,y, xlab="Time (s)", ylab="Normalised concentration")
points( t, yOut, col=2, type="l", lwd=2)
```

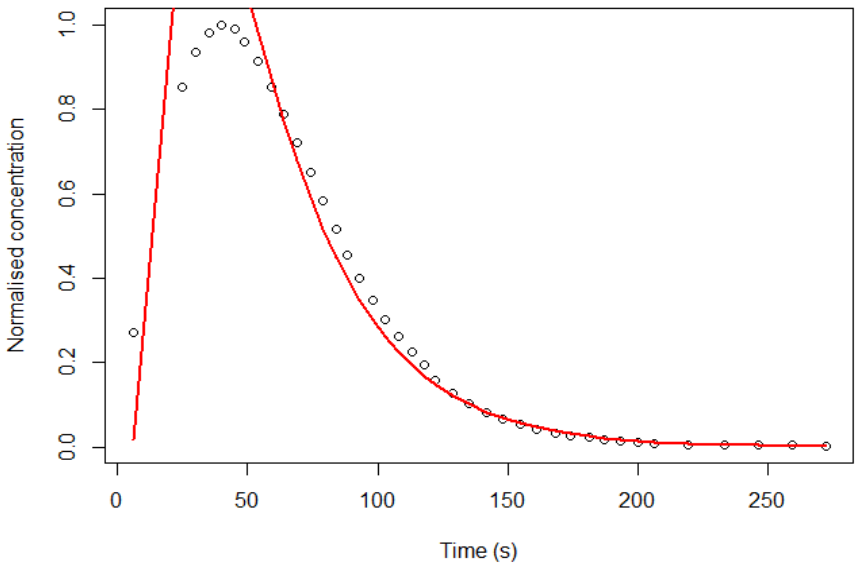


```
yOut <- fit2$coeff[1]  - 0.5*log(t) + fit2$coeff[2]*recT + fit2$coeff[3]*t
plot(t,log(y),xlab="Time (s)")
points( t, yOut, col=2, type="l", lwd=2)
```

```
summary(fit2)
```

```
##
## Call:
## lm(formula = y2 ~ recT[nStart:n] + t[nStart:n])
##
## Residuals:
##      Min       1Q   Median       3Q      Max
## -0.42110 -0.13677  0.00032  0.13884  0.56858
##
## Coefficients:
##                 Estimate Std. Error t value Pr(>|t|)
## (Intercept)      4.32059    0.30752  14.050 3.09e-15 ***
## recT[nStart:n] -43.73666   15.82541  -2.764   0.0094 **
## t[nStart:n]     -0.02836    0.00122 -23.243  < 2e-16 ***
## ---
## Signif. codes:  0 '***' 0.001 '**' 0.01 '*' 0.05 '.' 0.1 ' ' 1
##
## Residual standard error: 0.2081 on 32 degrees of freedom
##   (69 observations deleted due to missingness)
## Multiple R-squared:  0.9848, Adjusted R-squared:  0.9838
## F-statistic:  1036 on 2 and 32 DF,  p-value: < 2.2e-16
```

```
plot(fit2)
```

```
#Resulting Outputs
v; K; D; Ds
```

```
## [1] 0.02444706
```

```
## [1] 1.240017e-12
```

```
## [1] 0.0053
```

```
## [1] 0.215
```

40,000 Pa

Here are the outputs for krypton at pressure 40,000 Pa.

```
i<-4

if(i==1){ t <-  data1[,4] ; y <-  data1[,3]
        } else if (i==2){ t <-  data2[,4]   ; y <-  data2[,3]
        } else if (i==3){ t <-  data3[,4]   ; y <-  data3[,3]
        } else if (i==4){ t <-  data4[,4]   ; y <-  data4[,3]
        } else if (i==5){ t <-  data5[,4]   ; y <-  data5[,3]
   }

recT =  1/t

n<-length(y)
n<-131
nStart<-10


fit <-  lm( log(y[nStart:n]) ~    log(t[nStart:n]) +  recT[nStart:n] +  t[nSt
art:n]  )
summary(fit)

##
## Call:
## lm(formula = log(y[nStart:n]) ~ log(t[nStart:n]) + recT[nStart:n] +
##     t[nStart:n])
##
## Residuals:
##       Min        1Q    Median        3Q       Max
## -0.071854 -0.040368 -0.000255  0.027209  0.152472
##
## Coefficients:
##                   Estimate Std. Error t value Pr(>|t|)
## (Intercept)       2.569e+01  3.723e+00   6.900 7.00e-08 ***
## log(t[nStart:n]) -4.491e+00  7.591e-01  -5.916 1.23e-06 ***
## recT[nStart:n]   -3.858e+02  4.870e+01  -7.922 3.90e-09 ***
## t[nStart:n]      -1.711e-02  2.687e-03  -6.367 3.29e-07 ***
## ---
## Signif. codes:  0 '***' 0.001 '**' 0.01 '*' 0.05 '.' 0.1 ' ' 1
##
## Residual standard error: 0.04912 on 33 degrees of freedom
##   (85 observations deleted due to missingness)
## Multiple R-squared:  0.9993, Adjusted R-squared:  0.9992
## F-statistic: 1.537e+04 on 3 and 33 DF,  p-value: < 2.2e-16

#plot(fit)


par(mfrow=c(1,1))

yOut <-  exp(fit$coeff[1]  +  fit$coeff[2]*log(t) +  fit$coeff[3]*recT +
fit$coeff[4]*t)
#plot(t,y)
#points( t, yOut, col=2, type="l", lwd=2)

yOut <-  fit$coeff[1]  +  fit$coeff[2]*log(t) +  fit$coeff[3]*recT +  fit$c
```

```
oeff[4]*t
#plot(t,log(y))
#points( t, yOut, col=2, type="l", lwd=2)


y2 =  log(y[nStart:n]) +  0.5*log(t[nStart:n])
fit2 <-  lm( y2 ~      recT[nStart:n] +  t[nStart:n]  )

yOut <-  exp(fit2$coeff[1]  -  0.5*log(t) +  fit2$coeff[2]*recT +  fit2$c
oeff[3]*t)
plot(t,y, xlab="Time (s)", ylab="Normalised concentration")
points( t, yOut, col=2, type="l", lwd=2)
```

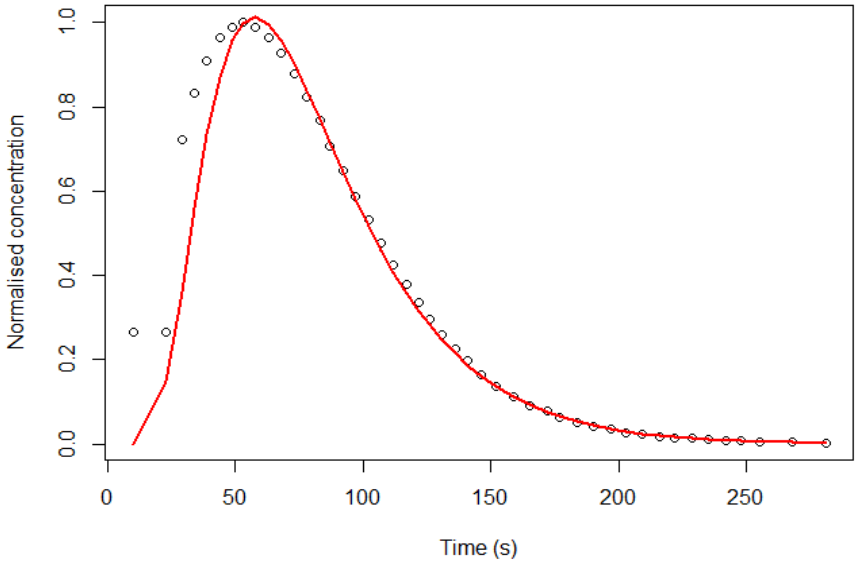


```
yOut <-  fit2$coeff[1]  -  0.5*log(t) +  fit2$coeff[2]*recT +  fit2$coeff[
3]*t
plot(t,log(y),xlab="Time (s)")
points( t, yOut, col=2, type="l", lwd=2)

summary(fit2)
```

```
##
## Call:
## lm(formula = y2 ~ recT[nStart:n] + t[nStart:n])
##
## Residuals:
##       Min        1Q    Median        3Q       Max
## -0.092961 -0.037746 -0.004218  0.035519  0.252525
##
## Coefficients:
##                  Estimate Std. Error t value Pr(>|t|)
## (Intercept)     6.123e+00  1.363e-01   44.93   <2e-16 ***
## recT[nStart:n] -1.321e+02  8.686e+00  -15.20   <2e-16 ***
## t[nStart:n]    -3.112e-02  4.621e-04  -67.34   <2e-16 ***
## ---
## Signif. codes:  0 '***' 0.001 '**' 0.01 '*' 0.05 '.' 0.1 ' ' 1
##
## Residual standard error: 0.0656 on 34 degrees of freedom
##   (85 observations deleted due to missingness)
## Multiple R-squared:  0.9983, Adjusted R-squared:  0.9982
## F-statistic: 1.009e+04 on 2 and 34 DF,  p-value: < 2.2e-16

plot(fit2)

#Resulting Outputs
v; K; D; Ds

## [1] 0.01473727

## [1] 9.343903e-13

## [1] 0.0017

## [1] 0.118
```

30,000 Pa

Here are the outputs for krypton at pressure 30,000 Pa.

```
i<-3

if(i==1){ t <-  data1[,4] ; y <-  data1[,3]
        } else if (i==2){ t <-  data2[,4]   ; y <-  data2[,3]
        } else if (i==3){ t <-  data3[,4]   ; y <-  data3[,3]
        } else if (i==4){ t <-  data4[,4]   ; y <-  data4[,3]
        } else if (i==5){ t <-  data5[,4]   ; y <-  data5[,3]
   }

recT =  1/t

n<-length(y)
n<-166
nStart<-4


fit <-  lm( log(y[nStart:n]) ~    log(t[nStart:n]) +  recT[nStart:n] +  t[nSt
art:n]  )
summary(fit)

##
## Call:
## lm(formula = log(y[nStart:n]) ~ log(t[nStart:n]) + recT[nStart:n] +
##     t[nStart:n])
##
## Residuals:
##      Min       1Q   Median       3Q      Max
## -0.26787 -0.11963  0.00766  0.10939  0.42925
##
## Coefficients:
##                   Estimate Std. Error t value Pr(>|t|)
## (Intercept)       1.199499   1.603289   0.748    0.457
## log(t[nStart:n])  0.479483   0.344126   1.393    0.169
## recT[nStart:n]   -89.165389  15.176407  -5.875  2.3e-07 ***
## t[nStart:n]       -0.027291   0.001418 -19.245  < 2e-16 ***
## ---
## Signif. codes:  0 '***' 0.001 '**' 0.01 '*' 0.05 '.' 0.1 ' ' 1
##
## Residual standard error: 0.15 on 57 degrees of freedom
##   (102 observations deleted due to missingness)
## Multiple R-squared:  0.9941, Adjusted R-squared:  0.9938
## F-statistic:  3194 on 3 and 57 DF,  p-value: < 2.2e-16

#plot(fit)


par(mfrow=c(1,1))

yOut <-  exp(fit$coeff[1]  +  fit$coeff[2]*log(t) +  fit$coeff[3]*recT +
fit$coeff[4]*t)
#plot(t,y)
#points( t, yOut, col=2, type="l", lwd=2)

yOut <-  fit$coeff[1]  +  fit$coeff[2]*log(t) +  fit$coeff[3]*recT +  fit$c
```

```
oeff[4]*t
#plot(t,log(y))
#points( t, yOut, col=2, type="l", lwd=2)


y2 =  log(y[nStart:n]) +  0.5*log(t[nStart:n])
fit2 <-  lm( y2 ~      recT[nStart:n] +  t[nStart:n]  )

yOut <-  exp(fit2$coeff[1]  -  0.5*log(t) +  fit2$coeff[2]*recT +  fit2$c
oeff[3]*t)
plot(t,y, xlab="Time (s)", ylab="Normalised concentration")
points( t, yOut, col=2, type="l", lwd=2)
```

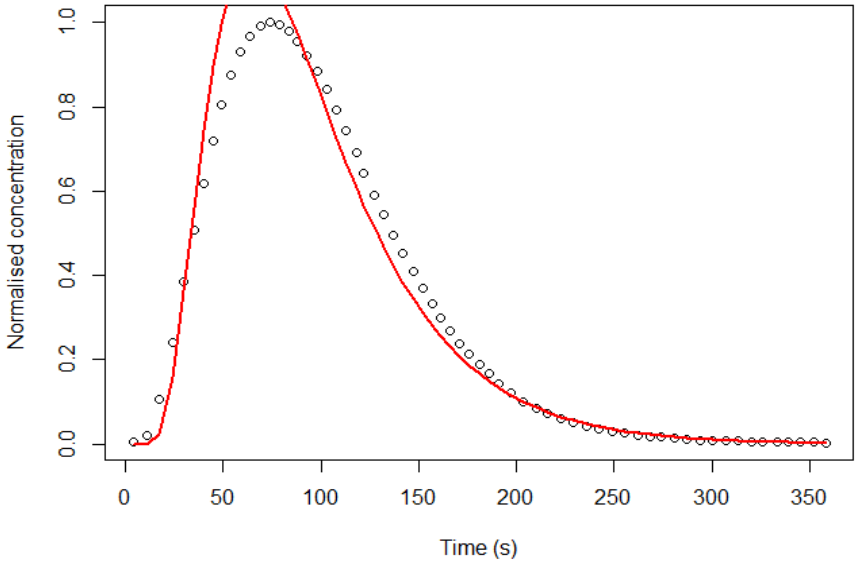


```
yOut <-  fit2$coeff[1]  -  0.5*log(t) +  fit2$coeff[2]*recT +  fit2$coeff[
3]*t
plot(t,log(y),xlab="Time (s)")
points( t, yOut, col=2, type="l", lwd=2)

summary(fit2)
```

```
##
## Call:
## lm(formula = y2 ~ recT[nStart:n] + t[nStart:n])
##
## Residuals:
##      Min       1Q   Median       3Q      Max
## -0.24736 -0.13998 -0.00432  0.12434  0.42950
##
## Coefficients:
##                  Estimate Std. Error t value Pr(>|t|)
## (Intercept)     5.756e+00  9.318e-02   61.77   <2e-16 ***
## recT[nStart:n] -1.309e+02  4.125e+00  -31.74   <2e-16 ***
## t[nStart:n]    -2.335e-02  3.317e-04  -70.40   <2e-16 ***
## ---
## Signif. codes:  0 '***' 0.001 '**' 0.01 '*' 0.05 '.' 0.1 ' ' 1
##
## Residual standard error: 0.1589 on 58 degrees of freedom
##   (102 observations deleted due to missingness)
## Multiple R-squared:  0.9908, Adjusted R-squared:  0.9905
## F-statistic:  3135 on 2 and 58 DF,  p-value: < 2.2e-16

plot(fit2)

#Resulting Outputs
v; K; D; Ds

## [1] 0.012822

## [1] 1.083941e-12

## [1] 0.0018

## [1] 0.137
```

20,000 Pa

Here are the outputs for krypton at pressure 20,000 Pa.

```
i<-2

if(i==1){ t <-  data1[,4] ; y <-  data1[,3]
        } else if (i==2){ t <-  data2[,4]   ; y <-  data2[,3]
        } else if (i==3){ t <-  data3[,4]   ; y <-  data3[,3]
        } else if (i==4){ t <-  data4[,4]   ; y <-  data4[,3]
        } else if (i==5){ t <-  data5[,4]   ; y <-  data5[,3]
   }

recT =  1/t

n<-length(y)
n<-228
nStart<-12


fit <-  lm( log(y[nStart:n]) ~    log(t[nStart:n]) +  recT[nStart:n] +  t[nSt
art:n]  )
summary(fit)

##
## Call:
## lm(formula = log(y[nStart:n]) ~ log(t[nStart:n]) + recT[nStart:n] +
##     t[nStart:n])
##
```

```
## Residuals:
##      Min       1Q   Median       3Q      Max
## -2.34758 -0.03513  0.01284  0.08909  1.81681
##
## Coefficients:
##                   Estimate Std. Error t value Pr(>|t|)
## (Intercept)     -32.920429  14.185795  -2.321  0.02331 *
## log(t[nStart:n])   7.818298   2.704433   2.891  0.00515 **
## recT[nStart:n]   217.795214 234.928611   0.927  0.35717
## t[nStart:n]       -0.052913   0.006602  -8.015 2.06e-11 ***
## ---
## Signif. codes:  0 '***' 0.001 '**' 0.01 '*' 0.05 '.' 0.1 ' ' 1
##
## Residual standard error: 0.5039 on 68 degrees of freedom
##   (145 observations deleted due to missingness)
## Multiple R-squared:  0.9718, Adjusted R-squared:  0.9705
## F-statistic: 780.1 on 3 and 68 DF,  p-value: < 2.2e-16

#plot(fit)


par(mfrow=c(1,1))

yOut <-  exp(fit$coeff[1]  +  fit$coeff[2]*log(t) +  fit$coeff[3]*recT +
fit$coeff[4]*t)
#plot(t,y)
#points( t, yOut, col=2, type="l", lwd=2)

yOut <-  fit$coeff[1]  +  fit$coeff[2]*log(t) +  fit$coeff[3]*recT +  fit$c
```

```
oeff[4]*t
#plot(t,log(y))
#points( t, yOut, col=2, type="l", lwd=2)


y2 =  log(y[nStart:n]) +  0.5*log(t[nStart:n])
fit2 <-  lm( y2 ~      recT[nStart:n] +  t[nStart:n]  )

yOut <-  exp(fit2$coeff[1]  -  0.5*log(t) +  fit2$coeff[2]*recT +  fit2$c
oeff[3]*t)
plot(t,y, xlab="Time (s)", ylab="Normalised concentration")
points( t, yOut, col=2, type="l", lwd=2)
```

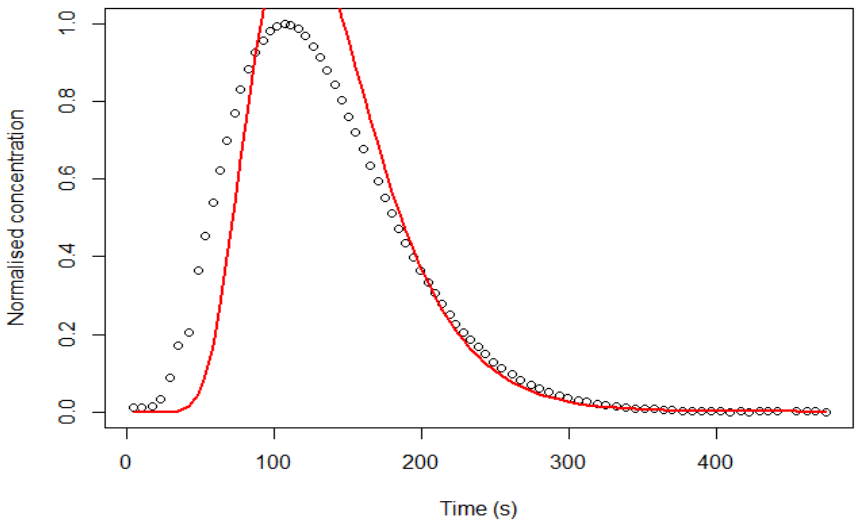


```
yOut <-  fit2$coeff[1]  -  0.5*log(t) +  fit2$coeff[2]*recT +  fit2$coeff[
3]*t
plot(t,log(y),xlab="Time (s)")
points( t, yOut, col=2, type="l", lwd=2)

summary(fit2)

##
## Call:
```

```
## lm(formula = y2 ~ recT[nStart:n] + t[nStart:n])
##
## Residuals:
##      Min       1Q   Median       3Q      Max
## -2.39049 -0.17649  0.05064  0.27178  1.53085
##
## Coefficients:
##                  Estimate Std. Error t value Pr(>|t|)
## (Intercept)     1.069e+01  4.954e-01   21.58   <2e-16 ***
## recT[nStart:n] -4.940e+02  4.292e+01  -11.51   <2e-16 ***
## t[nStart:n]    -3.287e-02  1.119e-03  -29.36   <2e-16 ***
## ---
## Signif. codes:  0 '***' 0.001 '**' 0.01 '*' 0.05 '.' 0.1 ' ' 1
##
## Residual standard error: 0.5339 on 69 degrees of freedom
##   (145 observations deleted due to missingness)
## Multiple R-squared:  0.9621, Adjusted R-squared:  0.961
## F-statistic: 876.8 on 2 and 69 DF,  p-value: < 2.2e-16
```

```
plot(fit2)
```

```
#Resulting Outputs
v; K; D; Ds
```

```
## [1] 0.007830885
```

```
## [1] 9.930063e-13
```

```
## [1] 0.0005
```

```
## [1] 0.059
```

10,000 Pa

Here are the outputs for krypton at pressure 10,000 Pa.

```
i<-1

if(i==1){ t <-  data1[,4] ; y <-  data1[,3]
        } else if (i==2){ t <-  data2[,4]   ; y <-  data2[,3]
        } else if (i==3){ t <-  data3[,4]   ; y <-  data3[,3]
        } else if (i==4){ t <-  data4[,4]   ; y <-  data4[,3]
        } else if (i==5){ t <-  data5[,4]   ; y <-  data5[,3]
   }

recT =  1/t

n<-length(y)
n<-399
nStart<-16


fit <-  lm( log(y[nStart:n]) ~    log(t[nStart:n]) +  recT[nStart:n] +  t[nSt
art:n]  )
summary(fit)

##
## Call:
## lm(formula = log(y[nStart:n]) ~ log(t[nStart:n]) + recT[nStart:n] +
##     t[nStart:n])
##
## Residuals:
##      Min       1Q   Median       3Q      Max
## -0.16584 -0.05850 -0.00262  0.05999  0.39284
##
## Coefficients:
##                   Estimate Std. Error t value Pr(>|t|)
## (Intercept)      -9.739e+00  2.340e+00  -4.162 6.55e-05 ***
## log(t[nStart:n])  3.197e+00  4.163e-01   7.680 9.57e-12 ***
## recT[nStart:n]   -4.514e+02  5.284e+01  -8.543 1.26e-13 ***
## t[nStart:n]      -2.471e-02  7.019e-04 -35.207  < 2e-16 ***
## ---
## Signif. codes:  0 '***' 0.001 '**' 0.01 '*' 0.05 '.' 0.1 ' ' 1
##
## Residual standard error: 0.08969 on 103 degrees of freedom
##   (277 observations deleted due to missingness)
## Multiple R-squared:  0.9977, Adjusted R-squared:  0.9976
## F-statistic: 1.5e+04 on 3 and 103 DF,  p-value: < 2.2e-16

#plot(fit)


par(mfrow=c(1,1))

yOut <-  exp(fit$coeff[1]  +  fit$coeff[2]*log(t) +  fit$coeff[3]*recT +
fit$coeff[4]*t)
#plot(t,y)
#points( t, yOut, col=2, type="l", lwd=2)

yOut <-  fit$coeff[1]  +  fit$coeff[2]*log(t) +  fit$coeff[3]*recT +  fit$c
```

```
oeff[4]*t
#plot(t,log(y))
#points( t, yOut, col=2, type="l", lwd=2)


y2 =  log(y[nStart:n]) +  0.5*log(t[nStart:n])
fit2 <-  lm( y2 ~      recT[nStart:n] +  t[nStart:n]  )

yOut <-  exp(fit2$coeff[1]  -  0.5*log(t) +  fit2$coeff[2]*recT +  fit2$c
oeff[3]*t)
plot(t,y, xlab="Time (s)", ylab="Normalised concentration")
points( t, yOut, col=2, type="l", lwd=2)
```

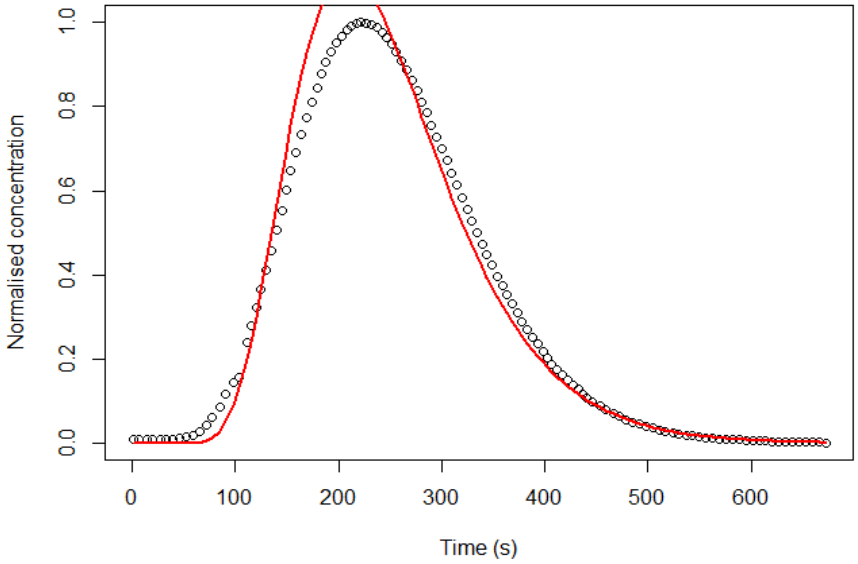


```
yOut <-  fit2$coeff[1]  -  0.5*log(t) +  fit2$coeff[2]*recT +  fit2$coeff[
3]*t
plot(t,log(y),xlab="Time (s)")
points( t, yOut, col=2, type="l", lwd=2)

summary(fit2)
```

```
##
## Call:
## lm(formula = y2 ~ recT[nStart:n] + t[nStart:n])
##
## Residuals:
##      Min       1Q   Median       3Q      Max
## -0.17982 -0.10300  0.00008  0.09914  0.47623
##
## Coefficients:
##                  Estimate Std. Error t value Pr(>|t|)
## (Intercept)     1.103e+01  9.468e-02  116.51   <2e-16 ***
## recT[nStart:n] -9.137e+02  1.201e+01  -76.11   <2e-16 ***
## t[nStart:n]    -1.856e-02  1.487e-04 -124.80   <2e-16 ***
## ---
## Signif. codes:  0 '***' 0.001 '**' 0.01 '*' 0.05 '.' 0.1 ' ' 1
##
## Residual standard error: 0.1186 on 104 degrees of freedom
##   (277 observations deleted due to missingness)
## Multiple R-squared:  0.995,  Adjusted R-squared:  0.9949
## F-statistic: 1.036e+04 on 2 and 104 DF,  p-value: < 2.2e-16

plot(fit2)

#Resulting Outputs
v; K; D; Ds

## [1] 0.004326527

## [1] 1.097263e-12

## [1] 0.0003

## [1] 0.058
```

Xenon results

50,000 Pa

Here are the outputs for xenon at pressure 50,000 Pa.

```
i<-5

if(i==1){ t <-  data1[,4] ; y <-  data1[,3]
        } else if (i==2){ t <-  data2[,4]   ; y <-  data2[,3]
        } else if (i==3){ t <-  data3[,4]   ; y <-  data3[,3]
        } else if (i==4){ t <-  data4[,2]   ; y <-  data4[,1]
        } else if (i==5){ t <-  data5[,4]   ; y <-  data5[,3]
   }

recT =  1/t

n<-length(y)
n<-119
nStart<-5


fit <-  lm( log(y[nStart:n]) ~    log(t[nStart:n]) +  recT[nStart:n] +  t[nSt
art:n]  )
summary(fit)

##
## Call:
## lm(formula = log(y[nStart:n]) ~ log(t[nStart:n]) + recT[nStart:n] +
##     t[nStart:n])
##
## Residuals:
##      Min       1Q   Median       3Q      Max
## -0.16523 -0.04164  0.00738  0.03547  0.22424
##
## Coefficients:
##                   Estimate Std. Error t value Pr(>|t|)
## (Intercept)       1.563e+01  2.512e+00   6.219 3.54e-07 ***
## log(t[nStart:n]) -2.799e+00  5.287e-01  -5.293 6.12e-06 ***
## recT[nStart:n]   -1.920e+02  2.815e+01  -6.820 5.65e-08 ***
## t[nStart:n]      -1.708e-02  2.125e-03  -8.037 1.51e-09 ***
## ---
## Signif. codes:  0 '***' 0.001 '**' 0.01 '*' 0.05 '.' 0.1 ' ' 1
##
## Residual standard error: 0.07382 on 36 degrees of freedom
##   (75 observations deleted due to missingness)
## Multiple R-squared:  0.9984, Adjusted R-squared:  0.9983
## F-statistic:  7658 on 3 and 36 DF,  p-value: < 2.2e-16

#plot(fit)


par(mfrow=c(1,1))

yOut <-  exp(fit$coeff[1]  +  fit$coeff[2]*log(t) +  fit$coeff[3]*recT +
fit$coeff[4]*t)
#plot(t,y)
#points( t, yOut, col=2, type="l", lwd=2)
```

```
yOut <-  fit$coeff[1]  +  fit$coeff[2]*log(t) +  fit$coeff[3]*recT +  fit$coeff[4]*t
#plot(t,log(y))
#points( t, yOut, col=2, type="l", lwd=2)


y2 =  log(y[nStart:n]) +  0.5*log(t[nStart:n])
fit2 <-  lm( y2 ~      recT[nStart:n] +  t[nStart:n]  )

yOut <-  exp(fit2$coeff[1]  -  0.5*log(t) +  fit2$coeff[2]*recT +  fit2$coeff[3]*t)
plot(t,y, xlab="Time (s)", ylab="Normalised concentration")
points( t, yOut, col=2, type="l", lwd=2)
```

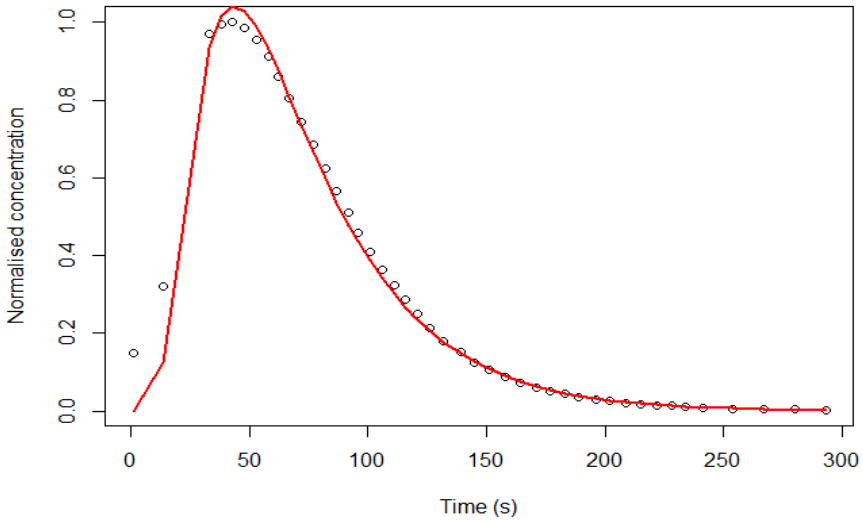


```
yOut <-  fit2$coeff[1]  -  0.5*log(t) +  fit2$coeff[2]*recT +  fit2$coeff[3]*t
plot(t,log(y),xlab="Time (s)")
points( t, yOut, col=2, type="l", lwd=2)

summary(fit2)

##
## Call:
```

```
## lm(formula = y2 ~ recT[nStart:n] + t[nStart:n])
##
## Residuals:
##      Min       1Q   Median       3Q      Max
## -0.16261 -0.04583 -0.01450  0.04169  0.34022
##
## Coefficients:
##                  Estimate Std. Error t value Pr(>|t|)
## (Intercept)     4.710e+00  1.145e-01   41.13  < 2e-16 ***
## recT[nStart:n] -7.150e+01  6.009e+00  -11.90 3.27e-14 ***
## t[nStart:n]    -2.619e-02  4.319e-04  -60.65  < 2e-16 ***
## ---
## Signif. codes:  0 '***' 0.001 '**' 0.01 '*' 0.05 '.' 0.1 ' ' 1
##
## Residual standard error: 0.08992 on 37 degrees of freedom
##   (75 observations deleted due to missingness)
## Multiple R-squared:  0.9968, Adjusted R-squared:  0.9966
## F-statistic:  5716 on 2 and 37 DF,  p-value: < 2.2e-16
```

```
plot(fit2)
```

```
#Resulting Outputs
v; K; D; Ds
```

```
## [1] 0.01837346
```

```
## [1] 9.319488e-13
```

```
## [1] 0.0032
```

```
## [1] 0.175
```

40,000 Pa

Here are the outputs for xenon at pressure 40,000 Pa.

```
i<-4

if(i==1){ t <-  data1[,4] ; y <-  data1[,3]
        } else if (i==2){ t <-  data2[,4]   ; y <-  data2[,3]
        } else if (i==3){ t <-  data3[,4]   ; y <-  data3[,3]
        } else if (i==4){ t <-  data4[,2]   ; y <-  data4[,1]
        } else if (i==5){ t <-  data5[,4]   ; y <-  data5[,3]
   }

recT =  1/t

n<-length(y)
n<-141
nStart<-6


fit <-  lm( log(y[nStart:n]) ~    log(t[nStart:n]) +  recT[nStart:n] +  t[nSt
art:n]  )
summary(fit)

##
## Call:
## lm(formula = log(y[nStart:n]) ~ log(t[nStart:n]) + recT[nStart:n] +
##     t[nStart:n])
##
## Residuals:
##       Min        1Q    Median        3Q       Max
## -0.047299 -0.019696  0.002504  0.016835  0.057892
##
## Coefficients:
##                   Estimate Std. Error t value Pr(>|t|)
## (Intercept)      -3.073e+00  6.620e-01  -4.642 4.03e-05 ***
## log(t[nStart:n])  1.342e+00  1.443e-01   9.300 2.46e-11 ***
## recT[nStart:n]   -2.254e+01  6.392e+00  -3.526  0.00112 **
## t[nStart:n]      -3.412e-02  6.745e-04 -50.581  < 2e-16 ***
## ---
## Signif. codes:  0 '***' 0.001 '**' 0.01 '*' 0.05 '.' 0.1 ' ' 1
##
## Residual standard error: 0.02511 on 38 degrees of freedom
##   (94 observations deleted due to missingness)
## Multiple R-squared:  0.9997, Adjusted R-squared:  0.9997
## F-statistic: 4.365e+04 on 3 and 38 DF,  p-value: < 2.2e-16

#plot(fit)


par(mfrow=c(1,1))

yOut <-  exp(fit$coeff[1]  +  fit$coeff[2]*log(t) +  fit$coeff[3]*recT +
fit$coeff[4]*t)
#plot(t,y)
#points( t, yOut, col=2, type="l", lwd=2)

yOut <-  fit$coeff[1]  +  fit$coeff[2]*log(t) +  fit$coeff[3]*recT +  fit$c
```

```
oeff[4]*t
#plot(t,log(y))
#points( t, yOut, col=2, type="l", lwd=2)


y2 =  log(y[nStart:n]) +  0.5*log(t[nStart:n])
fit2 <-  lm( y2 ~      recT[nStart:n] +  t[nStart:n]  )

yOut <-  exp(fit2$coeff[1]  -  0.5*log(t) +  fit2$coeff[2]*recT +  fit2$c
oeff[3]*t)
plot(t,y, xlab="Time (s)", ylab="Normalised concentration")
points( t, yOut, col=2, type="l", lwd=2)
```

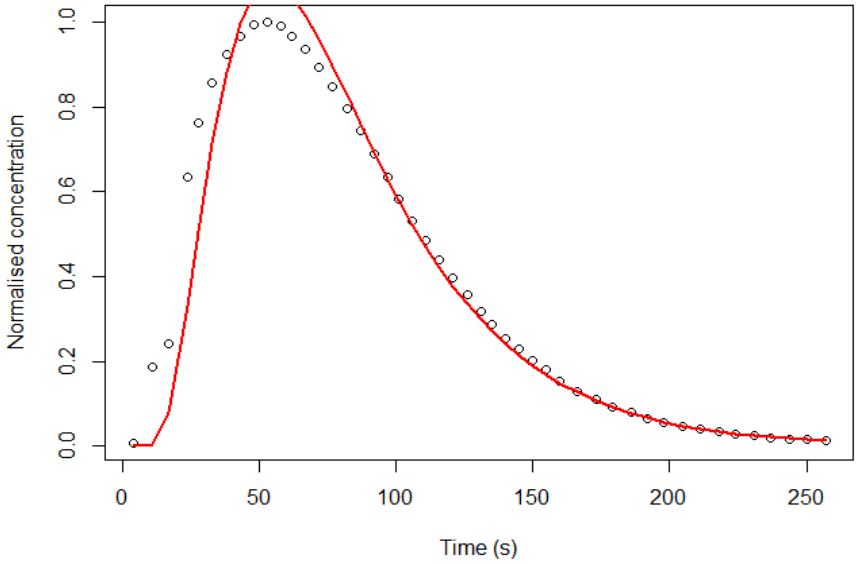


```
yOut <-  fit2$coeff[1]  -  0.5*log(t) +  fit2$coeff[2]*recT +  fit2$coeff[
3]*t
plot(t,log(y),xlab="Time (s)")
points( t, yOut, col=2, type="l", lwd=2)

summary(fit2)
```

```
##
## Call:
## lm(formula = y2 ~ recT[nStart:n] + t[nStart:n])
##
## Residuals:
##       Min        1Q    Median        3Q       Max
## -0.093149 -0.032335 -0.005251  0.042290  0.181660
##
## Coefficients:
##                  Estimate Std. Error t value Pr(>|t|)
## (Intercept)     5.370e+00  6.161e-02   87.16   <2e-16 ***
## recT[nStart:n] -1.027e+02  2.720e+00  -37.75   <2e-16 ***
## t[nStart:n]    -2.564e-02  2.647e-04  -96.87   <2e-16 ***
## ---
## Signif. codes:  0 '***' 0.001 '**' 0.01 '*' 0.05 '.' 0.1 ' ' 1
##
## Residual standard error: 0.057 on 39 degrees of freedom
##   (94 observations deleted due to missingness)
## Multiple R-squared:  0.9978, Adjusted R-squared:  0.9976
## F-statistic:  8662 on 2 and 39 DF,  p-value: < 2.2e-16
```

```
plot(fit2)
```

```
#Resulting Outputs
v; K; D; Ds
```

```
## [1] 0.01516905
```

```
## [1] 9.617662e-13
```

```
## [1] 0.0022
```

```
## [1] 0.148
```

30,000 Pa

Here are the outputs for xenon at pressure 30,000 Pa.

```
i<-3

if(i==1){ t <-  data1[,4] ; y <-  data1[,3]
        } else if (i==2){ t <-  data2[,4]   ; y <-  data2[,3]
        } else if (i==3){ t <-  data3[,4]   ; y <-  data3[,3]
        } else if (i==4){ t <-  data4[,2]   ; y <-  data4[,1]
        } else if (i==5){ t <-  data5[,4]   ; y <-  data5[,3]
   }

recT =  1/t

n<-length(y)
n<-180
nStart<-6


fit <-  lm( log(y[nStart:n]) ~    log(t[nStart:n]) +  recT[nStart:n] +  t[nSt
art:n]  )
summary(fit)

##
## Call:
## lm(formula = log(y[nStart:n]) ~ log(t[nStart:n]) + recT[nStart:n] +
##     t[nStart:n])
##
## Residuals:
##       Min        1Q    Median        3Q       Max
## -0.056658 -0.027211  0.000089  0.022689  0.107387
##
## Coefficients:
##                   Estimate Std. Error t value Pr(>|t|)
## (Intercept)      -4.959e+00  6.117e-01  -8.107 9.89e-11 ***
## log(t[nStart:n])  1.776e+00  1.295e-01  13.709  < 2e-16 ***
## recT[nStart:n]   -2.591e+01  6.376e+00  -4.064 0.000167 ***
## t[nStart:n]      -3.128e-02  5.171e-04 -60.489  < 2e-16 ***
## ---
## Signif. codes:  0 '***' 0.001 '**' 0.01 '*' 0.05 '.' 0.1 ' ' 1
##
## Residual standard error: 0.03614 on 51 degrees of freedom
##   (120 observations deleted due to missingness)
## Multiple R-squared:  0.9995, Adjusted R-squared:  0.9995
## F-statistic: 3.5e+04 on 3 and 51 DF,  p-value: < 2.2e-16

#plot(fit)


par(mfrow=c(1,1))

yOut <-  exp(fit$coeff[1]  +  fit$coeff[2]*log(t) +  fit$coeff[3]*recT +
fit$coeff[4]*t)
#plot(t,y)
#points( t, yOut, col=2, type="l", lwd=2)

yOut <-  fit$coeff[1]  +  fit$coeff[2]*log(t) +  fit$coeff[3]*recT +  fit$c
```

```
oeff[4]*t
#plot(t,log(y))
#points( t, yOut, col=2, type="l", lwd=2)


y2 =  log(y[nStart:n]) +  0.5*log(t[nStart:n])
fit2 <-  lm( y2 ~      recT[nStart:n] +  t[nStart:n]  )

yOut <-  exp(fit2$coeff[1]  -  0.5*log(t) +  fit2$coeff[2]*recT +  fit2$c
oeff[3]*t)
plot(t,y, xlab="Time (s)", ylab="Normalised concentration")
points( t, yOut, col=2, type="l", lwd=2)
```

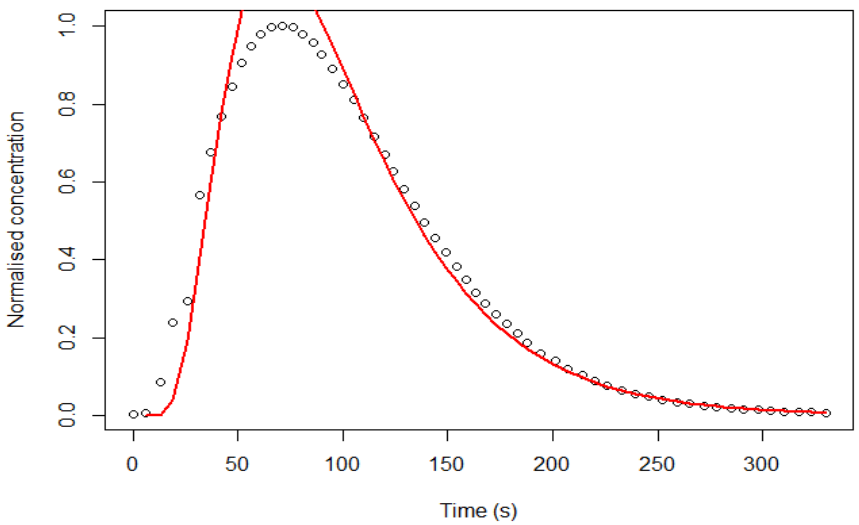


```
yOut <-  fit2$coeff[1]  -  0.5*log(t) +  fit2$coeff[2]*recT +  fit2$coeff[
3]*t
plot(t,log(y),xlab="Time (s)")
points( t, yOut, col=2, type="l", lwd=2)

summary(fit2)

##
## Call:
```

```
## lm(formula = y2 ~ recT[nStart:n] + t[nStart:n])
##
## Residuals:
##      Min       1Q   Median       3Q      Max
## -0.15877 -0.06536 -0.00512  0.07071  0.33134
##
## Coefficients:
##                  Estimate Std. Error t value Pr(>|t|)
## (Intercept)     5.777e+00  7.327e-02   78.84   <2e-16 ***
## recT[nStart:n] -1.353e+02  3.597e+00  -37.62   <2e-16 ***
## t[nStart:n]    -2.237e-02  2.623e-04  -85.28   <2e-16 ***
## ---
## Signif. codes:  0 '***' 0.001 '**' 0.01 '*' 0.05 '.' 0.1 ' ' 1
##
## Residual standard error: 0.09505 on 52 degrees of freedom
##   (120 observations deleted due to missingness)
## Multiple R-squared:  0.9951, Adjusted R-squared:  0.995
## F-statistic:  5328 on 2 and 52 DF,  p-value: < 2.2e-16
```

```
plot(fit2)
```

```
#Resulting Outputs
v; K; D; Ds
```

```
## [1] 0.01234241
```

```
## [1] 1.043398e-12
```

```
## [1] 0.0017
```

```
## [1] 0.138
```

20,000 Pa

Here are the outputs for xenon at pressure 20,000 Pa.

```
i<-2

if(i==1){ t <-  data1[,4] ; y <-  data1[,3]
        } else if (i==2){ t <-  data2[,4]   ; y <-  data2[,3]
        } else if (i==3){ t <-  data3[,4]   ; y <-  data3[,3]
        } else if (i==4){ t <-  data4[,2]   ; y <-  data4[,1]
        } else if (i==5){ t <-  data5[,4]   ; y <-  data5[,3]
   }

recT =  1/t

n<-length(y)
n<-229
nStart<-11


fit <-  lm( log(y[nStart:n]) ~    log(t[nStart:n]) +  recT[nStart:n] +  t[nSt
art:n]  )
summary(fit)

##
## Call:
## lm(formula = log(y[nStart:n]) ~ log(t[nStart:n]) + recT[nStart:n] +
##     t[nStart:n])
##
## Residuals:
##       Min        1Q    Median        3Q       Max
## -0.070602 -0.029214  0.005249  0.028383  0.109951
##
## Coefficients:
##                   Estimate Std. Error t value Pr(>|t|)
## (Intercept)      -5.527e+00  9.526e-01  -5.802 1.68e-07 ***
## log(t[nStart:n])  1.979e+00  1.833e-01  10.798  < 2e-16 ***
## recT[nStart:n]   -1.026e+02  1.504e+01  -6.822 2.48e-09 ***
## t[nStart:n]      -2.559e-02  4.671e-04 -54.777  < 2e-16 ***
## ---
## Signif. codes:  0 '***' 0.001 '**' 0.01 '*' 0.05 '.' 0.1 ' ' 1
##
## Residual standard error: 0.03948 on 71 degrees of freedom
##   (144 observations deleted due to missingness)
## Multiple R-squared:  0.9995, Adjusted R-squared:  0.9995
## F-statistic: 4.59e+04 on 3 and 71 DF,  p-value: < 2.2e-16

#plot(fit)


par(mfrow=c(1,1))

yOut <-  exp(fit$coeff[1]  +  fit$coeff[2]*log(t) +  fit$coeff[3]*recT +
fit$coeff[4]*t)
#plot(t,y)
#points( t, yOut, col=2, type="l", lwd=2)

yOut <-  fit$coeff[1]  +  fit$coeff[2]*log(t) +  fit$coeff[3]*recT +  fit$c
```

```
oeff[4]*t
#plot(t,log(y))
#points( t, yOut, col=2, type="l", lwd=2)


y2 =  log(y[nStart:n]) +  0.5*log(t[nStart:n])
fit2 <-  lm( y2 ~      recT[nStart:n] +  t[nStart:n]  )

yOut <-  exp(fit2$coeff[1]  -  0.5*log(t) +  fit2$coeff[2]*recT +  fit2$c
oeff[3]*t)
plot(t,y, xlab="Time (s)", ylab="Normalised concentration")
points( t, yOut, col=2, type="l", lwd=2)
```

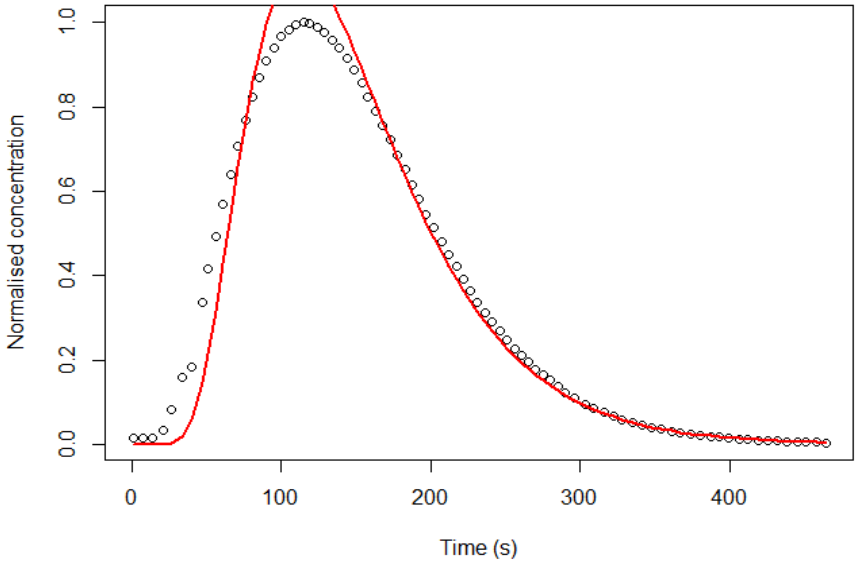


```
yOut <-  fit2$coeff[1]  -  0.5*log(t) +  fit2$coeff[2]*recT +  fit2$coeff[
3]*t
plot(t,log(y),xlab="Time (s)")
points( t, yOut, col=2, type="l", lwd=2)

summary(fit2)
```

```
##
## Call:
## lm(formula = y2 ~ recT[nStart:n] + t[nStart:n])
##
## Residuals:
##       Min        1Q    Median        3Q       Max
## -0.124497 -0.043460 -0.008412  0.060796  0.282259
##
## Coefficients:
##                  Estimate Std. Error t value Pr(>|t|)
## (Intercept)     7.349e+00  6.284e-02   117.0   <2e-16 ***
## recT[nStart:n] -3.026e+02  5.137e+00   -58.9   <2e-16 ***
## t[nStart:n]    -1.936e-02  1.479e-04  -130.9   <2e-16 ***
## ---
## Signif. codes:  0 '***' 0.001 '**' 0.01 '*' 0.05 '.' 0.1 ' ' 1
##
## Residual standard error: 0.07414 on 72 degrees of freedom
##   (144 observations deleted due to missingness)
## Multiple R-squared:  0.9975, Adjusted R-squared:  0.9975
## F-statistic: 1.455e+04 on 2 and 72 DF,  p-value: < 2.2e-16

plot(fit2)

#Resulting Outputs
v; K; D; Ds

## [1] 0.007678885

## [1] 9.737318e-13

## [1] 0.0008

## [1] 0.099
```

10,000 Pa

Here are the outputs for xenon at pressure 10,000 Pa.

```
i<-1

if(i==1){ t <-  data1[,4] ; y <-  data1[,3]
        } else if (i==2){ t <-  data2[,4]   ; y <-  data2[,3]
        } else if (i==3){ t <-  data3[,4]   ; y <-  data3[,3]
        } else if (i==4){ t <-  data4[,2]   ; y <-  data4[,1]
        } else if (i==5){ t <-  data5[,4]   ; y <-  data5[,3]
   }

recT =  1/t

n<-length(y)
n<-439
nStart<-25


fit <-  lm( log(y[nStart:n]) ~    log(t[nStart:n]) +  recT[nStart:n] +  t[nSt
art:n]  )
summary(fit)

##
## Call:
## lm(formula = log(y[nStart:n]) ~ log(t[nStart:n]) + recT[nStart:n] +
##     t[nStart:n])
##
## Residuals:
##       Min        1Q    Median        3Q       Max
## -0.151474 -0.006182 -0.000892  0.006669  0.079898
##
## Coefficients:
##                   Estimate Std. Error t value Pr(>|t|)
## (Intercept)      -3.962e+01  1.499e+00 -26.431  < 2e-16 ***
## log(t[nStart:n])  8.344e+00  2.596e-01  32.148  < 2e-16 ***
## recT[nStart:n]    2.868e+02  3.973e+01   7.219 1.46e-10 ***
## t[nStart:n]      -3.048e-02  3.848e-04 -79.203  < 2e-16 ***
## ---
## Signif. codes:  0 '***' 0.001 '**' 0.01 '*' 0.05 '.' 0.1 ' ' 1
##
## Residual standard error: 0.02636 on 92 degrees of freedom
##   (319 observations deleted due to missingness)
## Multiple R-squared:  0.9997, Adjusted R-squared:  0.9997
## F-statistic: 1.051e+05 on 3 and 92 DF,  p-value: < 2.2e-16

#plot(fit)


par(mfrow=c(1,1))

yOut <-  exp(fit$coeff[1]  +  fit$coeff[2]*log(t) +  fit$coeff[3]*recT +
fit$coeff[4]*t)
#plot(t,y)
#points( t, yOut, col=2, type="l", lwd=2)

yOut <-  fit$coeff[1]  +  fit$coeff[2]*log(t) +  fit$coeff[3]*recT +  fit$c
```

```
oeff[4]*t
#plot(t,log(y))
#points( t, yOut, col=2, type="l", lwd=2)


y2 =  log(y[nStart:n]) +  0.5*log(t[nStart:n])
fit2 <-  lm( y2 ~      recT[nStart:n] +  t[nStart:n]  )

yOut <-  exp(fit2$coeff[1]  -  0.5*log(t) +  fit2$coeff[2]*recT +  fit2$c
oeff[3]*t)
plot(t,y, xlab="Time (s)", ylab="Normalised concentration")
points( t, yOut, col=2, type="l", lwd=2)
```

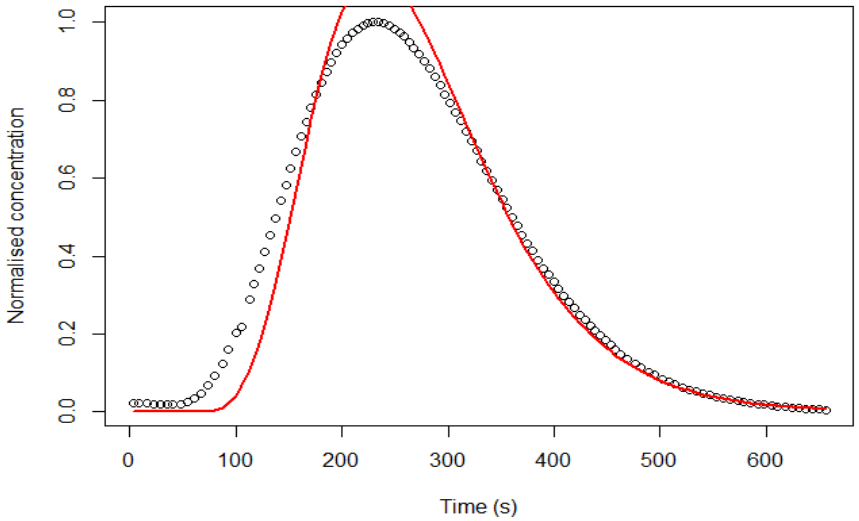


```
yOut <-  fit2$coeff[1]  -  0.5*log(t) +  fit2$coeff[2]*recT +  fit2$coeff[
3]*t
plot(t,log(y),xlab="Time (s)")
points( t, yOut, col=2, type="l", lwd=2)

summary(fit2)

##
## Call:
```

```
## lm(formula = y2 ~ recT[nStart:n] + t[nStart:n])
##
## Residuals:
##      Min       1Q   Median       3Q      Max
## -0.32137 -0.06854  0.01848  0.07479  0.25908
##
## Coefficients:
##                  Estimate Std. Error t value Pr(>|t|)
## (Intercept)     1.144e+01  1.253e-01   91.35   <2e-16 ***
## recT[nStart:n] -1.055e+03  1.910e+01  -55.25   <2e-16 ***
## t[nStart:n]    -1.747e-02  1.782e-04  -98.06   <2e-16 ***
## ---
## Signif. codes:  0 '***' 0.001 '**' 0.01 '*' 0.05 '.' 0.1 ' ' 1
##
## Residual standard error: 0.09675 on 93 degrees of freedom
##   (319 observations deleted due to missingness)
## Multiple R-squared:  0.9949, Adjusted R-squared:  0.9948
## F-statistic:  9138 on 2 and 93 DF,  p-value: < 2.2e-16
```

```
plot(fit2)
```

```
#Resulting Outputs
v; K; D; Ds
```

```
## [1] 0.003906233
```

```
## [1] 9.906708e-13
```

```
## [1] 0.0002
```

```
## [1] 0.056
```

SF_6 results

50,000 Pa

Here are the outputs for SF6 at pressure 50,000 Pa.

```
i<-5

if(i==1){ t <-  data1[,4] ; y <-  data1[,3]
        } else if (i==2){ t <-  data2[,4]   ; y <-  data2[,3]
        } else if (i==3){ t <-  data3[,4]   ; y <-  data3[,3]
        } else if (i==4){ t <-  data4[,10]   ; y <-  data4[,9]
        } else if (i==5){ t <-  data5[,2]   ; y <-  data5[,1]
   }

recT =  1/t

n<-length(y)
n<-118
nStart<-5


fit <-  lm( log(y[nStart:n]) ~    log(t[nStart:n]) +  recT[nStart:n] +  t[nSt
art:n]  )
summary(fit)

##
## Call:
## lm(formula = log(y[nStart:n]) ~ log(t[nStart:n]) + recT[nStart:n] +
##     t[nStart:n])
##
## Residuals:
##       Min        1Q    Median        3Q       Max
## -0.044440 -0.009613 -0.001406  0.010012  0.072936
##
## Coefficients:
##                   Estimate Std. Error t value Pr(>|t|)
## (Intercept)     -3.2746125  0.4116620  -7.955 1.92e-09 ***
## log(t[nStart:n])  1.3002689  0.0920772  14.122 2.99e-16 ***
## recT[nStart:n]   -2.9545623  3.5643157  -0.829    0.413
## t[nStart:n]      -0.0359053  0.0004763 -75.388  < 2e-16 ***
## ---
## Signif. codes:  0 '***' 0.001 '**' 0.01 '*' 0.05 '.' 0.1 ' ' 1
##
## Residual standard error: 0.01921 on 36 degrees of freedom
##   (74 observations deleted due to missingness)
## Multiple R-squared:  0.9999, Adjusted R-squared:  0.9999
## F-statistic: 8.727e+04 on 3 and 36 DF,  p-value: < 2.2e-16

#plot(fit)


par(mfrow=c(1,1))

yOut <-  exp(fit$coeff[1]  +  fit$coeff[2]*log(t) +  fit$coeff[3]*recT +
fit$coeff[4]*t)
#plot(t,y)
#points( t, yOut, col=2, type="l", lwd=2)
```

```
yOut <-  fit$coeff[1]  +  fit$coeff[2]*log(t) +  fit$coeff[3]*recT +  fit$c
oeff[4]*t
#plot(t,log(y))
#points( t, yOut, col=2, type="l", lwd=2)


y2 =  log(y[nStart:n]) +  0.5*log(t[nStart:n])
fit2 <-  lm( y2 ~      recT[nStart:n] +  t[nStart:n]  )

yOut <-  exp(fit2$coeff[1]  -  0.5*log(t) +  fit2$coeff[2]*recT +  fit2$c
oeff[3]*t)
plot(t,y, xlab="Time (s)", ylab="Normalised concentration")
points( t, yOut, col=2, type="l", lwd=2)
```

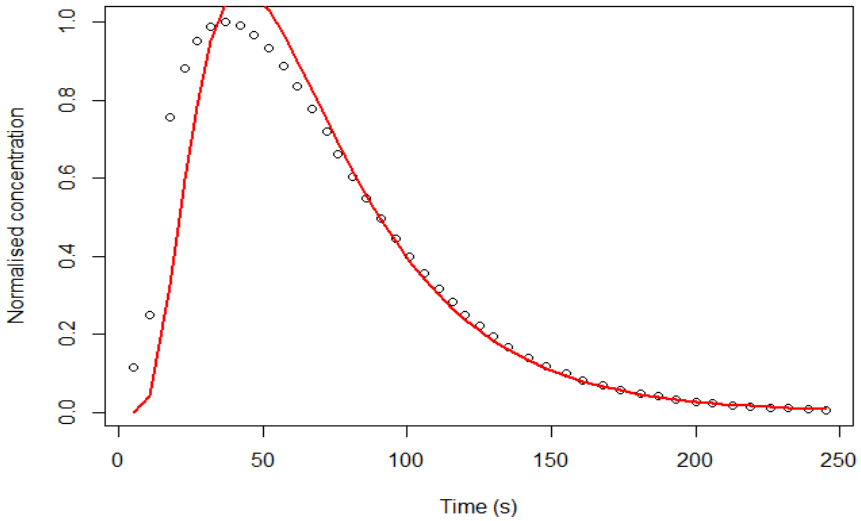


```
yOut <-  fit2$coeff[1]  -  0.5*log(t) +  fit2$coeff[2]*recT +  fit2$coeff[
3]*t
plot(t,log(y),xlab="Time (s)")
points( t, yOut, col=2, type="l", lwd=2)

summary(fit2)

##
## Call:
```

```
## lm(formula = y2 ~ recT[nStart:n] + t[nStart:n])
##
## Residuals:
##       Min        1Q    Median        3Q       Max
## -0.145532 -0.042976  0.007403  0.041535  0.191243
##
## Coefficients:
##                  Estimate Std. Error t value Pr(>|t|)
## (Intercept)     4.766e+00  6.266e-02   76.06   <2e-16 ***
## recT[nStart:n] -7.120e+01  2.424e+00  -29.38   <2e-16 ***
## t[nStart:n]    -2.675e-02  2.928e-04  -91.35   <2e-16 ***
## ---
## Signif. codes:  0 '***' 0.001 '**' 0.01 '*' 0.05 '.' 0.1 ' ' 1
##
## Residual standard error: 0.0646 on 37 degrees of freedom
##   (74 observations deleted due to missingness)
## Multiple R-squared:  0.9977, Adjusted R-squared:  0.9976
## F-statistic:  7944 on 2 and 37 DF,  p-value: < 2.2e-16
```

```
plot(fit2)
```

```
#Resulting Outputs
v; K; D; Ds
```

```
## [1] 0.01860746
```

```
## [1] 9.438181e-13
```

```
## [1] 0.0032
```

```
## [1] 0.174
```

40,000 Pa

Here are the outputs for SF6 at pressure 40,000 Pa.

```
i<-4

if(i==1){ t <-  data1[,4] ; y <-  data1[,3]
        } else if (i==2){ t <-  data2[,4]   ; y <-  data2[,3]
        } else if (i==3){ t <-  data3[,4]   ; y <-  data3[,3]
        } else if (i==4){ t <-  data4[,10]   ; y <-  data4[,9]
        } else if (i==5){ t <-  data5[,2]   ; y <-  data5[,1]
   }

recT =  1/t

n<-length(y)
n<-142
nStart<-3


fit <-  lm( log(y[nStart:n]) ~    log(t[nStart:n]) +  recT[nStart:n] +  t[nSt
art:n]  )
summary(fit)

##
## Call:
## lm(formula = log(y[nStart:n]) ~ log(t[nStart:n]) + recT[nStart:n] +
##     t[nStart:n])
##
## Residuals:
##      Min       1Q   Median       3Q      Max
## -0.57282 -0.04564 -0.00104  0.05320  0.18896
##
## Coefficients:
##                   Estimate Std. Error t value Pr(>|t|)
## (Intercept)     -15.678518   2.740782   -5.72 1.08e-06 ***
## log(t[nStart:n])   4.089854   0.586786    6.97 1.82e-08 ***
## recT[nStart:n]    98.313742  28.089103    3.50  0.00114 **
## t[nStart:n]       -0.046740   0.002505  -18.66  < 2e-16 ***
## ---
## Signif. codes:  0 '***' 0.001 '**' 0.01 '*' 0.05 '.' 0.1 ' ' 1
##
## Residual standard error: 0.1157 on 41 degrees of freedom
##   (95 observations deleted due to missingness)
## Multiple R-squared:  0.996,  Adjusted R-squared:  0.9957
## F-statistic:  3408 on 3 and 41 DF,  p-value: < 2.2e-16

#plot(fit)


par(mfrow=c(1,1))

yOut <-  exp(fit$coeff[1]  +  fit$coeff[2]*log(t) +  fit$coeff[3]*recT +
fit$coeff[4]*t)
#plot(t,y)
#points( t, yOut, col=2, type="l", lwd=2)

yOut <-  fit$coeff[1]  +  fit$coeff[2]*log(t) +  fit$coeff[3]*recT +  fit$c
```

```
oeff[4]*t
#plot(t,log(y))
#points( t, yOut, col=2, type="l", lwd=2)


y2 =  log(y[nStart:n]) +  0.5*log(t[nStart:n])
fit2 <-  lm( y2 ~      recT[nStart:n] +  t[nStart:n]  )

yOut <-  exp(fit2$coeff[1]  -  0.5*log(t) +  fit2$coeff[2]*recT +  fit2$c
oeff[3]*t)
plot(t,y, xlab="Time (s)", ylab="Normalised concentration")
points( t, yOut, col=2, type="l", lwd=2)
```

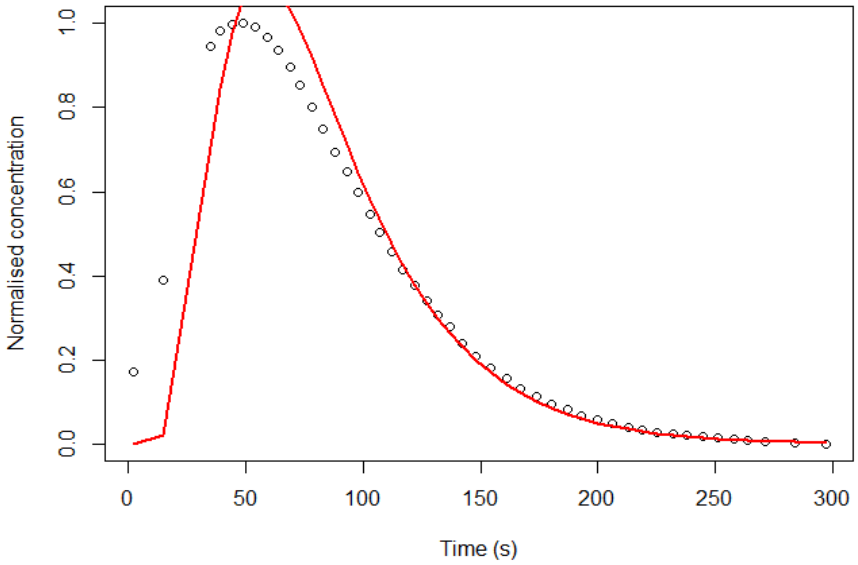


```
yOut <-  fit2$coeff[1]  -  0.5*log(t) +  fit2$coeff[2]*recT +  fit2$coeff[
3]*t
plot(t,log(y),xlab="Time (s)")
points( t, yOut, col=2, type="l", lwd=2)

summary(fit2)
```

```
##
## Call:
## lm(formula = y2 ~ recT[nStart:n] + t[nStart:n])
##
## Residuals:
##      Min       1Q   Median       3Q      Max
## -0.86205 -0.09327  0.03769  0.11558  0.29046
##
## Coefficients:
##                  Estimate Std. Error t value Pr(>|t|)
## (Intercept)     5.741e+00  1.775e-01   32.35   <2e-16 ***
## recT[nStart:n] -1.173e+02  8.438e+00  -13.90   <2e-16 ***
## t[nStart:n]    -2.745e-02  6.919e-04  -39.67   <2e-16 ***
## ---
## Signif. codes:  0 '***' 0.001 '**' 0.01 '*' 0.05 '.' 0.1 ' ' 1
##
## Residual standard error: 0.1804 on 42 degrees of freedom
##   (95 observations deleted due to missingness)
## Multiple R-squared:  0.9864, Adjusted R-squared:  0.9857
## F-statistic:  1519 on 2 and 42 DF,  p-value: < 2.2e-16

plot(fit2)

#Resulting Outputs
v; K; D; Ds

## [1] 0.01468714

## [1] 9.312116e-13

## [1] 0.0020

## [1] 0.134
```

30,000 Pa

Here are the outputs for SF6 at pressure 30,000 Pa.

```
i<-3

if(i==1){ t <-  data1[,4] ; y <-  data1[,3]
        } else if (i==2){ t <-  data2[,4]   ; y <-  data2[,3]
        } else if (i==3){ t <-  data3[,4]   ; y <-  data3[,3]
        } else if (i==4){ t <-  data4[,10]   ; y <-  data4[,9]
        } else if (i==5){ t <-  data5[,2]   ; y <-  data5[,1]
   }

recT =  1/t

n<-length(y)
n<-180
nStart<-5


fit <-  lm( log(y[nStart:n]) ~    log(t[nStart:n]) +  recT[nStart:n] +  t[nSt
art:n]  )
summary(fit)

##
## Call:
## lm(formula = log(y[nStart:n]) ~ log(t[nStart:n]) + recT[nStart:n] +
##     t[nStart:n])
##
## Residuals:
##       Min        1Q    Median        3Q       Max
## -0.175931 -0.045394 -0.007625  0.041092  0.173958
##
## Coefficients:
##                   Estimate Std. Error t value Pr(>|t|)
## (Intercept)       5.828e+00  1.263e+00   4.613 2.42e-05 ***
## log(t[nStart:n]) -6.041e-01  2.553e-01  -2.366   0.0215 *
## recT[nStart:n]   -1.289e+02  1.602e+01  -8.047 7.31e-11 ***
## t[nStart:n]      -1.932e-02  8.226e-04 -23.491  < 2e-16 ***
## ---
## Signif. codes:  0 '***' 0.001 '**' 0.01 '*' 0.05 '.' 0.1 ' ' 1
##
## Residual standard error: 0.06629 on 55 degrees of freedom
##   (117 observations deleted due to missingness)
## Multiple R-squared:  0.9987, Adjusted R-squared:  0.9987
## F-statistic: 1.447e+04 on 3 and 55 DF,  p-value: < 2.2e-16

#plot(fit)


par(mfrow=c(1,1))

yOut <-  exp(fit$coeff[1]  +  fit$coeff[2]*log(t) +  fit$coeff[3]*recT +
fit$coeff[4]*t)
#plot(t,y)
#points( t, yOut, col=2, type="l", lwd=2)

yOut <-  fit$coeff[1]  +  fit$coeff[2]*log(t) +  fit$coeff[3]*recT +  fit$c
```

```
oeff[4]*t
#plot(t,log(y))
#points( t, yOut, col=2, type="l", lwd=2)


y2 =  log(y[nStart:n]) +  0.5*log(t[nStart:n])
fit2 <-  lm( y2 ~      recT[nStart:n] +  t[nStart:n]  )

yOut <-  exp(fit2$coeff[1]  -  0.5*log(t) +  fit2$coeff[2]*recT +  fit2$c
oeff[3]*t)
plot(t,y, xlab="Time (s)", ylab="Normalised concentration")
points( t, yOut, col=2, type="l", lwd=2)
```

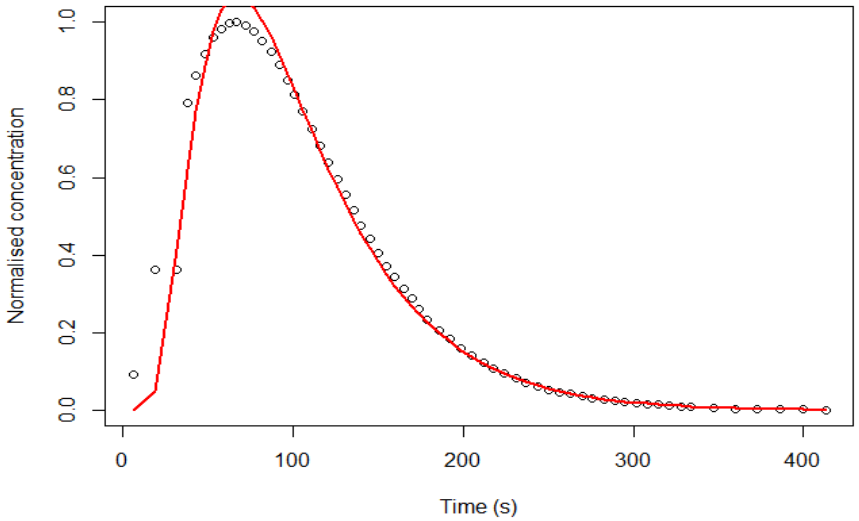


```
yOut <-  fit2$coeff[1]  -  0.5*log(t) +  fit2$coeff[2]*recT +  fit2$coeff[
3]*t
plot(t,log(y),xlab="Time (s)")
points( t, yOut, col=2, type="l", lwd=2)

summary(fit2)

##
## Call:
```

```
## lm(formula = y2 ~ recT[nStart:n] + t[nStart:n])
##
## Residuals:
##       Min        1Q    Median        3Q       Max
## -0.175407 -0.046215 -0.008491  0.040177  0.182047
##
## Coefficients:
##                  Estimate Std. Error t value Pr(>|t|)
## (Intercept)     5.313e+00  5.283e-02  100.57   <2e-16 ***
## recT[nStart:n] -1.225e+02  3.277e+00  -37.39   <2e-16 ***
## t[nStart:n]    -1.965e-02  1.559e-04 -126.02   <2e-16 ***
## ---
## Signif. codes:  0 '***' 0.001 '**' 0.01 '*' 0.05 '.' 0.1 ' ' 1
##
## Residual standard error: 0.0658 on 56 degrees of freedom
##   (117 observations deleted due to missingness)
## Multiple R-squared:  0.9982, Adjusted R-squared:  0.9982
## F-statistic: 1.597e+04 on 2 and 56 DF,  p-value: < 2.2e-16
```

```
plot(fit2)
```

```
#Resulting Outputs
v; K; D; Ds
```

```
## [1] 0.01215779
```

```
## [1] 1.027791e-12
```

```
## [1] 0.0019
```

```
## [1] 0.155
```

20,000 Pa

Here are the outputs for SF6 at pressure 20,000 Pa.

```
i<-2

if(i==1){ t <-  data1[,4] ; y <-  data1[,3]
        } else if (i==2){ t <-  data2[,4]   ; y <-  data2[,3]
        } else if (i==3){ t <-  data3[,4]   ; y <-  data3[,3]
        } else if (i==4){ t <-  data4[,10]   ; y <-  data4[,9]
        } else if (i==5){ t <-  data5[,2]   ; y <-  data5[,1]
   }

recT =  1/t

n<-length(y)
n<-254
nStart<-5


fit <-  lm( log(y[nStart:n]) ~    log(t[nStart:n]) +  recT[nStart:n] +  t[nSt
art:n]  )
summary(fit)

##
## Call:
## lm(formula = log(y[nStart:n]) ~ log(t[nStart:n]) + recT[nStart:n] +
##     t[nStart:n])
##
## Residuals:
##       Min        1Q    Median        3Q       Max
## -0.270665 -0.018254 -0.002943  0.012081  0.160746
##
## Coefficients:
##                   Estimate Std. Error t value Pr(>|t|)
## (Intercept)      -3.976e+00  1.064e+00  -3.738 0.000357 ***
## log(t[nStart:n])  1.548e+00  2.041e-01   7.586 6.79e-11 ***
## recT[nStart:n]   -9.417e+01  1.658e+01  -5.679 2.36e-07 ***
## t[nStart:n]      -2.208e-02  5.029e-04 -43.906  < 2e-16 ***
## ---
## Signif. codes:  0 '***' 0.001 '**' 0.01 '*' 0.05 '.' 0.1 ' ' 1
##
## Residual standard error: 0.0659 on 76 degrees of freedom
##   (170 observations deleted due to missingness)
## Multiple R-squared:  0.9988, Adjusted R-squared:  0.9988
## F-statistic: 2.111e+04 on 3 and 76 DF,  p-value: < 2.2e-16

#plot(fit)


par(mfrow=c(1,1))

yOut <-  exp(fit$coeff[1]  +  fit$coeff[2]*log(t) +  fit$coeff[3]*recT +
fit$coeff[4]*t)
#plot(t,y)
#points( t, yOut, col=2, type="l", lwd=2)

yOut <-  fit$coeff[1]  +  fit$coeff[2]*log(t) +  fit$coeff[3]*recT +  fit$c
```

```
oeff[4]*t
#plot(t,log(y))
#points( t, yOut, col=2, type="l", lwd=2)


y2 =  log(y[nStart:n]) +  0.5*log(t[nStart:n])
fit2 <-  lm( y2 ~      recT[nStart:n] +  t[nStart:n]  )

yOut <-  exp(fit2$coeff[1]  -  0.5*log(t) +  fit2$coeff[2]*recT +  fit2$c
oeff[3]*t)
plot(t,y, xlab="Time (s)", ylab="Normalised concentration")
points( t, yOut, col=2, type="l", lwd=2)
```

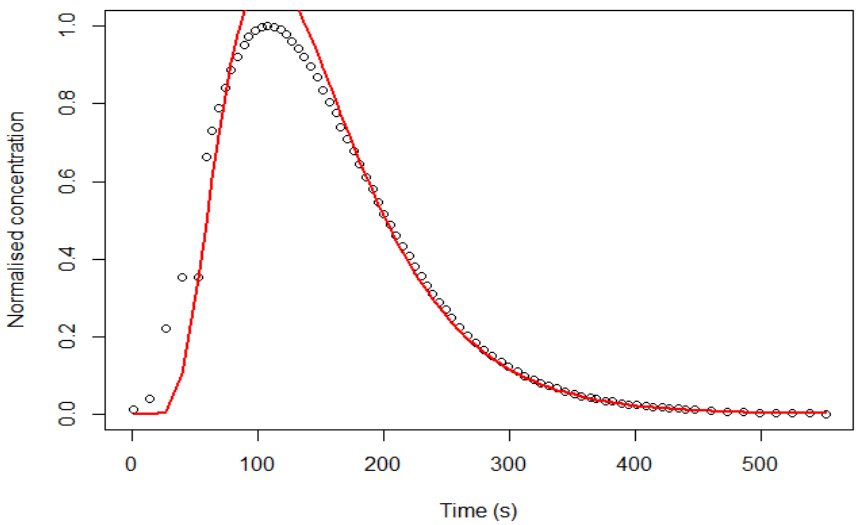


```
yOut <-  fit2$coeff[1]  -  0.5*log(t) +  fit2$coeff[2]*recT +  fit2$coeff[
3]*t
plot(t,log(y),xlab="Time (s)")
points( t, yOut, col=2, type="l", lwd=2)

summary(fit2)

##
## Call:
```

```
## lm(formula = y2 ~ recT[nStart:n] + t[nStart:n])
##
## Residuals:
##      Min       1Q   Median       3Q      Max
## -0.44174 -0.05465  0.03050  0.04533  0.30153
##
## Coefficients:
##                  Estimate Std. Error t value Pr(>|t|)
## (Intercept)     6.691e+00  6.634e-02  100.86   <2e-16 ***
## recT[nStart:n] -2.568e+02  5.352e+00  -47.97   <2e-16 ***
## t[nStart:n]    -1.713e-02  1.492e-04 -114.85   <2e-16 ***
## ---
## Signif. codes:  0 '***' 0.001 '**' 0.01 '*' 0.05 '.' 0.1 ' ' 1
##
## Residual standard error: 0.09983 on 77 degrees of freedom
##   (170 observations deleted due to missingness)
## Multiple R-squared:  0.9963, Adjusted R-squared:  0.9962
## F-statistic: 1.029e+04 on 2 and 77 DF,  p-value: < 2.2e-16
```

```
plot(fit2)
```

```
#Resulting Outputs
v; K; D; Ds
```

```
## [1] 0.007841369
```

```
## [1] 9.943358e-13
```

```
## [1] 0.0009
```

```
## [1] 0.114
```

10,000 Pa

Here are the outputs for SF6 at pressure 10,000 Pa.

```
i<-1

if(i==1){ t <-  data1[,4] ; y <-  data1[,3]
        } else if (i==2){ t <-  data2[,4]   ; y <-  data2[,3]
        } else if (i==3){ t <-  data3[,4]   ; y <-  data3[,3]
        } else if (i==4){ t <-  data4[,10]   ; y <-  data4[,9]
        } else if (i==5){ t <-  data5[,2]   ; y <-  data5[,1]
   }

recT =  1/t

n<-length(y)
n<-500
nStart<-11


fit <-  lm( log(y[nStart:n]) ~    log(t[nStart:n]) +  recT[nStart:n] +  t[nSt
art:n]  )
summary(fit)

##
## Call:
## lm(formula = log(y[nStart:n]) ~ log(t[nStart:n]) + recT[nStart:n] +
##     t[nStart:n])
##
## Residuals:
##       Min        1Q    Median        3Q       Max
## -0.135662 -0.017703  0.004218  0.020963  0.043791
##
## Coefficients:
##                   Estimate Std. Error t value Pr(>|t|)
## (Intercept)     -2.906e+01  4.088e-01  -71.10   <2e-16 ***
## log(t[nStart:n])  6.236e+00  7.451e-02   83.69   <2e-16 ***
## recT[nStart:n]    1.045e+02  7.896e+00   13.24   <2e-16 ***
## t[nStart:n]      -2.307e-02  1.391e-04 -165.89   <2e-16 ***
## ---
## Signif. codes:  0 '***' 0.001 '**' 0.01 '*' 0.05 '.' 0.1 ' ' 1
##
## Residual standard error: 0.03087 on 117 degrees of freedom
##   (369 observations deleted due to missingness)
## Multiple R-squared:  0.9994, Adjusted R-squared:  0.9994
## F-statistic: 6.467e+04 on 3 and 117 DF,  p-value: < 2.2e-16

#plot(fit)


par(mfrow=c(1,1))

yOut <-  exp(fit$coeff[1]  +  fit$coeff[2]*log(t) +  fit$coeff[3]*recT +
fit$coeff[4]*t)
#plot(t,y)
#points( t, yOut, col=2, type="l", lwd=2)

yOut <-  fit$coeff[1]  +  fit$coeff[2]*log(t) +  fit$coeff[3]*recT +  fit$c
```

```
oeff[4]*t
#plot(t,log(y))
#points( t, yOut, col=2, type="l", lwd=2)


y2 =  log(y[nStart:n]) +  0.5*log(t[nStart:n])
fit2 <-  lm( y2 ~      recT[nStart:n] +  t[nStart:n]  )

yOut <-  exp(fit2$coeff[1]  -  0.5*log(t) +  fit2$coeff[2]*recT +  fit2$c
oeff[3]*t)
plot(t,y, xlab="Time (s)", ylab="Normalised concentration")
points( t, yOut, col=2, type="l", lwd=2)
```

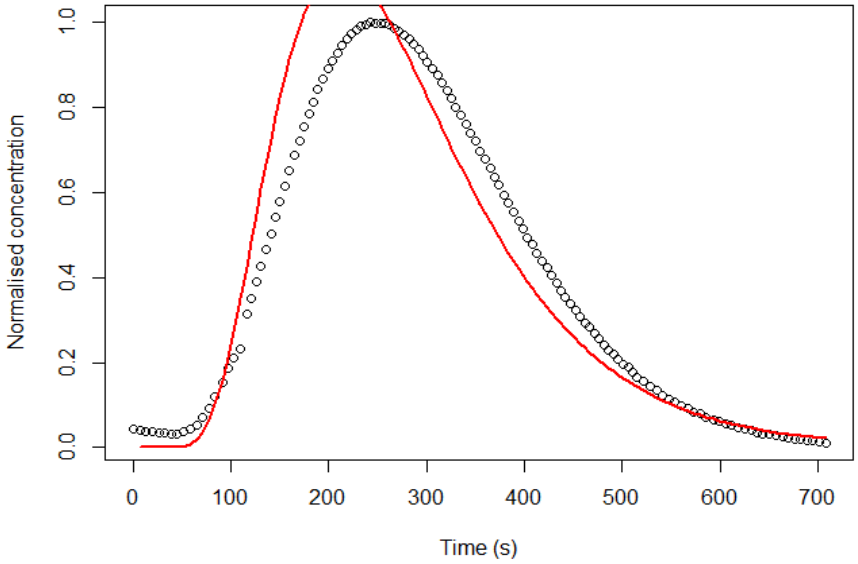


```
yOut <-  fit2$coeff[1]  -  0.5*log(t) +  fit2$coeff[2]*recT +  fit2$coeff[
3]*t
plot(t,log(y),xlab="Time (s)")
points( t, yOut, col=2, type="l", lwd=2)

summary(fit2)
```

```
##
## Call:
## lm(formula = y2 ~ recT[nStart:n] + t[nStart:n])
##
## Residuals:
##      Min       1Q   Median       3Q      Max
## -0.59840 -0.20457  0.04876  0.20175  1.08265
##
## Coefficients:
##                  Estimate Std. Error t value Pr(>|t|)
## (Intercept)     7.858e+00  1.384e-01   56.76   <2e-16 ***
## recT[nStart:n] -5.908e+02  1.496e+01  -39.48   <2e-16 ***
## t[nStart:n]    -1.075e-02  2.303e-04  -46.66   <2e-16 ***
## ---
## Signif. codes:  0 '***' 0.001 '**' 0.01 '*' 0.05 '.' 0.1 ' ' 1
##
## Residual standard error: 0.2587 on 118 degrees of freedom
##   (369 observations deleted due to missingness)
## Multiple R-squared:  0.9487, Adjusted R-squared:  0.9478
## F-statistic:  1090 on 2 and 118 DF,  p-value: < 2.2e-16

plot(fit2)

#Resulting Outputs
v; K; D; Ds

## [1] 0.004094744

## [1] 1.03848e-12

## [1] 0.0004

## [1] 0.095
```

CO_2 results

All pressures

Here are the outputs for all the CO_2 experiments accounting for sorption.

```
#i<-1


N<-array(NA, c(5,5))
N[1,] <-  c(800,800,800,800,700) #i=1 j=1,2,3,4,5
N[2,] <-  c(500,500,500,500,500) #1=2 j=1,2,3,4,5
N[3,] <-  c(450,450,450,450,450)
N[4,] <-  c(300,300,300,300,300)
N[5,] <-  c(200,200,200,200,200)


NStart<-array(NA, c(5,5))
NStart[1,] <-  c(200,200,200,200,200) #i=1 j=1,2,3,4,5
NStart[2,] <-  c(90,100,100,100,100) #1=2 j=1,2,3,4,5
NStart[3,] <-  c(50,50,50,50,50)
NStart[4,] <-  c(40,40,40,40,40)
NStart[5,] <-  c(40,40,40,40,40)

v<-array(NA,c(5,5))
K<-array(NA,c(5,5))
D<-array(NA,c(5,5))
Ds<-array(NA,c(5,5))
```

```
for (i in 1:5) {
 if (i==1){ Data <-  data1}
 if (i==2){ Data <-  data2}
 if (i==3){ Data <-  data3}
 if (i==4){ Data <-  data4}
 if (i==5){ Data <-  data5}

 for (j in 1:5) {
  t <-  Data[,2+((j-1)*2)] ; y <-  Data[,1+((j-1)*2)]



  recT =  1/t

  n<-length(y)
  n <-  N[i,j]
  nStart <-  NStart[i,j]
  #n<-850
  #nStart<-296


  fit <-  lm( log(y[nStart:n]) ~    log(t[nStart:n]) +  recT[nStart:n] +  t[
nStart:n]  )
  summary(fit)

  #plot(fit)
```

```
  par(mfrow=c(1,1))

  yOut <- exp(fit$coeff[1] + fit$coeff[2]*log(t) + fit$coeff[3]*recT
+ fit$coeff[4]*t)
  #plot(t,y)
  #points( t, yOut, col=2, type="l", lwd=2)

  yOut <- fit$coeff[1] + fit$coeff[2]*log(t) + fit$coeff[3]*recT + fi
t$coeff[4]*t
  #plot(t,log(y))
  #points( t, yOut, col=2, type="l", lwd=2)


  y2 = log(y[nStart:n]) + 0.5*log(t[nStart:n])
  fit2 <- lm( y2 ~      recT[nStart:n] + t[nStart:n] )

  yOut <- exp(fit2$coeff[1] - 0.5*log(t) + fit2$coeff[2]*recT + fit2
$coeff[3]*t)
  plot(t,y, xlab="Time (s)", ylab="Normalised concentration
")
  points( t, yOut, col=2, type="l", lwd=2)

  yOut <- fit2$coeff[1] - 0.5*log(t) + fit2$coeff[2]*recT + fit2$coe
ff[3]*t
  plot(t,log(y), xlab="Time (s)")
  points( t, yOut, col=2, type="l", lwd=2)
```

```
  summary(fit2)

  plot(fit2)

  ################################
  # Output pressure
  P <- i * 10000

  # Sample Length
  x <- 0.96

  # Dynamic viscosity
  mu <- 1.75E-5

  # Mass injection
  M0 <- 1

  # Effective porosity
  ne <- 0.1785

  #Diffusion
  Dg_List_Carbon<-c(1.5188E-5, 1.4506E-5, 1.3882E-5, 1.3310E-5, 1.
2784E-5)
  Dg<-Dg_List_Carbon[i]

  ###Retardation Factor Calculation###
  #Solid density (kg/m3)
  p <- 2063
```

```
#Variable Kd (ml/g)/1000
Kd <-  0.00008

Rf <-  1 +  (p*Kd*((1-ne)/ne))

#B = -(x^2/4*D)
B <-  coef(summary(fit2))["recT[nStart:n]","Estimate"]
#C =  -(v^2/4*D)
C <-  coef(summary(fit2))["t[nStart:n]","Estimate"]

#Calculate the following:

#Advective Velocity
v[i,j] <-  (sqrt((C*(x)^2)/B))*Rf

#Permeability
K[i,j] <-  v[i,j]*ne*x*mu/P

#Hydrodynamic Dispersion Coeffcient
D[i,j] <-  -(((x^2)/(4*B)))*Rf

#Mechanical Dispersion
Ds[i,j] <-  ((D[i,j] -  (ne *  Dg)) /  v[i,j])
```

```
  }
}
```

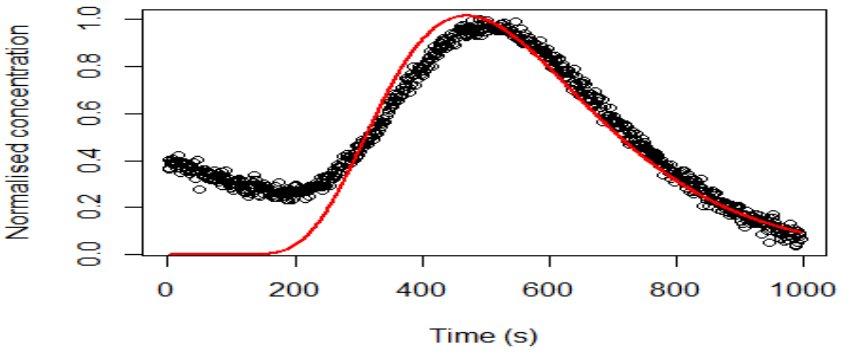

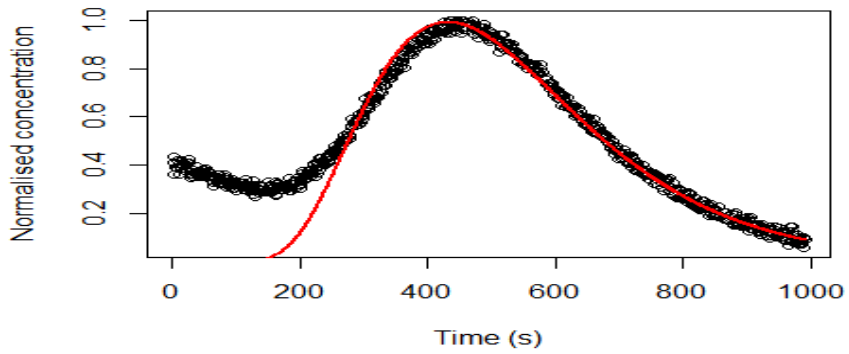
Normalised concentration
0.2
0.4
0.6
0.8
1.0
0
200
400
600
800
1000
Time (s)

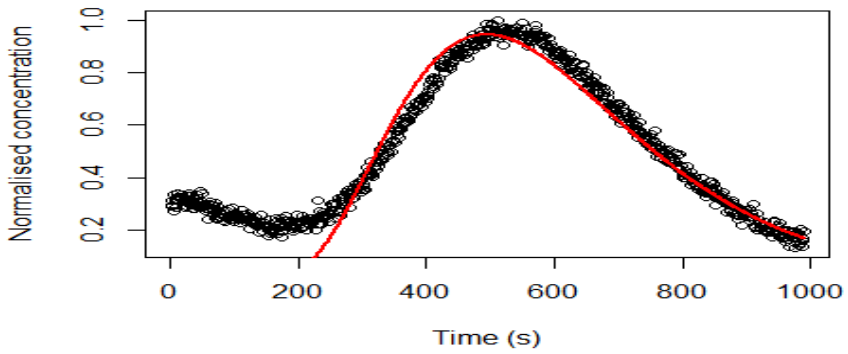
Normalised concentration
0.2
0.4
0.6
0.8
1.0
0
200
400
600
800
1000
Time (s)

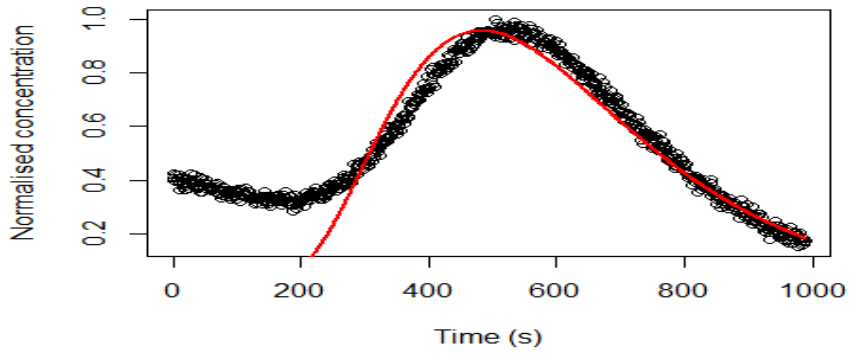
Normalised concentration
0.2
0.4
0.6
0.8
1.0
0
200
400
600
800
1000
Time (s)

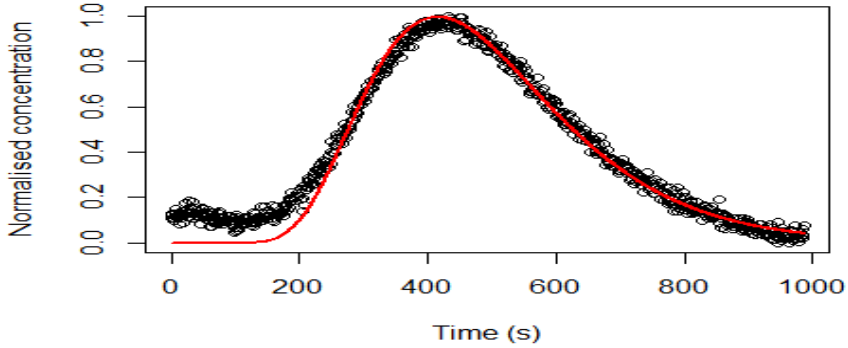
Normalised concentration
0.0
0.2
0.4
0.6
0.8
1.0
0
200
400
600
800
1000
Time (s)

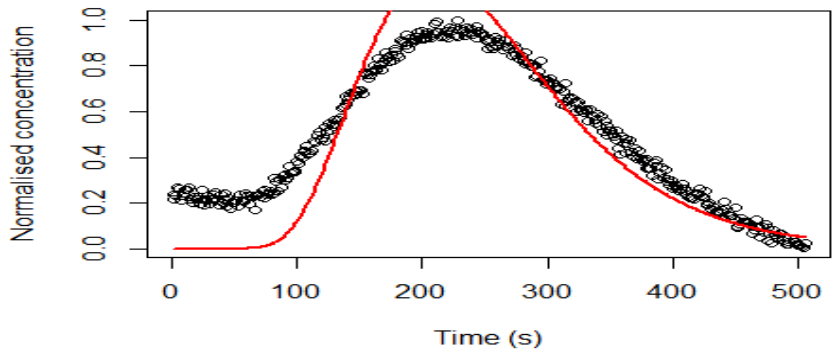
Normalised concentration
0.0
0.2
0.4
0.6
0.8
1.0
0
100
200
300
400
500
Time (s)

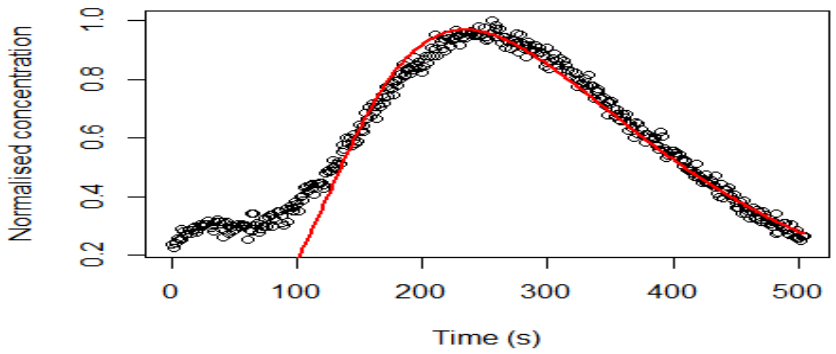
Normalised concentration
0.2
0.4
0.6
0.8
1.0
0
100
200
300
400
500
Time (s)

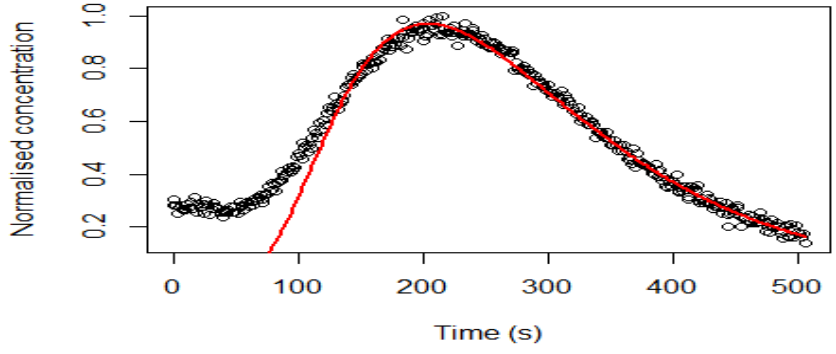
Normalised concentration
0.2
0.4
0.6
0.8
1.0
0
100
200
300
400
500
Time (s)

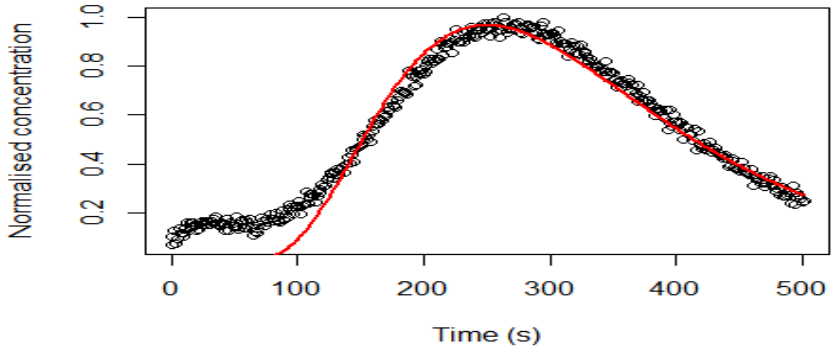
Normalised concentration
0.2
0.4
0.6
0.8
1.0
0
100
200
300
400
500
Time (s)

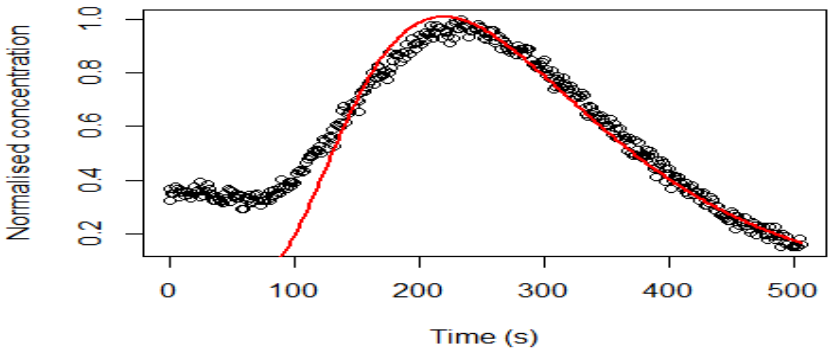
Normalised concentration
0.2
0.4
0.6
0.8
1.0
0
100
200
300
400
500
Time (s)

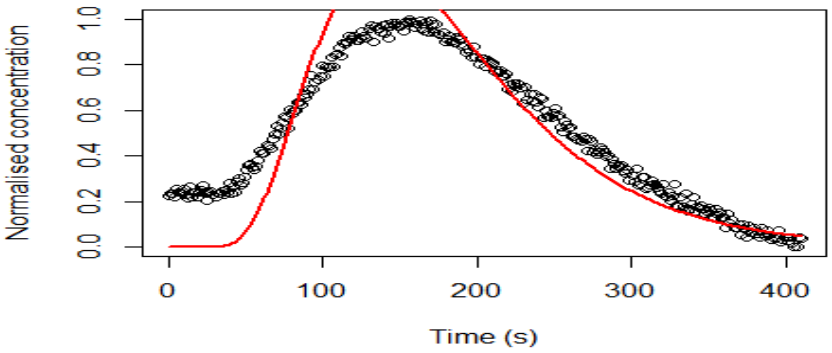
Normalised concentration
0.0
0.2
0.4
0.6
0.8
1.0
0
100
200
300
400
Time (s)

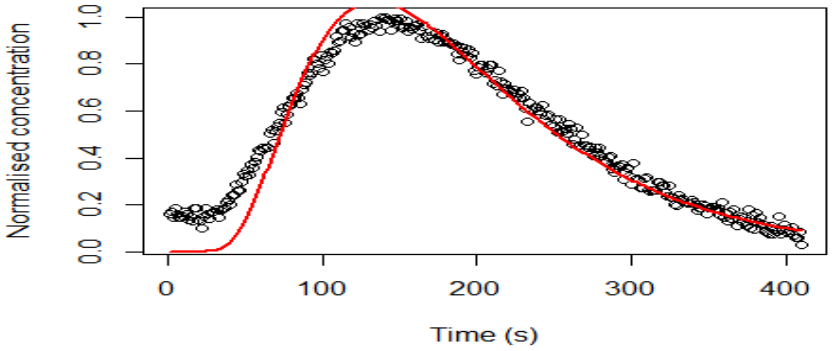
Normalised concentration
0.0
0.2
0.4
0.6
0.8
1.0
0
100
200
300
400
Time (s)

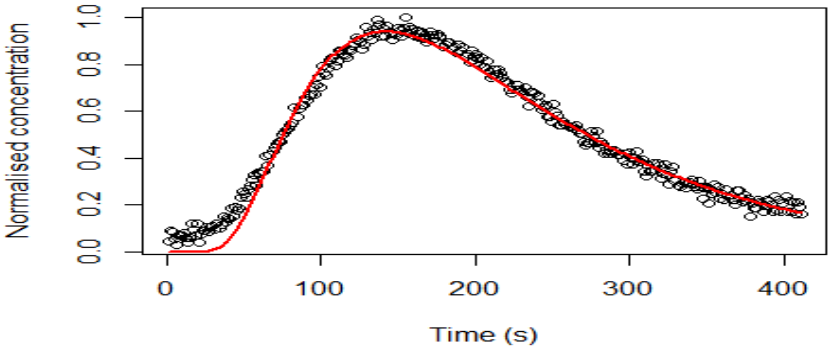
Normalised concentration
0.0
0.2
0.4
0.6
0.8
1.0
0
100
200
300
400
Time (s)

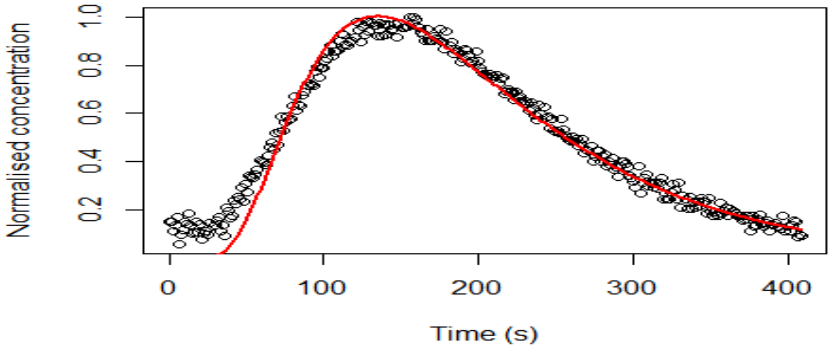
Normalised concentration
0.2
0.4
0.6
0.8
1.0
0
100
200
300
400
Time (s)

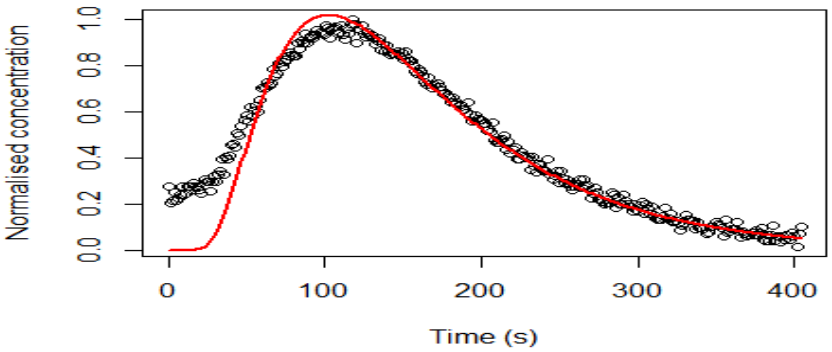
Normalised concentration
0.0
0.2
0.4
0.6
0.8
1.0
0
100
200
300
400
Time (s)

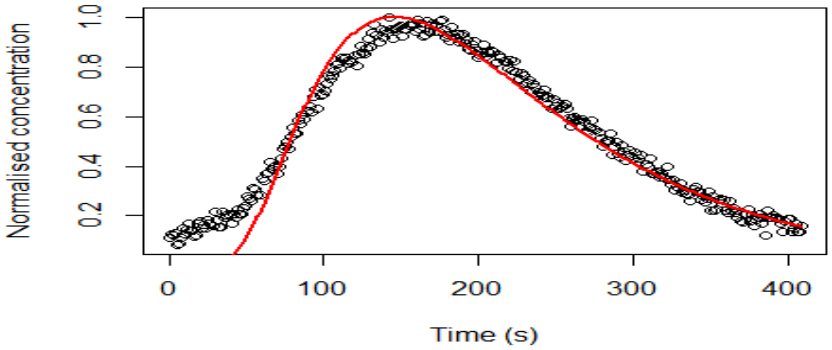
Normalised concentration
0.2
0.4
0.6
0.8
1.0
0
100
200
300
400
Time (s)

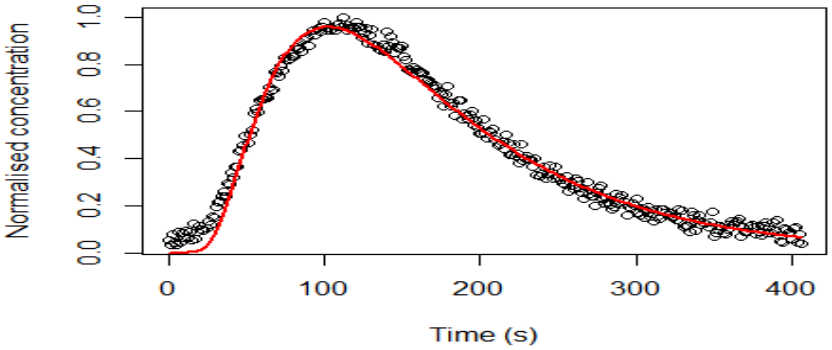
Normalised concentration
0.0
0.2
0.4
0.6
0.8
1.0
0
100
200
300
400
Time (s)

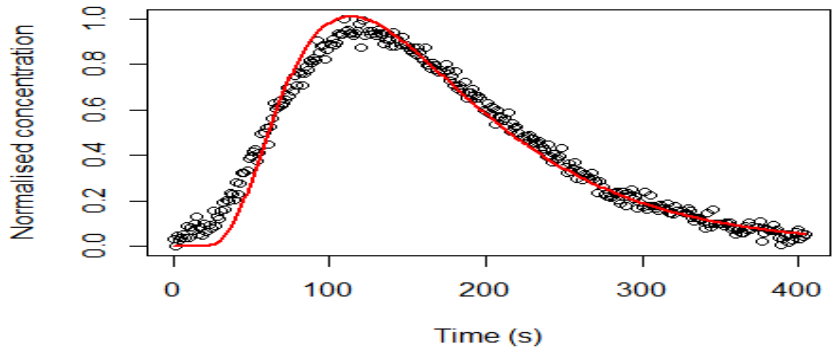
Normalised concentration
0.0
0.2
0.4
0.6
0.8
1.0
0
100
200
300
400
Time (s)

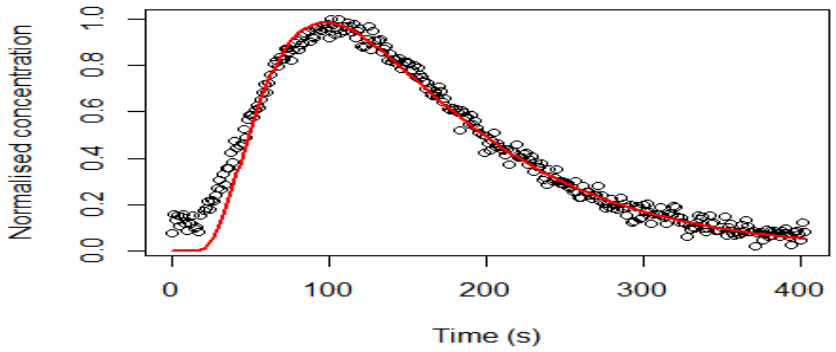
Normalised concentration
0.0
0.2
0.4
0.6
0.8
1.0
0
100
200
300
400
Time (s)

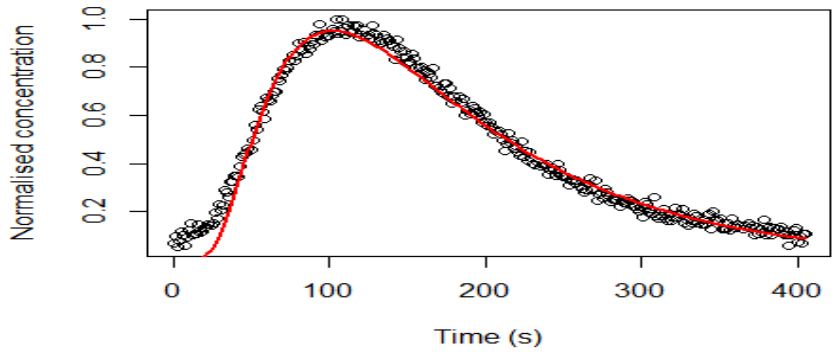
Normalised concentration
0.2
0.4
0.6
0.8
1.0
0
100
200
300
400
Time (s)

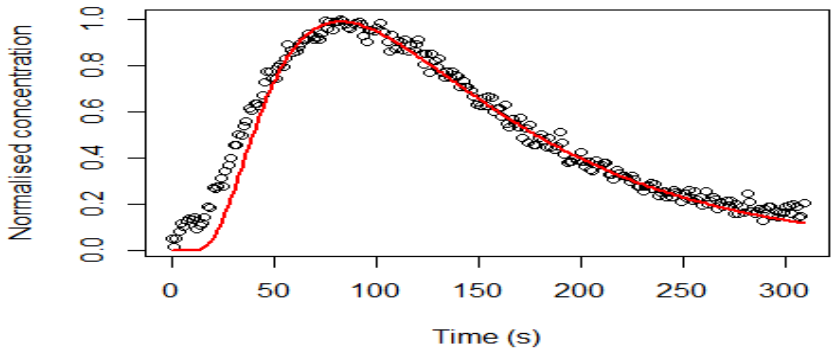
Normalised concentration
0.0
0.2
0.4
0.6
0.8
1.0
0
50
100
150
200
250
300
Time (s)

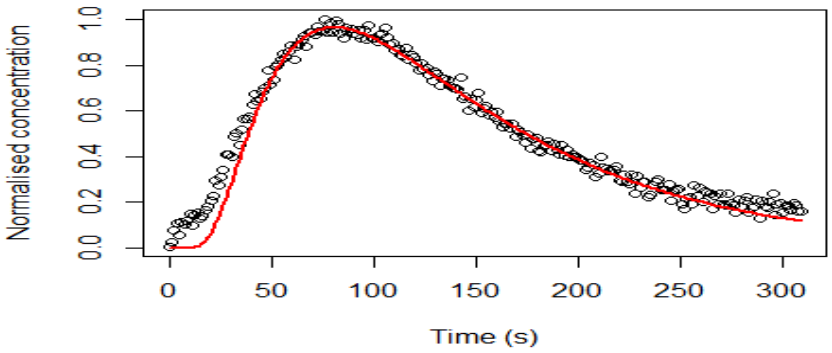
Normalised concentration
0.0
0.2
0.4
0.6
0.8
1.0
0
50
100
150
200
250
300
Time (s)

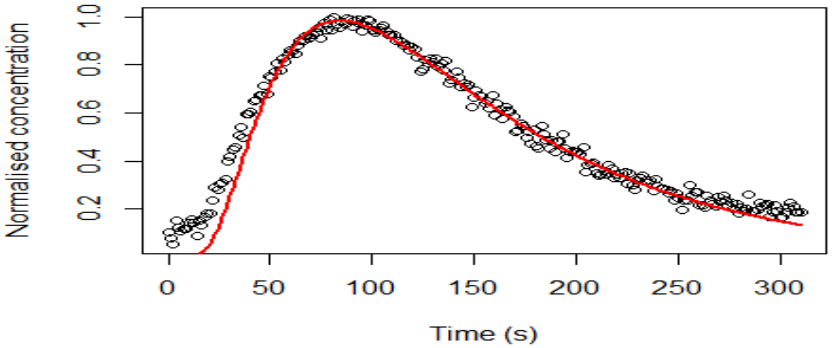
Normalised concentration
0.2
0.4
0.6
0.8
1.0
0
50
100
150
200
250
300
Time (s)

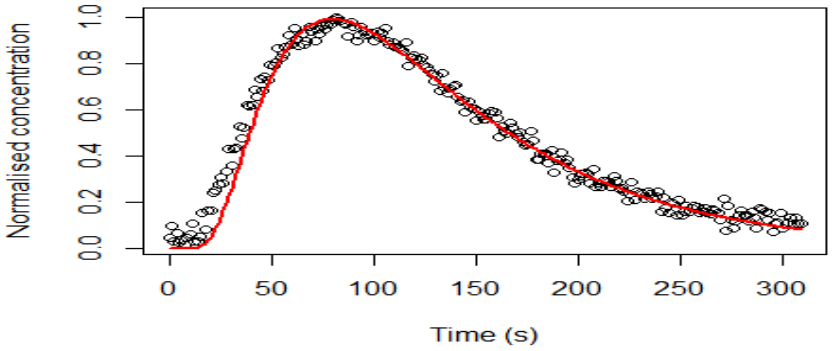
Normalised concentration
0.0
0.2
0.4
0.6
0.8
1.0
0
50
100
150
200
250
300
Time (s)

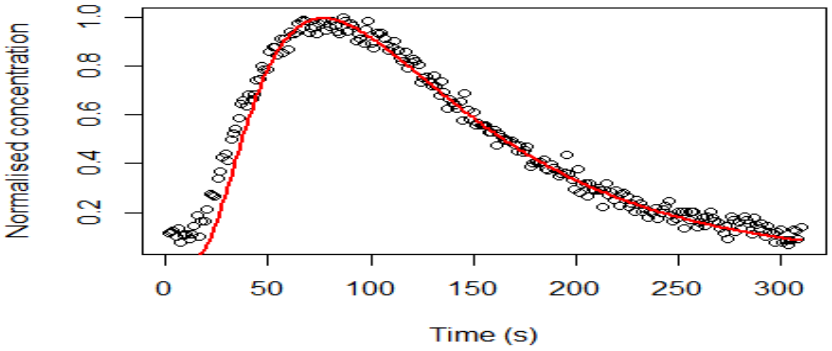
Normalised concentration
0.2
0.4
0.6
0.8
1.0
0
50
100
150
200
250
300
Time (s)

```
#Resulting Outputs
v; K; D; Ds

##            [,1]       [,2]       [,3]       [,4]       [,5]
## [1,] 0.003384400 0.003633294 0.003232686 0.003186002 0.003820
087
## [2,] 0.007567049 0.007349861 0.006406443 0.006138320 0.006968
028
## [3,] 0.011022502 0.011158778 0.010040029 0.010808700 0.010005
987
## [4,] 0.013902751 0.013664459 0.012854005 0.013337431 0.014334
988
## [5,] 0.016420423 0.016651207 0.017359597 0.016031321 0.017737
320

##            [,1]       [,2]       [,3]       [,4]       [,5]
## [1,] 1.014914e-12 1.089552e-12 9.694180e-13 9.554181e-13 1.1455
68e-12
## [2,] 1.134603e-12 1.102038e-12 9.605820e-13 9.203798e-13 1.0447
86e-12
## [3,] 1.101809e-12 1.115431e-12 1.003601e-12 1.080438e-12 1.0001
98e-12
## [4,] 1.042289e-12 1.024424e-12 9.636648e-13 9.999072e-13 1.0746
94e-12
## [5,] 9.848313e-13 9.986728e-13 1.041159e-12 9.614945e-13 1.0638
13e-12

##            [,1]       [,2]       [,3]       [,4]       [,5]
## [1,] 0.0001996711 0.0002618961 0.0002484457 0.0002203242 0.00
02269933
## [2,] 0.0004606409 0.0008440233 0.0007350608 0.0005744444 0.00
06689100
## [3,] 0.0014047794 0.0010418872 0.0016516067 0.0015581929 0.00
14459590
## [4,] 0.0023003604 0.0025045936 0.0018143672 0.0027376375 0.00
26003215
## [5,] 0.0034597256 0.0036725259 0.0033203308 0.0034964832 0.00
36581550

##            [,1]      [,2]      [,3]      [,4]      [,5]
## [1,] 0.05819645 0.07133610 0.0760156 0.06830290 0.05871129
## [2,] 0.06053240 0.11448299 0.1143336 0.09316148 0.09562544
## [3,] 0.12722170 0.09314723 0.1642554 0.14393173 0.14426174
## [4,] 0.16528991 0.18311869 0.1409671 0.20508159 0.18123111
## [5,] 0.21055753 0.22041909 0.1911363 0.21796091 0.20611192
```

Appendix IV

Analytical model outputs

Helium results

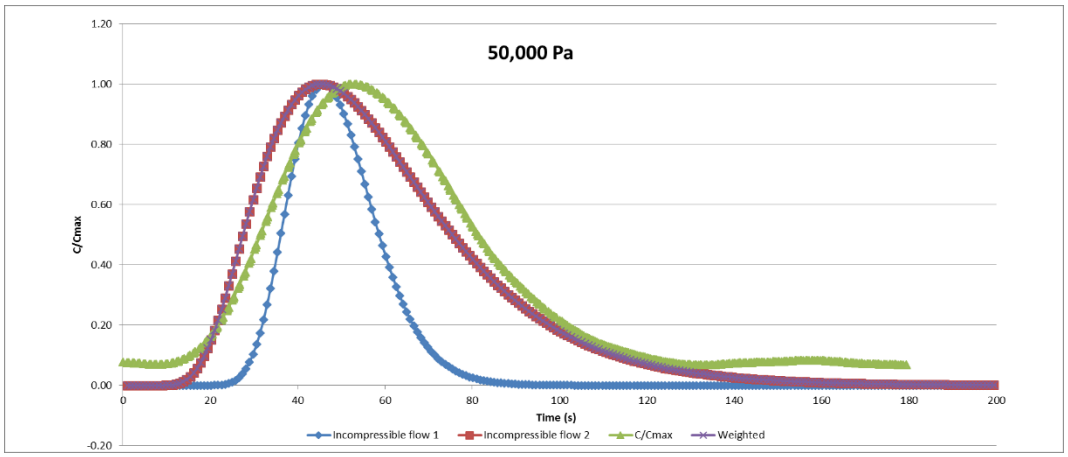

Analytical modelling results for helium at 50,000 Pa.

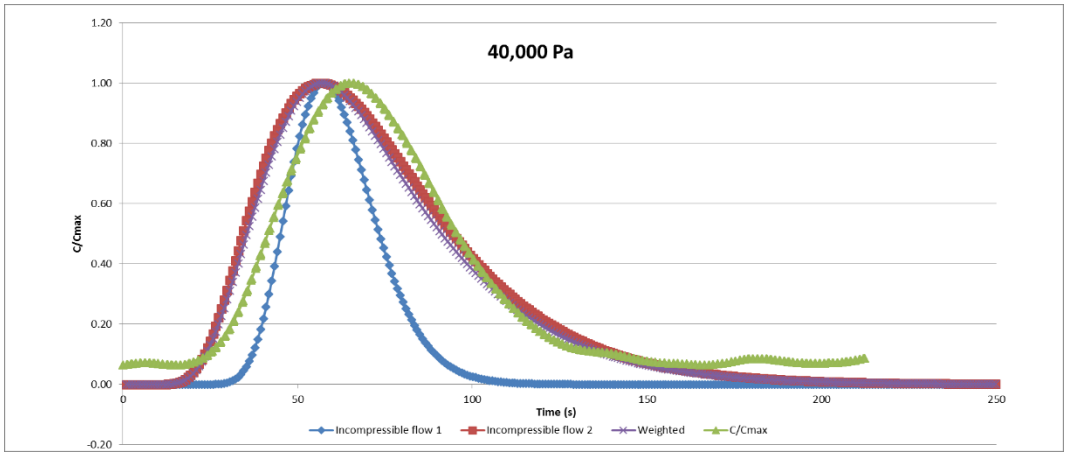

Analytical modelling results for helium at 40,000 Pa.

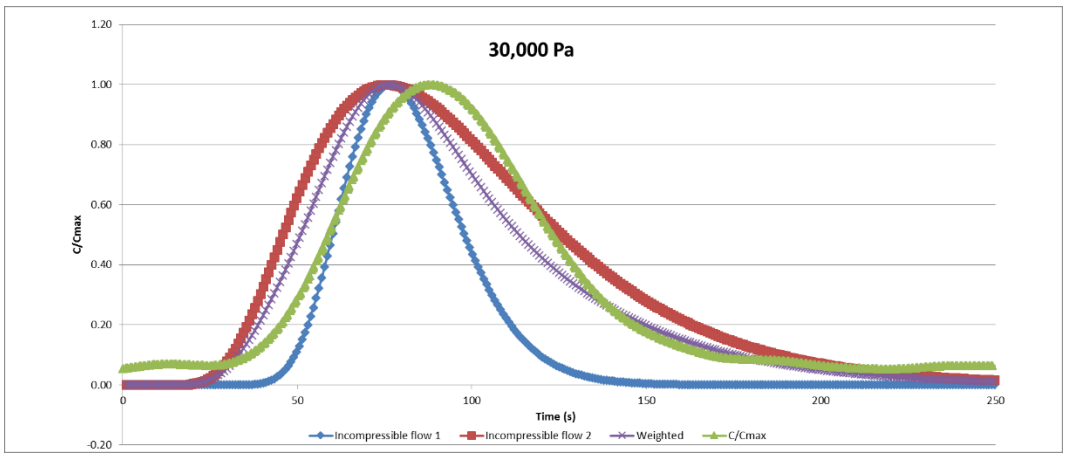

Analytical modelling results for helium at 30,000 Pa.

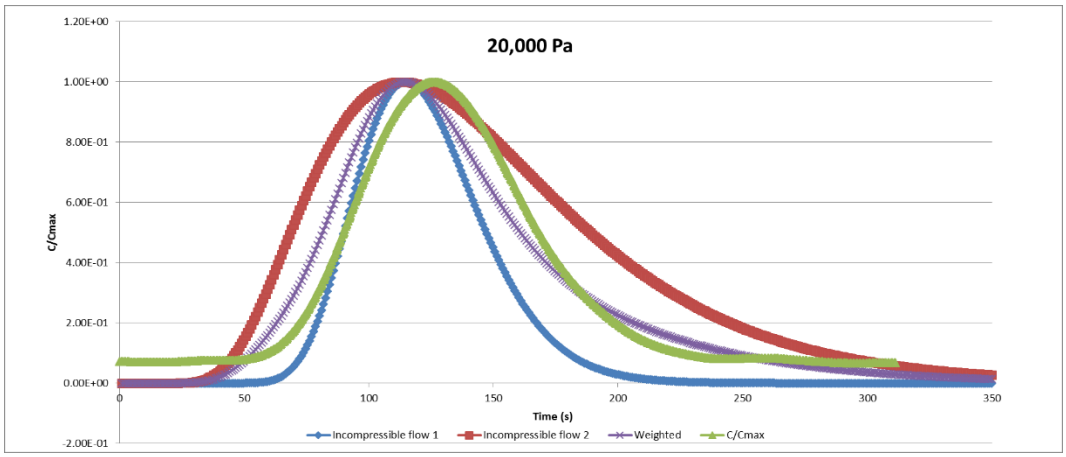

Analytical modelling results for helium at 20,000 Pa.

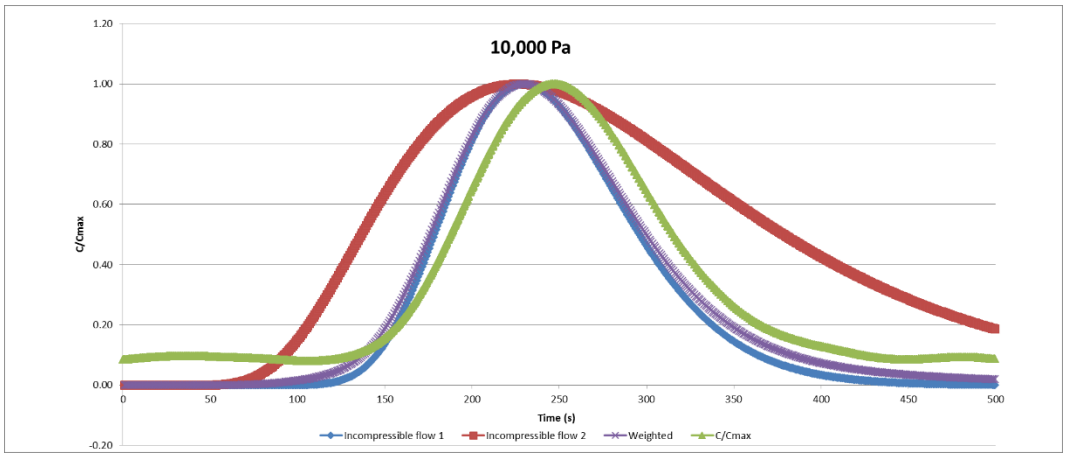

Analytical modelling results for helium at 10,000 Pa.

Neon results

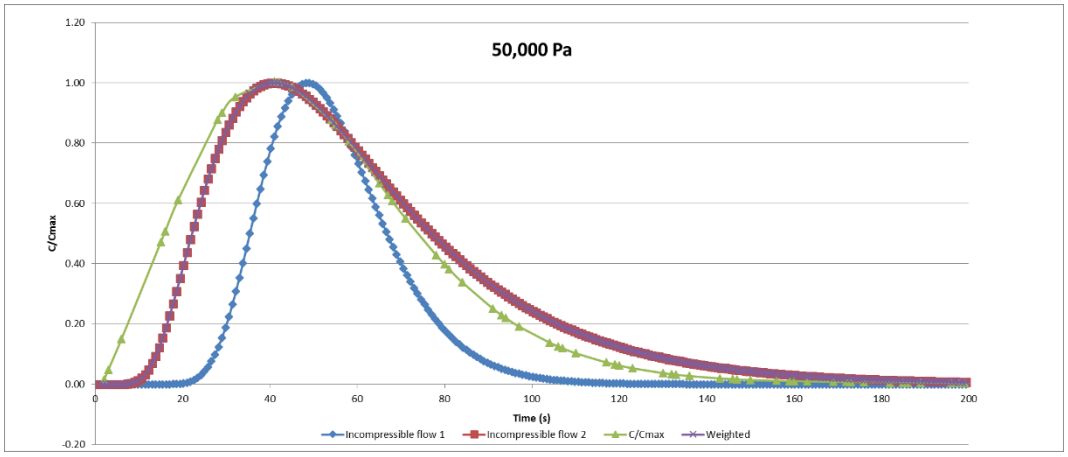

Analytical modelling results for neon at 50,000 Pa.

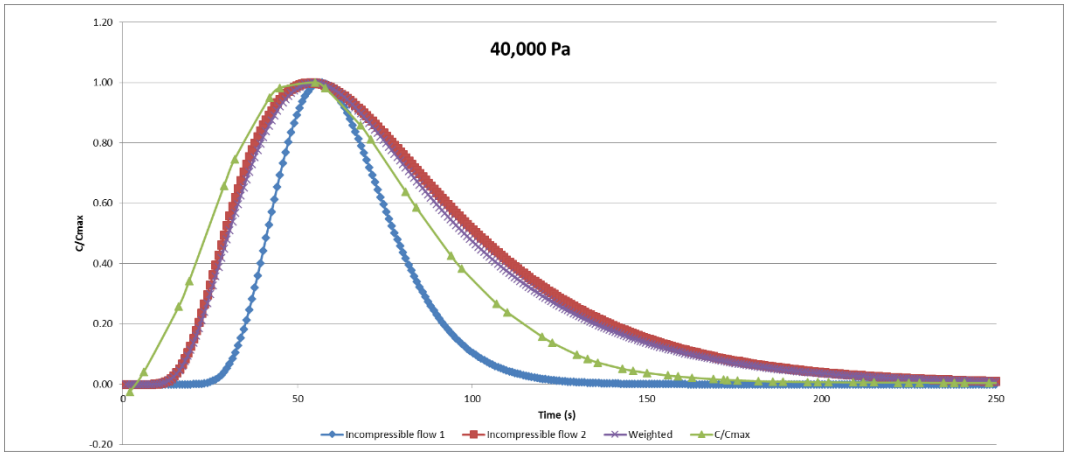

Analytical modelling results for neon at 40,000 Pa.

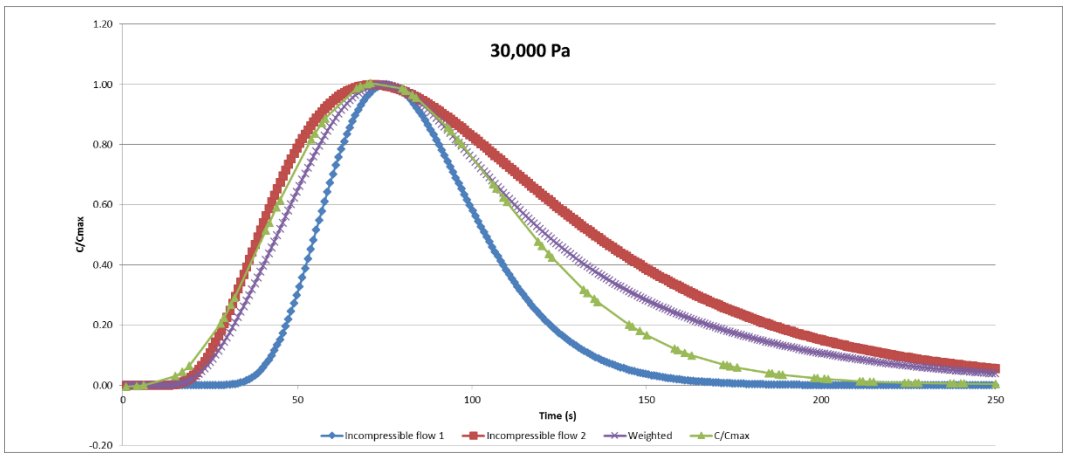

Analytical modelling results for neon at 30,000 Pa.

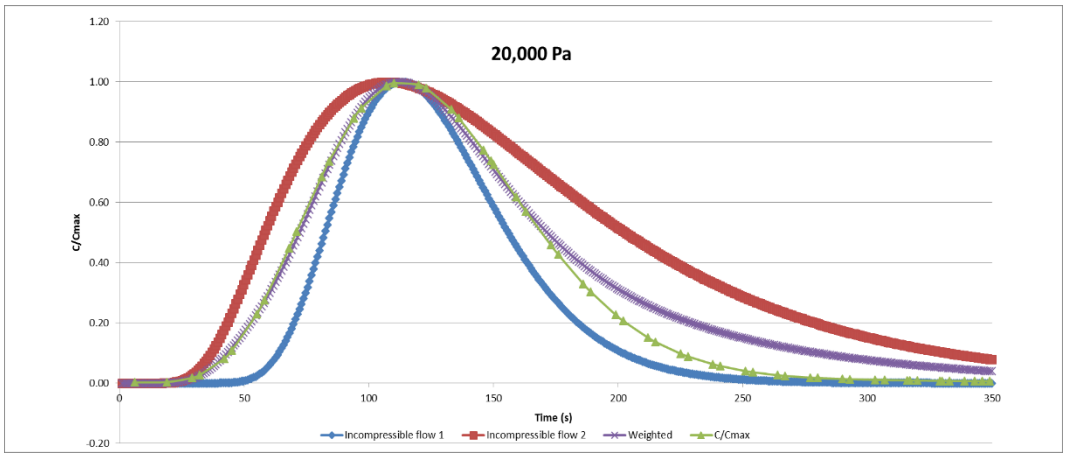

Analytical modelling results for neon at 20,000 Pa.

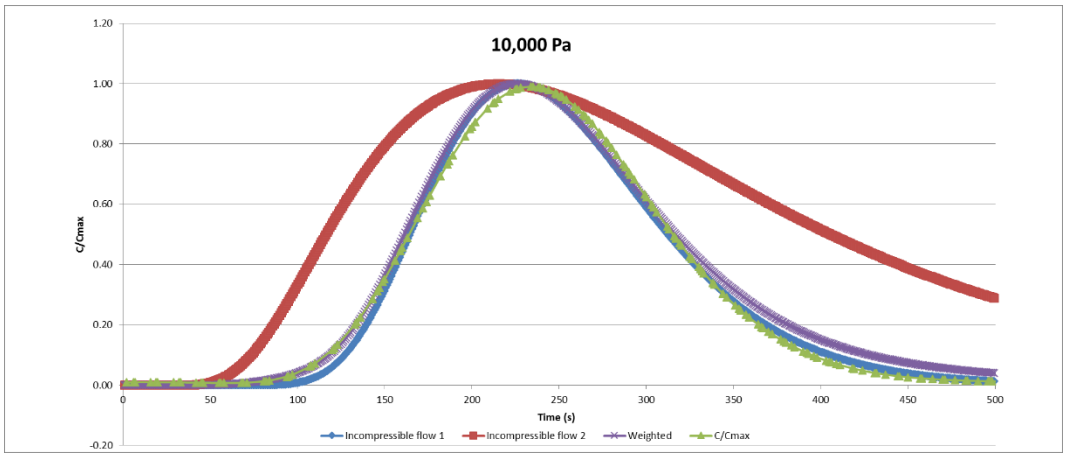

Analytical modelling results for neon at 10,000 Pa.

Argon results

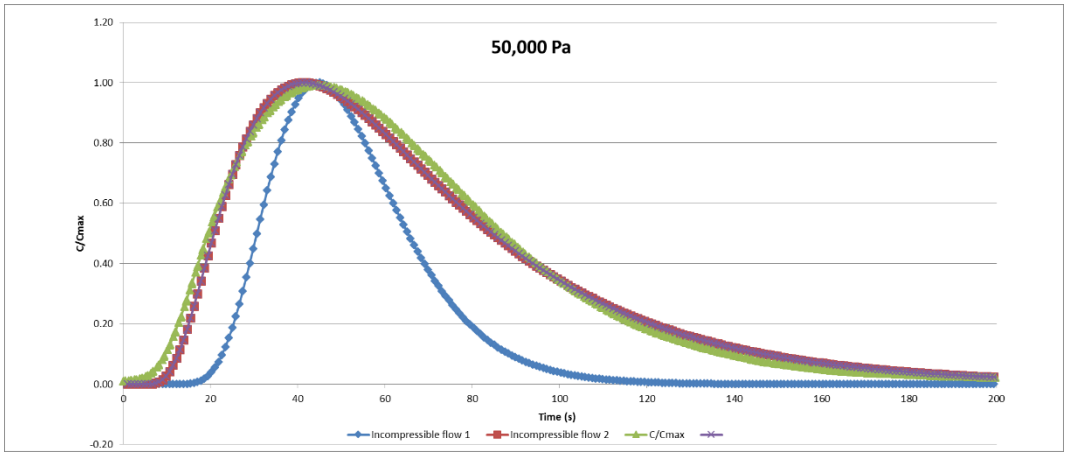

Analytical modelling results for argon at 50,000 Pa.

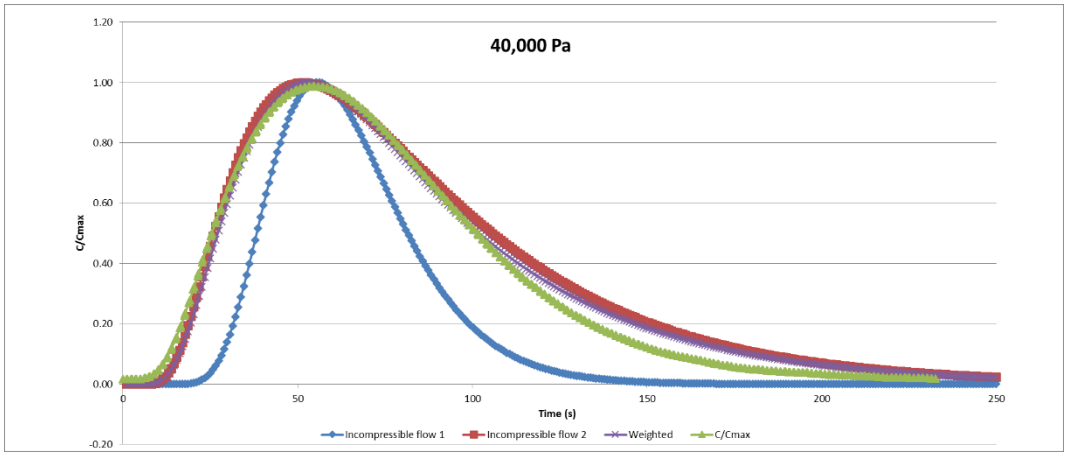

Analytical modelling results for argon at 40,000 Pa.

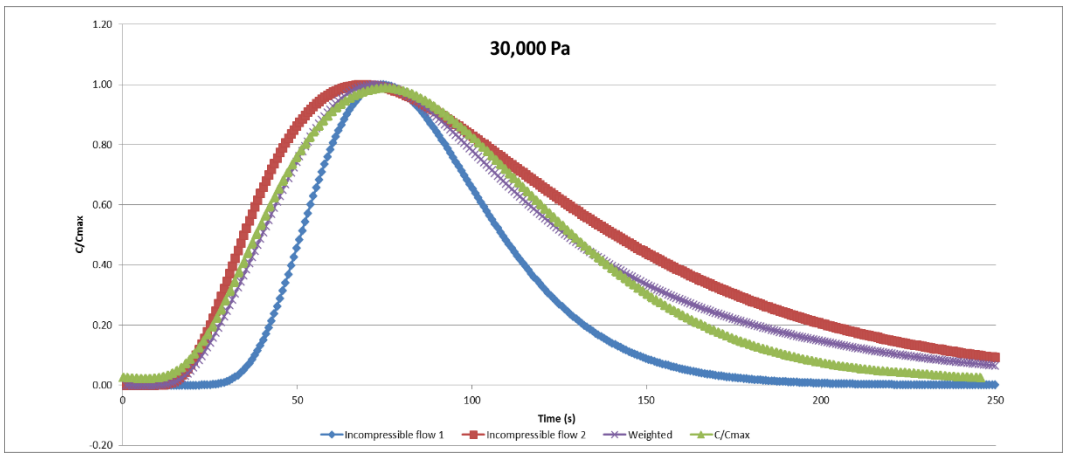

Analytical modelling results for argon at 30,000 Pa.

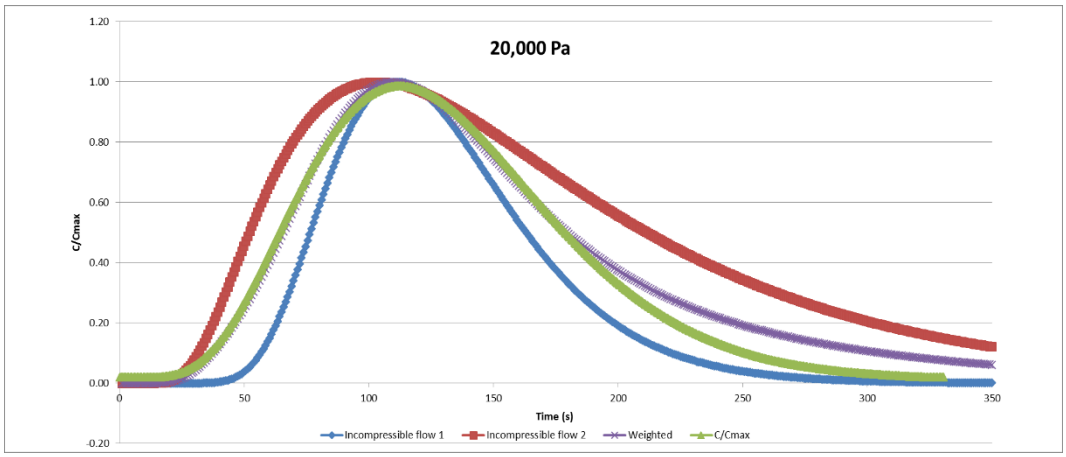

Analytical modelling results for argon at 20,000 Pa.

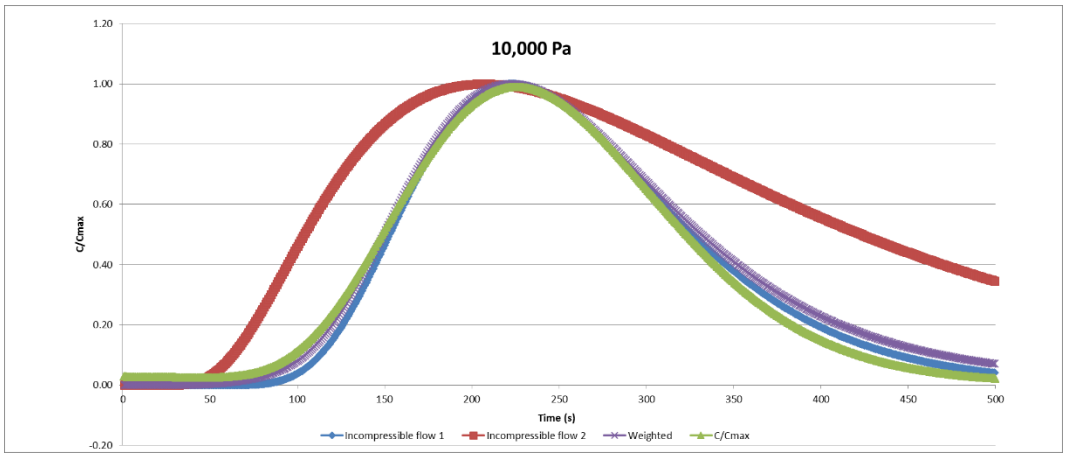

Analytical modelling results for argon at 10,000 Pa.

Krypton results

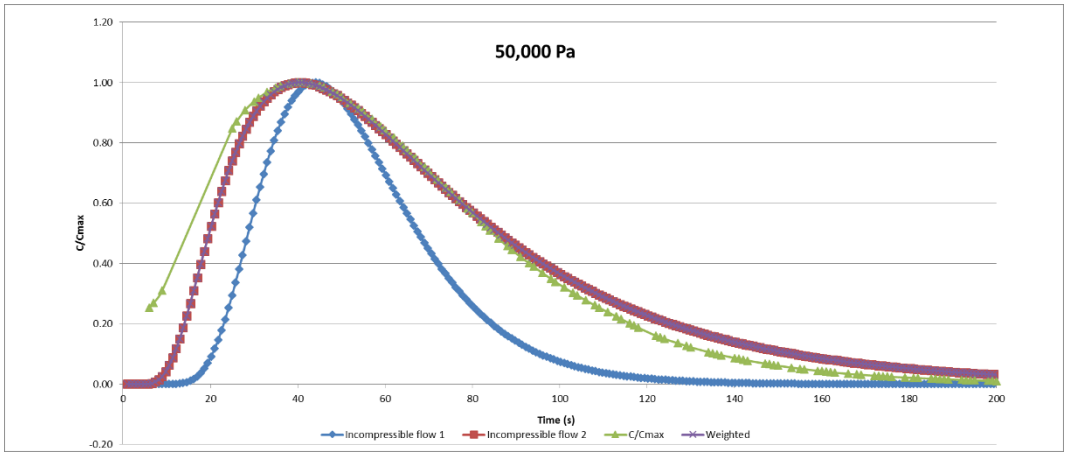

Analytical modelling results for krypton at 50,000 Pa.

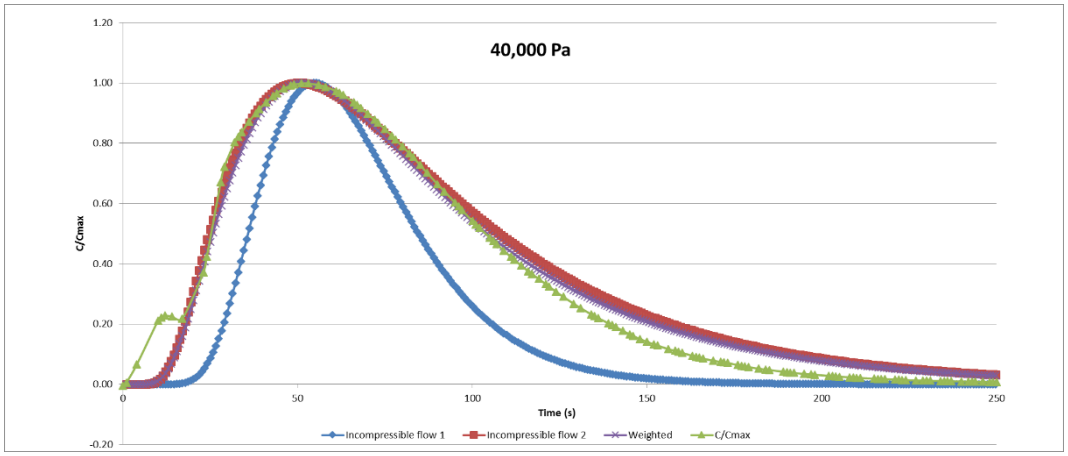

Analytical modelling results for krypton at 40,000 Pa.

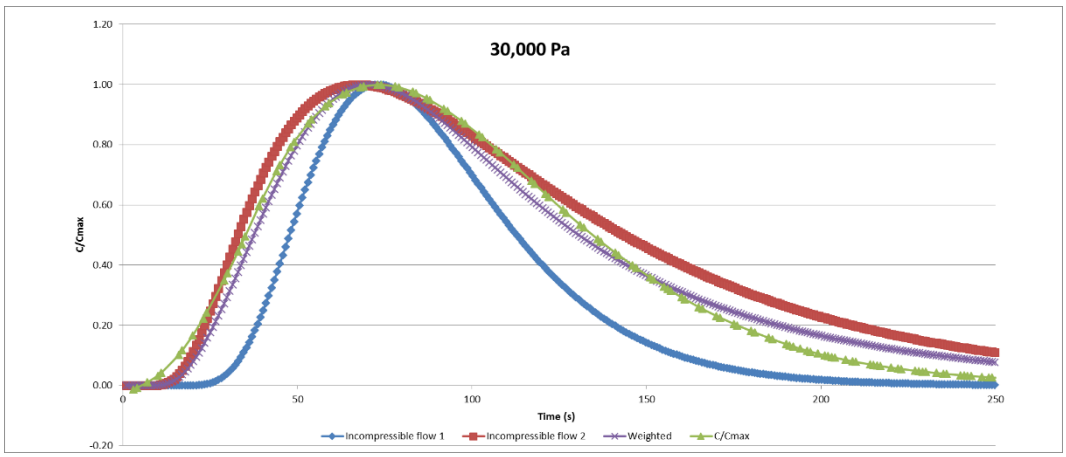

Analytical modelling results for krypton at 30,000 Pa.

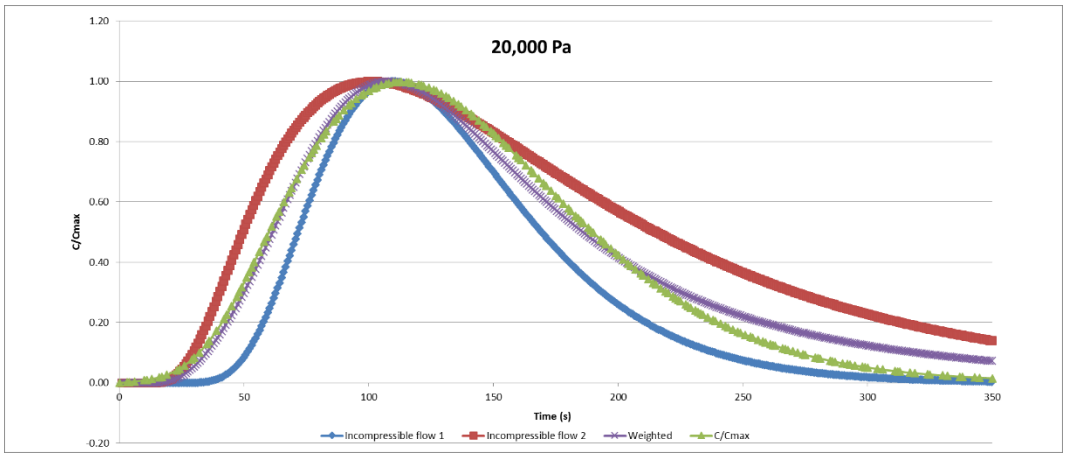

Analytical modelling results for krypton at 20,000 Pa.

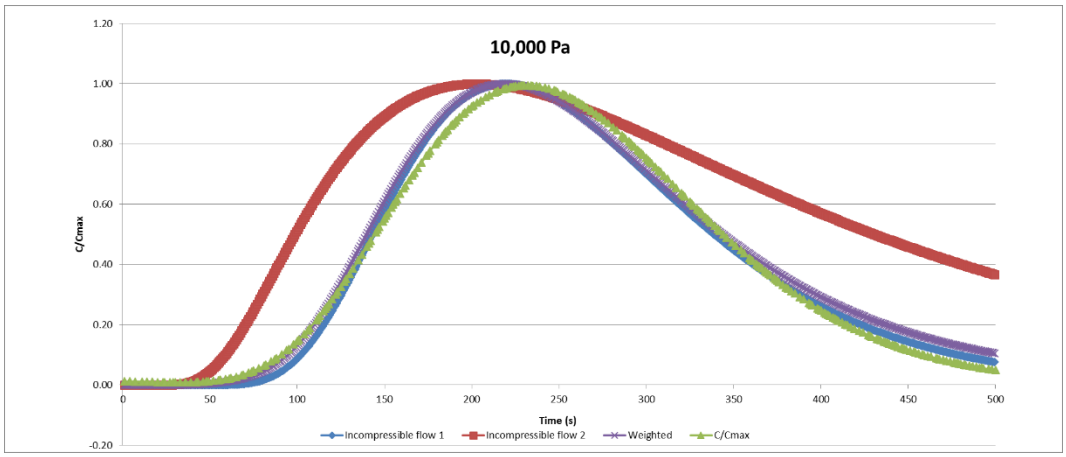

Analytical modelling results for krypton at 10,000 Pa.

Xenon results

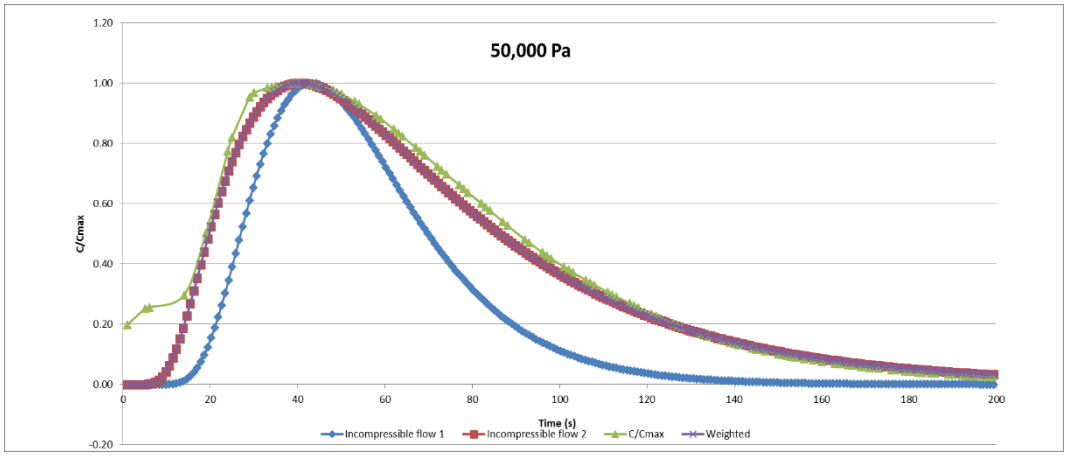

Analytical modelling results for xenon at 50,000 Pa.

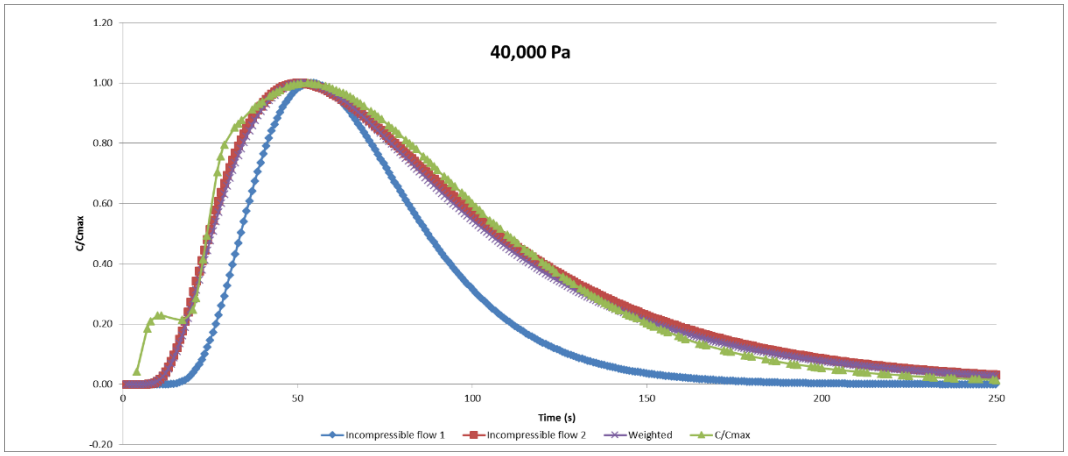

Analytical modelling results for xenon at 40,000 Pa.

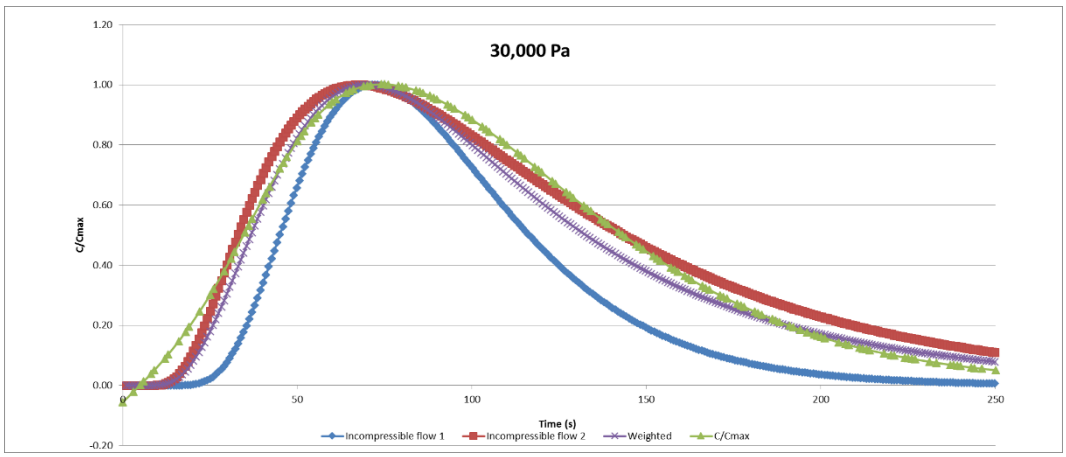

Analytical modelling results for xenon at 30,000 Pa.

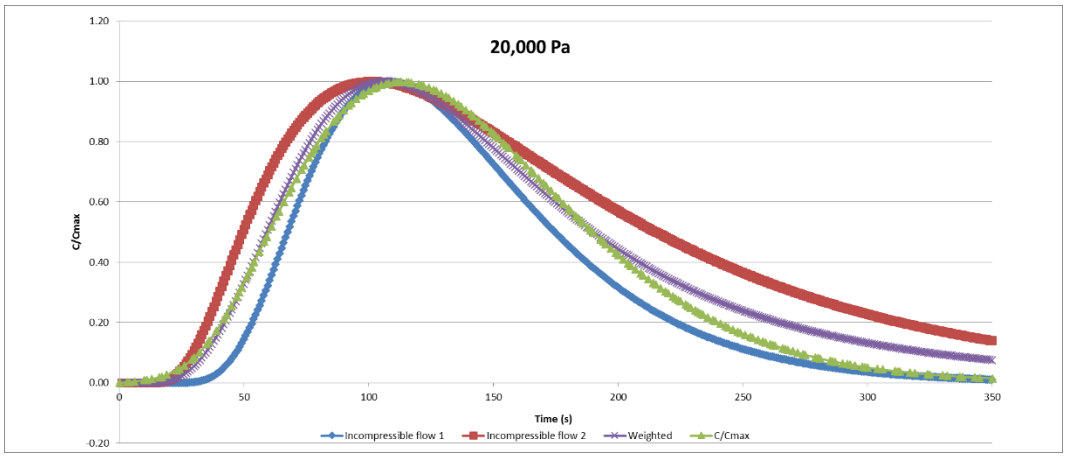

Analytical modelling results for xenon at 20,000 Pa.

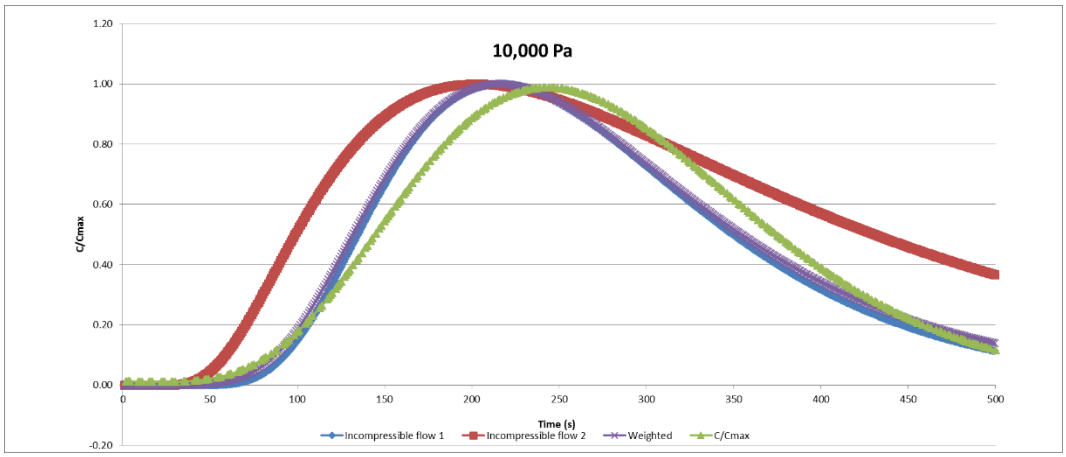

Analytical modelling results for xenon at 10,000 Pa.

SF_6 results

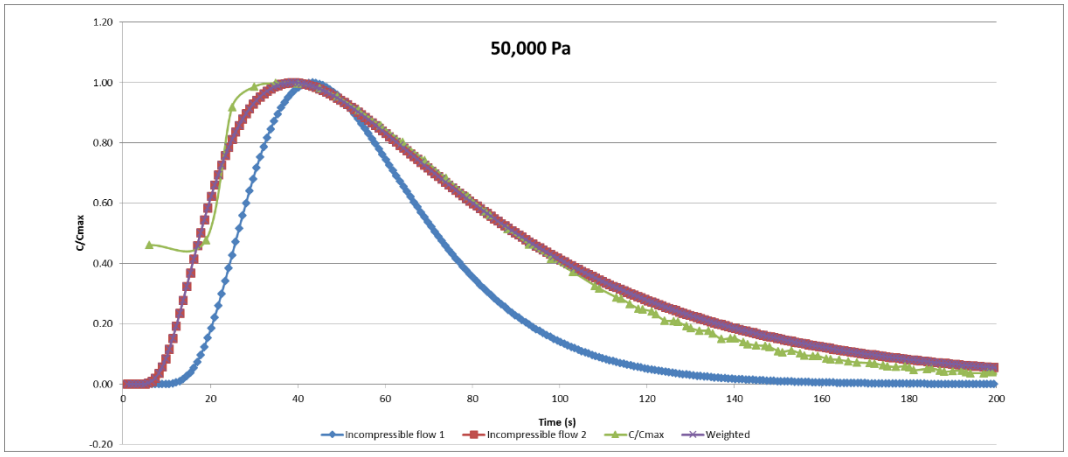

Analytical modelling results for SF_6 at 50,000 Pa.

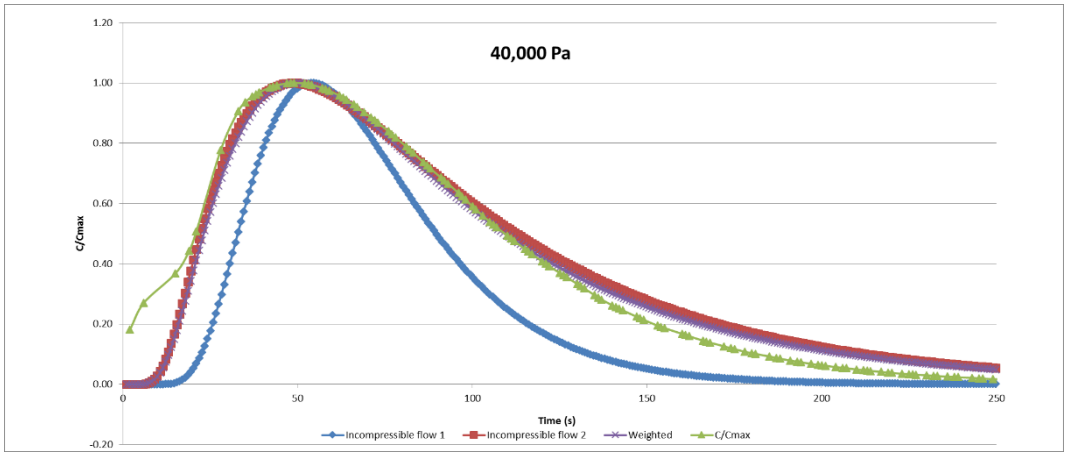

Analytical modelling results for SF_6 at 40,000 Pa.

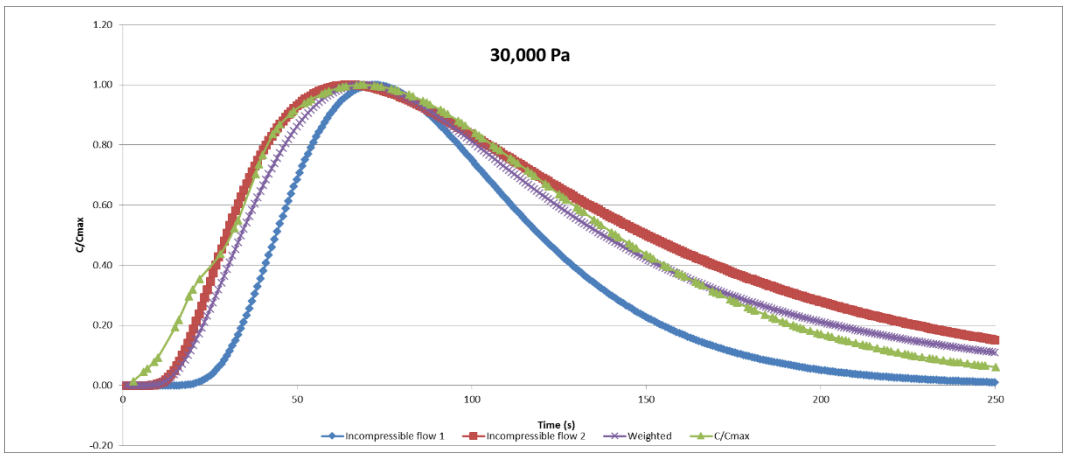

Analytical modelling results for SF_6 at 30,000 Pa.

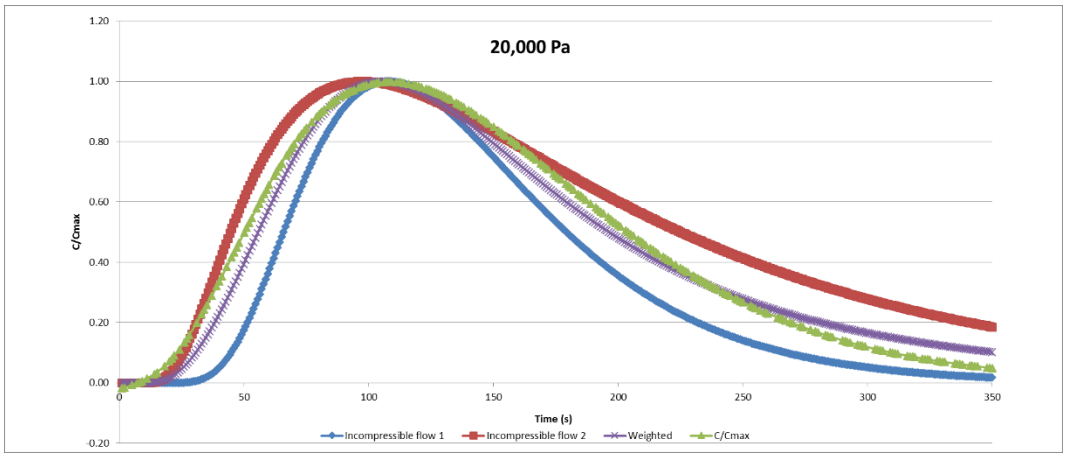

Analytical modelling results for SF_6 at 20,000 Pa.

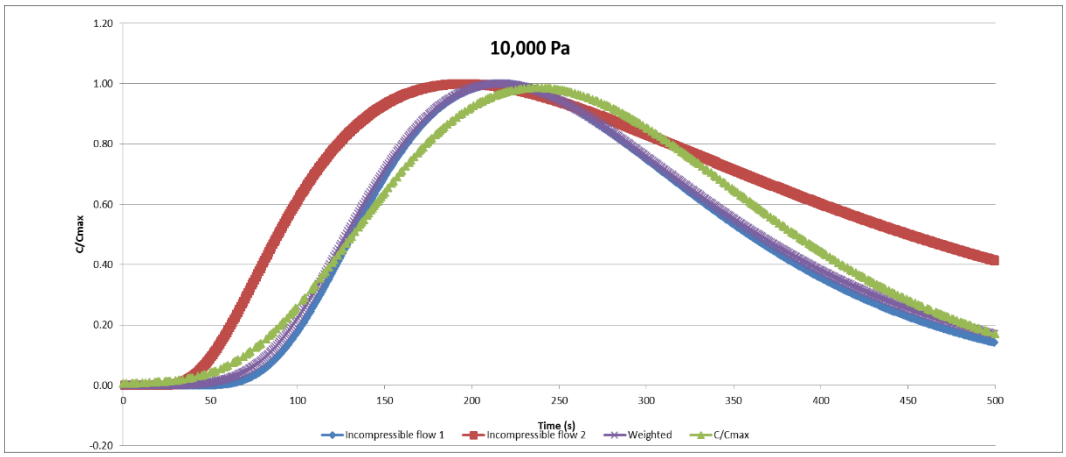

Analytical modelling results for SF_6 at 10,000 Pa.

CO_2 results

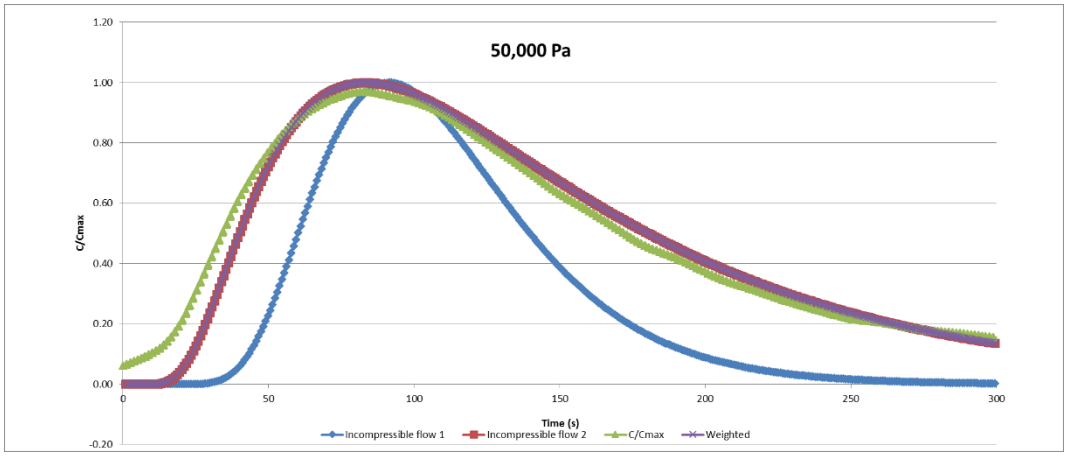

Analytical modelling results for CO_2 at 50,000 Pa.

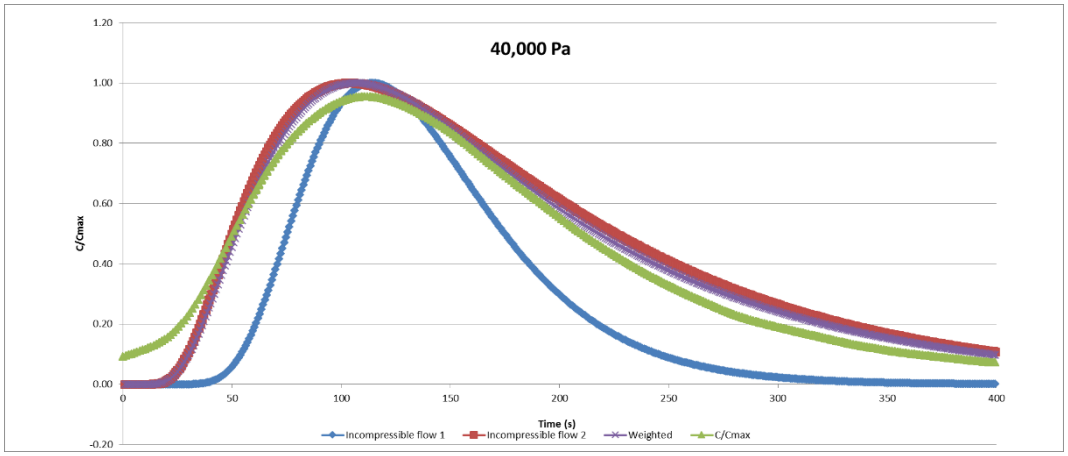

Analytical modelling results for CO_2 at 40,000 Pa.

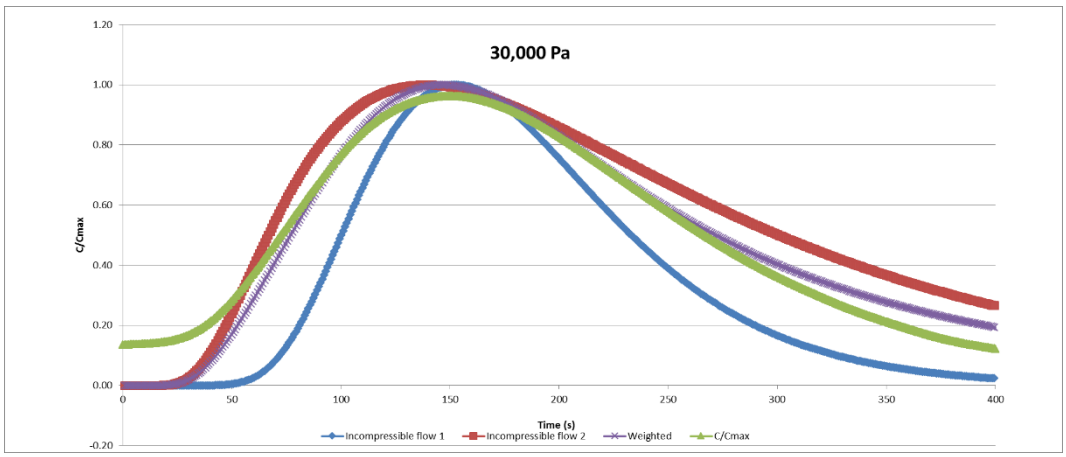

Analytical modelling results for CO_2 at 30,000 Pa.

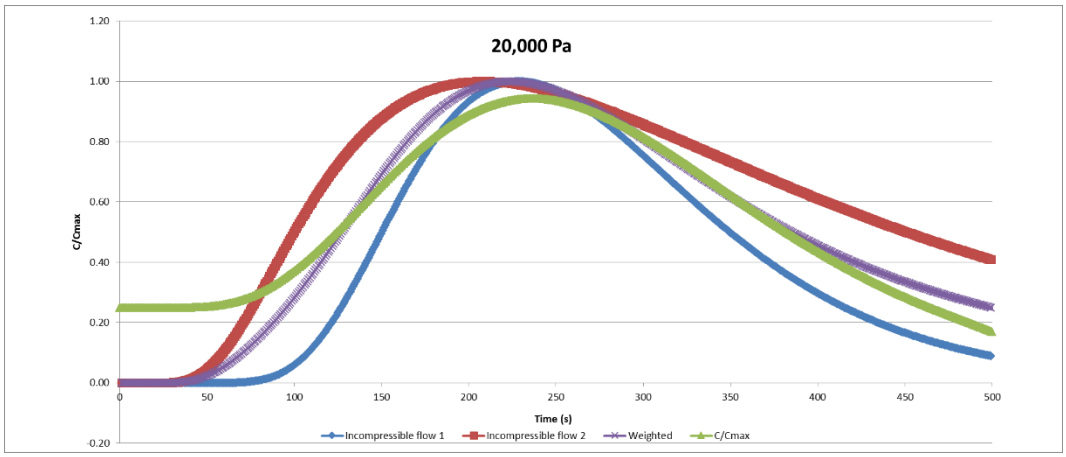

Analytical modelling results for CO_2 at 20,000 Pa.

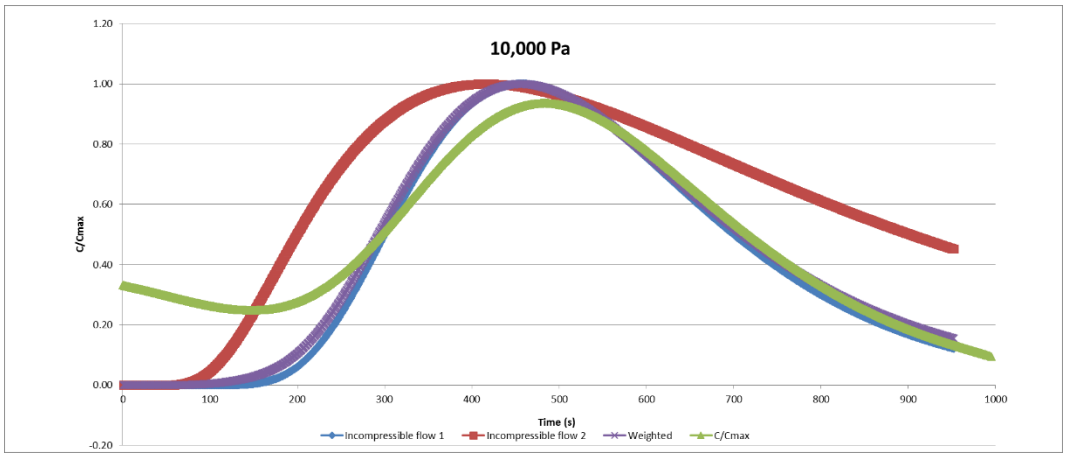

Analytical modelling results for CO_2 at 10,000 Pa.

Appendix V

Electronic version of raw output files

The raw output files for the experiments referenced in this research are available electronically.